Karlsruher Institut für Technologie

# Chiral Light–Matter Interactions Across Length Scales

Zur Erlangung des akademischen Grades eines

DOKTORS DER NATURWISSENSCHAFTEN (Dr. rer. nat.)

von der KIT-Fakultät für Physik des
Karlsruher Instituts für Technologie (KIT)
angenommene

DISSERTATION

von

M.Sc. Lukas Maria Rebholz

| | |
|---|---|
| Tag der mündlichen Prüfung: | 31. Juli 2026 |
| Referent: | Prof. Dr. Carsten Rockstuhl |
| Korreferent: | Prof. Dr. N. Asger Mortensen |

# *Acknowledgments*

Throughout the years of my doctoral research, I had the privilege to be surrounded by truly remarkable people. I want to take the opportunity to express my gratitude, as their support was indispensable.

First and foremost, I want to thank Prof. Dr. Carsten Rockstuhl for his guidance and continuous support throughout the past years. As others have remarked before me, his supervision strikes a well-tempered balance of insightful advice and intellectual freedom, and I feel very lucky to have experienced it. Despite leading a large group, he proactively took the time for in-person discussions, making me feel encouraged and valued. I value and admire his ability to communicate transparently, even in challenging times. I thank Dr. Ivan Fernandez-Corbaton for his mentorship and numerous discussions, and for seeding the topic that became an exciting playground for my thesis research. He fosters a sense of non-conformism that inspires me to approach established concepts from a different angle, deepening my understanding. I thank Prof. Dr. Asger Mortensen for kindly agreeing to serve as second examiner to this dissertation.

The research in this thesis is the result of collaborative efforts, and I would like to thank the following people for their contributions. I am grateful to Prof. Dr. Wiktor Lewandowski and his group, whose ideas and inquiries inspired several of the works in this thesis. I thank Dr. Maria Paszkiewicz-Idzik for our work on whispering gallery mode resonators, which allowed me to revisit topics from my Master's thesis. I am also grateful to her for proofreading my thesis and for simply being a wonderful person. I thank Dr. Marjan Krstić for quantum-chemical simulations, as well as for the board game nights and his respect (in actions, though never in words) for my dietary habits. I thank Dr. Benedikt Zerulla for his support with the multi-scale approach and for being a major inspiration when I was choosing where to pursue my doctorate. I thank PD Dr. Tilo Arens and Dr. Raphael Schurr from the Department of Mathematics for discussions on free-form optimization and boundary element methods, and for generously forgiving the occasional lack of rigor that physicists are rumored to exhibit.

I am grateful for funding by the Deutsche Forschungsgemeinschaft (DFG, German Research Foundation) – Project-ID 258734477 – SFB 1173. I am also grateful for funding by the Karlsruhe School of Optics & Photonics (KSOP)

and for the extracurricular modules they offer, which allowed me to gain insights outside of my research. Within KSOP, I am thankful to Dr. Danays Kunka for her warm and understanding mentorship.

For support in administrative and organizational matters, I thank Helena Wöhr and Hannah Belli. I consider my ability to remain largely unaware of many of these aspects as evidence of their excellent work. Similarly, I thank Laurette Lauffer and Sonja Becker for administrative support related to SFB 1173. I thank Dr. Andreas Poenicke for IT support, and Christian Knieling for being a kind and always helpful contact for various aspects.

My daily life was enriched by the many people I got to work alongside in this endeavor. While this applies to all members of the group (truly), I want to highlight some of them: I thank Dr. Dominik Beutel and Dr. Yannick Augenstein, members of the "old guard" (purely honorary)—shining examples of scientific mastery who helped me in various ways get started with my doctoral research. Thanks to Dr. Elli Stamatopoulou, whose own thesis I not only regard as an exceptional example, but who also read parts of my thesis, which helped me refine it. And I thank Jan David Fischbach, who has an unparalleled ability to act as a conversation partner for bouncing ideas off, seemingly regardless of the topic at hand, and who also proofread parts of this thesis. I was lucky to be surrounded by kind and inspiring people in my office. While all of them had a lasting impact on my experience, I have to mention Pascal Scherer, who single-handedly created an unmatched office atmosphere that regularly brightened my days (and for his exquisite taste in music). I also want to thank Oliver Kuster for his friendship throughout my studies and for inspiring my choice of working group.

Finally, I want to thank Dr. Markus Neuwirth and Dr. Simon Woska, who not only were excellent supervisors and mentors accompanying me through the various stages of my studies but remained close friends since then; Dr. Pascal Rietz, who, as a peer and a friend, continues to inspire me, not least by exhibiting a pool of foundational knowledge that is hard to find; and Dr. Max Neukum, who appears as an unconditional, calm presence in my life and who helped alleviate stressful moments during the writing phase. My thanks go to my family, especially for their patience; particularly to my brother, Augustinus, and my sister-in-law, Claudi, who were there for me in so many ways; to my parents, whom I can never thank enough for their unwavering support; and to Ivanina, without whom none of this would make nearly as much sense.

# *Abstract*

Chiral light–matter interactions underpin the spectroscopic characterization of chiral molecular systems and are central to prospective all-optical implementations of enantioselective applications in chemistry and pharmacology. This dissertation develops and applies theoretical and numerical methods to describe chiral light–matter interactions across length scales, from microscopic scatterers to macroscopic photonic structures, and in particular uses them to design a highly helicity-biased chiral optical cavity.

As a theoretical foundation, we formulate linear optical media via constitutive relations, discussing in particular the magnetic–electric cross-coupling characterizing chirality, and we express electromagnetic waves in terms of helicity eigenfunctions. Combining these formulations, we employ transition and scattering matrix formalisms for chiral light–matter interactions with localized and planar systems, respectively, including analytic expressions for spherical scatterers and planar interfaces between chiral media.

Utilizing these formalisms, we investigate how different manifestations of chirality contribute to the overall optical response. For finite scatterers with chiral geometries and composed of chiral media, we show that circular dichroism can be decomposed, to an excellent approximation, into separate material and geometric contributions. We exploit the smallness of typical material chirality parameters to devise an efficient approximation scheme for chirality-dependent transition matrices and derived spectroscopic quantities. For chiral arrangements of achiral plasmonic nanoparticles, we demonstrate strongly enhanced, bisignate circular dichroism arising from the coupling between the particles and analyze the role of higher multipoles in accurate modeling.

Finally, we optimize an electromagnetically chiral silver helix, reaching 95 % of the ideal helicity selectivity, and use arrays of such helices to realize a chiral optical cavity that supports eigenmodes of nearly pure helicity and exhibits a helicity-selective contrast in resonant intensity enhancement of three orders of magnitude. The resulting dissymmetry of up to 94 % illustrates how microscopic chiral building blocks can imprint their response onto macroscopic devices, providing a chiral electromagnetic environment suitable for future enantioselective optical applications.

# *Kurzfassung*

Chirale Licht-Materie-Wechselwirkungen bilden die Grundlage für die spektroskopische Charakterisierung chiraler Moleküle und spielen eine zentrale Rolle bei der weiteren Entwicklung enantioselektiver Anwendungen in der Chemie und Pharmakologie. In dieser Dissertation werden theoretische und numerische Methoden entwickelt und angewendet, um chirale Licht-Materie-Wechselwirkungen über verschiedene Längenskalen hinweg zu beschreiben – von mikroskopischen Streuern bis hin zu makroskopischen photonischen Strukturen. Diese Methoden werden insbesondere genutzt, um einen chiralen optischen Resonator aus Spiegeln mit stark ausgeprägter Helizitätselektivität zu entwerfen.

Die theoretische Grundlage bildet die Beschreibung linearer optischer Medien mittels Konstitutivgleichungen. Hierbei wird insbesondere die für chirale Medien charakteristische magnetoelektrische Kopplung diskutiert. Des Weiteren werden elektromagnetische Wellen als Eigenfunktionen der Helizität dargestellt. Darauf aufbauend kommen T-Matrix- und Streumatrixformalismen bei der Beschreibung chiraler Licht-Materie-Wechselwirkungen in lokalisierten beziehungsweise planaren Systemen zur Anwendung, einschließlich analytischer Ausdrücke für sphärische Streuer und planare Grenzflächen zwischen chiralen Medien.

Unter Verwendung dieser Formalismen wird untersucht, wie verschiedene Ausprägungen von Chiralität zur optischen Gesamtantwort beitragen. Für endliche Streuer mit chiralen Geometrien, die aus chiralen Medien bestehen, lässt sich der Zirkulardichroismus in ausgezeichneter Näherung in getrennte material- und geometriebezogene Beiträge zerlegen. Die geringe Größe typischer Materialchiralitätsparameter ermöglicht zudem die Entwicklung eines effizienten Approximationsschemas für chiralitätsabhängige T-Matrizen und davon abgeleitete spektroskopische Größen. Darüber hinaus zeigen chirale Anordnungen achiraler plasmonischer Nanopartikel einen stark ausgeprägten, bisignaten Zirkulardichroismus, der durch die Kopplung zwischen den Partikeln hervorgerufen wird. Hierbei wird unter anderem die Relevanz höherer Multipole für eine genaue Modellierung analysiert.

Abschließend wird eine elektromagnetisch chirale Silberhelix optimiert, wobei 95 % der maximal möglichen Helizitätsselektivität erreicht werden.

Mit Gitteranordnungen solcher Helices lässt sich ein chiraler optischer Resonator realisieren, der Eigenmoden nahezu reiner Helizität unterstützt und einen helizitätsselektiven Kontrast der resonanten Intensitätsüberhöhung von drei Größenordnungen aufweist. Die daraus resultierende Dissymmetrie von bis zu 94 % veranschaulicht, wie mikroskopische chirale Bausteine ihr Ansprechverhalten auf makroskopische Strukturen übertragen können. Dadurch wird eine chirale elektromagnetische Umgebung geschaffen, die sich für zukünftige enantioselektive optische Anwendungen eignet.

# *Contents*

# *List of Figures*

# *Acronyms*

Acronyms are introduced and used within the main body of text. Full terms are retained in the Introduction and Conclusions for contextual independence.

CD circular dichroism 24, 85

FEM finite element method 56

OR optical rotation 24, 86

SVD singular value decomposition 139

TIR total internal reflection 77

VPW vector plane wave 34, 203, 220
VSH vector spherical harmonic 35, 193, 217
VSW vector spherical wave 35, 191, 215

# 1 *Introduction*

In 1811, French physicist François Arago observed colors when he looked through a polarizer at white light passing through a quartz crystal [1]. He had just seen, for the first time, the effect of optical rotatory dispersion. An explanation followed soon after, brought forward in 1812 by Jean-Baptiste Biot. Biot also discovered that optical rotation could be observed in naturally occurring liquids such as turpentines and solutions of camphor or cane sugar [1]. This series of discoveries culminated in 1848, when Louis Pasteur demonstrated that molecular chirality was the cause of optical rotation and physically separated the mirror-image crystals of tartaric acid, thus providing the first active separation of enantiomers of a chiral molecule [2].

These discoveries mark the beginnings of the concept of chirality, which refers to objects—for instance, molecules—that cannot be brought to coincide with their own mirror image, as in the example of a left and a right hand. From its very conceptualization, chirality was innately manifested in the interaction between light and matter, and, stated in summary, "[no natural phenomenon] has had so profound an effect on chemical thought as that of natural optical rotatory power." [3] Subsequent investigations in the late 19th and the early 20th century revealed the vital importance of molecular chirality for the biochemical reactions occurring in living organisms [4]. The efficacy of these reactions often critically depends on matching enantiomers [5–8], and adverse effects of a mismatch can be as harsh as toxicity, as vividly demonstrated by the thalidomide scandal of the 1960s [9]. Optical rotation and the closely related phenomenon of circular dichroism—which is the contrast between the absorption of left-handed and right-handed circularly polarized light—provide powerful tools to sense and detect the enantiomeric composition of chiral molecular compounds, and thus enable the control and quality assurance of medical drugs [10–14].

The vital importance of chirality in pharmaceutical and pharmacological contexts, however, necessitates not only the detection but also the direct manipulation of the enantiomeric composition of a medical drug. In the ideal case, the active control of the enantiomeric composition happens directly during the synthesis of the compound. The importance of controlling the synthesis of enantiomers for contemporary societal needs was recognized

with two Nobel prizes in chemistry, awarded in 2001 and 2021, respectively [15, 16]. Current established techniques are based on asymmetric catalytic reactions [17–19]. Despite the historic inseparability of chirality and light–matter interactions, the potential of all-optical realizations for the active manipulation of the enantiomeric composition of a chiral chemical compound remains largely untapped. While the principal possibility of biasing chemical synthesis toward one of the enantiomers, creating enantiomeric excess, has been demonstrated, the extent of the effect remains extremely small [20, 21]. Therefore, while conceptually proven, utilizing light–matter interactions for these purposes is far from a practical implementation that would support the purity and throughput needed for large-scale bulk synthesis of medically active compounds. The reason can be seen in the typically weak chiral optical response of molecules, which can be related to the small spatial dimensions of chiral molecules as compared to the wavelength of light, ranging from the ultraviolet to the infrared, that excites such molecules [22–25]. However, a large-scale realization of optical technologies for these endeavors, enabling asymmetric *photocatalysis*, offers unique advantages: Conventional asymmetric synthesis requires complex chiral catalysts, often metal complexes with chiral ligands, which themselves have to be prepared enantiomerically pure, or sacrificial chiral auxiliaries, which must later be separated and disposed of or regenerated for reuse [21, 26–28]. Utilizing light for these purposes instead reduces the chemical footprint, offering a green alternative [29–31].

Consolidating the chiral interaction between light and matter, to facilitate not only a passive, observing role but to enact an active influence on vital applications as the ones outlined above, requires overcoming the faintness of effects due to the innate weakness of chiral molecular optical responses. This challenge is faced on two sides: On the side of chemical reactions, certain pathways hold promise in amplifying the influence of circularly polarized light on enantiomeric excess. These pathways rely on autocatalytic amplification, which means that a product of the reaction acts itself as a catalyst for the reaction. Such reactions have been shown to amplify the enantiomeric excess induced by circularly polarized light, which is usually characterized by a single-digit percentage, up to more than 99 % [32, 33]. However, as such possibilities are inherently tied to the specific chemical compound and pathway under consideration, these schemes do not yet

provide a universal solution to the challenge and may be out of reach for many of the medically active substances of relevance.

On the other side stands our control of chiral light and its enhancement, to overcome the small effects tied to weak responses by concentrating the power of the light and thereby scaling the resulting outcome. Structures exhibiting strong chiral near fields or configurations of superchiral light can locally compensate the weak response by a high-powered stimulus [34, 35]. A particular technology to be highlighted in this context are chiral optical cavities—optical devices that enable the resonant enhancement of light while maintaining and enforcing a strong bias toward one helicity or circular polarization handedness of light [36–39]. Such cavities have the potential to extend the small volumes, to which the effect of near-field-based structures or localized superchiral hot spots are confined, to electromagnetically large volumes. With the further potential to process liquid-phase reactants inside the cavity using microfluidic techniques [40, 41], chiral optical cavities have the potential to be scaled to match the demands of commercial, large-scale pharmaceutical applications.

All of these devices, from structures enhancing chiral near fields to chiral optical cavities, hinge on our ever-increasing understanding of chiral light–matter interactions. They rely on our ability to devise and manufacture mesoscopic and macroscopic photonic structures—matter—to manipulate light and tailor its chiral properties. These chiral properties in turn influence chiral molecular matter, as in the outlined enantioselective applications. All such approaches require a fundamental understanding of the chiral interactions between light and matter, which, in turn, enables the rational design of structures for enantioselective and other chiral applications.

Situated within this broader effort, this dissertation aims to deepen our understanding of the chiral interaction between light and matter, and uses these aspects, along with the formalisms introduced, to propose a chiral optical cavity. To this end, the results of several published investigations on these topics—which were developed as part of the author's doctoral research—are presented and augmented and extended by previously unpublished original contributions to this dissertation. In particular, this dissertation acknowledges the different causes whose interplay determines the chiral optical response of a given object: The chirality of a medium, which derives from the chirality of its molecular constituents, as well as the chirality of the

geometric shape of an object composed of this material, both contribute to the object's overall chiral response. Both causes of chirality—material and geometric—are fundamentally linked to the absence of spatial inversion and mirror symmetry in the entity in question. In physical reality, however, these causes of chirality are separated from one another by the length scales on which they manifest, and consequently, they are distinguished in the formalism by the concepts used to represent them. As one moves up the scales, chirality may not be bound to a single object, or the medium of which it is composed, at all: Assemblies of resonant metallic nanoparticles demonstrate how strong chiral responses arise solely based on their spatially distributed, chiral arrangement, even though the individual particles are achiral. In this case, chirality is not represented by a dedicated concept at the level of formalism, but rather becomes an emergent feature of the description of the interaction between the particles, thereby drawing attention to the coupling of the responses of the individual objects. The research in this dissertation focuses on systems subject to various influences of these causes of chirality and investigates how these causes can be isolated under suitable conditions and, in turn, utilized to tailor or optimize chiral optical responses. Finally, a microscopic chiral object can influence the chirality in a macroscopic structure by imprinting its chiral optical response onto the electromagnetic waves hosted inside the larger optical device. This principle underlies the specific design of the chiral optical cavity that we propose here. Taken together, the results presented in this dissertation provide insights into the interplay of the causes of chirality on different length scales and propose a design for a chiral optical cavity that might enable us to find all-optical solutions to the challenges posed by vital enantioselective applications.

*Outline* · This thesis is structured in two parts. Chapters 2 to 4 introduce the concepts used in our explanations and the formalisms employed in our numerical modeling, thereby laying the foundation for the subsequent investigations into chiral light–matter interactions across multiple length scales. Chapters 5 and 6 primarily present and discuss the results of several studies we have published on aspects of chiral light–matter interactions and chiral optical cavities, as well as original contributions in this dissertation. Although the dissertation follows a logical progression in the order in which various aspects are presented, the first part (Chapters 2 to 4) may be regarded

as reference for the discussion of the results in the second part. This applies in particular to Chapter 4, which contains detailed derivations for relevant quantities in the introduced formalisms, formulated explicitly with chirality in mind; a summary of the most important relations is included at the end of that chapter as a reference. In our works in Chapters 5 and 6, we refer as needed to the relations and discussions relevant for understanding the subject matter. In the following, we provide a brief overview of the topics covered in the individual chapters.

In Chapter 2, we introduce the fundamental description of linear optical media in electrodynamics. We discuss the representation of linear media using constitutive relations. We focus in particular on the origins of the chirality parameter, which provides the effective description of the chirality of a macroscopic medium resulting from its chiral molecular constituents.

In Chapter 3, we discuss monochromatic electromagnetic waves in chiral media. We specify two types of wave solutions, namely vector spherical waves and vector plane waves. These are used, respectively, in the subsequent description of the interaction of light with spatially localized and planar systems. The structure of the equations governing electromagnetic waves in chiral media reveals the significance of circular polarization in facilitating their solution. Therefore, we introduce helicity, which generalizes the concept of the handedness of circular polarization—generally well-defined only for vector plane waves—to arbitrary field configurations and, in particular, to vector spherical waves. Helicity is the appropriate representation of the chirality of light.

In Chapter 4, we combine the descriptions of light and matter to characterize their interaction. We consider the scattering of electromagnetic waves by spatially localized, finite scatterers as well as by planar, infinitely extended systems. For these cases, we introduce the transition matrix formalism and the scattering matrix formalism, respectively, which facilitate our subsequent investigations. Spectroscopically relevant quantities, such as cross-sections of finite scatterers and the power transmission and reflection coefficients of a planar system, are expressed within the framework of the respective formalism, and their detailed derivations are provided. With regard to chiral light–matter interactions, the derivations and discussions in this chapter are formulated taking chirality and helicity into account.

In Chapter 5, we turn our attention to the chiral interaction between light

and matter and begin by discussing the interaction with localized objects on microscopic to mesoscopic length scales. We start with an introduction to the geometric concept of chirality and the spectroscopic quantities used in its analysis, namely, optical rotation and circular dichroism. Focusing on circular dichroism, in Section 5.2 we discuss the interplay of material and geometric chirality in shaping the chiral optical response of a scattering object. We investigate the possibility of isolating contributions associated with the two separate causes, and we propose an approximation scheme that enables the efficient computation of transition matrices and spectroscopic quantities for objects when their dispersive material chirality parameter is varied. The results presented here include, in particular, our work published in Ref. [P9] as well as original contributions to this dissertation, which expand upon the scope of the previously published study.

In Section 5.3, we consider chirality as an emergent property of the distributed spatial arrangement of achiral metallic nanoparticles. Their strong chiral optical response is related to plasmonic resonances supported by the individual particles, and we identify the coupling between the particles, which is the primary cause of the pronounced circular dichroism signals observed in these systems. Results discussed here include those published in Ref. [P3] and are refined and augmented by additional considerations.

The final section of Chapter 5, Section 5.4, addresses the optimization of small chiral scatterers with the objective of maximizing their chiral optical response. To this end, we introduce the concept of electromagnetic chirality, which provides a holistic measure for the chirality of the optical response. Using electromagnetic chirality as the objective function, we obtain optimized scatterers that exhibit a pronounced contrast between their interaction with light of positive and negative helicity (e.g., left- and right-handed circularly polarized light). These optimized scatterers are at the core of the proposed design for a chiral optical cavity, and their optimization was discussed in the corresponding publication, Ref. [P2].

In the concluding thematic chapter, Chapter 6, we present our design for a chiral optical cavity. The results discussed there were largely published in Ref. [P2]. First, we investigate planar mirrors consisting of a periodic array of the optimized chiral scatterers placed on a substrate. We characterize their reflection properties, evaluate their performance, and explain the underlying physical effects. Next, we examine the cavity formed by these chiral mirrors

and analyze its eigenmodes. We demonstrate the preference for a specific helicity induced by the optimized chiral scatterers, which could enable the large-scale optical implementation of enantioselective applications in future work.

We conclude with a summary of the most important aspects and results of this dissertation and an outlook on possible future research directions in Chapter 7.

# 2 *Fundamentals of Classical Electrodynamics*

In preparation for our study of chiral light–matter interactions, the first chapters of this work introduce the concepts and formalisms that we rely on in our analyses. At their foundation lies the description of electromagnetic fields in optical media. In the subsequent chapters, the fundamentals introduced here extend to the description light—electromagnetic waves—and its scattering from systems made of chiral media.

In this chapter, we introduce the electromagnetic fields and their governing equations, Maxwell's equations. We consider the linear optical properties of media, leading to constitutive relations for the fields. Particular emphasis is put on the properties and origins of chirality in the constitutive relations. Finally, we discuss the continuity of the electromagnetic fields at interfaces between media, a prerequisite for our description of scattering of electromagnetic waves.

At its core, classical electrodynamics deals with electric charges and electric and magnetic fields. Formally, the charges constitute two related quantities, the spatially distributed and time-dependent charge density $\rho(\boldsymbol{r}, t)$ as well as the current density $\boldsymbol{J}(\boldsymbol{r}, t)$ capturing the charges' motion. As total charge is conserved, the local change of the charge density is entirely determined by the in- and outflow given by the current density. Formally, these densities are related by the continuity equation

$$\frac{\partial}{\partial t}\rho(\boldsymbol{r}, t) + \boldsymbol{\nabla} \cdot \boldsymbol{J}(\boldsymbol{r}, t) = 0. \tag{2.1}$$

The fields are represented by two more quantities, namely, the spatially and time-dependent electric field strength $\boldsymbol{E}(\boldsymbol{r}, t)$ as well as the magnetic flux density $\boldsymbol{B}(\boldsymbol{r}, t)$. The effects of the electric and magnetic fields are evident in the forces they exert on charges. Particularly, an isolated particle at a position $\boldsymbol{r}$ with electric charge $q$ moving with a velocity $\boldsymbol{v} \coloneqq \frac{\mathrm{d}}{\mathrm{d}t}\boldsymbol{r}$ in the presence of electric and magnetic fields experiences the Lorentz force

$$\boldsymbol{F} = q(\boldsymbol{E} + \boldsymbol{v} \times \boldsymbol{B}). \tag{2.2}$$

Conversely, the charges source the electric and magnetic fields. This fact is captured in Maxwell's equations.

## 2.1 *Maxwell's Equations*

Maxwell's equations read [42]

$$\boldsymbol{\nabla} \cdot \boldsymbol{E}(\boldsymbol{r}, t) = \frac{1}{\varepsilon_0} \rho(\boldsymbol{r}, t), \tag{2.3a}$$

$$\boldsymbol{\nabla} \times \boldsymbol{B}(\boldsymbol{r}, t) - \varepsilon_0 \mu_0 \frac{\partial}{\partial t} \boldsymbol{E}(\boldsymbol{r}, t) = \mu_0 \boldsymbol{J}(\boldsymbol{r}, t), \tag{2.3b}$$

$$\boldsymbol{\nabla} \times \boldsymbol{E}(\boldsymbol{r}, t) + \frac{\partial}{\partial t} \boldsymbol{B}(\boldsymbol{r}, t) = 0, \tag{2.3c}$$

$$\boldsymbol{\nabla} \cdot \boldsymbol{B}(\boldsymbol{r}, t) = 0, \tag{2.3d}$$

with the physical constants $\varepsilon_0$, the vacuum permittivity, and $\mu_0$, the vacuum permeability. Equations (2.3a) and (2.3b), the inhomogeneous equations, describe how electric charges act as sources to the electric and magnetic fields. These equations are complemented by the homogeneous equations, Eqs. (2.3c) and (2.3d). In analogy to Eq. (2.3a), Eq. (2.3d) expresses the absence of magnetic charges. Equation (2.3c) unveils the interdependence of electric and magnetic fields independently of the presence of sources. It links the electric and magnetic fields, which is why they are collectively referred to as *electromagnetic* fields. We will expand on this notion in Chapter 3.

Combined with Newton's second law of motion, Eqs. (2.2) and (2.3) are conceptually sufficient to describe the classical dynamics of electrically charged particles and electromagnetic fields. However, in most material systems, it is neither feasible nor useful to capture the entire dynamics of numerous charges and the related fields. Instead, one tries to describe the collective behavior of the charges contained in a material as a bulk property. For this purpose, auxiliary fields are being introduced, which alter the appearance of Maxwell's equations. Attesting the fact that an exact description on the microscopic scale is given up in favor of a simpler description, the resulting modified set of equations is also called the *macroscopic* Maxwell equations.

### 2.1.1 *External and induced charge and current densities*

Following phenomenological considerations, we acknowledge that it is impractical to treat all charges the same; for example, the charges bound in

molecules inside a material medium express themselves differently from free ones. Therefore, it is convenient to separate the charge density into an *external* and an *induced* part,

$$\rho(\boldsymbol{r},t) = \rho_{\text{ext}}(\boldsymbol{r},t) + \rho_{\text{ind}}(\boldsymbol{r},t). \tag{2.4}$$

Above separation is chosen such that the external charge density, integrated over a macroscopic volume, accounts for the total contained charge. Conversely, the induced part is restricted to have net zero charge. For instance, it may account for the relative dislocation between opposite charges as a result of being exposed to an electric field. To capture such contributions, we introduce the *electric polarization density* $\boldsymbol{P}(\boldsymbol{r},t)$, with $\rho_{\text{ind}}(\boldsymbol{r},t) = -\boldsymbol{\nabla}\cdot\boldsymbol{P}(\boldsymbol{r},t)$.

Similarly, the current density is separated as

$$\boldsymbol{J}(\boldsymbol{r},t) = \boldsymbol{J}_{\text{ext}}(\boldsymbol{r},t) + \boldsymbol{J}_{\text{ind}}(\boldsymbol{r},t) + \boldsymbol{J}_{\text{mag}}(\boldsymbol{r},t), \tag{2.5}$$

including an external contribution related to external charges by Eq. (2.1) and the contribution of induced currents, $\boldsymbol{J}_{\text{ind}}(\boldsymbol{r},t) = \frac{\partial}{\partial t}\boldsymbol{P}(\boldsymbol{r},t)$, which also satisfies the corresponding continuity relation with $\rho_{\text{ind}}(\boldsymbol{r},t)$. The third term on the right-hand side captures stationary[1] current loops, which, for example, can describe the effect of magnetic moments in magnetic media. Using that the divergence of such current density vanishes, we recast it by introducing the *magnetization density* $\boldsymbol{M}(\boldsymbol{r},t)$ satisfying $\boldsymbol{J}_{\text{mag}}(\boldsymbol{r},t) = \boldsymbol{\nabla}\times\boldsymbol{M}(\boldsymbol{r},t)$. Generally, we use the magnetization density to describe the response of magnetic media.

1 *Stationary* referring to currents that leave the local charge density unchanged. Accordingly, the magnetization current density is free of divergence.

### 2.1.2 *Macroscopic equations and auxiliary fields*

To collectively account for the fields as well as their induced responses, the auxiliary fields $\boldsymbol{D}$ and $\boldsymbol{H}$ are defined. The *electric flux density* or *electric displacement field* is defined as

$$\boldsymbol{D}(\boldsymbol{r},t) = \varepsilon_0\boldsymbol{E}(\boldsymbol{r},t) + \boldsymbol{P}(\boldsymbol{r},t) \tag{2.6a}$$

and the *magnetic field strength* as

$$\boldsymbol{H}(\boldsymbol{r},t) = \mu_0^{-1}\boldsymbol{B}(\boldsymbol{r},t) - \boldsymbol{M}(\boldsymbol{r},t). \tag{2.6b}$$

Adopting the auxiliary fields, Maxwell's equations read

$$\boldsymbol{\nabla} \cdot \boldsymbol{D}(\boldsymbol{r}, t) = \rho_{\text{ext}}(\boldsymbol{r}, t), \tag{2.7a}$$

$$\boldsymbol{\nabla} \times \boldsymbol{H}(\boldsymbol{r}, t) - \frac{\partial}{\partial t} \boldsymbol{D}(\boldsymbol{r}, t) = \boldsymbol{J}_{\text{ext}}(\boldsymbol{r}, t), \tag{2.7b}$$

$$\boldsymbol{\nabla} \times \boldsymbol{E}(\boldsymbol{r}, t) + \frac{\partial}{\partial t} \boldsymbol{B}(\boldsymbol{r}, t) = 0, \tag{2.7c}$$

$$\boldsymbol{\nabla} \cdot \boldsymbol{B}(\boldsymbol{r}, t) = 0. \tag{2.7d}$$

For a complete description, the macroscopic Maxwell equations, Eqs. (2.7), additionally require relations between the auxiliary fields and the fundamental electric and magnetic fields causing them or, equivalently, between the polarization and magnetization densities and the fields. Explicitly, we seek relations for $\boldsymbol{D}(\boldsymbol{E}, \boldsymbol{B})$ and $\boldsymbol{H}(\boldsymbol{E}, \boldsymbol{B})$ to complement Eqs. (2.6). These relations constitute the macroscopic description of continuous matter and are called *constitutive relations*. We discuss constitutive relations that describe the optical properties of linear media in the next section.

## 2.2 *Linear Media*

Below, we describe linear electromagnetic properties of media using suitable constitutive relations. We focus on constitutive relations exhibiting magnetic–electric cross-coupling, a prerequisite for chiral media. Based on the structure of the constitutive relations, we introduce a classification of linear media.

### 2.2.1 *Time domain response functions*

To arrive at constitutive relations, the auxiliary fields are interpreted as a medium's response to the electromagnetic fields. We continue with the following two assumptions. First, we assume the response to be *linear* in the fields. Second, we restrict ourselves to a *local* response, that is, the auxiliary fields at a position $\boldsymbol{r}$ depend only on the fields at that same position $\boldsymbol{r}$. We will

revisit the second assumption later. For now, however, these assumptions allow us to write, for a homogeneous medium [43],

$$D_i(\boldsymbol{r},t) = \varepsilon_0 E_i(\boldsymbol{r},t) + \int_{-\infty}^{\infty} \mathrm{d}t' \, \left( R_{ij}^{\mathrm{ee}}(t,t') E_j(\boldsymbol{r},t') + R_{ij}^{\mathrm{em}}(t,t') B_j(\boldsymbol{r},t') \right), \tag{2.8a}$$

$$H_i(\boldsymbol{r},t) = \mu_0^{-1} B_i(\boldsymbol{r},t) + \int_{-\infty}^{\infty} \mathrm{d}t' \, \left( R_{ij}^{\mathrm{me}}(t,t') E_j(\boldsymbol{r},t') + R_{ij}^{\mathrm{mm}}(t,t') B_j(\boldsymbol{r},t') \right). \tag{2.8b}$$

$R_{ij}(t,t')$ denote the media-dependent response functions, and $i$ and $j$ specify Cartesian components of the vector fields, where summation over repeated indices is implied.

Equations (2.8) describe the most general dependence of the auxiliary fields in terms of local linear response functions. The functional dependence of the response functions is simplified by further physical considerations. Excluding an explicit time dependence of the medium (i.e., assuming time homogeneity) restricts the temporal dependencies to be of the form $(t - t')$, turning the integrals in Eqs. (2.8) into convolutions. Furthermore, for a causal relation, the response functions need to be zero for $t' > t$. This restricts the upper bound of integration to $t$, and the auxiliary fields depend on the past but not the future of $\boldsymbol{E}$ and $\boldsymbol{B}$. [44]

### 2.2.2 *Frequency domain description*

Temporal homogeneity turns Eqs. (2.8) into convolutions between the response functions and the fields. We define the Fourier transform of a time dependent function $f(t)$ as

$$\tilde{f}(\omega) \coloneqq (\mathcal{F} f)(\omega) \coloneqq \frac{1}{\sqrt{2\pi}} \int_{-\infty}^{\infty} \mathrm{d}t \, f(t) \mathrm{e}^{\mathrm{i}\omega t} \tag{2.9a}$$

and the inverse Fourier transform as

$$\left(\mathcal{F}^{-1} \tilde{f}\right)(t) \coloneqq \frac{1}{\sqrt{2\pi}} \int_{-\infty}^{\infty} \mathrm{d}\omega \, \tilde{f}(\omega) \mathrm{e}^{-\mathrm{i}\omega t}, \tag{2.9b}$$

where, for suitable functions,[2] $f(t) = \left(\mathcal{F}^{-1} \tilde{f}\right)(t)$ by the Fourier inversion

[2] Including distributions.

theorem, allowing the original function to be reconstructed from its Fourier transform.

Applying the Fourier transform component-wise to Eqs. (2.8) and using the convolution theorem yields

$$\tilde{D}_i(\boldsymbol{r},\omega) = \left[\varepsilon_0\delta_{ij} + \sqrt{2\pi}\tilde{R}^{\mathrm{ee}}_{ij}(\omega)\right]\tilde{E}_j(\boldsymbol{r},\omega) + \sqrt{2\pi}\tilde{R}^{\mathrm{em}}_{ij}(\omega)\tilde{B}_j(\boldsymbol{r},\omega), \tag{2.10a}$$

$$\tilde{H}_i(\boldsymbol{r},\omega) = \sqrt{2\pi}\tilde{R}^{\mathrm{me}}_{ij}(\omega)\tilde{E}_j(\boldsymbol{r},\omega) + \left[\mu_0^{-1}\delta_{ij} + \sqrt{2\pi}\tilde{R}^{\mathrm{mm}}_{ij}(\omega)\right]\tilde{B}_j(\boldsymbol{r},\omega), \tag{2.10b}$$

$\delta_{ij} = \begin{cases} 1 & \text{if } i = j, \\ 0 & \text{otherwise.} \end{cases}$

with the Kronecker delta $\delta_{ij}$. According to Eqs. (2.10), the constitutive relations linking the auxiliary and the fundamental fields in frequency-domain are algebraic. For some discussions, including the ones in this work, it is useful to transform these relations into equivalent ones that relate $(\tilde{\boldsymbol{D}}, \tilde{\boldsymbol{B}})$ with $(\tilde{\boldsymbol{E}}, \tilde{\boldsymbol{H}})$. These can be written concisely as

$$\begin{pmatrix}\tilde{\boldsymbol{D}}(\boldsymbol{r},\omega)\\ \tilde{\boldsymbol{B}}(\boldsymbol{r},\omega)\end{pmatrix} = \begin{pmatrix}\varepsilon_0\boldsymbol{\varepsilon}(\omega) & \sqrt{\varepsilon_0\mu_0}\boldsymbol{\xi}(\omega)\\ \sqrt{\varepsilon_0\mu_0}\boldsymbol{\zeta}(\omega) & \mu_0\boldsymbol{\mu}(\omega)\end{pmatrix}\begin{pmatrix}\tilde{\boldsymbol{E}}(\boldsymbol{r},\omega)\\ \tilde{\boldsymbol{H}}(\boldsymbol{r},\omega)\end{pmatrix}. \tag{2.11}$$

With these relations, we introduce and define the relative *electric permittivity* tensor $\boldsymbol{\varepsilon}(\omega)$ and the relative *magnetic permeability* tensor $\boldsymbol{\mu}(\omega)$, as well as the magnetic–electric cross-coupling tensors $\boldsymbol{\xi}(\omega)$, $\boldsymbol{\zeta}(\omega)$, all of which are represented by $3 \times 3$ matrices. We will alternatively refer to these tensors collectively as *material parameters*.

Under the stated restrictions to linear responses, locality, and spatial and temporal homogeneity, Eq. (2.11) describes the most general constitutive relations in frequency domain, which complete the macroscopic Maxwell equations, Eqs. (2.7), if the material parameters are known. The material parameters are also the basis for the classification of linear media, which we will discuss later. However, so far, little motivation has been given for the origin of such constitutive relations and the magnetic–electric cross-coupling terms contained in Eqs. (2.8). For the remainder of this work, we are concerned with *chiral* matter. We will introduce the concept of chirality in more detail in Chapter 5; for now, we proceed with the notion that chirality implies that spatial inversion and mirror symmetries are broken. Considering fields of electric character, $\boldsymbol{D}$ and $\boldsymbol{E}$, as vectors and magnetic ones, $\boldsymbol{B}$ and $\boldsymbol{H}$, as pseudovectors,[3] we see that precisely the cross-coupling terms are responsible for breaking spatial inversion, as they relate fields of opposite character and must, therefore, themselves be odd under spatial

3 We call *vectors* such fields that change sign under spatial inversion (i.e., parity-odd) and *pseudovectors* those that do not (parity-even).

inversion. Hence, we recognize the cross-coupling terms as a prerequisite for discussing chiral aspects of matter and its interaction with light, and will illuminate this aspect first. Specifically, we highlight two perspectives for motivating Eqs. (2.8), one related to the derivation of the macroscopic Maxwell equations from microscopic considerations, and the other as a result of relaxing our previous assumption of purely local responses.

### 2.2.3 *Microscopic origins of magnetic–electric cross-coupling*

The aim of assuming a microscopic perspective on Maxwell's equations is to establish the macroscopic equations, Eqs. (2.7), from a consideration of the microscopic point charges that make up matter and their related fields. Assuming this perspective, and following largely the discussion in [42, Section 6.6], we postulate the microscopic Maxwell equations,

$$\boldsymbol{\nabla} \cdot \boldsymbol{e}(\boldsymbol{r},t) = \frac{1}{\varepsilon_0}\eta(\boldsymbol{r},t), \tag{2.12a}$$

$$\boldsymbol{\nabla} \times \boldsymbol{b}(\boldsymbol{r},t) - \varepsilon_0\mu_0\frac{\partial}{\partial t}\boldsymbol{e}(\boldsymbol{r},t) = \mu_0\boldsymbol{j}(\boldsymbol{r},t), \tag{2.12b}$$

$$\boldsymbol{\nabla} \times \boldsymbol{e}(\boldsymbol{r},t) + \frac{\partial}{\partial t}\boldsymbol{b}(\boldsymbol{r},t) = 0, \tag{2.12c}$$

$$\boldsymbol{\nabla} \cdot \boldsymbol{b}(\boldsymbol{r},t) = 0. \tag{2.12d}$$

The lowercase fields represent the microscopic electric and magnetic fields and

$$\eta(\boldsymbol{r},t) = \sum_i q_i\delta^{(3)}\big(\boldsymbol{r} - \boldsymbol{r}_i(t)\big), \tag{2.13a}$$

$$\boldsymbol{j}(\boldsymbol{r},t) = \sum_i q_i\boldsymbol{v}_i\delta^{(3)}\big(\boldsymbol{r} - \boldsymbol{r}_i(t)\big), \tag{2.13b}$$

are the microscopic charge and current densities, made up by point charges $q_i$ located at positions $\boldsymbol{r}_i(t)$, moving with velocities $\boldsymbol{v}_i(t) = \frac{\mathrm{d}}{\mathrm{d}t}\boldsymbol{r}_i(t)$. Further, $\delta^{(3)}(\boldsymbol{r})$ denotes the (three-dimensional) delta distribution. We continue by spatially averaging the quantities of interest over volumes that are big enough to enclose the usual constituents of matter—atoms and molecules—but still small compared to the spatial variations in the fields.[4] The

4 Such assumption is reasonable for visible or infrared electromagnetic fields, whose spatial variations are determined by wavelengths roughly two or more orders of magnitude larger than typical molecules.

averaging is done by convolving the microscopic quantities with a smooth test function, a Gaussian for instance, which smooths out the fine-scale details. We apply such averaging to both sides of Eqs. (2.12). Acknowledging that the order of averaging and differentiation may be exchanged for suitable test functions, Eqs. (2.3) are obtained from Eqs. (2.12) after the macroscopic quantities have been identified according to

$$\boldsymbol{B} = \langle \boldsymbol{b} \rangle, \qquad \boldsymbol{E} = \langle \boldsymbol{e} \rangle, \qquad \rho = \langle \eta \rangle, \qquad \boldsymbol{J} = \langle \boldsymbol{j} \rangle,$$

where $\langle \cdot \rangle$ denotes the spatial average.

Distinguishing between the charges that are bound in, say, molecules and the free ones, we write

$$\eta(\boldsymbol{r}, t) = \eta_{\mathrm{f}}(\boldsymbol{r}, t) + \sum_n \underbrace{\sum_{i(n)} q_i \delta^{(3)}\big(\boldsymbol{r} - \boldsymbol{r}_n(t) - \boldsymbol{r}_{in}(t)\big)}_{\eta_n(\boldsymbol{r}, t)} . \tag{2.14}$$

The first term on the right-hand side represents the free charges. The term for the bound charges is expressed as a sum over molecules $n$, which have been assigned a central location $\boldsymbol{r}_n(t)$. For each molecule $n$, the inner sum runs over all charges associated with that molecule, expressing their position relative to the center of the molecule by $\boldsymbol{r}_{in}(t) = \boldsymbol{r}_i(t) - \boldsymbol{r}_n(t)$. The usual way to continue from here consists of utilizing the smallness of $\boldsymbol{r}_{in}$ due to the limited molecular extent and expanding $\langle \eta_n(\boldsymbol{r}, t) \rangle$ in a Taylor series around $\boldsymbol{r} - \boldsymbol{r}_n(t)$. This procedure is well documented and we refer to Refs. [45, 46] for details. Here, we restrict ourselves to highlighting the main points. As a result, we find

$$\begin{aligned} \langle \eta_n(\boldsymbol{r}, t) \rangle = \Big\langle q_n \delta^{(3)}\big(\boldsymbol{r} - \boldsymbol{r}_n(t)\big) \Big\rangle - \boldsymbol{\nabla} \cdot \Big\langle \boldsymbol{p}_n(t) \delta^{(3)}\big(\boldsymbol{r} - \boldsymbol{r}_n(t)\big) \Big\rangle \\ + \frac{1}{2} \partial_\alpha \partial_\beta \Big\langle [\boldsymbol{q}_n(t)]_{\alpha\beta} \delta^{(3)}\big(\boldsymbol{r} - \boldsymbol{r}_n(t)\big) \Big\rangle + \dots , \end{aligned} \tag{2.15}$$

where the shorthand notation $\partial_\alpha \equiv \frac{\partial}{\partial x_\alpha}$ is used; $\alpha$, $\beta$ specify Cartesian components and summation over repeated indices is implied. Furthermore, we identify the molecular electric multipole moments

$$q_n = \sum_{i(n)} q_i, \qquad \boldsymbol{p}_n(t) = \sum_{i(n)} q_i \boldsymbol{r}_{in}(t), \qquad [\boldsymbol{q}_n(t)]_{\alpha\beta} = \sum_{i(n)} q_i [\boldsymbol{r}_{in}(t)]_\alpha [\boldsymbol{r}_{in}(t)]_\beta, \tag{2.16}$$

that is, the electric monopole (charge), dipole, and quadrupole, respectively. We count the monopole term to the external charges,[5] defining

$$\rho_{\text{ext}}(\boldsymbol{r},t) = \langle \eta_{\text{f}}(\boldsymbol{r},t)\rangle + \sum_n \Big\langle q_n \delta^{(3)}\big(\boldsymbol{r}-\boldsymbol{r}_n(t)\big)\Big\rangle. \tag{2.17}$$

5 The monopole term is the only term in the expansion that contributes to a net charge when integrated over a macroscopic volume.

With the further definition of the macroscopic multipole densities, which collect all molecular contributions,

$$\boldsymbol{P}(\boldsymbol{r},t) = \sum_n \Big\langle \boldsymbol{p}_n(t)\delta^{(3)}\big(\boldsymbol{r}-\boldsymbol{r}_n(t)\big)\Big\rangle, \tag{2.18a}$$

$$Q_{\alpha\beta}(\boldsymbol{r},t) = \sum_n \Big\langle [\boldsymbol{q}_n(t)]_{\alpha\beta}\delta^{(3)}\big(\boldsymbol{r}-\boldsymbol{r}_n(t)\big)\Big\rangle, \tag{2.18b}$$

inserting Eqs. (2.14) and (2.15) into Eq. (2.3a) yields

$$\rho_{\text{ext}}(\boldsymbol{r},t) = \partial_\alpha\left(\varepsilon_0 E_\alpha(\boldsymbol{r},t) + P_\alpha(\boldsymbol{r},t) - \frac{1}{2}\partial_\beta Q_{\alpha\beta}(\boldsymbol{r},t) + \dots\right), \tag{2.19}$$

which we may compare to Eq. (2.7a). After processing the microscopic current density $\boldsymbol{j}(\boldsymbol{r},t)$ in a similar manner, we are able to reproduce Eqs. (2.7) and we define the auxiliary fields via their Cartesian components [47]

$$D_\alpha = \varepsilon_0 E_\alpha + P_\alpha - \frac{1}{2}\partial_\beta Q_{\alpha\beta} + \dots, \tag{2.20a}$$

$$H_\alpha = \mu_0^{-1} B_\alpha - M_\alpha + \dots. \tag{2.20b}$$

Equation (2.20b) contains the macroscopic magnetic dipole density,

$$\boldsymbol{M}(\boldsymbol{r},t) = \sum_n \Big\langle \boldsymbol{m}_n(t)\delta^{(3)}\big(\boldsymbol{r}-\boldsymbol{r}_n(t)\big)\Big\rangle, \tag{2.21}$$

with the molecular magnetic dipole moment,

$$\boldsymbol{m}_n(t) = \frac{1}{2}\sum_{i(n)} q_i \boldsymbol{r}_{in}(t)\times \boldsymbol{v}_{in}(t), \tag{2.22}$$

which is obtained in the multipole decomposition (i.e., Taylor expansion) of the molecular microscopic current densities.

A few notes are in order regarding Eqs. (2.20): First, as pointed out by Raab and Lange [46], the fields $\boldsymbol{D}$ and $\boldsymbol{H}$ are not unique. To demonstrate, if we modify

$$\boldsymbol{D} \mapsto \boldsymbol{D} + \boldsymbol{\nabla}\times\boldsymbol{F}, \qquad \boldsymbol{H} \mapsto \boldsymbol{H} + \frac{\partial}{\partial t}\boldsymbol{F} \tag{2.23}$$

for some vector field $\boldsymbol{F}(\boldsymbol{r}, t)$, the left-hand sides of Eqs. (2.7a) and (2.7b) are unaffected. However, certain requirements regarding the physicality of the fields, such as requiring them to be independent of the chosen molecular central coordinates, restrict the possible choices [48]. We will see a useful application of this freedom in the next subsection. Second, keeping only the explicitly written terms in the right-hand side expansions of Eqs. (2.20) corresponds to truncating the multipole decomposition at electric quadrupole and magnetic dipole order. This is in line with a hierarchy of multipolar terms, where a magnetic multipole of a given order is generally paired up with the electric multipole of the respective next higher order.[6] The truncation of both expansions may not be chosen independently, as it would lead to nonphysical results [46]. Correspondingly, the often encountered assumption that the electric quadrupole moment can be neglected, while keeping magnetic dipolar terms, is generally to be seen as nonphysical. In this context, it is important to note that the polarization density defined in the discussion of Eqs. (2.7) is not equal to the macroscopic electric dipole density but rather to the sum of all terms on the right-hand side of Eq. (2.20a) except the first one; the same applies to the magnetization density. We will see that a truncation at electric quadrupole–magnetic dipole order retains the lowest orders necessary for obtaining chiral material parameters.

6 The discussed pairing of multipolar orders and the corresponding hierarchy appear naturally in a multipolar decomposition of the electromagnetic potentials. [49]

In order to establish how $\boldsymbol{D}$ and $\boldsymbol{H}$ of Eqs. (2.20) fully depend on the fields $\boldsymbol{E}$ and $\boldsymbol{B}$, that is, to derive the constitutive relations, one needs to know how the macroscopic multipole densities are influenced by the fields. No general solution is readily available as this step requires specifying the properties of the medium and the interacting fields. For a monochromatic plane wave (which we introduce in Chapter 3) in a linear, homogeneous, anisotropic, and nonmagnetic medium, Ref. [50] derives the multipole densities [47, Eqs. (10) to (12)]

$$P_\alpha = \alpha_{\alpha\beta} E_\beta + \frac{\mathrm{i}}{2} a_{\alpha\beta\gamma} k_\gamma E_\beta + \cdots - \mathrm{i} G'_{\alpha\beta} B_\beta + \dots , \tag{2.24a}$$

$$Q_{\alpha\beta} = a_{\gamma\alpha\beta} E_\gamma + \dots , \tag{2.24b}$$

$$M_\alpha = \mathrm{i} G'_{\beta\alpha} E_\beta + \dots . \tag{2.24c}$$

We will not concern ourselves with the prefactors in the equations above, called the *dynamic polarizability densities* [47], but focus on the fact that the

multipole densities depend on both the electric and magnetic fields.[7] The different terms in Eqs. (2.24) are themselves linked to the multipole orders. Explicitly, $\alpha_{\alpha\beta}$, $a_{\alpha\beta\gamma}$, and $G'_{\alpha\beta}$ appear in electric dipole, electric quadrupole, and magnetic dipole order, respectively.

After inserting Eqs. (2.24), Eqs. (2.20) turn into

$$\begin{pmatrix} D_\alpha \\ H_\alpha \end{pmatrix} = \boldsymbol{K} \begin{pmatrix} E_\beta \\ B_\beta \end{pmatrix}, \tag{2.25}$$

with

$$\boldsymbol{K} = \begin{pmatrix} \varepsilon_0 \delta_{\alpha\beta} & 0 \\ 0 & \mu_0^{-1} \delta_{\alpha\beta} \end{pmatrix} + \underbrace{\begin{pmatrix} \alpha_{\alpha\beta} & 0 \\ 0 & 0 \end{pmatrix}}_{\text{electric dipole}} + \underbrace{\begin{pmatrix} \frac{\mathrm{i}}{2}(a_{\alpha\beta\gamma} - a_{\beta\alpha\gamma})k_\gamma & -\mathrm{i}G'_{\alpha\beta} \\ -\mathrm{i}G'_{\beta\alpha} & 0 \end{pmatrix}}_{\text{electric quadrupole–magnetic dipole}} + \dots . \tag{2.26}$$

Finally, we found constitutive relations[8] with the cross-coupling terms between electric and magnetic fields that we were after. Their appearance requires including the electric quadrupole and magnetic dipole moments in the multipolar expansion of the charge and current densities. For the purpose of intuition, it should be noted that the polarizability densities $G'_{\alpha\beta}$, which facilitate such cross-coupling, depend on an interplay of the molecular electric and magnetic dipoles, $\boldsymbol{p}_n$ and $\boldsymbol{m}_n$; the explicit expression can be found in Eq. (16) of Ref. [47]. On a side note, we remark that $\boldsymbol{K}$ considered up to electric quadrupole–magnetic dipole order does not include a modification of the magnetic permeability, which is even found to be true for magnetic media [48]. Instead, magnetic properties become apparent only upon including the next order of the expansion. Having convinced ourselves of the appearance of magnetic–electric cross-coupling from a microscopic consideration of media, we highlight yet another perspective in the following.

7 Generally, the multipole densities depend on the fields as well as their derivatives. In Eqs. (2.24) we have inserted the explicit derivatives for the specified fields.

8 While Eq. (2.25) is formulated for time and space dependent fields, it is still instructive to liken it to Eq. (2.11), particularly for monochromatic fields. We refer to the discussion of monochromatic fields in Chapter 3.

### 2.2.4 *Magnetic–electric cross-coupling as a result of nonlocality*

Another perspective on the origin of cross-coupling terms is given in Ref. [51], particularly in the discussion of artificial magnetism in metamaterials. To this end, we revisit Eqs. (2.10) for nonmagnetic materials, starting from an exclusively electric response but relaxing the restriction of locality. For ho-

We return to denoting Cartesian components with roman indices.

mogeneous media, a nonlocal response is expressed as a spatial convolution. Hence, we write

$$\tilde{D}_i(\boldsymbol{r},\omega) = \varepsilon_0 \tilde{E}_i(\boldsymbol{r},\omega) + \sqrt{2\pi} \iiint_{\mathbb{R}^3} \mathrm{d}^3 r'\, \tilde{R}^{\mathrm{ee}}_{ij}(\boldsymbol{r}-\boldsymbol{r'},\omega)\tilde{E}_j(\boldsymbol{r'},\omega), \tag{2.27a}$$

$$\tilde{\boldsymbol{H}}(\boldsymbol{r},\omega) = \mu_0^{-1}\tilde{\boldsymbol{B}}(\boldsymbol{r},\omega). \tag{2.27b}$$

A local response is recovered when restricting the spatial dependence of $\tilde{R}^{\mathrm{ee}}_{ij}$ to a delta distribution, $\delta^{(3)}(\boldsymbol{r}-\boldsymbol{r'})$. Using a three-dimensional Fourier transform for the spatial variable, choosing $\boldsymbol{k}$ as the conjugate variable to $\boldsymbol{r}$, the convolution can be expressed as a multiplication. Note that we choose the opposite sign convention for the exponential functions in Eqs. (2.9) for the Fourier transform of spatial variables. We then expand the Fourier transform of $\tilde{R}^{\mathrm{ee}}_{ij}$, which we denote by $\underline{R}^{\mathrm{ee}}_{ij}$, in a Taylor series around $\boldsymbol{k} = 0$,

$$\underline{R}^{\mathrm{ee}}_{ij}(\boldsymbol{k},\omega) = \underline{R}^{\mathrm{ee}}_{ij}(0,\omega) + k_k \frac{\partial}{\partial k_k}\underline{R}^{\mathrm{ee}}_{ij}(0,\omega) + \dots . \tag{2.28}$$

A dependence of the response function on $\boldsymbol{k}$ is also termed *spatial dispersion*; the chosen truncation corresponds to the case of weak spatial dispersion.

Truncating at the linear contribution corresponds to allowing only short-ranged nonlocal influences in the spatial convolution. It can be seen as a first order nonlocal correction to the previously purely local relation. After applying an inverse Fourier transform and defining

$$r_{ij}(\omega) \coloneqq (2\pi)^2 \underline{R}^{\mathrm{ee}}_{ij}(0,\omega), \qquad s_{ijk}(\omega) \coloneqq -\mathrm{i}(2\pi)^2 \frac{\partial}{\partial k_k}\underline{R}^{\mathrm{ee}}_{ij}(0,\omega), \tag{2.29}$$

Eq. (2.27a) turns into

$$\tilde{D}_i(\boldsymbol{r},\omega) = \left(\varepsilon_0\delta_{ij} + r_{ij}(\omega)\right)\tilde{E}_j(\boldsymbol{r},\omega) + s_{ijk}(\omega)\partial_k \tilde{E}_j(\boldsymbol{r},\omega); \tag{2.30}$$

Eq. (2.27b) remains unchanged.

The downside of constitutive relations as given above becomes apparent when considering the continuity of fields at media interfaces. We derive the continuity relations in Section 2.3, valid for local constitutive relations as given in Eqs. (2.10). For continuity relations including derivatives of the fields, the corresponding relations would turn out more complicated. However, one can exploit the non-uniqueness of $\boldsymbol{D}$ and $\boldsymbol{H}$ discussed in the

previous subsection to simplify the continuity relations in the case of weakly nonlocal responses. To this end, we define[9]

$$u_{ij} \coloneqq \frac{\omega}{4}\epsilon_{jkl}\left(s_{ikl} - s_{ilk} + s_{lki}\right), \tag{2.31}$$

$\epsilon_{jkl}$ denoting the Levi-Civita symbol, and a vector field $\tilde{\boldsymbol{F}}$ with components

$$\tilde{F}_i = \omega^{-1} u_{ji} \tilde{E}_j. \tag{2.32}$$

Reciprocity [43] further requires that $s_{ijk}$ be antisymmetric in its first two indices, $s_{ijk} = -s_{jik}$ [44, 51]. Upon using $\tilde{\boldsymbol{F}}$ to transform $\tilde{\boldsymbol{D}}, \tilde{\boldsymbol{H}}$ according to Eq. (2.23), replacing $\frac{\partial}{\partial t} \mapsto -\mathrm{i}\omega$ in frequency domain, Eqs. (2.27b) and (2.30) turn into

$$\tilde{D}_i(\boldsymbol{r},\omega) = \left(\varepsilon_0\delta_{ij} + r_{ij}(\omega)\right)\tilde{E}_j(\boldsymbol{r},\omega) - \mathrm{i}u_{ij}(\omega)\tilde{B}_j(\boldsymbol{r},\omega), \tag{2.33a}$$

$$\tilde{H}_i(\boldsymbol{r},\omega) = -\mathrm{i}u_{ji}(\omega)\tilde{E}_j(\boldsymbol{r},\omega) + \mu_0^{-1}\tilde{B}_i(\boldsymbol{r},\omega). \tag{2.33b}$$

Equations (2.33) resemble Eqs. (2.10) (with trivial permeability) and we may understand the magnetic–electric cross-coupling as an effect of weak spatial dispersion, recast into constitutive relations of local character for convenience. With regard to chiral media, we can interpret the result above as a statement that the geometric nature of chirality, that is, a broken spatial inversion symmetry, cannot be appreciated at a single point without spatial extent but requires knowledge of the local environment. That is, it requires a (weakly) nonlocal response.

### 2.2.5 *Constitutive relations and classification of linear media*

We have seen how constitutive relations given in Eqs. (2.10) or, equivalently, Eq. (2.11) can be obtained from various considerations. Unsurprisingly, such considerations were predated by phenomenological aspects, which motivated constitutive relations of the given form. In fact, in the mid-19th century, Pasteur concluded that molecules of optically active[10] substances must break spatial inversion symmetry, that is, be chiral [52]. To explain this phenomenon, Drude [53, p. 390ff.] considered helical oscillators, effectively leading to constitutive relations [52, Eq. (2.5)]

$$\boldsymbol{D} = \varepsilon_0\boldsymbol{\varepsilon}\boldsymbol{E} - f\boldsymbol{\nabla}\times\boldsymbol{E}, \qquad \boldsymbol{B} = \mu_0\boldsymbol{H}. \tag{2.34}$$

9 These definitions follow Section 2.2 of Ref. [51]. Note, however, that Eq. (2.38) therein pairs the indices to contract erroneously.

10 Optical activity encompasses both optical rotation and circular dichroism. We discuss these phenomena in Chapter 5.

*Table 2.1: Classification of linear media* · The constitutive relations are used to classify linear media. The different classes correspond to restrictions on the material parameters in Eq. (2.11) [cf. 43, Tab. 1.4].

| Class | $\boldsymbol{\varepsilon}, \boldsymbol{\mu}$ | $\boldsymbol{\xi}, \boldsymbol{\zeta}$ |
|---|---|---|
| Isotropic | $\propto \mathbf{1}$ | $= \mathbf{0}$ |
| Bi-isotropic | $\propto \mathbf{1}$ | $\propto \mathbf{1}$ |
| Anisotropic | Some $\not\propto \mathbf{1}$ | $= \mathbf{0}$ |
| Bi-anisotropic | All other cases | |

Many other suggestions for suitable constitutive relations have been made and we refer for an overview as well as a discussion of the physical shortcomings of above equations to Refs. [54, 55]. Tellegen [56], albeit in a different context, first introduced the constitutive relations equivalent to Eq. (2.11). We will henceforth choose these relations to work with. Based on the properties of the material parameter tensors, a classification of media is established [43]. The different classes discussed below correspond to the restrictions on the material parameters collected in Tab. 2.1.

Isotropy, from Ancient Greek ἴσος (*ísos*; equal) and τρόπος (*trópos*; turn), refers to sameness in all directions.

*Isotropic media* · In the simplest case, we consider orientation independent, that is, isotropic, media without cross-coupling terms, that is, $\boldsymbol{\xi} = \boldsymbol{\zeta} = 0$. The material parameters then assume the form

$$\boldsymbol{\varepsilon} = \varepsilon \mathbf{1}, \qquad \boldsymbol{\mu} = \mu \mathbf{1}, \tag{2.35}$$

where $\mathbf{1}$ is the three-dimensional identity matrix.

*Bi-isotropic media* · Building on Eq. (2.35) but including isotropic cross-coupling parameters,

$$\boldsymbol{\xi} = \xi \mathbf{1}, \qquad \boldsymbol{\zeta} = \zeta \mathbf{1}, \tag{2.36}$$

yields the description of *bi-isotropic* media. For $\xi = -\zeta$, we obtain chiral isotropic media; a special case of bi-isotropic media, which is of particular interest in this work. Below the current classification, we reformulate the parameters $\boldsymbol{\xi}$ and $\boldsymbol{\zeta}$ to better account for chiral media.

*Anisotropic media* · In the general case, where $\boldsymbol{\varepsilon}$ and $\boldsymbol{\mu}$ are not proportional to $\mathbf{1}$, the response of the medium depends on its orientation, hence, it is

anisotropic. Within the context of the currently discussed classification of media, the term *anisotropic* medium is used when referring to such a medium with no cross-coupling terms.

An interesting subgroup of anisotropic media is obtained when either $\boldsymbol{\varepsilon}$ or $\boldsymbol{\mu}$ are not symmetric matrices. The corresponding skew-symmetric contribution can be found in media that are exposed to an external static magnetic field. In a simple representation, for instance, the permittivity is given by

$$\boldsymbol{\varepsilon} = \begin{pmatrix} \varepsilon_1 & \mathrm{i}g_z & 0 \\ -\mathrm{i}g_z & \varepsilon_1 & 0 \\ 0 & 0 & \varepsilon_2 \end{pmatrix}, \tag{2.37}$$

where we assume the external magnetic field to be aligned to $\hat{\boldsymbol{z}}$. If the permittivity reacts to an external field as shown above, the medium is referred to as *gyroelectric*. Similarly, a medium with an analogous behavior of the permeability is called *gyromagnetic*. Collectively, we speak of *gyrotropic* media. While gyrotropic media break mirror symmetries with respect to any plane that includes the direction of the external magnetic field, Eq. (2.37) is still symmetric under $z \mapsto -z$, transforming the external field as a pseudovector. Hence, while gyrotropic media can directionally act as if inversion symmetry were broken, they are not, by themselves, chiral.

*Bi-anisotropic media* · Finally, orientation dependent media including cross-coupling parameters are referred to as *bi-anisotropic* media. They correspond to the full constitutive relations of Eq. (2.11) without further simplifications. These are the constitutive relations introduced by Tellegen [56]. The name "bi-anisotropic" was suggested by Cheng and Kong [57], who point out another important aspect of such media: Even media that are isotropic in their rest frame appear bi-anisotropic to an observer if moving relative to the laboratory frame [57, 58]. Consequently, for a relativistically covariant formulation, media should be described as bi-anisotropic such that the structure of the constitutive relations does not change when changing frame.

As a last modification to Eq. (2.11), we rewrite the constitutive relations as

$$\begin{pmatrix} \tilde{\boldsymbol{D}}(\boldsymbol{r},\omega) \\ \tilde{\boldsymbol{B}}(\boldsymbol{r},\omega) \end{pmatrix} = \begin{pmatrix} \varepsilon_0 \boldsymbol{\varepsilon}(\omega) & \sqrt{\varepsilon_0\mu_0}\big(\boldsymbol{\chi}(\omega) + \mathrm{i}\boldsymbol{\kappa}(\omega)\big) \\ \sqrt{\varepsilon_0\mu_0}\big(\boldsymbol{\chi}(\omega) - \mathrm{i}\boldsymbol{\kappa}(\omega)\big)^{\mathsf{T}} & \mu_0 \boldsymbol{\mu}(\omega) \end{pmatrix} \begin{pmatrix} \tilde{\boldsymbol{E}}(\boldsymbol{r},\omega) \\ \tilde{\boldsymbol{H}}(\boldsymbol{r},\omega) \end{pmatrix}, \tag{2.38}$$

where [59]

$$\boldsymbol{\chi} = \frac{1}{2}\left(\boldsymbol{\xi} + \boldsymbol{\zeta}^{\mathsf{T}}\right), \qquad \boldsymbol{\kappa} = \frac{1}{2\mathrm{i}}\left(\boldsymbol{\xi} - \boldsymbol{\zeta}^{\mathsf{T}}\right). \tag{2.39}$$

Referring for a detailed discussion to Ref. [43], we note that the newly introduced parameters are physically meaningful. It can be shown that a nonzero $\boldsymbol{\chi}$ breaks reciprocity in the medium, while the parameter $\boldsymbol{\kappa}$ describes phenomena related to media made of chiral constituents; particularly, optical rotation (OR) and circular dichroism (CD), which we discuss in Chapter 5. $\boldsymbol{\kappa}$ is correspondingly called the *chirality* parameter. In this work we restrict ourselves to reciprocal media and set $\boldsymbol{\chi} = 0$. We will further limit all media to be either isotropic or bi-isotropic; correspondingly, all material parameters are represented by scalar quantities. In the special case of chiral isotropic (i.e., reciprocal bi-isotropic) media, the scalar chirality parameter $\kappa$ is also referred to as *Pasteur parameter*, paying tribute to its historical roots.

### 2.2.6 *Energy conservation*

Below, we state the conditions obtained from considering the conservation of energy in media, following Ref. [43]. We distinguish between lossless and passive (i.e., lossless or absorptive) media.

*Lossless media* · For lossless media, the material tensors have to satisfy

$$\boldsymbol{\varepsilon} = \boldsymbol{\varepsilon}^{\mathsf{H}}, \qquad \boldsymbol{\mu} = \boldsymbol{\mu}^{\mathsf{H}}, \qquad \text{and} \qquad \boldsymbol{\kappa} = \boldsymbol{\kappa}^{*}, \tag{2.40}$$

that is, $\boldsymbol{\varepsilon}$ and $\boldsymbol{\mu}$ are Hermitian, and $\boldsymbol{\kappa}$ is real.

*Passive media* · We write the conditions for passive media for the simpler case of bi-isotropic media. For positive frequencies, $\omega > 0$, these conditions read

$$\operatorname{Im}\varepsilon \geq 0, \qquad \operatorname{Im}\mu \geq 0, \qquad \text{and} \qquad (\operatorname{Im}\kappa)^2 \leq \operatorname{Im}\varepsilon \operatorname{Im}\mu. \tag{2.41}$$

For the general relations concerning bi-anisotropic media, we refer to Ref. [43]. From the condition on the chirality parameter, specifically, we see that the assumption of nonmagnetic media (i.e., $\mu \equiv 1$) restricts the chirality parameter to be real, lest the medium become active, thereby violating the conservation of energy. However, for typical materials, $\operatorname{Im}\varepsilon$ exceeds $\operatorname{Im}\kappa$ by multiple orders of magnitude, consequently leading to relatively small lower bound for $\operatorname{Im}\mu$. Under such conditions, the approximation of nonmagnetic media causes only negligible gain, which is further hidden by the absorption predominant in most such materials. We will revisit the issue of nonphysical gain, particularly in a numerical setting, at a later stage.

## 2.3 *Continuity of Fields at Media Interfaces*

So far, we have considered infinitely extended media, in which the relation between the fundamental and the auxiliary fields is the same everywhere in space. Arguably, not many interesting systems can be constructed considering a single infinite medium only. In this work, all systems of interest feature bounded domains of media, posing interfaces between different domains. While we might solve Maxwell's equations individually in each domain, constructing whole solutions in the entire space requires stitching the fields together at the interfaces. The guidelines for how to do this are the continuity relations for fields at media interfaces, which can be derived from Maxwell's equations. To this end, it is useful to turn Eqs. (2.7), which apply locally at every point $(\boldsymbol{r}, t)$, into integral form [42, Section I.5].

Integrating Eqs. (2.7a) and (2.7d) spatially over a volume $V$ and using the divergence theorem, which equates the divergence of a vector field integrated over a bounded volume to its flux through the enclosing surface, the boundary of the volume $S = \partial V$, we obtain

$$\oiint_S \mathrm{d}\boldsymbol{S} \cdot \boldsymbol{D}(\boldsymbol{r}, t) = \iiint_V \mathrm{d}^3 r\, \rho_{\mathrm{ext}}(\boldsymbol{r}, t), \tag{2.42a}$$

$$\oiint_S \mathrm{d}\boldsymbol{S} \cdot \boldsymbol{B}(\boldsymbol{r}, t) = 0. \tag{2.42b}$$

Here, $\mathrm{d}\boldsymbol{S} = \mathrm{d}S\,\hat{\boldsymbol{n}}$ is the area element $\mathrm{d}S$ oriented along the outwards pointing surface normal $\hat{\boldsymbol{n}}$. Equation (2.42a) states that the flux of $\boldsymbol{D}$ out of a volume is

The validity of the expressions derived here hinges on the restriction to local constitutive relations. Even then, as remarked in Ref. [60], the given relations are not generally true when any terms beyond electric dipole order are included in the microscopic multipole expansion. For nonmagnetic media up to electric quadrupole–magnetic dipole order, as discussed in this work, the relations are valid [60].

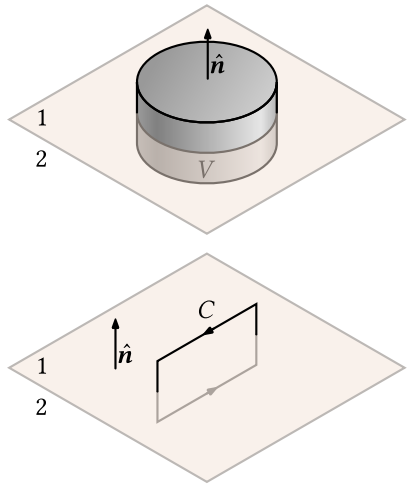


*Figure 2.1: Domains of integration for continuity relations at media interfaces* · To derive the continuity relations, special domains for the integration located at the interface between two media ("1" and "2") are chosen. For the divergence equations, the volume of integration is a cylinder that is intersected by the media interface (upper panel). In the limit of vanishing height, only the fluxes through the circular surfaces remain relevant. For the curl equations, a rectangular contour crossing the interface is considered (lower panel).

given by the total charge inside; it is known as Gauss's law. Equation (2.42b) is its magnetic counterpart, explicitly stating the absence of magnetic charges.

Similarly, we integrate Eqs. (2.7b) and (2.7c) over an open oriented surface $S'$ and use Stokes' theorem, which relates the surface integral of a vector field's curl to the line integral of the vector field around the boundary of the surface, $C = \partial S'$. Doing so yields the Ampère–Maxwell equation,

$$\oint_C \mathrm{d}\boldsymbol{l} \cdot \boldsymbol{H}(\boldsymbol{r},t) = \iint_{S'} \mathrm{d}\boldsymbol{S}' \cdot \left( \boldsymbol{J}_{\mathrm{ext}}(\boldsymbol{r},t) + \frac{\partial}{\partial t}\boldsymbol{D}(\boldsymbol{r},t) \right), \tag{2.42c}$$

and Faraday's law of induction,

$$\oint_C \mathrm{d}\boldsymbol{l} \cdot \boldsymbol{E}(\boldsymbol{r},t) = -\iint_{S'} \mathrm{d}\boldsymbol{S}' \cdot \frac{\partial}{\partial t}\boldsymbol{B}(\boldsymbol{r},t), \tag{2.42d}$$

where $\mathrm{d}\boldsymbol{l}$ denotes a line element of the contour $C$.

After choosing suitable volumes and surfaces, involving the interface between two media, the integral equations above allow us to relate different field components across the interface. Such choices are illustrated in Fig. 2.1. Considering Eqs. (2.42a) and (2.42b), we let the height of the depicted cylindrical volume shrink rapidly as compared to its diameter. If we further

consider the diameter small as compared to variations in the fields, such that they may be regarded constant on each circular surface, then only the contributions from those surfaces matter. Consequently, we find

$$\hat{\boldsymbol{n}} \cdot (\boldsymbol{D}_1 - \boldsymbol{D}_2) = \sigma_{\text{surf}}, \tag{2.43a}$$
$$\hat{\boldsymbol{n}} \cdot (\boldsymbol{B}_1 - \boldsymbol{B}_2) = 0. \tag{2.43b}$$

Here, $\sigma_{\text{surf}}$ denotes the surface charge density on the idealized abrupt interface. In the absence of external sources, Eqs. (2.43) determine the components normal to the interface of both electric and magnetic flux densities as continuous.

Analogous considerations for the rectangular contour in Fig. 2.1 yield

$$\hat{\boldsymbol{n}} \times (\boldsymbol{H}_1 - \boldsymbol{H}_2) = \boldsymbol{K}_{\text{surf}}, \tag{2.44a}$$
$$\hat{\boldsymbol{n}} \times (\boldsymbol{E}_1 - \boldsymbol{E}_2) = 0, \tag{2.44b}$$

with $\boldsymbol{K}_{\text{surf}}$ being the surface current density. The time derivatives of the fields on the right-hand sides of Eqs. (2.42c) and (2.42d) are considered finite and hence do not contribute to Eqs. (2.44) in the limit of a vanishing area $S'$. Excluding surface currents, Eqs. (2.44) state the continuity of the tangential components of the electric and magnetic field strengths across the interface.

*Chapter summary* · Above, we introduced Maxwell's equations and the constitutive relations capturing the linear optical properties of media, with a focus on chiral media. Together, these relations govern the electric and magnetic fields and are used in the next chapter to describe electromagnetic waves in chiral isotropic media. This discussion is expanded in Chapter 4 to describe scattering of electromagnetic waves from systems incorporating chiral media. There, the continuity relations for the fields, Eqs. (2.43) and (2.44), provide necessary restrictions to relate the waves illuminating an object to its scattering response.

# 3 *Electromagnetic Waves in Chiral Media*

Maxwell's equations, particularly, Eqs. (2.3b) and (2.3c), tell us about the interdependence of electric and magnetic fields, irrespective of the presence of sources. Combining them yields the wave equation, which governs the behavior of electromagnetic waves—light—in free space. In media, a similar analysis has to be done based on Eqs. (2.7b) and (2.7c), taking into account the constitutive relations between the fields.

In this chapter, we consider electromagnetic waves in media, particularly allowing for chiral media. We work in frequency domain, where the wave equation is replaced by the Helmholtz equation. First, we show how the Helmholtz equation follows from the Maxwell equations and the constitutive relations. Afterwards, we discuss specific classes of solutions to the Helmholtz equation, which aids us in describing the systems considered in the following chapters. Finally, we discuss helicity, a concept of electromagnetic waves closely related to the notion of chirality. Complementing the description of linear media established in the previous chapter, the discussion of electromagnetic waves prepares us for the remainder of this work, where we consider the interaction of electromagnetic waves with various systems. The aspect of helicity turns out to be particularly useful for studying interactions with chiral systems.

## 3.1 *Helmholtz Equation for Electromagnetic Waves*

The Helmholtz equation, determining the behavior of electromagnetic waves, is obtained from a joint consideration of Maxwell's equations and the constitutive relations for matter. In chiral media, the magnetic–electric cross-coupling couples the equations for electric and magnetic fields. To resolve the coupling, we define linear combinations of the fields that lead to uncoupled equations. We show that these combined fields are of particular interest when considering electromagnetic helicity, the concept introduced in Section 3.2. We proceed by discussing selected general solutions to the Helmholtz equation and describe how to use them to construct *monochromatic* (i.e., oscillating in time with a single frequency) waves. The presented solutions serve as suitable basis sets for describing electromagnetic waves

in their interaction with planar and localized systems in the subsequent chapter.

### 3.1.1 *Diagonalization of the curl equations*

Equations (2.7b) and (2.7c) can be jointly written—in frequency domain and in absence of external currents—as

$$\begin{pmatrix} \boldsymbol{\nabla}\times & 0 \\ 0 & \boldsymbol{\nabla}\times \end{pmatrix} \begin{pmatrix} \tilde{\boldsymbol{E}}(\boldsymbol{r},\omega) \\ \tilde{\boldsymbol{H}}(\boldsymbol{r},\omega) \end{pmatrix} = \begin{pmatrix} 0 & \mathrm{i}\omega \\ -\mathrm{i}\omega & 0 \end{pmatrix} \begin{pmatrix} \tilde{\boldsymbol{D}}(\boldsymbol{r},\omega) \\ \tilde{\boldsymbol{B}}(\boldsymbol{r},\omega) \end{pmatrix}. \tag{3.1}$$

Using Eq. (2.38) for chiral isotropic media to replace $\left(\tilde{\boldsymbol{D}}(\boldsymbol{r},\omega), \tilde{\boldsymbol{B}}(\boldsymbol{r},\omega)\right)^{\mathsf{T}}$ on the right-hand side yields

$$\begin{pmatrix} \boldsymbol{\nabla}\times & 0 \\ 0 & \boldsymbol{\nabla}\times \end{pmatrix} \begin{pmatrix} \tilde{\boldsymbol{E}}(\boldsymbol{r},\omega) \\ \tilde{\boldsymbol{H}}(\boldsymbol{r},\omega) \end{pmatrix} = \omega\sqrt{\varepsilon_0\mu_0} \underbrace{\begin{pmatrix} \kappa(\omega) & \mathrm{i}\sqrt{\frac{\mu_0}{\varepsilon_0}}\mu(\omega) \\ -\mathrm{i}\sqrt{\frac{\varepsilon_0}{\mu_0}}\varepsilon(\omega) & \kappa(\omega) \end{pmatrix}}_{=:\boldsymbol{\mathscr{K}}} \begin{pmatrix} \tilde{\boldsymbol{E}}(\boldsymbol{r},\omega) \\ \tilde{\boldsymbol{H}}(\boldsymbol{r},\omega) \end{pmatrix}. \tag{3.2}$$

$\boldsymbol{\mathscr{K}}$ is diagonalizable as long as $\kappa(\omega)^2 \neq \varepsilon(\omega)\mu(\omega)$,[1] allowing us to factorize Eq. (3.2) [52]. To this end, similar to Bohren [61], we use a linear transformation of the fields,

1 In virtually all natural materials, $|\kappa| \ll |\varepsilon|, |\mu|$.

$$\begin{pmatrix} \tilde{\boldsymbol{E}}(\boldsymbol{r},\omega) \\ \tilde{\boldsymbol{H}}(\boldsymbol{r},\omega) \end{pmatrix} = \boldsymbol{\mathscr{G}}^{-1} \begin{pmatrix} \tilde{\boldsymbol{G}}_+(\boldsymbol{r},\omega) \\ \tilde{\boldsymbol{G}}_-(\boldsymbol{r},\omega) \end{pmatrix}, \tag{3.3}$$

with

$$\boldsymbol{\mathscr{G}} = \frac{1}{\sqrt{2}} \begin{pmatrix} \sqrt{\varepsilon_0\varepsilon(\omega)} & \mathrm{i}\sqrt{\mu_0\mu(\omega)} \\ \sqrt{\varepsilon_0\varepsilon(\omega)} & -\mathrm{i}\sqrt{\mu_0\mu(\omega)} \end{pmatrix}, \quad \boldsymbol{\mathscr{G}}^{-1} = \frac{1}{\sqrt{2}} \begin{pmatrix} \frac{1}{\sqrt{\varepsilon_0\varepsilon(\omega)}} & \frac{1}{\sqrt{\varepsilon_0\varepsilon(\omega)}} \\ \frac{-\mathrm{i}}{\sqrt{\mu_0\mu(\omega)}} & \frac{\mathrm{i}}{\sqrt{\mu_0\mu(\omega)}} \end{pmatrix}. \tag{3.4}$$

The given transformation diagonalizes $\boldsymbol{\mathscr{K}}$ and we find

$$\boldsymbol{\mathscr{G}}\boldsymbol{\mathscr{K}}\boldsymbol{\mathscr{G}}^{-1} = \begin{pmatrix} \kappa(\omega) + \sqrt{\varepsilon(\omega)\mu(\omega)} & 0 \\ 0 & \kappa(\omega) - \sqrt{\varepsilon(\omega)\mu(\omega)} \end{pmatrix}. \tag{3.5}$$

With $k_0 := \omega\sqrt{\varepsilon_0\mu_0}$, $n_\pm(\omega) := \sqrt{\varepsilon(\omega)\mu(\omega)} \pm \kappa(\omega)$, and $k_\pm := k_0 n_\pm(\omega)$, Eq. (3.2) finally yields two independent equations after inserting Eq. (3.3), conjointly expressed as

$$\boldsymbol{\nabla} \times \tilde{\boldsymbol{G}}_\pm(\boldsymbol{r},\omega) = \pm k_\pm \tilde{\boldsymbol{G}}_\pm(\boldsymbol{r},\omega). \tag{3.6a}$$

We furthermore note that the fields $\tilde{\boldsymbol{G}}_\pm(\boldsymbol{r},\omega)$ are divergence-free,

$$\boldsymbol{\nabla}\cdot\tilde{\boldsymbol{G}}_\pm(\boldsymbol{r},\omega)=0, \tag{3.6b}$$

which follows from the divergence equations, (2.7a) and (2.7d), in absence of external charges, together with Eqs. (2.38) and (3.3).[2] Equation (3.6a) states that the curl of the field $\tilde{\boldsymbol{G}}_\pm$ is everywhere parallel to $\tilde{\boldsymbol{G}}_\pm$ itself. Such vector fields are known as *Beltrami fields* [52, 62]. The transformation in Eq. (3.3), defining the fields $\tilde{\boldsymbol{G}}_\pm$, is furthermore closely related to that of the *Riemann–Silberstein* [63] or *Weber vector* [64][65, § 138].

2 Presuming again $\kappa(\omega)^2 \neq \varepsilon(\omega)\mu(\omega)$.

Taking the curl of Eq. (3.6a) and using Eq. (3.6b), we arrive at

$$\left(\nabla^2+k_\pm^2\right)\tilde{\boldsymbol{G}}_\pm(\boldsymbol{r},\omega)=0, \tag{3.7}$$

which we recognize as the vector Helmholtz equation, with the vector Laplacian of a vector field $\boldsymbol{F}$ defined as $\nabla^2\boldsymbol{F}\coloneqq\boldsymbol{\nabla}(\boldsymbol{\nabla}\cdot\boldsymbol{F})-\boldsymbol{\nabla}\times(\boldsymbol{\nabla}\times\boldsymbol{F})$ and *wavenumbers* $k_\pm$.

Before moving on, we remark the following: In vacuum, the quantities defined leading up to Eq. (3.6a) are $n_\pm(\omega)=1$, identically, and $k_\pm=k_0$. We refer to $k_0$ as the *vacuum wavenumber*. The proportionality constant $c_0=\omega/k_0=1/\sqrt{\varepsilon_0\mu_0}$ between the angular frequency $\omega$ and the vacuum wavenumber is the speed of light in vacuum. Inside a medium, the wavenumbers $k_\pm$ are related to $k_0$ by the proportionality factor $n_\pm(\omega)$, the medium's *refractive index*. For a nonvanishing chirality parameter $\kappa$, there are two distinct wavenumbers for a given angular frequency, $k_+\neq k_-$, following from different refractive indices; we will understand this effect as *circular birefringence*, a phenomenon of chiral media. In achiral isotropic media, $n_\pm$ become degenerate and only a single wavenumber enters Eq. (3.7). We now turn our attention to solutions to the Helmholtz equation.

### 3.1.2 *Solutions to the scalar Helmholtz equation*

In order to find solutions to Eq. (3.7), let us first look at the simpler problem given by the scalar Helmholtz equation. The solutions to the scalar Helmholtz equation will allow us to construct solutions to the vector Helmholtz equation. The Helmholtz equation for a scalar field $f(\boldsymbol{r})$ reads

$$\left(\nabla^2+k^2\right)f(\boldsymbol{r})=0, \tag{3.8}$$

for a nonzero wavenumber $k$ and with the (scalar) Laplacian $\nabla^2 f \coloneqq \boldsymbol{\nabla} \cdot (\boldsymbol{\nabla} f)$.

When constructing solutions to the Helmholtz equation, it is useful to consider the coordinate system in which the spatial dependence is expressed. For suitable coordinate systems, solutions can be found following a separation ansatz with respect to the coordinates. Naturally, such solutions conform to the geometry that is inherent to the coordinate system and are best suited when describing systems of similar geometric properties. Here, we highlight two sets of solutions obtained following these considerations. [66, Chapter 5]

*Plane waves* · Considering the Helmholtz equation in Cartesian coordinates, we find the set of solutions

$$f_{\hat{\boldsymbol{k}}}(\boldsymbol{r}) = \mathrm{e}^{\mathrm{i}k\hat{\boldsymbol{k}}\cdot\boldsymbol{r}} \tag{3.9}$$

$\hat{\boldsymbol{k}}$ may contain imaginary components. The resulting exponentially decaying solutions can be used to describe *inhomogeneous* and *evanescent* waves, which we encounter in Chapter 4.

for an arbitrary direction $\hat{\boldsymbol{k}}$ satisfying $\hat{\boldsymbol{k}}\cdot\hat{\boldsymbol{k}} = 1$. Since the surfaces of constant complex phase of $f_{\hat{\boldsymbol{k}}}(\boldsymbol{r})$ are planes normal to $\hat{\boldsymbol{k}}$, we call such solutions *plane waves*.

*Spherical waves* · For spherical coordinates, a separation ansatz with respect to the coordinates leads to solutions

$$f^{(n)}_{\ell m}(\boldsymbol{r}) = z^{(n)}_{\ell}(kr) Y_{\ell m}(\theta, \varphi) \tag{3.10}$$

for a pair of indices $\ell \in \mathbb{N}_0$ and $m \in \mathbb{Z}$, $|m| \leq \ell$. $Y_{\ell m}$ are the spherical harmonics and $z^{(n)}_{\ell}$ is a stand-in for the spherical Bessel function $j_\ell$ (for $n = 1$), the spherical Neumann function $y_\ell$ (for $n = 2$), or the spherical Hankel functions of first, $h^{(1)}_\ell = j_\ell + \mathrm{i}y_\ell$ ($n = 3$), or second kind, $h^{(2)}_\ell = j_\ell - \mathrm{i}y_\ell$ ($n = 4$). Their definitions and useful relations are collected in Appendix A. In correspondence with the separation of the radial from the angular dependence, the solutions in Eq. (3.10) are called *spherical waves*.

### 3.1.3 *Solutions to the vector Helmholtz equation*

We can construct solutions to the vector Helmholtz equation,

$$(\nabla^2 + k^2)\boldsymbol{F}(\boldsymbol{r}) = 0, \tag{3.11}$$

with the vector Laplacian as defined below Eq. (3.7), from the solutions to the scalar equation introduced above [67, Chapter 13]. Various coordinate systems, including Cartesian and spherical, permit the same procedure; hence we will briefly discuss it jointly.

The other suitable coordinate systems for this procedure are: circular, elliptic, and parabolic cylindrical; as well as conical coordinates [67].

Given a solution of the scalar Helmholtz equation $f_\nu(\boldsymbol{r})$, where the composite index $\nu$ represents either $\hat{\boldsymbol{k}}$ or $(\ell, m, (n))$, solutions to Eq. (3.11) can be constructed as

$$\boldsymbol{L}_\nu(\boldsymbol{r}) \coloneqq \boldsymbol{\nabla} f_\nu(\boldsymbol{r}), \tag{3.12a}$$

$$\boldsymbol{M}_\nu(\boldsymbol{r}) \coloneqq \boldsymbol{\nabla} \times [\boldsymbol{v} f_\nu(\boldsymbol{r})], \tag{3.12b}$$

$$\boldsymbol{N}_\nu(\boldsymbol{r}) \coloneqq \frac{1}{k} \boldsymbol{\nabla} \times \boldsymbol{M}_\nu(\boldsymbol{r}). \tag{3.12c}$$

For $\boldsymbol{M}_\nu(\boldsymbol{r})$, we have introduced a steering vector $\boldsymbol{v}$ that depends on the chosen coordinate system. By construction, $\boldsymbol{M}_\nu(\boldsymbol{r})$ is orthogonal to $\boldsymbol{v}$ and hence tangential to surfaces normal to $\boldsymbol{v}$. We can choose these surfaces to conform to the geometries imprinted in the respective coordinate system. These are naturally represented by isosurfaces of (one of) the coordinates. The specific choices for the two considered coordinate systems are discussed below.

We note that $\boldsymbol{L}_\nu$, constructed as a gradient field, is curl-free and hence longitudinal. Since we are ultimately interested in fields satisfying Eq. (3.6b), these solutions will not be of further interest. In contrast, both $\boldsymbol{M}_\nu$ and $\boldsymbol{N}_\nu$ are divergence-free, that is, transverse. However, while fields given by Eqs. (3.12b) and (3.12c) would be valid solutions to Eq. (3.7) subject to the constraint in Eq. (3.6b), they are not Beltrami fields and violate Eq. (3.6a). In order to obtain suitable solutions, we make use of the fact that

$$\frac{1}{k} \boldsymbol{\nabla} \times \boldsymbol{N}_\nu(\boldsymbol{r}) = \boldsymbol{M}_\nu(\boldsymbol{r}). \tag{3.13}$$

This can be seen from $\boldsymbol{M}_\nu$ being free of divergence and a solution to Eq. (3.11), using its definition in Eq. (3.12c) to identify $\boldsymbol{N}_\nu$. We define the linear combinations

$$\boldsymbol{A}_{\nu,\pm}(\boldsymbol{r}) \coloneqq \frac{1}{\sqrt{2}} \left[\boldsymbol{N}_\nu(\boldsymbol{r}) \pm \boldsymbol{M}_\nu(\boldsymbol{r})\right], \tag{3.14}$$

which—by virtue of the Helmholtz equation being linear—are themselves

solutions to Eq. (3.11). Using Eqs. (3.12c) and (3.13), we see that $\boldsymbol{A}_{\nu,\pm}$ are Beltrami fields,

$$\boldsymbol{\nabla} \times \boldsymbol{A}_{\nu,\pm} = \pm k \boldsymbol{A}_{\nu,\pm}. \tag{3.15}$$

Equivalently, $\boldsymbol{A}_{\nu,\pm}$ are eigenfunctions of the differential operator $k^{-1}\boldsymbol{\nabla}\times$ with eigenvalues $\pm 1$. In Section 3.2, we recognize this operator as representation of the helicity operator in the frequency domain and note that the functions defined in Eq. (3.14) are, accordingly, the eigenfunctions of helicity.

### 3.1.4 *Vector plane waves*

We will now apply the general procedure outlined in the previous subsection to the specific solutions given earlier, first to plane waves and, in the next subsection, to spherical waves. To this end, we insert the scalar solutions of Eq. (3.9) into Eqs. (3.12). As discussed above, we further need to choose a suitable steering vector $\boldsymbol{v}$. For Cartesian coordinates, the three coordinates $x$, $y$, and $z$ are equivalent and their corresponding isosurfaces are planes; hence the choice of coordinate is arbitrary. We define the wave vector $\boldsymbol{k} \coloneqq k\hat{\boldsymbol{k}}$ with Cartesian components $k_i$, $i \in \{x, y, z\}$, and the unit vectors

$$\hat{\boldsymbol{\varphi}}_{\boldsymbol{k}} \coloneqq \begin{cases} \hat{\boldsymbol{y}} & \text{if } \hat{\boldsymbol{z}} \times \boldsymbol{k} = 0, \\ \frac{\hat{\boldsymbol{z}} \times \boldsymbol{k}}{\sqrt{k_x^2 + k_y^2}} & \text{otherwise,} \end{cases} \qquad \text{and} \qquad \hat{\boldsymbol{\theta}}_{\boldsymbol{k}} \coloneqq \hat{\boldsymbol{\varphi}}_{\boldsymbol{k}} \times \hat{\boldsymbol{k}}. \tag{3.16}$$

Together, $\hat{\boldsymbol{k}}$, $\hat{\boldsymbol{\theta}}_{\boldsymbol{k}}$, and $\hat{\boldsymbol{\varphi}}_{\boldsymbol{k}}$ span a spherical coordinate system for $\boldsymbol{k}$. Choosing $\boldsymbol{v} = -\hat{\boldsymbol{\theta}}_{\boldsymbol{k}}/k$, we arrive at

To the same effect, we can choose $\boldsymbol{v} = \hat{\boldsymbol{z}}/\sqrt{k_x^2 + k_y^2}$ ($\boldsymbol{v} = -\hat{\boldsymbol{x}}/k$ if $\boldsymbol{k} \parallel \hat{\boldsymbol{z}}$)

$$\boldsymbol{M}_{\hat{\boldsymbol{k}}}(\boldsymbol{r}) = -\mathrm{i}\hat{\boldsymbol{\varphi}}_{\boldsymbol{k}} \mathrm{e}^{\mathrm{i}\boldsymbol{k}\cdot\boldsymbol{r}}, \tag{3.17a}$$

$$\boldsymbol{N}_{\hat{\boldsymbol{k}}}(\boldsymbol{r}) = -\hat{\boldsymbol{\theta}}_{\boldsymbol{k}} \mathrm{e}^{\mathrm{i}\boldsymbol{k}\cdot\boldsymbol{r}}. \tag{3.17b}$$

For real $\boldsymbol{k}$, Eqs. (3.17) describe linearly polarized vector plane waves (VPWs) of unit amplitude. We further note that $\boldsymbol{M}_{\hat{\boldsymbol{k}}} \perp \hat{\boldsymbol{z}}$. In the context of the interaction of VPWs with a planar interface parallel to the $xy$-plane, it allows us to identify $\boldsymbol{M}_{\hat{\boldsymbol{k}}}$ and $\boldsymbol{N}_{\hat{\boldsymbol{k}}}$ as s- and p-polarized plane waves,[3] respectively.

3 For $\boldsymbol{k} \parallel \hat{\boldsymbol{z}}$ (i.e., normal incidence w.r.t. the interface), the meaning of s- and p-polarization becomes arbitrary.

Finally, we follow Eq. (3.14) to obtain the Beltrami fields

$$\boldsymbol{A}_{\hat{\boldsymbol{k}},\pm}(\boldsymbol{r}) = \frac{-1}{\sqrt{2}} \left( \hat{\boldsymbol{\theta}}_{\boldsymbol{k}} \pm \mathrm{i}\hat{\boldsymbol{\varphi}}_{\boldsymbol{k}} \right) \mathrm{e}^{\mathrm{i}\boldsymbol{k}\cdot\boldsymbol{r}} =: \hat{\boldsymbol{e}}_{\pm}(\boldsymbol{k}) \mathrm{e}^{\mathrm{i}\boldsymbol{k}\cdot\boldsymbol{r}}. \tag{3.18}$$

For real $\boldsymbol{k}$, these are circularly polarized VPWS and we have defined the circular polarization vectors $\hat{\boldsymbol{e}}_\pm(\boldsymbol{k})$, which obey the orthogonality and normalization relations

$$\hat{\boldsymbol{e}}_\pm^*(\boldsymbol{k}) \cdot \hat{\boldsymbol{e}}_\mp(\boldsymbol{k}) = 0, \qquad \hat{\boldsymbol{e}}_\pm^*(\boldsymbol{k}) \cdot \hat{\boldsymbol{e}}_\pm(\boldsymbol{k}) = 1, \tag{3.19}$$

and further satisfy

$$\mathrm{i}\hat{\boldsymbol{k}} \times \hat{\boldsymbol{e}}_\pm(\boldsymbol{k}) = \pm\hat{\boldsymbol{e}}_\pm(\boldsymbol{k}). \tag{3.20}$$

Specifically, $\hat{\boldsymbol{e}}_+(\boldsymbol{k})$ corresponds to *left-handed* and $\hat{\boldsymbol{e}}_-(\boldsymbol{k})$ to *right-handed* circular polarization.

The polarization handedness refers to how the field twists spatially around its axis of propagation given by $\boldsymbol{k}$.

### 3.1.5 *Vector spherical waves*

Applying Eqs. (3.12) to the spherical waves of Eq. (3.10) yields vector spherical waves (VSWS). The geometry inherent in spherical coordinates is illustrated by concentric spheres that form the isosurfaces of the radial coordinate $r$. We set $\boldsymbol{v} = \mathrm{i}\boldsymbol{r}/\sqrt{\ell(\ell+1)}$, with the prefactor chosen for a convenient scaling of the resulting vector solutions. Correspondingly,

The operator $(\boldsymbol{r} \times \boldsymbol{\nabla})/\mathrm{i}$ can be identified with the orbital angular momentum operator. [42, Eq. (9.101)]

$$\boldsymbol{M}_{\ell m}^{(n)}(\boldsymbol{r}) = z_\ell^{(n)}(kr)\frac{\mathrm{i}}{\sqrt{\ell(\ell+1)}}\boldsymbol{\nabla} \times [\boldsymbol{r}Y_{\ell m}(\theta,\varphi)] =: z_\ell^{(n)}(kr)\boldsymbol{X}_{\ell m}(\theta,\varphi), \tag{3.21a}$$

where we define the vector spherical harmonic (VSH) $\boldsymbol{X}_{\ell m}$, and

$$\begin{aligned}\boldsymbol{N}_{\ell m}^{(n)}(\boldsymbol{r}) = &\left(\frac{z_\ell^{(n)}(kr)}{kr} + \frac{1}{k}\frac{\mathrm{d}}{\mathrm{d}r}z_\ell^{(n)}(kr)\right)\hat{\boldsymbol{r}} \times \boldsymbol{X}_{\ell m}(\theta,\varphi) \\ &+ \sqrt{\ell(\ell+1)}\frac{z_\ell^{(n)}(kr)}{kr}\mathrm{i}Y_{\ell m}(\theta,\varphi)\hat{\boldsymbol{r}}.\end{aligned} \tag{3.21b}$$

Further details and useful relations for the VSWS are collected in Appendix A. Equations (3.21) are valid for $\ell \geq 1$. Since the vector fields $\boldsymbol{M}_{\ell m}^{(n)}$ and $\boldsymbol{N}_{\ell m}^{(n)}$ appear in the description of the electric fields radiated by magnetic or electric multipolar sources [42, Section 9.7], they are referred to as *magnetic* and *electric* VSWS, respectively. For the purpose of finding valid solutions to Eq. (3.7), we are particularly interested in the Beltrami fields

$$\boldsymbol{A}_{\ell m,\pm}^{(n)}(\boldsymbol{r}) = \frac{1}{\sqrt{2}}\left(\boldsymbol{N}_{\ell m}^{(n)}(\boldsymbol{r}) \pm \boldsymbol{M}_{\ell m}^{(n)}(\boldsymbol{r})\right). \tag{3.22}$$

While the polarization of the VSWS $\boldsymbol{A}^{(n)}_{\ell m,\pm}$ is not as readily interpreted as for their plane wave counterpart, they are, again, the even and odd eigenfunctions of the helicity operator. Appendix A further shows that, in the far field (i.e., considering their asymptotic behavior far away from the origin), $\boldsymbol{A}^{(n)}_{\ell m,\pm}$ appear locally circularly polarized as well.

### 3.1.6 *Monochromatic fields*

Before we use the VSWS $\boldsymbol{A}_{\nu,\pm}$ to express the fields $\tilde{\boldsymbol{G}}_{\pm}$, we start with a note on monochromatic fields. The Fourier transforms of the fields, such as $\tilde{\boldsymbol{E}}(\boldsymbol{r},\omega)$, are functions of the angular frequency $\omega$, the conjugate variable to time. In the Helmholtz equation, we introduced the wavenumber $k$, which, as inspired by the discussion leading up to Eq. (3.7), is related to the angular frequency. However, in solving the Helmholtz equation, we treat $k$ as a given parameter. This further manifests in our notation of solutions to the Helmholtz equation, which endows them with a functional dependence on the spatial variable $\boldsymbol{r}$ only. While the dependence on $k$ in Eqs. (3.17) and (3.21) and Eqs. (3.18) and (3.22) would allow us to treat the solutions as continuous functions of $k$, there is also another way to consolidate these considerations. To this end, we consider that the relevant equations, Eq. (3.2) and, accordingly, Eqs. (3.6a) and (3.7), treat separate values of $\omega$ independently—a consequence of Maxwell's equations as well as the constitutive relations for the considered media being linear. Hence, we can consider monochromatic fields for a fixed parameter $\omega$, given by

$$\boldsymbol{E}(\boldsymbol{r},t) = \mathrm{Re}\{\boldsymbol{E}_{\omega}(\boldsymbol{r})\mathrm{e}^{-\mathrm{i}\omega t}\}. \tag{3.23}$$

The Fourier transform of such a field, allowing for distributional terms, is given by

$$\tilde{\boldsymbol{E}}(\boldsymbol{r},\omega') = \sqrt{\frac{\pi}{2}}\left[\delta(\omega'-\omega)\boldsymbol{E}_{\omega}(\boldsymbol{r}) + \delta(\omega'+\omega)\boldsymbol{E}^{*}_{\omega}(\boldsymbol{r})\right]. \tag{3.24}$$

We can further simplify our treatment by acknowledging that the electric and magnetic fields in time domain as observable quantities are real-valued.[4] The Fourier transform of any real-valued function $f(t)$ is a *Hermitian function*, that is, it obeys *conjugate symmetry*,

$$\tilde{f}(-\omega) = \tilde{f}^{*}(\omega). \tag{3.25}$$

4 The time domain fields $\boldsymbol{G}_{\pm}(\boldsymbol{r},t)$, obtained as the inverse Fourier transform of $\tilde{\boldsymbol{G}}_{\pm}(\boldsymbol{r},\omega)$, are, by construction, complex-valued in time domain.

As a consequence, all physical information about the fields is entirely contained in both the positive and negative frequency half of its Fourier transform, or *spectrum*. We, therefore, disregard negative $\omega$ and restrict our analysis to positive frequencies. It allows us to associate the Fourier transforms, such as $\tilde{\boldsymbol{E}}(\boldsymbol{r},\omega')$ in Eq. (3.24), directly with the monochromatic field amplitudes, $\boldsymbol{E}_\omega(\boldsymbol{r})$. The relations derived in Subsection 3.1.1 then yield corresponding relations for the monochromatic field amplitudes which we strip of the common frequency distribution $\delta(\omega-\omega')$. We note that a more general frequency dependence of a field can be reconstructed as a (continuous) superposition of monochromatic contributions.

Any real-valued time domain function has a complex-valued representation, obtained by dropping the negative frequency part of its Fourier transform. Such representation (scaled by a factor of 2) is called an *analytic signal*. [68, Section 10.2]

Following these considerations, we express the fields $\tilde{\boldsymbol{G}}_\pm$, represented by their monochromatic amplitudes $\boldsymbol{G}^\omega_\pm(\boldsymbol{r})$, as linear combinations of solutions to the vector Helmholtz equation. Because of Eq. (3.6a), only the fields of Eqs. (3.18) and (3.22) are suitable, and we write

$$\boldsymbol{G}^\omega_\pm(\boldsymbol{r}) = \sqrt{2}\sqrt{\varepsilon_0\varepsilon(\omega)}\sum_\nu a_{\nu,\pm}\,\boldsymbol{A}_{\nu,\pm}(\boldsymbol{r})\big|_{k=k_\pm}\,, \tag{3.26}$$

with $k_\pm$ as introduced right before Eq. (3.6a). Equation (3.3) yields the corresponding electric and magnetic fields,

$$\boldsymbol{E}_\omega(\boldsymbol{r}) = \sum_\nu \sum_{\lambda\in\{+,-\}} a_{\nu,\lambda}\,\boldsymbol{A}_{\nu,\lambda}(\boldsymbol{r})\big|_{k=k_\lambda}\,, \tag{3.27a}$$

$$\boldsymbol{H}_\omega(\boldsymbol{r}) = -\mathrm{i}\sqrt{\frac{\varepsilon_0}{\mu_0}}\sqrt{\frac{\varepsilon(\omega)}{\mu(\omega)}}\sum_\nu \sum_{\lambda\in\{+,-\}} \lambda a_{\nu,\lambda}\,\boldsymbol{A}_{\nu,\lambda}(\boldsymbol{r})\big|_{k=k_\lambda}\,. \tag{3.27b}$$

The prefactor in Eq. (3.26) was chosen to simplify Eq. (3.27a). As a consequence, the coefficients $a_{\nu,\lambda}$ are measured in units of the electric field strength, $\mathrm{V\,m^{-1}}$.

## 3.2 *Helicity of the Electromagnetic Field*

When discussing light in the context of its interaction with chiral matter, there appears a useful concept called the *helicity* of light. Helicity emerged first in the field of fluid dynamics, but became a fundamental aspect of electrodynamics as it is linked to an underlying symmetry of Maxwell's

equations. In the following, we discuss the helicity of electromagnetic fields and find that we may consider it a generalization of the notion of circular polarization handedness. We consider two separate perspectives on helicity, and demonstrate that they yield equivalent results.

### 3.2.1 *Helicity density and duality symmetry*

The helicity of a vector field $\boldsymbol{F}$ is determined by

$$h_{\boldsymbol{F}} = \iiint_V \mathrm{d}^3 r \boldsymbol{F}(\boldsymbol{r}) \cdot [\boldsymbol{\nabla} \times \boldsymbol{F}(\boldsymbol{r})] \,. \tag{3.28}$$

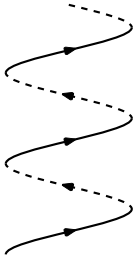

*"The combined action of the muscles of the arm when we turn the upper side of the right-hand outwards, and at the same time thrust the hand forwards, will impress the right-handed screw motion on the memory more firmly than any verbal definition."* [70, p. 24]

Since helicity is obtained as a volume integral, the integrand is identified as the *helicity density*. The above given definition of helicity has its origins in fluid dynamics. Considering $\boldsymbol{F}$ to be the flow velocity, $\boldsymbol{\nabla} \times \boldsymbol{F}$ is its *vorticity*, which describes how the motion of the flow spins locally [69]. Projecting the vorticity onto the velocity retrieves the particular motion, where the flow twists around its axis of motion while advancing; a motion resembling a corkscrew or helix. Related to the considerations of vorticity in the works of Helmholtz and Kelvin, the helicity of a fluid is of relevance as it is an invariant of ideal fluid flow [71].

Realizing the resemblance of the differential equations governing the magnetic field in conducting fluids to those of the vorticity, Elsasser [72] introduced the magnetic helicity, which he and, independently, Woltjer [73] showed to be an ideal invariant of magnetohydrodynamics. Evoking the circular motion of charges in the presence of a magnetic field $\boldsymbol{B}$ captured in Eq. (2.2) may help us understand the likeness of the magnetic field and the vorticity of a fluid. Completing the analogy, the vector potential $\boldsymbol{A}$, related to the magnetic field as $\boldsymbol{\nabla} \times \boldsymbol{A} = \boldsymbol{B}$, takes the place of velocity, and we find the magnetic helicity $h_{\boldsymbol{A}}$ by inserting $\boldsymbol{A}$ in Eq. (3.28). However, even in the absence of matter, we find the concept of helicity to be relevant when describing free electromagnetic fields [74]:

Helicity is strongly related to a symmetry of Maxwell's equations in the absence of sources [75].[5] Looking at Eqs. (2.3), we see that the transformation

$$\begin{aligned} \boldsymbol{E} \mapsto \boldsymbol{E}' &= \boldsymbol{E} \cos\alpha - c_0 \boldsymbol{B} \sin\alpha, \\ \boldsymbol{B} \mapsto \boldsymbol{B}' &= \boldsymbol{B} \cos\alpha + c_0^{-1} \boldsymbol{E} \sin\alpha, \end{aligned} \tag{3.29}$$

5 The symmetry including sources can be retained by introducing magnetic source terms [76].

for an arbitrary angle $\alpha$, leaves Maxwell's equations without sources invariant. That is, if $(\boldsymbol{E}, \boldsymbol{B})$ is a valid set of solutions, then so is $(\boldsymbol{E}', \boldsymbol{B}')$. This symmetry of Maxwell's equations and the related transformation, that structurally resembles a rotation, are referred to as *duality*.

The conserved charge associated with the duality transformation by Noether's theorem works out to [77]

$$\begin{aligned} h_{\mathrm{em}} &= \frac{\varepsilon_0}{2} \iiint_{\mathbb{R}^3} \mathrm{d}^3 r \left( c_0 \boldsymbol{A}(\boldsymbol{r}, t) \cdot \boldsymbol{B}(\boldsymbol{r}, t) - c_0^{-1} \boldsymbol{C}(\boldsymbol{r}, t) \cdot \boldsymbol{E}(\boldsymbol{r}, t) \right) \\ &= \frac{\varepsilon_0}{2} \left( c_0 h_{\boldsymbol{A}} + c_0^{-1} h_{\boldsymbol{C}} \right), \end{aligned} \tag{3.30}$$

which we recognize in the second line as the helicity, according to Eq. (3.28), of the vector potential $\boldsymbol{A}$, with $\boldsymbol{B} = \boldsymbol{\nabla} \times \boldsymbol{A}$, and the dual, or electric, vector potential $\boldsymbol{C}$, with $\boldsymbol{E} = -\boldsymbol{\nabla} \times \boldsymbol{C}$. The electromagnetic helicity $h_{\mathrm{em}}$ has units of angular momentum. Reference [76] identifies the integral in Eq. (3.30) as the generator of the duality transformation, see Eq. (2.17b) therein. To this end, the fields are treated as operators and the duality transformation follows from their canonical commutation relation. An interpretation of the conserved charge is given in Ref. [78], where it is shown to be proportional to the difference in the number of right and left circularly polarized photons in the field. While the vector potentials in Eq. (3.30) are not unique as they allow for gauge transformations, the conserved charge is gauge-independent. This can be seen as a consequence of projecting the vector potentials onto their curl—the fields—which isolates their transverse components, while a gauge transformation only introduces longitudinal, curl-free components.

We note here that by means of a Helmholtz decomposition, we can express the vector potentials in Coulomb gauge as

$$\boldsymbol{A}(\boldsymbol{r}, t) = \frac{1}{4\pi} \iiint_{\mathbb{R}^3} \mathrm{d}^3 r' \, \frac{\boldsymbol{\nabla}' \times \boldsymbol{B}(\boldsymbol{r}', t)}{|\boldsymbol{r} - \boldsymbol{r}'|}, \tag{3.31a}$$

$$\boldsymbol{C}(\boldsymbol{r}, t) = \frac{-1}{4\pi} \iiint_{\mathbb{R}^3} \mathrm{d}^3 r' \, \frac{\boldsymbol{\nabla}' \times \boldsymbol{E}(\boldsymbol{r}', t)}{|\boldsymbol{r} - \boldsymbol{r}'|}. \tag{3.31b}$$

The primed curl acts with respect to the primed variable $\boldsymbol{r}'$. The Helmholtz decomposition is usually stated to be valid for fields that decay faster than $1/r$ as $r \to \infty$ [79]. However, it can also be shown to hold for radiation fields

The radiation condition is discussed for VSWS in Appendix A.

[80]. Inserting the expressions for $\boldsymbol{A}(\boldsymbol{r},t)$ and $\boldsymbol{C}(\boldsymbol{r},t)$ into Eq. (3.30), we obtain

$$h_{\mathrm{em}} = \frac{\varepsilon_0}{8\pi} \iiint_{\mathbb{R}^3} \mathrm{d}^3 r \iiint_{\mathbb{R}^3} \mathrm{d}^3 r' \left( c_0 \frac{\boldsymbol{B}(\boldsymbol{r},t) \cdot [\boldsymbol{\nabla}' \times \boldsymbol{B}(\boldsymbol{r}',t)]}{|\boldsymbol{r}-\boldsymbol{r}'|} + c_0^{-1} \frac{\boldsymbol{E}(\boldsymbol{r},t) \cdot [\boldsymbol{\nabla}' \times \boldsymbol{E}(\boldsymbol{r}',t)]}{|\boldsymbol{r}-\boldsymbol{r}'|} \right). \tag{3.32}$$

When expressing the helicity density using only the fields and their curl, we find that it is not a purely local expression anymore as per the inner integral over space. This aspect is hidden in Eq. (3.30), involving the vector potentials. We make use of the expression above in Appendix B to show its equivalence to another expression for the electromagnetic helicity, the origins of which we discuss in the next subsection.

### 3.2.2 *Helicity operator and polarization handedness*

Another way to introduce helicity adopts a dynamical perspective. In this context, helicity is defined as the projection of angular momentum $\boldsymbol{J}$ onto the direction of propagation as indicated by linear momentum $\boldsymbol{p}$ [81, Section 8.4.1],

$$\Lambda = \boldsymbol{J} \cdot \frac{\boldsymbol{p}}{|\boldsymbol{p}|}. \tag{3.33}$$

This ties into the notion of translation with simultaneous rotation around the axis of translation, evoking the image of a helix. When applied to vector fields in frequency domain, helicity is represented by the operator

$$\boldsymbol{\Lambda} = \frac{\boldsymbol{\nabla} \times}{k}, \tag{3.34}$$

where $k$ is the frequency-dependent wavenumber. We recognize this differential operator from Subsection 3.1.1, where it naturally arose in the diagonalization of the curl equations. It leads us to understand Eq. (3.6) as defining $\tilde{\boldsymbol{G}}_{\pm}(\boldsymbol{r},\omega)$ to be divergence-free eigenfunctions of the helicity operator with eigenvalues $\pm 1$. Equation (3.34) emphasizes a strong relation between Beltrami fields and the concept of helicity [52]. We also observe a close relationship between helicity and the polarization of an electromagnetic wave, which is best illustrated using plane waves. The field vector of

a circularly polarized wave twists around its axis of propagation, which is given by the wave vector $\boldsymbol{k}$, spatially tracing the threads of a helix. Fittingly, we find left-handed (resp. right-handed) circularly polarized plane waves (Eq. (3.18)) to be the even (resp. odd) eigenfunctions of the helicity operator, as per Eq. (3.15). In this light, we intuit helicity as the generalization of circular polarization handedness to field configurations other than plane waves, and the eigenvalues of the helicity operator the equivalent of polarization handedness. Considering the possible eigenvalues, we further refer to fields that are eigenfunctions of the helicity operator as having positive or negative helicity.

The action of the helicity operator in Eq. (3.34) on the electric and magnetic (frequency domain) fields exchanges them, following from Maxwell's equations,

$$\tilde{\boldsymbol{E}} \overset{\Lambda}{\longleftrightarrow} \mathrm{i}c_0\tilde{\boldsymbol{B}}, \tag{3.35}$$

and we can relate this exchange to the abstract rotation between the fields that is the duality transformation in (3.29). Specifically,

$$\mathrm{e}^{\mathrm{i}\alpha\Lambda}\tilde{\boldsymbol{E}} = \tilde{\boldsymbol{E}}\cos\alpha - c_0\tilde{\boldsymbol{B}}\sin\alpha. \tag{3.36}$$

Combined with the analog expression for the magnetic field, we recover precisely the transformation of Eq. (3.29). Using the language of group theory, we find $\boldsymbol{\Lambda}$ to be the generator of the duality transformation.

To hint at the importance of helicity when discussing the interaction of light with chiral matter, we turn to Eq. (3.34) to find that the helicity operator and the *parity* operator, defined by the action of spatial inversion, $\boldsymbol{r} \mapsto -\boldsymbol{r}$, anticommute. After being subjected to the parity operator, an eigenfunction of the helicity operator becomes an eigenfunction with opposite eigenvalue; consistently, we find the action of spatial inversion to $\tilde{\boldsymbol{G}}_{\pm}(\boldsymbol{r},\omega) \mapsto -\tilde{\boldsymbol{G}}_{\mp}(-\boldsymbol{r},\omega)$. We say that parity, or spatial inversion, flips the helicity of a field.

The helicity operator can be used in conjunction with the scalar product for free electromagnetic fields introduced in Ref. [82] to arrive at another expression for the electromagnetic helicity. By applying the helicity operator to a field, represented by the combinations $\boldsymbol{G}_{\pm}$, and evaluating its scalar

product with the original field, we obtain an expectation value of the helicity operator. It reads [83, Eqs. (9) and (10)]:

$$\begin{aligned}\langle \Lambda \rangle &= \sum_{\lambda=\pm 1} \iiint_{\mathbb{R}^3} \frac{\mathrm{d}^3 k}{c_0 |\boldsymbol{k}|}\, \boldsymbol{G}_\lambda^*(\boldsymbol{k}) \cdot \left[\mathrm{i}\hat{\boldsymbol{k}} \times \boldsymbol{G}_\lambda(\boldsymbol{k})\right] \\ &= \iiint_{\mathbb{R}^3} \frac{\mathrm{d}^3 k}{c_0 |\boldsymbol{k}|} \left( \left|\boldsymbol{G}_+(\boldsymbol{k})\right|^2 - \left|\boldsymbol{G}_-(\boldsymbol{k})\right|^2 \right).\end{aligned} \tag{3.37}$$

$\boldsymbol{G}_\lambda(\boldsymbol{k})$ are the plane wave components of the fields defined in Eq. (3.3), further discussed in Appendix B. As discussed in Section 5.1 of Ref. [84], the norm induced by the scalar product used here is proportional to the number of photons of the radiation fields. Hence, the second line of Eq. (3.37) relates helicity to the difference between the number of right- and left-handed photons, tying back to the interpretation mentioned above. Ultimately, it can be shown that the expectation value of the helicity operator, Eq. (3.37), and the integrated helicity density obtained as the Noether charge associated with duality symmetry, Eqs. (3.30) and (3.32), are equivalent.[6] We do so in Appendix B.

6 With the given conventions up to a constant prefactor of 4.

### 3.2.3 *Optical chirality density*

The helicity density of electromagnetic fields is related to another concept termed *optical chirality density* [69],

$$\chi = \frac{1}{2\mu_0} \boldsymbol{B} \cdot (\boldsymbol{\nabla} \times \boldsymbol{B}) + \frac{\varepsilon_0}{2} \boldsymbol{E} \cdot (\boldsymbol{\nabla} \times \boldsymbol{E}). \tag{3.38}$$

Lipkin [85] introduced it as one of the "*zilches*," a group of ten quantities that he showed to be invariants of free electromagnetic fields; yet, he assigned no physical significance to this term. Tang and Cohen [86] provided such significance in showing that the dissymmetry in the excitation of a chiral dipolar particle when interacting with monochromatic light—how differently it is excited by left-handed as compared to right-handed circularly polarized light—is proportional to the ratio of the light's optical chirality density divided by its energy density. Subsequently, they coined the term *superchiral* light to refer to such light fields where said ratio (locally) exceeds that of a circularly polarized plane wave.

For monochromatic fields, helicity density and optical chirality density are proportional to each other with the proportionality factor being primarily determined by the square of the angular frequency $\omega$. In this case, we can obtain a common expression for the chirality density by expressing the fields according to Eq. (3.23) and using Maxwell's equations, which yields[7]

$$\chi_\omega(\boldsymbol{r}) = -\frac{\omega\varepsilon_0}{2}\,\mathrm{Im}\{\boldsymbol{E}_\omega^*(\boldsymbol{r})\cdot\boldsymbol{B}_\omega(\boldsymbol{r})\}. \tag{3.39}$$

7 In this form, a notable similarity is found between the chirality density and energy density of the fields [87].

For polychromatic fields, Refs. [69, 88] discuss that the optical chirality density becomes harder to interpret. Conversely, the discussion of helicity (density) does not require a restriction to monochromatic fields.

*Chapter summary* · In this chapter, we derived the equations governing electromagnetic waves in chiral isotropic media by combining Maxwell's equations with the appropriate constitutive relations. In contrast to achiral media, where these equations can be reformulated as separate wave equations for the electric and magnetic fields, chiral media cause an additional coupling between the fields. This coupling is resolved by introducing suitable linear combinations of the fields, which leads to the Helmholtz equation for electromagnetic waves in chiral media. Importantly, these combinations correspond to eigenfunctions of the helicity operator, showing that electromagnetic waves in chiral media are naturally described in terms of circular polarization, or more generally, their helicity eigenvalue.

In the next chapter, we turn to the scattering of electromagnetic waves from localized and planar systems. The two sets of solutions to the Helmholtz equation introduced above—VSWS and VPWS—provide well-suited bases to express the electromagnetic waves, conforming to the geometries inherent to such systems. The helicity-based formulation employed here readily allows chiral media to be incorporated in the scattering formalism established in the next chapter.

# 4 *Scattering from Localized Objects and Planar Systems*

In the preceding chapters, we discussed the electrodynamical description of chiral media via constitutive relations and electromagnetic waves in such media. We now turn toward the interaction between monochromatic electromagnetic waves and objects made from chiral media. Two setups are important in the following chapters: First, we discuss scattering from spatially localized objects with sizes comparable to or smaller than the illuminating wavelength. We introduce scattering from spherical particles and the transition matrix formalism to handle arbitrarily shaped scatterers. The transition matrix formalism extends to periodic arrays of scatterers, leading our discussion to planar (i.e., infinitely extended in two dimensions) systems. Next, we discuss scattering at a planar interface between media, and we conclude by introducing the scattering matrix formalism for a general treatment of planar and stratified systems.

The transition and scattering matrix formalisms, as well as the quantities derived from them, supply us with the tools we use in our in-depth investigations of aspects of chiral light–matter interactions in Chapter 5 and Chapter 6. Here, we provide the detailed derivations and explanations underlying these tools. They serve as reference for the results we discuss in the following chapters. An overview of the key relations can be found in the summary at the end of the chapter.

## 4.1 *Scattering from Localized Objects*

In this section, we consider the scattering of monochromatic electromagnetic waves from localized objects. First, we describe scattering from a general spherical multilayered core-shell particle made of chiral media in a chiral embedding. We also introduce explicit expressions in the form of Mie coefficients for the basic cases of spheres made from chiral or achiral media in an achiral embedding. Examining these coefficients, we comment on the appearance of resonances in the scattering response. Afterwards, we introduce the transition matrix formalism for the description of arbitrarily

shaped scatterers. We introduce cross-sections as the primary observable quantities and discuss the extension of the transition matrix formalism to clusters and periodic arrays of scatterers. Finally, we introduce a numerical scheme to ensure the passivity of numerically obtained transition matrices.

Transition matrices and derived cross-sections constitute the core formalism for our discussion of CD and electromagnetic chirality in Chapter 5. The purpose of this section is to provide the detailed derivations and explanations of this formalism. An overview of the main relations is given at the end of the chapter.

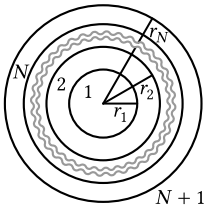


Cross-sectional view of a multilayered core-shell particle, consisting of a core with radius $r_1$ surrounded by spherical shells with outer radii $r_i$, $i \in \{2, \dots, N\}$. The separate regions are filled by media specified via the material parameters $(\varepsilon_i, \mu_i, \kappa_i)$, with $i = N+1$ representing the embedding.

### 4.1.1 *Multilayered spherical core-shell scatterers*

We consider a monochromatic wave scattering off a spherical particle. As the expressions for a single sphere (e.g., [89, Section 9.25]) can easily be derived from the general case of a multilayered core-shell particles [90], we first discuss the general setup. To this end, we consider a particle defined by a sequence of $N$ increasing radii $r_i$, $i \in \{1, \dots, N\}$, and isotropic material parameters $(\varepsilon_i, \mu_i, \kappa_i)$, omitting the common angular frequency dependence for brevity, where $i \in \{1, \dots, N+1\}$. These parameters specify a core-shell particle, consisting of a core with radius $r_1$ and the given material parameters for index $i = 1$, and concentric shells with inner radii $r_{i-1}$ and outer radii $r_i$ with corresponding material parameters for $i \in \{2, \dots, N\}$. The last set of material parameters, for $i = N+1$, defines the embedding, which is assumed to fill all of space outside the largest shell, where $|\boldsymbol{r}| > r_N$.

We represent the monochromatic fields according to Eq. (3.23). We expand the monochromatic field amplitudes in VSWS, naturally conforming to the spherical geometry of the system, separately in each region (i.e., core, shell, or embedding) $i$. Following Eqs. (3.27), the general ansatz for the fields reads

$$\boldsymbol{E}^i_\omega(\boldsymbol{r}) = \sum_{\ell,m,\lambda} a^i_{\ell m,\lambda}\, \boldsymbol{A}^{(1)}_{\ell m,\lambda}(\boldsymbol{r})\Big|_{k=k_{i,\lambda}} + \sum_{\ell,m,\lambda} p^i_{\ell m,\lambda}\, \boldsymbol{A}^{(3)}_{\ell m,\lambda}(\boldsymbol{r})\Big|_{k=k_{i,\lambda}}, \tag{4.1a}$$

$$\boldsymbol{H}^i_\omega(\boldsymbol{r}) = \frac{-\mathrm{i}}{Z_0 Z_i}\left(\sum_{\ell,m,\lambda} \lambda a^i_{\ell m,\lambda}\, \boldsymbol{A}^{(1)}_{\ell m,\lambda}(\boldsymbol{r})\Big|_{k=k_{i,\lambda}} + \sum_{\ell,m,\lambda} \lambda p^i_{\ell m,\lambda}\, \boldsymbol{A}^{(3)}_{\ell m,\lambda}(\boldsymbol{r})\Big|_{k=k_{i,\lambda}}\right), \tag{4.1b}$$

for $r_{i-1} < |\boldsymbol{r}| < r_i$.[1] The sums run over the multipolar degrees $\ell \in \mathbb{Z}^+$, mul-

1 Here, $r_0 = 0$ and $r_{N+1} = \infty$.

tipolar orders $m \in \{-\ell, \dots, \ell\}$, and helicity eigenvalues $\lambda \in \{+1, -1\}$. To express $\boldsymbol{H}^i_\omega(\boldsymbol{r})$, we have introduced the impedance of free space, $Z_0 = \sqrt{\mu_0/\varepsilon_0}$, and the relative impedances of the different media, $Z_i = \sqrt{\mu_i/\varepsilon_i}$. Further, $k_{i,\lambda} = \omega\sqrt{\varepsilon_0\mu_0}\left(\sqrt{\varepsilon_i\mu_i} + \lambda\kappa_i\right)$ is the helicity- and material-dependent wavenumber as introduced right before Eq. (3.6a).

As discussed in Appendix A, the VSWs with superscript (3) describe outwards radiating fields. Hence, the expansion coefficients $p^{N+1}_{\ell m,\lambda}$ outside the scatterer specify the scattered field radiating away from the core-shell particle. On the other hand, the coefficients $a^{N+1}_{\ell m,\lambda}$ describe the field incident onto the particle. In order to solve the scattering problem, we search for relations between the incident and the scattered expansion coefficients. As derived in Section 2.3, the tangential components of $\boldsymbol{E}$ and $\boldsymbol{H}$ are continuous across interfaces, which relates the coefficients in neighboring regions. At every interface, specified by $|\boldsymbol{r}| = r_i$, the fields have to satisfy (cf. Eqs. (2.44))

$$\hat{\boldsymbol{r}} \times \boldsymbol{E}^i_\omega(\boldsymbol{r}) = \hat{\boldsymbol{r}} \times \boldsymbol{E}^{i+1}_\omega(\boldsymbol{r}), \qquad \hat{\boldsymbol{r}} \times \boldsymbol{H}^i_\omega(\boldsymbol{r}) = \hat{\boldsymbol{r}} \times \boldsymbol{H}^{i+1}_\omega(\boldsymbol{r}). \tag{4.2}$$

We multiply both sides of Eqs. (4.2) by the VSHs $\boldsymbol{X}^*_{\ell m}(\theta,\varphi)$ or $\boldsymbol{V}^*_{\ell m}(\theta,\varphi)$ and integrate over the solid angle. Inserting Eqs. (4.1) and using the orthogonality relations for the VSHs, Eqs. (A.27), we find four relations for the expansion coefficients, jointly expressed as

$$\begin{pmatrix} \boldsymbol{\Psi}^{(1)}_{\ell,i+1,i} & \boldsymbol{\Psi}^{(3)}_{\ell,i+1,i} \\ \Xi^{(1)}_{\ell,i+1,i} & \Xi^{(3)}_{\ell,i+1,i} \end{pmatrix} \begin{pmatrix} a^{i+1}_{\ell m,+} \\ a^{i+1}_{\ell m,-} \\ p^{i+1}_{\ell m,+} \\ p^{i+1}_{\ell m,-} \end{pmatrix} = \begin{pmatrix} \boldsymbol{\Psi}^{(1)}_{\ell,i,i} & \boldsymbol{\Psi}^{(3)}_{\ell,i,i} \\ \Xi^{(1)}_{\ell,i,i} & \Xi^{(3)}_{\ell,i,i} \end{pmatrix} \begin{pmatrix} a^{i}_{\ell m,+} \\ a^{i}_{\ell m,-} \\ p^{i}_{\ell m,+} \\ p^{i}_{\ell m,-} \end{pmatrix}. \tag{4.3}$$

Here, we mostly align our notation with the one used in Section 2.2 of [91]. The matrices $\boldsymbol{\Psi}^{(n)}_{\ell,j,i}$ and $\Xi_{\ell,j,i}$ follow from the continuity of $\boldsymbol{E}$ and $\boldsymbol{H}$, respectively, and read

$$\boldsymbol{\Psi}^{(n)}_{\ell,j,i} = \begin{pmatrix} z^{(n)}_\ell\left(k_{j,+}r_i\right) & -z^{(n)}_\ell\left(k_{j,-}r_i\right) \\ \dfrac{\zeta^{(n)\prime}_\ell\left(k_{j,+}r_i\right)}{k_{j,+}r_i} & \dfrac{\zeta^{(n)\prime}_\ell\left(k_{j,-}r_i\right)}{k_{j,-}r_i} \end{pmatrix}, \tag{4.4a}$$

$$\Xi^{(n)}_{\ell,j,i} = \frac{1}{Z_j}\begin{pmatrix} z^{(n)}_\ell\left(k_{j,+}r_i\right) & z^{(n)}_\ell\left(k_{j,-}r_i\right) \\ \dfrac{\zeta^{(n)\prime}_\ell\left(k_{j,+}r_i\right)}{k_{j,+}r_i} & -\dfrac{\zeta^{(n)\prime}_\ell\left(k_{j,-}r_i\right)}{k_{j,-}r_i} \end{pmatrix}, \tag{4.4b}$$

where we have introduced the Riccati–Bessel functions,

$$\psi_\ell(x) = \zeta_\ell^{(1)}(x) = x j_\ell(x) \qquad \text{and} \qquad \xi_\ell(x) = \zeta_\ell^{(3)}(x) = x h_\ell^{(1)}(x), \tag{4.5}$$

denoting their derivatives with a prime, $\zeta_\ell^{(n)\prime}(x) = \frac{\mathrm{d}}{\mathrm{d}x}\zeta^{(n)}(x)$. Note that Eqs. (4.4) are independent of the multipolar order $m$. Solving Eq. (4.3) for the outer coefficients, we define

$$\begin{aligned} \boldsymbol{M}_{\ell,i} &:= \begin{pmatrix} \boldsymbol{\Psi}^{(1)}_{\ell,i+1,i} & \boldsymbol{\Psi}^{(3)}_{\ell,i+1,i} \\ \Xi^{(1)}_{\ell,i+1,i} & \Xi^{(3)}_{\ell,i+1,i} \end{pmatrix}^{-1} \begin{pmatrix} \boldsymbol{\Psi}^{(1)}_{\ell,i,i} & \boldsymbol{\Psi}^{(3)}_{\ell,i,i} \\ \Xi^{(1)}_{\ell,i,i} & \Xi^{(3)}_{\ell,i,i} \end{pmatrix} \\ &= -\mathrm{i} \begin{pmatrix} \mathfrak{m}^{3,1}_{+,+} & \mathfrak{m}^{3,1}_{+,-} & \mathfrak{m}^{3,3}_{+,+} & \mathfrak{m}^{3,3}_{+,-} \\ \mathfrak{m}^{3,1}_{-,+} & \mathfrak{m}^{3,1}_{-,-} & \mathfrak{m}^{3,3}_{-,+} & \mathfrak{m}^{3,3}_{-,-} \\ -\mathfrak{m}^{1,1}_{+,+} & -\mathfrak{m}^{1,1}_{+,-} & -\mathfrak{m}^{1,3}_{+,+} & -\mathfrak{m}^{1,3}_{+,-} \\ -\mathfrak{m}^{1,1}_{-,+} & -\mathfrak{m}^{1,1}_{-,-} & -\mathfrak{m}^{1,3}_{-,+} & -\mathfrak{m}^{1,3}_{-,-} \end{pmatrix}, \end{aligned} \tag{4.6a}$$

where[2]

$$\begin{aligned} \mathfrak{m}^{n,w}_{\lambda,\sigma} = \frac{Z_{i+1} + \lambda\sigma Z_i}{2Z_i} \left(k_{i+1,\lambda} r_i\right)^2 \Bigg( & \frac{\zeta_\ell^{(n)\prime}\left(k_{i+1,\lambda} r_i\right)}{k_{i+1,\lambda} r_i} z_\ell^{(w)}\left(k_{i,\sigma} r_i\right) \\ & - \lambda\sigma z_\ell^{(n)}\left(k_{i+1,\lambda} r_i\right) \frac{\zeta_\ell^{(w)\prime}\left(k_{i,\sigma} r_i\right)}{k_{i,\sigma} r_i} \Bigg). \end{aligned} \tag{4.6b}$$

2 Note that the factor involving impedances in Eq. (E.1) of Ref. [91] contains a sign error.

In deriving Eq. (4.6b), we used the Wronskian of the spherical Bessel functions, particularly, [92, Eq. (10.50.1)]

$$\mathcal{W}\left\{j_\ell(x), h_\ell^{(1)}(x)\right\} = j_\ell(x) \frac{\mathrm{d}}{\mathrm{d}x} h_\ell^{(1)}(x) - h_\ell^{(1)}(x) \frac{\mathrm{d}}{\mathrm{d}x} j_\ell(x) = \frac{\mathrm{i}}{x^2}. \tag{4.7}$$

Finally, we can use Eqs. (4.6) and Eq. (4.3) iteratively to relate the expansion coefficients in the exterior embedding to the ones in the core to find

$$\begin{pmatrix} a^{N+1}_{\ell m,+} \\ a^{N+1}_{\ell m,-} \\ p^{N+1}_{\ell m,+} \\ p^{N+1}_{\ell m,-} \end{pmatrix} = \boldsymbol{M}_{\ell,N} \ldots \boldsymbol{M}_{\ell,1} \begin{pmatrix} a^{1}_{\ell m,+} \\ a^{1}_{\ell m,-} \\ 0 \\ 0 \end{pmatrix}. \tag{4.8}$$

On the right-hand side, we have set the expansion coefficients of the singular VSWS in the core region, $p^1_{\ell m,\pm}$, to zero because the radiating VSWS are singular at the origin, but the fields must be finite. As a result, the internal field coefficients in the core region, $a^1_{\ell m,\pm}$, are related to the incident field coefficients by the upper two rows of Eq. (4.8) and to the scattered field coefficients by the lower two rows. By inverting the upper two rows, the internal coefficients can be eliminated, yielding the final relations between the incident and the scattered field coefficients. We derive such relations explicitly for the simplified setup of a single achiral sphere below.

*Mie coefficients for an achiral sphere* · While Eq. (4.8) is general and useful, it is insightful to connect it to other known expressions for the scattering coefficients. Particularly, we recover the scattering coefficients for a single achiral sphere ($N = 1$ and $\kappa_1 = 0$ identically) given by Bohren and Huffman [93, Section 4.4]. To this end, we consider a sphere of radius $r_1$ made from an achiral isotropic medium with material parameters $\varepsilon_1$ and $\mu_1$, embedded in an infinitely extended medium specified by $\varepsilon$ and $\mu$. Here, we drop the index $N + 1 = 2$ when referring to quantities in the embedding. For this setup, we only have one matrix on the right-hand side of Eq. (4.8), namely $\boldsymbol{M}_{\ell,1}$, and we can ignore its two rightmost columns as they are multiplied by zero. Inverting the upper two rows of the remaining $4 \times 2$ matrix to eliminate the internal coefficients, we find

$$\begin{pmatrix} p_{\ell m,+} \\ p_{\ell m,-} \end{pmatrix} = -\begin{pmatrix} \mathfrak{m}^{1,1}_{+,+} & \mathfrak{m}^{1,1}_{+,-} \\ \mathfrak{m}^{1,1}_{-,+} & \mathfrak{m}^{1,1}_{-,-} \end{pmatrix} \begin{pmatrix} \mathfrak{m}^{3,1}_{+,+} & \mathfrak{m}^{3,1}_{+,-} \\ \mathfrak{m}^{3,1}_{-,+} & \mathfrak{m}^{3,1}_{-,-} \end{pmatrix}^{-1} \begin{pmatrix} a_{\ell m,+} \\ a_{\ell m,-} \end{pmatrix}. \tag{4.9}$$

We define the relative refractive index $\nu \coloneqq n_1/n$, where $n_{(1)} = \sqrt{\varepsilon_{(1)}\mu_{(1)}}$, and the size parameter $x \coloneqq kr_1$, with $k = \omega\sqrt{\varepsilon_0\mu_0}n$ denoting the wavenumber in the embedding.

In Ref. [93], the fields are expressed not in terms of the helicity eigenfunction VSWS but the parity ones. Using the fact that, in achiral media, the wavenumbers for both helicities are the same, $k_+ = k_- = k$, we use the definition in Eq. (3.22) to restate the fields in terms of the parity eigenfunctions $\boldsymbol{N}^{(n)}_{\ell m}$ and $\boldsymbol{M}^{(n)}_{\ell m}$. For instance, the incident electric field reads

$$\boldsymbol{E}^{\mathrm{inc}}_{\omega}(\boldsymbol{r}) = \sum_{\ell,m} \left( a^{\mathrm{N}}_{\ell m} \boldsymbol{N}^{(1)}_{\ell m}(\boldsymbol{r}) + a^{\mathrm{M}}_{\ell m} \boldsymbol{M}^{(1)}_{\ell m}(\boldsymbol{r}) \right), \tag{4.10}$$

where the new expansion coefficients are related to the previous ones by

$$\begin{pmatrix} a^{\mathrm{N}}_{\ell m} \\ a^{\mathrm{M}}_{\ell m} \end{pmatrix} = \frac{1}{\sqrt{2}} \begin{pmatrix} 1 & 1 \\ 1 & -1 \end{pmatrix} \begin{pmatrix} a_{\ell m,+} \\ a_{\ell m,-} \end{pmatrix}. \tag{4.11}$$

Analogous expressions hold for the scattered electric field and the corresponding expansion coefficients. The magnetic fields follow accordingly. Transforming Eq. (4.9) based on Eq. (4.11) and inserting the explicit expressions from Eq. (4.6b), we find that the right-hand side matrix becomes diagonal, that is, we find separate relations between the scattered and incident coefficients with regard to the VSW type N or M:

$$\begin{pmatrix} p^{\mathrm{N}}_{\ell m} \\ p^{\mathrm{M}}_{\ell m} \end{pmatrix} = \begin{pmatrix} -\mathfrak{a}_\ell & 0 \\ 0 & -\mathfrak{b}_\ell \end{pmatrix} \begin{pmatrix} a^{\mathrm{N}}_{\ell m} \\ a^{\mathrm{M}}_{\ell m} \end{pmatrix}, \tag{4.12}$$

with

$$\mathfrak{a}_\ell = \frac{\mu\nu^2 j_\ell(\nu x)\psi'_\ell(x) - \mu_1 j_\ell(x)\psi'_\ell(\nu x)}{\mu\nu^2 j_\ell(\nu x)\xi'_\ell(x) - \mu_1 h^{(1)}_\ell(x)\psi'_\ell(\nu x)}, \tag{4.13a}$$

$$\mathfrak{b}_\ell = \frac{\mu_1 j_\ell(\nu x)\psi'_\ell(x) - \mu j_\ell(x)\psi'_\ell(\nu x)}{\mu_1 j_\ell(\nu x)\xi'_\ell(x) - \mu h^{(1)}_\ell(x)\psi'_\ell(\nu x)}. \tag{4.13b}$$

Equations (4.13) are precisely the coefficients for scattering off an achiral sphere given in Eqs. (4.53) of Ref. [93], called the *Mie coefficients*. The negative sign with which they enter Eq. (4.12) is due to differences in the definitions of the scattered and incident fields.[3]

3 Cf. the relative sign difference between the incident, Eqs. (4.37) and (4.38), and the scattered fields, Eqs. (4.45), of Ref. [93].

*Resonances of the Mie coefficients* · If we analyze Eqs. (4.13), we find that the scattering response of a sphere becomes large for configurations of the media and the radius that lead to small values of the denominators. We recast the denominators to find that such resonant scattering appears when [cf. 93, Eqs. (4.54) and (4.55)]

$$\frac{\xi'_\ell(x)}{\xi_\ell(x)} \approx \frac{\mu_1}{\mu\nu} \frac{\psi'_\ell(\nu x)}{\psi_\ell(\nu x)}, \tag{4.14a}$$

in the case of $\mathfrak{a}_\ell$, or

$$\frac{\xi_\ell'(x)}{\xi_\ell(x)} \approx \frac{\mu\nu}{\mu_1}\frac{\psi_\ell'(\nu x)}{\psi_\ell(\nu x)} \tag{4.14b}$$

for $\mathfrak{b}_\ell$. For passive media, equality in the equations above is only reached at complex frequencies [93]; hence, at real frequencies, the Mie coefficients remain finite. Nevertheless, the scattering response can be strongly dominated by one of the coefficients, namely if the considered frequency approaches the real part of the corresponding complex resonant frequency. In Chapter 3, we remarked on the electric and magnetic character of the VSWS $\boldsymbol{N}_{\ell m}^{(n)}$ and $\boldsymbol{M}_{\ell m}^{(n)}$, respectively. Considering that such a resonant response generally appears at different frequencies for different multipolar degrees $\ell$, resonances of a given $\mathfrak{a}_\ell$ (resp. $\mathfrak{b}_\ell$) are referred to as electric (resp. magnetic) multipolar resonances.

*Fröhlich resonance* · For spheres that are small relative to the illuminating wavelength, that is, for small size parameters $x$, we analyze the asymptotic behavior of the Mie coefficients. Using Eqs. (A.10a) and (A.10b) for the spherical Bessel and Neumann functions, we obtain (cf. [94, Eq. (47)], [42, Eq. (10.69)])

$$\mathfrak{a}_\ell \sim -\mathrm{i}\frac{(\ell+1)(2\ell+1)}{\ell[(2\ell+1)!!]^2}\frac{\varepsilon_1-\varepsilon}{\varepsilon_1+\frac{\ell+1}{\ell}\varepsilon}x^{2\ell+1} \quad (\text{as } x\to 0), \tag{4.15a}$$

$$\mathfrak{b}_\ell \sim -\mathrm{i}\frac{(\ell+1)(2\ell+1)}{\ell[(2\ell+1)!!]^2}\frac{\mu_1-\mu}{\mu_1+\frac{\ell+1}{\ell}\mu}x^{2\ell+1} \quad (\text{as } x\to 0). \tag{4.15b}$$

Here, we have used $\mu\nu^2 = \varepsilon_1\mu_1/\varepsilon$ to reveal the dependence of the electric and magnetic Mie coefficients on the contrast in the electric permittivity and magnetic permeability, respectively. As $\mu_1-\mu$ is typically small, $\mathfrak{a}_\ell$ dominates the interaction.[4] Furthermore, due to the powers in $x$, the interaction is mostly mediated by the contribution for the smallest $\ell$, that is, the dipolar term, $\ell = 1$.

Examining the denominator of $\mathfrak{a}_1$, a strong response is caused when $\varepsilon_1 \approx -2\varepsilon$. As this condition requires a negative real part of $\varepsilon_1$, such response is for instance found in small metallic particles. This resonance, called the

4 Equation (4.15b) is only valid for $\mu_1 \neq \mu$. For nonmagnetic particles, the asymptotic behavior of $\mathfrak{b}_\ell$is determined by higher order terms, making it negligible as compared to $\mathfrak{a}_\ell$.

*Fröhlich resonance*, predominantly determines the response of the metallic particles that we consider in Section 5.3.

*Mie coefficients for chiral spheres* · The more involved case of scattering by a chiral sphere was treated by Bohren [61, 93]. We will show that we obtain the same results from the general procedure introduced before. To this end, we allow for a nonzero chirality parameter $\kappa_1$ for the medium of the sphere. Other than that, we keep the setup from the achiral case discussed earlier (particularly, the embedding is considered achiral). Inside the medium of the sphere, we now have the helicity-dependent refractive indices $n_{1,\pm} = \sqrt{\varepsilon_1\mu_1} \pm \kappa_1$, for which we introduce the relative quantities $\nu_\pm := n_{1,\pm}/n$, with $n$ being the refractive index of the embedding. We further introduce

$$\bar{\nu} := \frac{\nu_+ + \nu_-}{2}\frac{\mu}{\mu_1} = \frac{Z}{Z_1}, \tag{4.16}$$

the mean of the helicity-dependent refractive indices scaled by the permeability ratio,[5] which in total equals the ratio between the relative impedances of the embedding and the sphere. Computing Eq. (4.9) with Eq. (4.6b) and using the transformation Eq. (4.11), we find

$$\begin{pmatrix} p^{\mathrm{N}}_{\ell m} \\ p^{\mathrm{M}}_{\ell m} \end{pmatrix} = \begin{pmatrix} -\mathfrak{a}_\ell & \mathrm{i}\mathfrak{c}_\ell \\ \mathrm{i}\mathfrak{c}_\ell & -\mathfrak{b}_\ell \end{pmatrix} \begin{pmatrix} a^{\mathrm{N}}_{\ell m} \\ a^{\mathrm{M}}_{\ell m} \end{pmatrix}, \tag{4.17}$$

with

$$\mathfrak{a}_\ell = \frac{A^+_\ell V^-_\ell + A^-_\ell V^+_\ell}{V^+_\ell W^-_\ell + V^-_\ell W^+_\ell}, \tag{4.18a}$$

$$\mathfrak{b}_\ell = \frac{B^+_\ell W^-_\ell + B^-_\ell W^+_\ell}{V^+_\ell W^-_\ell + V^-_\ell W^+_\ell}, \tag{4.18b}$$

$$\begin{aligned} \mathfrak{c}_\ell &= \mathrm{i}\frac{A^+_\ell W^-_\ell - A^-_\ell W^+_\ell}{V^+_\ell W^-_\ell + V^-_\ell W^+_\ell} \\ &= \mathrm{i}\frac{B^+_\ell V^-_\ell - B^-_\ell V^+_\ell}{V^+_\ell W^-_\ell + V^-_\ell W^+_\ell}, \end{aligned} \tag{4.18c}$$

5 $\bar{\nu}$ and $\nu_+$ (resp. $\nu_-$) are equal to the mean refractive index $m$ and the relative $m_{\mathrm{L}}$ (resp. $m_{\mathrm{R}}$) defined in Section 8.3 of Ref. [93]. There, $m$ is defined using a harmonic mean, which traces back to Ref. [93] using different material parameters (namely, Drude–Born–Fedorov parameters [52]) to describe the chiral sphere. In particular, the permeability of the chiral medium differs from the one used here.

where we have introduced

$$A_\ell^\pm \coloneqq \bar{\nu}\psi_\ell(\nu_\pm x)\psi_\ell'(x) - \psi_\ell(x)\psi_\ell'(\nu_\pm x), \tag{4.19a}$$
$$B_\ell^\pm \coloneqq \psi_\ell(\nu_\pm x)\psi_\ell'(x) - \bar{\nu}\psi_\ell(x)\psi_\ell'(\nu_\pm x), \tag{4.19b}$$
$$V_\ell^\pm \coloneqq \psi_\ell(\nu_\pm x)\xi_\ell'(x) - \bar{\nu}\xi_\ell(x)\psi_\ell'(\nu_\pm x), \tag{4.19c}$$
$$W_\ell^\pm \coloneqq \bar{\nu}\psi_\ell(\nu_\pm x)\xi_\ell'(x) - \xi_\ell(x)\psi_\ell'(\nu_\pm x). \tag{4.19d}$$

Equations (4.18) and (4.19) are equivalent to the scattering coefficients given in Section 8.3 of Ref. [93]. Comparing to the discussion of the achiral sphere above, if we set $\kappa_1 = 0$, then $\nu_+ = \nu_- = \nu$ and $\bar{\nu} = \nu\mu/\mu_1$, with $\nu$ introduced below Eq. (4.9). From this, it follows immediately that Eqs. (4.18a) and (4.18b) reduce to Eqs. (4.13), while $\mathfrak{c}_\ell$ vanishes identically.

### 4.1.2 *Transition matrix formalism*

The use of VSWS to describe scattering from a spherical object appears as a natural choice due to the considered spherical geometry. However, even for non-spherical scatterers they prove to be useful, as long as the scatterer is finite in size and, for numerical purposes, not too large. This fact is used in the transition matrix, or T-matrix, formalism, which we discuss next. The T-matrix was introduced by Waterman [95, 96] and describes the linear optical response of a scatterer, thereby entirely capturing an object's linear optical properties. Furthermore, the formalism can be extended to clusters of particles [97, 98] or periodic arrays of scatterers arranged on a lattice [99]. In the following, we introduce the underlying idea and describe the extension to more than a single scatterer. As this work makes extensive use of a particular implementation of the T-matrix formalism for numerical studies, treams [100], our description follows the related Refs. [99, 101, 102].

We consider a scattering scenario of a finite object, localized close to the origin of the coordinate system, interacting with an incident monochromatic electromagnetic wave. We consider the object to be embedded in an otherwise infinitely extended, homogeneous, isotropic, and lossless medium, specified by the material parameters $(\varepsilon, \mu, \kappa)$. The total electric and magnetic fields outside of the region occupied by the object are split into incident and scattered fields,

$$\boldsymbol{E}_\omega(\boldsymbol{r}) = \boldsymbol{E}_\omega^{\mathrm{inc}}(\boldsymbol{r}) + \boldsymbol{E}_\omega^{\mathrm{sca}}(\boldsymbol{r}), \qquad \boldsymbol{H}_\omega(\boldsymbol{r}) = \boldsymbol{H}_\omega^{\mathrm{inc}}(\boldsymbol{r}) + \boldsymbol{H}_\omega^{\mathrm{sca}}(\boldsymbol{r}). \tag{4.20}$$

In turn, the incident and scattered fields are expanded in VSWS, following Eqs. (3.27) and Eq. (A.33). Considering the incident field to be finite (regular) everywhere in space, we choose regular VSWS (denoted by the superscript $n = 1$) to expand $\boldsymbol{E}_\omega^{\mathrm{inc}}$. In Appendix A, specifically in Eq. (A.66), we see that such fields are appropriate for expressing, for instance, an illumination by a plane wave. Conversely, the scattered field originates from the localized scatterer and must appear as outgoing radiation towards the far field. We discuss the outgoing radiation condition, which is satisfied by the singular ($n = 3$) VSWS, in Appendix A. Therefore, the electric field is given as the sum of

$$\boldsymbol{E}_\omega^{\mathrm{inc}}(\boldsymbol{r}) = \sum_{\ell=1}^{\infty} \sum_{m=-\ell}^{\ell} \sum_{\lambda\in\{+,-\}} a_{\ell m,\lambda}\, \boldsymbol{A}^{(1)}_{\ell m,\lambda}(\boldsymbol{r})\Big|_{k=k_\lambda} \tag{4.21a}$$

and

$$\boldsymbol{E}_\omega^{\mathrm{sca}}(\boldsymbol{r}) = \sum_{\ell=1}^{\infty} \sum_{m=-\ell}^{\ell} \sum_{\lambda\in\{+,-\}} p_{\ell m,\lambda}\, \boldsymbol{A}^{(3)}_{\ell m,\lambda}(\boldsymbol{r})\Big|_{k=k_\lambda}, \tag{4.21b}$$

where $k_\lambda$ are the helicity-dependent wavenumbers in the embedding.

The linear optical response of the given object, that is, the mapping of an incident field to its corresponding scattered field can be represented by a matrix–vector product,

$$\underbrace{\begin{pmatrix}\boldsymbol{p}_+\\ \boldsymbol{p}_-\end{pmatrix}}_{\boldsymbol{p}} = \underbrace{\begin{pmatrix}\boldsymbol{T}_{++} & \boldsymbol{T}_{+-}\\ \boldsymbol{T}_{-+} & \boldsymbol{T}_{--}\end{pmatrix}}_{\boldsymbol{T}} \underbrace{\begin{pmatrix}\boldsymbol{a}_+\\ \boldsymbol{a}_-\end{pmatrix}}_{\boldsymbol{a}}, \tag{4.22}$$

where all expansion coefficients in Eqs. (4.21) for a given helicity $\lambda \in \{+1, -1\}$ are collected in column vectors $\boldsymbol{a}_\lambda$ and $\boldsymbol{p}_\lambda$. The linear operator $\boldsymbol{T}$, mapping between the incident and scattered field coefficients, is called the *transition matrix* (T-matrix). Above, we have further expressed the full T-matrix as a combination of four submatrices, each specified by the helicity of the incident VSWS (right index) and the scattered VSWS (left index), between which it maps. Such helicity-resolved representation proves useful when discussing chiral aspects of light–matter interaction, such as in Chapter 5.

The field expansions in Eqs. (4.21) include infinitely many terms. Correspondingly, the coefficient vectors as well as the T-matrix are infinite-dimensional. The usefulness of the T-matrix formalism, however, is due

to the fact that the series of terms can be truncated with vanishing error, allowing for efficient numerical computations. In this regard, we consider that a strong response to a large multipolar degree $\ell$ requires an optically large particle. For the simple case of a sphere, for instance, we can evaluate Eqs. (4.13) for a given $x$ to find that past a certain value for $\ell$ the coefficients become negligible. Similar observations are made for non-spherical scatterers as well. Particularly, if the size of the particle is small relative to the wavelength in the embedding, the summation over $\ell$ in Eqs. (4.21) can be truncated at some small upper bound $\ell_{\max}$, resulting in a finite T-matrix of dimension $2\ell_{\max}(\ell_{\max}+2) \times 2\ell_{\max}(\ell_{\max}+2)$.

Furthermore, the convergence and validity of the VSW-expansion of the scattered field Eq. (4.21b) is generally only guaranteed outside the smallest circumscribed sphere of the scatterer [103, 104]. Hence, the question if Eq. (4.21b) properly describes the near field depends on the given scatterer. For spheroids, for instance, the expansion diverges inside the sphere enclosing the focal points [103]. Depending on the spheroid's aspect ratio, the near field is described correctly inside some parts of the circumscribed sphere but not necessarily up to the surface of the scatterer. For spherical scatterers, the argument becomes trivial, as the object coincides with its circumscribed sphere.

### 4.1.3 *Computation of transition matrices*

In the following, we discuss how to obtain the T-matrix for a given scatterer. We distinguish between the case of spherical scatterers and non-spherical scatterers. In the former case, we find the T-matrix analytically, following our previous discussion of Mie scattering. In the non-spherical case, we outline the procedure by which the T-matrix of a general object can be obtained from numerical scattering simulations.

*Spherical scatterer* · We have discussed the scattering coefficients of a general multilayered spherical core-shell particle before. These results can immediately be cast into a T-matrix describing the spherical scatterer. For instance, in the case of a single chiral sphere in an achiral embedding, we found Eq. (4.17) relating the incident to the scattered VSW coefficients. Transform-

ing Eq. (4.17) accroding to Eq. (4.11) and using the orthogonality of VSHs for different multipolar degree $\ell$ or order $m$, the entries of the T-matrix read

$$(\boldsymbol{T}_{\lambda'\lambda})_{\ell'm',\ell m} = T_{\ell'm'\lambda',\ell m\lambda} = \left(-\frac{\mathfrak{a}_\ell + \lambda\lambda'\mathfrak{b}_\ell}{2} + \delta_{\lambda\lambda'}\lambda \mathrm{i}\mathfrak{c}_\ell\right)\delta_{\ell\ell'}\delta_{mm'}, \tag{4.23}$$

in terms of the chiral Mie coefficients introduced in Eqs. (4.18). Importantly, for any scatterer with spherical symmetry, the scattered coefficients $p_{\ell m,\lambda}$ only ever depend on the incident coefficients for matching multipolar degree $\ell$ and order $m$. As visible from Eq. (4.8), the mapping is further independent of the explicit value of $m$. Hence, the T-matrix associated with any general multilayered spherical core-shell particle is diagonal with respect to $\ell$ and $m$, with entries for same $\ell$ but different $m$ being degenerate.

*General non-spherical scatterer* · For non-spherical scatterers, we fall back to numerical scattering simulations to obtain the T-matrix [105, 106]. In this work, in particular, we use finite element method (FEM) simulations [107–112]. Here, we follow the argument of Ref. [91]. To obtain the T-matrix up to a chosen $\ell_{\max}$, at least $N = 2\ell_{\max}(\ell_{\max} + 2)$ independent scattering simulations are necessary. The resulting scattered electric fields for each simulation $i$ are expanded in outgoing VSWs, procuring a corresponding coefficient vector $\boldsymbol{p}_i$. Likewise, the incident fields for each scattering simulation correspond to a coefficient vector, $\boldsymbol{a}_i$. The T-matrix is found after solving the system of linear equations

$$\boldsymbol{p}_i = \boldsymbol{T}\boldsymbol{a}_i, \qquad i \in \{1, \dots, N\}, \tag{4.24}$$

for $\boldsymbol{T}$. Writing the coefficient vectors as columns of matrices $\boldsymbol{A}$ and $\boldsymbol{P}$, for instance $\boldsymbol{P} = (\boldsymbol{p}_1 \cdots \boldsymbol{p}_N)$, the solution is $\boldsymbol{T} = \boldsymbol{P}\boldsymbol{A}^{-1}$. The notion of independent scattering simulations above refers to the invertibility of the incident coefficient matrix, requiring the coefficient vectors $\boldsymbol{a}_i$ to be linearly independent. In the FEM simulations used in this work, we directly choose VSWs of unit amplitude as incident fields. In that case, $\boldsymbol{A} = \mathbf{1}$ and its inversion becomes trivial; each vector of scattered field coefficients $\boldsymbol{p}_i$ directly determines one column of the T-matrix. Another option is to use plane waves, choosing different illumination directions and polarizations [113]. As shown in Ref. [113], it can also be beneficial to perform more simulations than the dimension of $\boldsymbol{T}$, solving the resulting overdetermined system of linear equations

to obtain a better numerical approximation of the T-matrix. An overview over multiple numerical methods as well as their implementation used to compute T-matrices can be found in Ref. [106]. It includes the FEM-based procedure used in this work using the simulation software JCMsuite [114, 115], hence we refer to this work for implementation details.

In order to expand the scattered electric fields into expansion coefficients, we can utilize the orthogonality of the VSHS, as given in Eqs. (A.27). Choosing a spherical surface with a radius $R$ whose center lies at the origin and which surrounds the scatterer, we find [cf. 91, Eq. (2.47)]

$$\begin{pmatrix} p_{\ell m,+} \\ p_{\ell m,-} \end{pmatrix} = \sqrt{2} \left( \boldsymbol{\Psi}_\ell^{(3)} \right)^{-1} \iint \mathrm{d}\Omega \begin{pmatrix} \boldsymbol{X}_{\ell m}^*(\theta,\varphi) \cdot \boldsymbol{E}_\omega^{\mathrm{sca}}(\boldsymbol{r}) \\ \boldsymbol{V}_{\ell m}^*(\theta,\varphi) \cdot \boldsymbol{E}_\omega^{\mathrm{sca}}(\boldsymbol{r}) \end{pmatrix}, \tag{4.25}$$

where $\boldsymbol{r}$ is given by the spherical coordinates $(R,\theta,\varphi)$ and the matrix $\boldsymbol{\Psi}_\ell^{(3)}$ is given in Eq. (4.4a), replacing $k_{j,\lambda}$ by the embedding wavenumbers $k_\lambda$ and $r_i$ by $R$. Instead of projecting onto VSHS, it is also possible to directly use VSWS for the decomposition. In that case, it is further possible to perform the decomposition on an arbitrary surface surrounding the scatterer [116].

### 4.1.4 *Extinction, scattering, and absorption cross-sections*

The electromagnetic response of an object is frequently quantified in the form of cross-sections. In the following, we mostly provide the formulas for the cross-sections in terms of an object's T-matrix. We give a detailed derivation in Appendix C. First, we consider the power absorbed by the scatterer, $W_{\mathrm{abs}}$, which has to equal the net energy flux of the electromagnetic field across a surface surrounding the scatterer. The energy flux is given by the time-averaged Poynting vector [42, Section 6.9] and we choose the integration surface to be a sphere enclosing the scatterer;

$$W_{\mathrm{abs}} = -\iint \mathrm{d}\Omega\, \hat{\boldsymbol{r}} \cdot \langle \boldsymbol{S} \rangle = -\frac{1}{2} \iint \mathrm{d}\Omega\, \hat{\boldsymbol{r}} \cdot \mathrm{Re}\{\boldsymbol{E}_\omega \times \boldsymbol{H}_\omega^*\}. \tag{4.26}$$

Since no power is absorbed in the lossless embedding, $W_{\mathrm{abs}}$ is fully determined by the absorption of the scatterer [93]. Consequently, the precise shape of the integration surface is arbitrary, as long as the surface encloses the scatterer.

Separating the total fields into incident and scattered parts according to Eq. (4.20), we find that $W_{\text{abs}}$ is given by the sum of four terms (cf. Eq. (C.5)): the energy flux across the surface of the incident field, the energy flux of the scattered field, and two mixed terms. The incident energy flux is found to vanish identically, expressing the fact that the energy transported by the incident wave enters and leaves any volume at the same rate. For another way to see this, one can interpret the regular VSWS (superscript $n = 1$) used to expand the incident fields as balanced superpositions of outwards ($n = 3$) and inwards ($n = 4$) radiating VSWS, providing the same energy flux into and out of the volume enclosing the scatterer. This leaves the integrated energy flux associated with the scattered field, which we denote $W_{\text{sca}}$, and the mixed terms. We identify the mixed terms as the extinction power, $W_{\text{ext}}$, and find, after rewriting Eq. (4.26), that it is determined by the sum of scattered and absorbed power,

$$W_{\text{ext}} = W_{\text{abs}} + W_{\text{sca}}. \tag{4.27}$$

All power terms scale with the power delivered to the scatterer by the incident wave. The power of the incident wave is best expressed via its intensity $I_{\text{inc}}$, which is the energy flux per unit area in the direction of propagation associated with the incident wave. As we are mostly interested in the ratio of the scattered and absorbed powers to the incident one, we define the relative quantities

$$C_{\text{sca}} \coloneqq \frac{W_{\text{sca}}}{I_{\text{inc}}} = \frac{1}{2Z_0 Z I_{\text{inc}}} \sum_{\lambda,\lambda',\lambda''} \frac{1}{k_{\lambda'}^2} \boldsymbol{a}_\lambda^{\mathsf{H}} \boldsymbol{T}_{\lambda'\lambda}^{\mathsf{H}} \boldsymbol{T}_{\lambda'\lambda''} \boldsymbol{a}_{\lambda''}, \tag{4.28a}$$

$$C_{\text{ext}} \coloneqq \frac{W_{\text{ext}}}{I_{\text{inc}}} = \frac{-1}{2Z_0 Z I_{\text{inc}}} \sum_{\lambda,\lambda'} \frac{1}{k_\lambda^2} \operatorname{Re}\{\boldsymbol{a}_\lambda^{\mathsf{H}} \boldsymbol{T}_{\lambda\lambda'} \boldsymbol{a}_{\lambda'}\}, \tag{4.28b}$$

$$C_{\text{abs}} \coloneqq \frac{W_{\text{abs}}}{I_{\text{inc}}} = C_{\text{ext}} - C_{\text{sca}}. \tag{4.28c}$$

The explicit expressions on the right-hand sides are obtained after inserting Eqs. (4.21), the field expansions in VSWS, see Appendix C. The quantities defined in Eqs. (4.28) have dimensions of area and provide a relative measure for how strongly an object absorbs and scatters, independent of the total scaling of the incident power. Interpreting them as an effective size of the scatterer with regard to its electromagnetic interaction, we call them *cross-sections*.

*Directional cross-sections* · We are frequently interested in the cross-sections of a scatterer with respect to a given direction of illumination. The incident field is then expressed via VPWs for a fixed direction $\hat{\boldsymbol{k}}$,

$$\boldsymbol{E}_\omega^{\mathrm{inc}}(\boldsymbol{r}) = c_{\hat{\boldsymbol{k}},+}\, \boldsymbol{A}_{\hat{\boldsymbol{k}},+}(\boldsymbol{r})\Big|_{k=k_+} + c_{\hat{\boldsymbol{k}},-}\, \boldsymbol{A}_{\hat{\boldsymbol{k}},-}(\boldsymbol{r})\Big|_{k=k_-}, \tag{4.29}$$

and the corresponding $\boldsymbol{H}_\omega^{\mathrm{inc}}$. In an achiral embedding, such superposition of a left-handed ($\lambda = +1$) and right-handed ($\lambda = -1$) circularly polarized VPW describes a general elliptically polarized plane wave propagating in the direction of $\hat{\boldsymbol{k}}$. The intensity of the wave in Eq. (4.29) works out to (see Eq. (C.18))

$$I_{\mathrm{inc}} = \frac{1}{2Z_0 Z} \sum_\lambda \left| c_{\hat{\boldsymbol{k}},\lambda} \right|^2. \tag{4.30}$$

To expand $\boldsymbol{E}_\omega^{\mathrm{inc}}(\boldsymbol{r})$ in VSWs, we use Eq. (A.66) and find the expansion coefficients

$$a_{\ell m,\lambda}\big(\hat{\boldsymbol{k}}\big) = c_{\hat{\boldsymbol{k}},\lambda} 4\pi \mathrm{i}^\ell \left( X^{\varphi}_{\ell m}(\theta_{\boldsymbol{k}}, \varphi_{\boldsymbol{k}}) + \mathrm{i}\lambda X^{\theta}_{\ell m}(\theta_{\boldsymbol{k}}, \varphi_{\boldsymbol{k}}) \right)^*. \tag{4.31}$$

With the help of Eqs. (4.30) and (4.31), Eqs. (4.28) can be evaluated to obtain the directional cross-sections of a scatterer.

*Directionally averaged cross-sections* · Often, the orientation of a scatterer relative to the incident light cannot be controlled, for instance, when considering scatterers suspended in a liquid. To account for such situations, we average the directional cross-sections with respect to the illumination direction $\hat{\boldsymbol{k}}$ to obtain *directionally averaged* cross-sections. Denoting the directional average by $\langle \cdot \rangle_{\hat{\boldsymbol{k}}}$ and choosing a specific helicity $\lambda$ for the incident field, we obtain the helicity-dependent directionally averaged cross-sections (see Eqs. (C.21))

$$\big\langle C_{\mathrm{sca},\lambda} \big\rangle_{\hat{\boldsymbol{k}}} = \sum_{\lambda'} \frac{4\pi}{k_{\lambda'}^2} \| \boldsymbol{T}_{\lambda'\lambda} \|_{\mathrm{HS}}^2, \tag{4.32a}$$

$$\big\langle C_{\mathrm{ext},\lambda} \big\rangle_{\hat{\boldsymbol{k}}} = \frac{-4\pi}{k_\lambda^2} \mathrm{Re}\{\mathrm{tr}(\boldsymbol{T}_{\lambda\lambda})\}, \tag{4.32b}$$

and

$$\big\langle C_{\mathrm{abs},\lambda} \big\rangle_{\hat{\boldsymbol{k}}} = \big\langle C_{\mathrm{ext},\lambda} \big\rangle_{\hat{\boldsymbol{k}}} - \big\langle C_{\mathrm{sca},\lambda} \big\rangle_{\hat{\boldsymbol{k}}}. \tag{4.32c}$$

$\|\boldsymbol{T}_{\lambda'\lambda}\|_{\mathrm{HS}}^2 = \mathrm{tr}\big(\boldsymbol{T}_{\lambda'\lambda}^{\mathsf{H}}\boldsymbol{T}_{\lambda'\lambda}\big)$ is the squared Hilbert–Schmidt norm of $\boldsymbol{T}_{\lambda'\lambda}$ and equal to the sum of squared moduli of all entries of $\boldsymbol{T}_{\lambda'\lambda}$. Finally, to eliminate the dependency on the incident helicity, we consider the helicity- and direction-averaged cross sections,

$$\langle C_{\mathrm{sca}}\rangle_{\hat{\boldsymbol{k}}} = \frac{1}{2}\sum_{\lambda}\langle C_{\mathrm{sca},\lambda}\rangle_{\hat{\boldsymbol{k}}} = \sum_{\lambda,\lambda'}\frac{2\pi}{k_{\lambda'}^2}\|\boldsymbol{T}_{\lambda'\lambda}\|_{\mathrm{HS}}^2, \tag{4.33a}$$

$$\langle C_{\mathrm{ext}}\rangle_{\hat{\boldsymbol{k}}} = \frac{1}{2}\sum_{\lambda}\langle C_{\mathrm{ext},\lambda}\rangle_{\hat{\boldsymbol{k}}} = \sum_{\lambda}\frac{-2\pi}{k_{\lambda}^2}\,\mathrm{Re}\{\mathrm{tr}(\boldsymbol{T}_{\lambda\lambda})\}. \tag{4.33b}$$

As discussed in Appendix C, these relations become equivalent to Eqs. (42) and (43) of Ref. [117] when considering an achiral embedding.

### 4.1.5 *Clusters of scatterers*

Suppose we have a composite particle, consisting of $N$ scatterers with T-matrices $\boldsymbol{T}_i$, $i \in \{1,\dots,N\}$ located at positions $\boldsymbol{r}_i$. Correspondingly, we express the total field as the sum of the incident and $N$ particle-related scattered fields $\boldsymbol{E}_\omega^{\mathrm{sca},i}$, each expressed as a sum over VSWS according to Eqs. (4.21) with $\boldsymbol{r}_i$ serving as the origin for the VSWS [117].[6] Each $\boldsymbol{E}_\omega^{\mathrm{sca},i}$ is represented by a vector of expansion coefficients $\boldsymbol{p}_i$.

6 Explicitly, the expansions of the individual scattered fields $\boldsymbol{E}_\omega^{\mathrm{sca},i}$ appear as Eq. (4.21b), with the functional dependence of the VSWS on the right-hand side modified to $(\boldsymbol{r}-\boldsymbol{r}_i)$.

When considering a scatterer $i$, it is most convenient to expand the incident field $\boldsymbol{E}_\omega^{\mathrm{inc}}$ into VSWS centered on the location of that scatterer, $\boldsymbol{r}_i$. Hence, we construct $N$ equivalent descriptions of the incident field, each represented by the coefficient vector $\boldsymbol{a}_i$. Every scatterer $i$ is illuminated not just by the incident field but also by the fields scattered off the other particles [91, 97], hence,

$$\boldsymbol{p}_i = \boldsymbol{T}_i\left(\boldsymbol{a}_i + \sum_{j\neq i}\boldsymbol{C}^{(3)}\big(\boldsymbol{r}_i-\boldsymbol{r}_j\big)\boldsymbol{p}_j\right), \tag{4.34}$$

where the matrix $\boldsymbol{C}^{(3)}\big(\boldsymbol{r}_i-\boldsymbol{r}_j\big)$ is responsible for expanding the outward radiating VSWS centered around $\boldsymbol{r}_j$ into regular VSWS at $\boldsymbol{r}_i$, converting the scattered field of scatterer $j$ into an incident field for scatterer $i$. Its definition is given in Eq. (A.46). We rewrite Eq. (4.34) as [101]

$$\boldsymbol{p}_{\mathrm{loc}} = \boldsymbol{T}_{\mathrm{diag}}\left(\boldsymbol{a}_{\mathrm{loc}} + \boldsymbol{C}^{(3)}\boldsymbol{p}_{\mathrm{loc}}\right), \tag{4.35}$$

where $\boldsymbol{p}_{\mathrm{loc}} \coloneqq (\boldsymbol{p}_1^{\mathsf{T}}, \dots, \boldsymbol{p}_N^{\mathsf{T}})^{\mathsf{T}}$ (and, analogously, $\boldsymbol{a}_{\mathrm{loc}}$) combines all scattered (resp. incident) expansion coefficients in a single column vector. $\boldsymbol{T}_{\mathrm{diag}}$ is the corresponding block-diagonal matrix of the individual T-matrices,

$$\boldsymbol{T}_{\mathrm{diag}} \coloneqq \begin{pmatrix} \boldsymbol{T}_1 & \cdots & 0 \\ \vdots & \ddots & \vdots \\ 0 & \cdots & \boldsymbol{T}_N \end{pmatrix}, \tag{4.36}$$

and $C^{(3)}$ is responsible for the translation of VSWS between the locations of the scatterers,

$$C^{(3)} \coloneqq \begin{pmatrix} 0 & C_{1,2}^{(3)} & \cdots & C_{1,N}^{(3)} \\ C_{2,1}^{(3)} & 0 & \cdots & C_{2,N}^{(3)} \\ \vdots & \vdots & \ddots & \vdots \\ C_{N,1}^{(3)} & C_{N,2}^{(3)} & \cdots & 0 \end{pmatrix}, \tag{4.37}$$

using the shorthand notation $C_{i,j}^{(3)} = C^{(3)}(\boldsymbol{r}_i - \boldsymbol{r}_j)$. Solving for $\boldsymbol{p}_{\mathrm{loc}}$, we obtain

$$\boldsymbol{p}_{\mathrm{loc}} = \underbrace{\left(\mathbf{1} - \boldsymbol{T}_{\mathrm{diag}} C^{(3)}\right)^{-1} \boldsymbol{T}_{\mathrm{diag}}}_{=: \boldsymbol{T}_{\mathrm{loc}}} \boldsymbol{a}_{\mathrm{loc}}. \tag{4.38}$$

The T-matrix of the cluster of scatterers, $\boldsymbol{T}_{\mathrm{loc}}$, describes the scattering response of the composite particles, taking a similar form as in the case of the description of a single scatterer, Eq. (4.22). We refer to such T-matrix as well as the expansion coefficient vectors as *local*, accounting for the multiple expansion centers $\boldsymbol{r}_i$ (defining the origins of the VSWS), one per scatterer.

Often, the description of clusters of scatterers as given above is stated to be restricted to arrangements where the smallest circumscribed spheres of the scatterers do not overlap. Arguments for such restriction concern the region of validity of the scattered field expansion for a single scatterer mentioned before [103, 104] as well as mathematical properties of the translation coefficients for VSWS [97]. However, the exclusion of overlapping circumscribed spheres is a sufficient but not a necessary condition [118] and the overall validity again depends on the specific properties of the arrangement and the scatterers.

With the help of the translation coefficients for VSWS, the expansion coefficients $\boldsymbol{a}_i$ of the incident field with respect to an expansion center $\boldsymbol{r}_i$

can be expressed via the coefficients $\boldsymbol{a}$ of an expansion with respect to the global origin of the coordinate system $\boldsymbol{r}_0$ [100],

$$\boldsymbol{a}_i = \boldsymbol{C}^{(1)}(\boldsymbol{r}_i - \boldsymbol{r}_0)\boldsymbol{a} = \boldsymbol{C}^{(1)}_{i,0}\boldsymbol{a}. \tag{4.39}$$

The total scattered field, the sum of all scattered fields represented by the coefficient vectors $\boldsymbol{p}_i$, can also be expressed as a single expansion in VSWS centered at the global origin, yielding the coefficient vector

$$\boldsymbol{p} = \sum_i \boldsymbol{C}^{(1)}(\boldsymbol{r}_0 - \boldsymbol{r}_i)\boldsymbol{p}_i. \tag{4.40}$$

In combination, we obtain another representation of the T-matrix of the cluster of scatterers with respect to a single global origin,

$$\boldsymbol{T} = \left(\boldsymbol{C}^{(1)}_{0,1} \cdots \boldsymbol{C}^{(1)}_{0,N}\right) \boldsymbol{T}_{\text{loc}} \left(\boldsymbol{C}^{(1)\mathsf{T}}_{1,0} \cdots \boldsymbol{C}^{(1)\mathsf{T}}_{N,0}\right)^{\mathsf{T}}. \tag{4.41}$$

Such a global T-matrix is formally entirely equivalent to the T-matrix introduced for a single scatterer; hence, the previous discussions of Subsection 4.1.2 apply. In particular, we recover Eq. (4.22), relating the expansion coefficients of the incident and the total scattered wave with regard to expansions around common origin $\boldsymbol{r}_0$. Conceptually, the global description of the T-matrix corresponds to interpreting the cluster of individual scatterers $i$ as a single composite object and representing it via a "single-scatterer" T-matrix. For clusters of numerous closely packed scatterers, the global T-matrix often provides a more efficient description than the local one. On the other hand, the total scattered field expressed as a single expansion around the origin might lose validity inside the circumscribed sphere of the entire composite object as compared to the sum of individual scattered fields in the local description, particularly in the space between individual scatterers.

*Directional cross-sections from the local T-matrix* · The directional cross-sections for a cluster of scatterers can also be evaluated using the local T-matrix, see Appendix C. The scattered fields in the derivation in Appendix C are now given by sums over the scattered fields from each scatterer $i$. Using the translation formulas for VSWS and utilizing that the integration surface

can be chosen arbitrarily as long as it encloses the cluster of scatterers, the directional cross-sections follow as

$$C_{\mathrm{sca}} = \frac{1}{2Z_0 Z I_{\mathrm{inc}}} \sum_{\lambda} \frac{1}{k_\lambda^2} \boldsymbol{p}_{\mathrm{loc},\lambda}^{\mathsf{H}} \boldsymbol{C}_{\lambda\lambda}^{(1)} \boldsymbol{p}_{\mathrm{loc},\lambda}, \tag{4.42a}$$

$$C_{\mathrm{ext}} = \frac{-1}{2Z_0 Z I_{\mathrm{inc}}} \sum_{\lambda} \frac{1}{k_\lambda^2} \mathrm{Re}\left\{\boldsymbol{a}_{\mathrm{loc},\lambda}^{\mathsf{H}} \boldsymbol{p}_{\mathrm{loc},\lambda}\right\}, \tag{4.42b}$$

where the matrix $\boldsymbol{C}^{(1)}$ contains the translation coefficient matrices $\boldsymbol{C}_{ij}^{(1)}$, defined in Appendix A. As given in Eq. (A.49), $\boldsymbol{C}^{(1)}$ is Hermitian and its diagonal entries are $\boldsymbol{C}_{ii}^{(1)} = \boldsymbol{C}^{(1)}(0) = \mathbf{1}$. For Eqs. (4.42), we implicitly define the submatrices and -vectors corresponding to specific helicity eigenvalues $\lambda$.

Equation (4.38) can be inserted into Eqs. (4.42) to express the cross-sections via $\boldsymbol{T}_{\mathrm{loc}}$ and $\boldsymbol{a}_{\mathrm{loc}}$; the explicit expressions are given in Eqs. (C.36). As an alternative, it is possible to obtain the cross-sections, both directional and directionally averaged, using the global T-matrix of the composite scatterer in Eq. (4.41), directly applying the formulas given in Subsection 4.1.4.

### 4.1.6 *Periodic arrays of scatterers*

Another setup considered in this work is scattering off planar (i.e., infinitely extended in two dimensions) periodic arrays of scatterers. Such an array is formed by identical copies of a given scatterer located at every position of a two-dimensional lattice $L_2 = \{n_1\boldsymbol{\alpha}_1 + n_2\boldsymbol{\alpha}_2 \,|\, n_1, n_2 \in \mathbb{Z}\}$. Here, we choose the plane of the lattice, spanned by the basis vectors $\boldsymbol{\alpha}_i$, to coincide with the $xy$-plane. Such setup is equivalent to considering the scattering off an object with imposed periodic boundary conditions in two dimensions.

Each unit cell of the lattice contains one copy of the scatterer, represented by its T-matrix $\boldsymbol{T}$. Complex unit cells, comprising multiple different scatterers, can be accommodated as well, describing each unit cell as a cluster of scatterers as in the previous subsection [101, 102]. Here, we restrict ourselves to the simpler case. To satisfy the periodic boundary conditions, each unit cell has to experience the same illumination. By the same arguments underlying the Bloch theorem [cf. 119, Chapter 7], the illumination may only differ by a fixed phase difference between unit cells, expressed via the

phase factor $\mathrm{e}^{\mathrm{i}\boldsymbol{k}_\parallel\cdot\boldsymbol{R}}$ for every lattice vector $\boldsymbol{R}\in L_2$. Such a relation is satisfied if we, for example, consider illumination via plane waves, where the wave vector component tangential to the lattice determines $\boldsymbol{k}_\parallel$.

The scattered field at each lattice site $\boldsymbol{R}$ is represented by the expansion coefficients $\boldsymbol{p}_{\boldsymbol{R}}$ and, analogously, satisfy $\boldsymbol{p}_{\boldsymbol{R}} = \boldsymbol{p}_0\mathrm{e}^{\mathrm{i}\boldsymbol{k}_\parallel\cdot\boldsymbol{R}}$. Considering the multi-scattering, where each unit cell's scattered field poses another incident field for all other unit cells, we write

$$\boldsymbol{p}_0 = \boldsymbol{T}\left(\boldsymbol{a}_0 + \sum_{\boldsymbol{R}\in L_2\setminus\{\boldsymbol{0}\}} \boldsymbol{C}^{(3)}(-\boldsymbol{R})\boldsymbol{p}_{\boldsymbol{R}}\right), \tag{4.43}$$

in analogy to Eq. (4.34). Solving for $\boldsymbol{p}_0$, we obtain [99]

$$\boldsymbol{p}_0 = \underbrace{\left(\boldsymbol{1} + \boldsymbol{T}\sum_{\boldsymbol{R}\in L_2\setminus\{\boldsymbol{0}\}} \boldsymbol{C}^{(3)}(-\boldsymbol{R})\mathrm{e}^{\mathrm{i}\boldsymbol{k}_\parallel\cdot\boldsymbol{R}}\right)^{-1}\boldsymbol{T}}_{=:\boldsymbol{T}_{L_2,\boldsymbol{k}_\parallel}}\boldsymbol{a}_0 \tag{4.44}$$

The scattering scenario is fully described by the lattice T-matrix $\boldsymbol{T}_{L_2,\boldsymbol{k}_\parallel}$, yielding the scattered expansion coefficients $\boldsymbol{p}_0$ in the unit cell at $\boldsymbol{R} = 0$. We emphasize that only a uniform illumination satisfying $\boldsymbol{a}_{\boldsymbol{R}} = \boldsymbol{a}_0\mathrm{e}^{\mathrm{i}\boldsymbol{k}_\parallel\cdot\boldsymbol{R}}$ may be considered. The scattered field from every other unit cell only differs by the phase factor introduced above and the total scattered field is given by the lattice sum

$$\boldsymbol{E}^{\mathrm{sca}}_\omega(\boldsymbol{r}) = \sum_{\boldsymbol{R}\in L_2}\sum_{\ell,m,\lambda} p^0_{\ell m,\lambda}\,\boldsymbol{A}^{(3)}_{\ell m,\lambda}(\boldsymbol{r}-\boldsymbol{R})\Big|_{k=k_\lambda}\mathrm{e}^{\mathrm{i}\boldsymbol{k}_\parallel\cdot\boldsymbol{R}}. \tag{4.45}$$

We revisit the expression above in Section 4.2, where we introduce another formalism to describe scattering off planar systems. There, such lattice sums are converted to VPWs better suited for the inherent geometry. The interference of the contributions from every unit cell causes the scattered field to radiate energy only into certain directions, specified by $\boldsymbol{k}_\parallel$ up to integer multiples of the reciprocal lattice vectors. These directions correspond to the diffraction orders of the lattice.

The numerical usability of the expressions above requires efficient computations of the infinite lattice sums contained in $\boldsymbol{T}_{L_2,\boldsymbol{k}_\parallel}$ and $\boldsymbol{E}^{\mathrm{sca}}_\omega$. To this

end, Ewald's method [120, 121] is used [101]. The lattice sum is split into a short-range (small distances) and a long-range part, each of which results in an exponentially convergent series [102].

### 4.1.7 *Reactance matrix and passivation of numerically obtained transition matrices*

When numerically computing T-matrices, the limited precision can introduce gain even when all materials considered are passive. While typically negligible, such spurious gain has the potential to become harmful in a multi-scattering scenario, building up over consecutive scattering events. To mitigate such errors, we introduce a passivation scheme, ensuring the passivity of a given numerically obtained T-matrix.

While the utility of the T-matrix for describing electromagnetic scattering is apparent in the discussions above, aspects concerning the conservation or absorption of energy are not as readily accessible. For instance, a scatterer made from lossless media has to exhibit $C_{\text{abs}} = 0$ for all illuminations $\boldsymbol{a}$. From the equivalent condition $C_{\text{sca}} = C_{\text{ext}}$ and Eqs. (4.28), we find that the corresponding T-matrix has to satisfy the condition [cf. 117, Eq. (45)]

$$2\boldsymbol{T}^{\mathsf{H}}\boldsymbol{T} + \boldsymbol{T} + \boldsymbol{T}^{\mathsf{H}} = 0\,. \tag{4.46}$$

For the general passive case, an even less insightful condition follows: The left-hand side above has to be Hermitian negative semidefinite [122]. Instead, we make use of a concept closely related to the T-matrix, namely, the *reactance matrix* or *K-matrix* [122, 123]. In Eq. (4.20), we split the total field into incident and scattered parts, which we subsequently expanded in regular ($n = 1$) and outwards radiating ($n = 3$) VSWs, respectively. Alternatively, we can separate the regular and *irregular* ($n = 2$) parts of the total field, the latter isolating the singular behavior of the VSWs at the position of the scatterer. With $\boldsymbol{A}^{(3)}_{\ell m,\lambda} = \boldsymbol{A}^{(1)}_{\ell m,\lambda} + \mathrm{i}\boldsymbol{A}^{(2)}_{\ell m,\lambda}$, we find

$$\boldsymbol{E}_\omega = \sum_{\ell,m,\lambda} \left(a_{\ell m,\lambda} + p_{\ell m,\lambda}\right) \boldsymbol{A}^{(1)}_{\ell m,\lambda}\Big|_{k_\lambda} + \sum_{\ell,m,\lambda} \mathrm{i}p_{\ell m,\lambda}\, \boldsymbol{A}^{(2)}_{\ell m,\lambda}\Big|_{k_\lambda}\,. \tag{4.47}$$

Similar to before, we define the K-matrix as a mapping between coefficients, particularly,

$$\mathrm{i}\boldsymbol{p} = -\boldsymbol{K}(\boldsymbol{a} + \boldsymbol{p})\,. \tag{4.48}$$

It may be interpreted as relating the coefficients of the regular field—the incident field and the non-divergent part of the scattered field generated by the scatterer at its own position [122]—to the irregular field or directly to the scattered field, in either case up to a factor, $-1$ or i, respectively. From Eq. (4.48) and Eq. (4.22), we find [122, Eq. (12)]

$$\boldsymbol{K} = -\mathrm{i}\boldsymbol{T}(\mathbf{1} + \boldsymbol{T})^{-1}. \tag{4.49}$$

The benefit of using the K-matrix formalism for the purpose at hand lies in the fact that conditions for passive or lossless systems are more simply expressed (and numerically enforced) in terms of $\boldsymbol{K}$ than they are in terms of $\boldsymbol{T}$. Considering the lossless case, Eq. (4.46) is equivalent to the formally simpler condition

$$\boldsymbol{K} = \boldsymbol{K}^{\mathrm{H}}, \tag{4.50}$$

that is, the K-matrix is Hermitian. The general case of passivity corresponds to $\boldsymbol{K}$ being a dissipative matrix, that is, $\left(\mathrm{i}\boldsymbol{K}^{\mathrm{H}} - \mathrm{i}\boldsymbol{K}\right)$, which is proportional to the skew-Hermitian part of $\boldsymbol{K}$, is a Hermitian positive semidefinite matrix.

To passivate a numerically obtained T-matrix, we use Eq. (4.49) and obtain its corresponding K-matrix, which we decompose into its Hermitian and skew-Hermitian part,

$$\boldsymbol{K} = \frac{1}{2}\left(\boldsymbol{K} + \boldsymbol{K}^{\mathrm{H}}\right) + \frac{\mathrm{i}}{2}\underbrace{\left(\mathrm{i}\boldsymbol{K}^{\mathrm{H}} - \mathrm{i}\boldsymbol{K}\right)}_{=:\boldsymbol{K}_{\mathrm{s}}}. \tag{4.51}$$

7 $\boldsymbol{K}_{\mathrm{s}}$ is Hermitian by construction.

Passivity is satisfied if the term on the right, $\boldsymbol{K}_{\mathrm{s}}$, is positive semidefinite.[7] In the next step, we perform an eigendecomposition of $\boldsymbol{K}_{\mathrm{s}}$ and eliminate all negative eigenvalues, replacing them by 0. Reassembling $\boldsymbol{K}_{\mathrm{s}}$ from the positive clipped eigenvalues yields its passive, energy-conserving counterpart. We insert it into Eq. (4.51) and combine it with the unaltered Hermitian part of $\boldsymbol{K}$ to obtain the dissipative matrix $\boldsymbol{K}_{\mathrm{pass}}$. Finally, we reconstruct the passivated T-matrix using [122, Eq. (14)]

$$\boldsymbol{T}_{\mathrm{pass}} = \mathrm{i}\left(\mathbf{1} - \mathrm{i}\boldsymbol{K}_{\mathrm{pass}}\right)^{-1}\boldsymbol{K}_{\mathrm{pass}}. \tag{4.52}$$

The use of $\boldsymbol{T}_{\mathrm{pass}}$ ensures that subsequent computations are not affected by artificial gain resulting from the limited precision of numerically obtained T-matrices.

## 4.2 *Scattering from Planar Systems*

In this section, we introduce the formalism to describe the interaction of monochromatic electromagnetic waves with planar systems. First, we consider a plane wave impinging on a planar interface between two chiral media. We derive the reflection and transmission coefficients that relate the amplitudes of the waves in the two media. We further derive the expressions for transmittance and reflectance, which describe the transmission and reflection of power at the interface. Afterward, we introduce scattering matrices as a general formalism for planar systems. It enables the joint analysis of homogeneous planar and stratified systems, such as the interface between media, as well as two-dimensional periodic arrays of scatterers that introduce diffraction.

The scattering matrix formalism facilitates our investigation of chiral optical cavities in Chapter 6, which combine extended media and arrays of electromagnetically chiral scatterers. The following subsections provide a detailed explanation of the formalism and serve as reference for the subsequent chapters. The main results are summarized at the end of the chapter.

### 4.2.1 *Transmission and reflection at a planar interface between chiral media*

We consider a planar, infinitely extended interface between two media, located in the $xy$-plane. We label the medium occupying the lower halfspace, $z < 0$, "1" and the medium in the upper halfspace "2". We now consider a monochromatic plane wave of a given helicity $\lambda$ (i.e., circular polarization handedness) in medium "1" incident onto the planar interface. As a consequence of the incident wave, there are reflected waves in medium "1" and transmitted waves in medium "2", each propagating away from the interface, see Fig. 4.1.

The wave vector components parallel (i.e., tangential) to the interface, $\boldsymbol{k}_\parallel = (k_x, k_y)^\mathsf{T}$, suffice to specify the setup together with the material parameters, the incident helicity $\lambda$, and the angular frequency $\omega$. Both $\omega$ as well as $\boldsymbol{k}_\parallel$ are conserved in the interaction, which results from time homogeneity and the translational invariance within the $xy$-plane, respectively. Hence, only waves sharing these quantities need to be considered. Since the helicity-dependent wavenumbers in the two media are fixed to $k_{j,\sigma} = k_0 n_{j,\sigma}$,

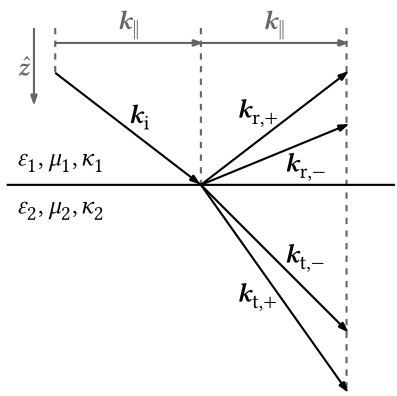


*Figure 4.1: Reflection and transmission at a planar interface between chiral media* · A monochromatic plane wave of a given helicity incident on a planar interface between two media gives rise to two reflected and transmitted plane waves in the separate media, one of each helicity. All waves exhibit the same wave vector components parallel to the interface. In chiral media, the wave vectors of different helicity are, consequently, not parallel, resulting in *circular birefringence*.

for $\sigma \in \{+1, -1\}$ and $j \in \{1, 2\}$,[8] we can find the remaining $z$-components to fully determine the involved wave vectors. To this end, we define $k^z_{j,\sigma}$, satisfying

8 Recall $k_0 = \omega\sqrt{\varepsilon_0\mu_0}$, $n_{j,\lambda} = \sqrt{\varepsilon_j\mu_j} + \lambda\kappa_j$.

$$\left(k^z_{j,\sigma}\right)^2 = \left(k_{j,\sigma}\right)^2 - \left|\boldsymbol{k}_\parallel\right|^2, \qquad \arg k^z_{j,\sigma} \in [0, \pi). \tag{4.53}$$

In the simple case of a lossless medium, $k_{j,\sigma} \in \mathbb{R}$, hence, $k^z_{j,\sigma}$ is either purely real or purely imaginary. In the real case (if $\left|\boldsymbol{k}_\parallel\right| \leq k_{j,\sigma}$), the overall real wave vector describes an undamped plane wave propagating in the corresponding direction. If $\left|\boldsymbol{k}_\parallel\right| > k_{j,\sigma}$, $k^z_{j,\sigma}$ becomes purely imaginary and the corresponding plane wave changes its phase only in the $xy$-plane, while exponentially decaying in the $z$-direction; such waves are called *evanescent*. In general, $k^z_{j,\sigma}$ has both an imaginary and a real part. In passive media, the restriction of its argument narrows to $[0, \frac{\pi}{2}]$, that is, both real and imaginary part of $k^z_{j,\sigma}$ are nonnegative, representing propagation and decay in the direction of positive $z$, respectively. As the direction of propagation (normal to planes of equal phase), given by the real part of the wave vector, is generally not the same as the direction of decay (normal to planes of equal amplitude), the corresponding plane waves are sometimes referred to as *inhomogeneous*

[89]. Since we consider the infinitely extended interface, we always restrict $k_x$ and $k_y$ to be real.

Considering the incident (resp. reflected and transmitted) wave as propagating or decaying towards (resp. away from) the interface, we find the wave vectors

$$\boldsymbol{k}_{\mathrm{i}} = \left(k_x, k_y, k^z_{1,\lambda}\right)^{\mathsf{T}}, \quad \boldsymbol{k}_{\mathrm{r},\sigma} = \left(k_x, k_y, -k^z_{1,\sigma}\right)^{\mathsf{T}}, \quad \boldsymbol{k}_{\mathrm{t},\sigma} = \left(k_x, k_y, k^z_{2,\sigma}\right)^{\mathsf{T}}. \tag{4.54}$$

The wave vectors depicted in Fig. 4.1 only represent the direction of propagation. In the case of absorptive media, the imaginary parts of the wave vectors are all parallel to $\hat{\boldsymbol{z}}$. With regard to chirality of the involved media, we remark the following: First, in chiral media, that is, if $\kappa_j \neq 0$, the wave vectors for different helicity are not parallel and hence the wave fronts propagate in different directions. Hence, we find *circular birefringence*. Second, if $\kappa_1 \neq 0$ specifically, the common notion of the angle of incidence (i.e., the angle between $\boldsymbol{k}_{\mathrm{i}}$ and the interface normal $\hat{\boldsymbol{z}}$) and the angle of reflection (i.e., the analogue for $\boldsymbol{k}_{\mathrm{i},\sigma}$) being equal only holds for the *co-polarized* reflected wave, matching the incident helicity, $\sigma = \lambda$.

Ultimately, we are interested in the amplitudes of the reflected and transmitted waves given a specific incident wave. To this end, we use Eqs. (3.27) to represent the monochromatic fields in terms of the VPWS, Eq. (3.18). For the electric field, omitting the $\boldsymbol{r}$-dependence for brevity, we have

$$\boldsymbol{E}_\omega = a_{\hat{\boldsymbol{k}}_{\mathrm{i}},\lambda}\, \boldsymbol{A}_{\hat{\boldsymbol{k}}_{\mathrm{i}},\lambda}\Big|_{k_{1,\lambda}} + a_{\hat{\boldsymbol{k}}_{\mathrm{r},+},+}\, \boldsymbol{A}_{\hat{\boldsymbol{k}}_{\mathrm{r},+},+}\Big|_{k_{1,+}} + a_{\hat{\boldsymbol{k}}_{\mathrm{r},-},-}\, \boldsymbol{A}_{\hat{\boldsymbol{k}}_{\mathrm{r},-},-}\Big|_{k_{1,-}}, \tag{4.55a}$$

for $z < 0$, and

$$\boldsymbol{E}_\omega = a_{\hat{\boldsymbol{k}}_{\mathrm{t},+},+}\, \boldsymbol{A}_{\hat{\boldsymbol{k}}_{\mathrm{t},+},+}\Big|_{k_{2,+}} + a_{\hat{\boldsymbol{k}}_{\mathrm{t},-},-}\, \boldsymbol{A}_{\hat{\boldsymbol{k}}_{\mathrm{t},-},-}\Big|_{k_{2,-}}, \tag{4.55b}$$

for $z > 0$. The corresponding $\boldsymbol{H}_\omega$ follows according to Eq. (3.27b).

In Section 2.3, we discussed the continuity of the tangential components of $\boldsymbol{E}$ and $\boldsymbol{H}$ across media interfaces. Consequently, we demand the continuity of $\hat{\boldsymbol{z}} \times \boldsymbol{E}_\omega$ and $\hat{\boldsymbol{z}} \times \boldsymbol{H}_\omega$ at $z = 0$, which allows us to determine the coefficients of the reflected and transmitted waves. Normalizing all coefficients by the incident one, we define $\mathfrak{r}_{\sigma,\lambda} \coloneqq a_{\hat{\boldsymbol{k}}_{\mathrm{r},\sigma}} / a_{\hat{\boldsymbol{k}}_{\mathrm{i},\lambda}}$ and $\mathfrak{t}_{\sigma,\lambda} \coloneqq a_{\hat{\boldsymbol{k}}_{\mathrm{t},\sigma}} / a_{\hat{\boldsymbol{k}}_{\mathrm{i},\lambda}}$, which we call the reflection and transmission coefficients, respectively. Inserting the

explicit form of the VPWs from Eq. (3.18) into Eqs. (4.55), we find that the exponential factor reduces to $e^{i\boldsymbol{k}_\parallel\cdot\boldsymbol{r}}$ in the plane given by $z = 0$. Since the parallel wave vector is the same for all terms, we eliminate it from the equations. The continuity of the tangential field components requires

$$\begin{aligned}\hat{\boldsymbol{z}}\times\left[\hat{\boldsymbol{e}}_\lambda(\boldsymbol{k}_\mathrm{i})+\mathfrak{r}_{+,\lambda}\hat{\boldsymbol{e}}_+(\boldsymbol{k}_{\mathrm{r},+})+\mathfrak{r}_{-,\lambda}\hat{\boldsymbol{e}}_-(\boldsymbol{k}_{\mathrm{r},-})\right]\\ =\hat{\boldsymbol{z}}\times\left[\mathfrak{t}_{+,\lambda}\hat{\boldsymbol{e}}_+(\boldsymbol{k}_{\mathrm{t},+})+\mathfrak{t}_{-,\lambda}\hat{\boldsymbol{e}}_-(\boldsymbol{k}_{\mathrm{t},-})\right],\end{aligned} \tag{4.56a}$$

$$\begin{aligned}\frac{1}{Z_1}\hat{\boldsymbol{z}}\times\left[\lambda\hat{\boldsymbol{e}}_\lambda(\boldsymbol{k}_\mathrm{i})+\mathfrak{r}_{+,\lambda}\hat{\boldsymbol{e}}_+(\boldsymbol{k}_{\mathrm{r},+})-\mathfrak{r}_{-,\lambda}\hat{\boldsymbol{e}}_-(\boldsymbol{k}_{\mathrm{r},-})\right]\\ =\frac{1}{Z_2}\hat{\boldsymbol{z}}\times\left[\mathfrak{t}_{+,\lambda}\hat{\boldsymbol{e}}_+(\boldsymbol{k}_{\mathrm{t},+})-\mathfrak{t}_{-,\lambda}\hat{\boldsymbol{e}}_-(\boldsymbol{k}_{\mathrm{t},-})\right],\end{aligned} \tag{4.56b}$$

where $Z_j=\sqrt{\mu_j/\varepsilon_j}$ denotes the relative impedance of medium $j$ and the circular polarization vectors were defined in Eq. (3.18). The first equation corresponds to the continuity of the tangential components of $\boldsymbol{E}_\omega$, the second one to that of $\boldsymbol{H}_\omega$. We further use that

$$\hat{\boldsymbol{z}}\times\hat{\boldsymbol{e}}_\pm(\boldsymbol{k})=\frac{-1}{\sqrt{2}}\left(\hat{\boldsymbol{z}}\times\hat{\boldsymbol{\theta}}_{\boldsymbol{k}}\pm\mathrm{i}\hat{\boldsymbol{z}}\times\hat{\boldsymbol{\varphi}}_{\boldsymbol{k}}\right)=\frac{-1}{\sqrt{2}}\left(\frac{k_z}{k}\frac{\hat{\boldsymbol{z}}\times\boldsymbol{k}_\parallel}{|\boldsymbol{k}_\parallel|}\mp\mathrm{i}\frac{\boldsymbol{k}_\parallel}{|\boldsymbol{k}_\parallel|}\right), \tag{4.57}$$

where $\boldsymbol{k}_\parallel/|\boldsymbol{k}_\parallel|$ and $\hat{\boldsymbol{z}}\times\boldsymbol{k}_\parallel/|\boldsymbol{k}_\parallel|$ serve as two mutually orthogonal unit vectors. Splitting Eqs. (4.56) into two parts each by projecting onto these unit vectors, we find a system of linear equations for the reflection and transmission coefficients:

$$\begin{cases}\lambda+\mathfrak{r}_{+,\lambda}-\mathfrak{r}_{-,\lambda}=\mathfrak{t}_{+,\lambda}-\mathfrak{t}_{-,\lambda},\\ \dfrac{k^z_{1,\lambda}}{k_{1,\lambda}}-\mathfrak{r}_{+,\lambda}\dfrac{k^z_{1,+}}{k_{1,+}}-\mathfrak{r}_{-,\lambda}\dfrac{k^z_{1,-}}{k_{1,-}}=\mathfrak{t}_{+,\lambda}\dfrac{k^z_{2,+}}{k_{2,+}}+\mathfrak{t}_{-,\lambda}\dfrac{k^z_{2,-}}{k_{2,-}},\\ \dfrac{Z_2}{Z_1}\left(1+\mathfrak{r}_{+,\lambda}+\mathfrak{r}_{-,\lambda}\right)=\mathfrak{t}_{+,\lambda}+\mathfrak{t}_{-,\lambda},\\ \dfrac{Z_2}{Z_1}\left(\lambda\dfrac{k^z_{1,\lambda}}{k_{1,\lambda}}-\mathfrak{r}_{+,\lambda}\dfrac{k^z_{1,+}}{k_{1,+}}+\mathfrak{r}_{-,\lambda}\dfrac{k^z_{1,-}}{k_{1,-}}\right)=\mathfrak{t}_{+,\lambda}\dfrac{k^z_{2,+}}{k_{2,+}}-\mathfrak{t}_{-,\lambda}\dfrac{k^z_{2,-}}{k_{2,-}}.\end{cases} \tag{4.58}$$

Equations (4.59) are equivalent to Eqs. (S4) of Ref. [99], which are implemented in the software treams [100].

Solving for the reflection and transmission coefficients, we find

$$\mathfrak{r}_{\sigma,\lambda} = \frac{\sigma k_{1,\sigma}}{k_{1,\lambda}} \frac{B_\lambda^+ A_{-\sigma}^- - B_\lambda^- A_{-\sigma}^+}{A_+^+ A_-^- - A_+^- A_-^+}, \tag{4.59a}$$

$$\mathfrak{t}_{\sigma,\lambda} = \frac{4\sigma\lambda Z_2 k_{2,\sigma} k_{1,\lambda}^z A_{-\lambda}^{-\sigma}}{A_+^+ A_-^- - A_+^- A_-^+}, \tag{4.59b}$$

where

$$A_\sigma^\pm \coloneqq (Z_1 \pm \sigma Z_2)\left(k_{2,\pm} k_{1,\sigma}^z \pm \sigma k_{1,\sigma} k_{2,\pm}^z\right), \tag{4.60a}$$

$$B_\lambda^\pm \coloneqq (Z_1 \pm \lambda Z_2)\left(k_{2,\pm} k_{1,\lambda}^z \mp \lambda k_{1,\lambda} k_{2,\pm}^z\right). \tag{4.60b}$$

The reflection and transmission coefficients derived above are generally applicable to planar interfaces between chiral media. We consider a few special cases in the following.

*Normal incidence* · In the special case of normal incidence (i.e., $k_x = k_y = 0$), the expressions for the transmission and reflection coefficients simplify considerably. As $|\boldsymbol{k}_\parallel| = 0$, the $z$-components in the media are equal to the wavenumbers, $k_{j,\pm}^z = k_{j,\pm}$. Adjusting Eqs. (4.59) or directly considering the simplified system of linear equations, we obtain

$$\mathfrak{r}_{\sigma,\lambda} = \delta_{-\sigma,\lambda} \frac{Z_1 - Z_2}{Z_1 + Z_2}, \tag{4.61a}$$

$$\mathfrak{t}_{\sigma,\lambda} = \delta_{\sigma,\lambda} \frac{2Z_2}{Z_1 + Z_2}. \tag{4.61b}$$

Hence, at normal incidence, only the helicity-preserving (i.e., co-polarized) transmitted wave and only the helicity-converting (i.e., cross-polarized) reflected wave persist. Notably, the coefficients do not depend on the chirality parameters of either medium, as the impedances only involve the permittivities and permeabilities.

*Media with matching impedance* · For an interface between two media satisfying $Z_1 = Z_2$, we find that both $A_\sigma^\pm$ and $B_\lambda^\pm$ are proportional to $\delta_{\pm,\sigma}$ (resp. $\delta_{\pm,\lambda}$). As a consequence, we find $\mathfrak{r}_{\sigma,\lambda}, \mathfrak{t}_{\sigma,\lambda} \propto \delta_{\sigma,\lambda}$. Only the co-polarized coefficients are nonzero, that is, helicity is conserved in both transmission and reflection. For the special case of normal incidence, we find $\mathfrak{t}_{+,+} = \mathfrak{t}_{-,-} = 1$

and all other coefficients vanish, which directly follows from Eqs. (4.61). Hence, no reflection occurs, and an incident wave of a given helicity simply propagates through the interface without change of amplitude, phase, or helicity, even though the wavenumbers in the two media may vary.

*Grazing incidence* · We consider grazing incidence, that is, the limiting case where the $z$-component of the incident wave goes to zero, $k^z_{1,\lambda} \to 0$. This corresponds to the angle between the incident wave vector and the surface normal $\hat{\boldsymbol{z}}$ approaching 90°. Note that such consideration requires medium "1" to be lossless (at least for the incident helicity), such that $k_{1,\lambda} \in \mathbb{R}$. From Eqs. (4.59) and (4.60) follow

$$\mathfrak{r}_{\sigma,\lambda} \to -\delta_{\sigma,\lambda}, \qquad \mathfrak{t}_{\sigma,\lambda} \to 0. \tag{4.62}$$

In the limiting case of grazing incidence, the wave is fully reflected and helicity is conserved, picking up only a phase factor of $-1$. As $\boldsymbol{k}_{\mathrm{i}}$ and $\boldsymbol{k}_{\mathrm{r},\lambda}$ are equal when their $z$-component is zero, above result simply leads to $\boldsymbol{E}_\omega = \boldsymbol{H}_\omega = 0$ identically everywhere when $\left|\boldsymbol{k}_\parallel\right|$ matches the wavenumber $k_{1,\lambda}$ exactly. Consequently, the case of grazing incidence and the limiting behavior of the reflection and transmission coefficients is only meaningful when approaching this case, that is, for incidence angles close to but smaller than 90°. Note that this result is derived without any restrictions on the material parameters of medium "2", nor on the wavenumber of the off-helicity in the incidence medium. Particularly, if medium "1" is chiral, $\kappa_1 \neq 0$, grazing incidence does not correspond to the same $\boldsymbol{k}_\parallel$ for the two helicities.

### 4.2.2 *Transmittance and reflectance*

The reflection and transmission coefficients of Eqs. (4.59) relate the complex amplitudes of reflected and transmitted VPWS to that of an incident VPWS of a given helicity $\lambda$. Relatedly, we can derive the power transmission coefficient, or *transmittance*, and the power reflection coefficient, or *reflectance*, which describe the relative transmitted and reflected energy flux across the interface. To this end, we consider the temporally averaged Poynting vector.

Due to the infinite extension of the system, we only consider the normal component by projecting onto the interface normal $\hat{\boldsymbol{z}}$,

$$\langle S_z \rangle = \frac{1}{2} \operatorname{Re}\{\boldsymbol{E}_\omega \times \boldsymbol{H}_\omega^*\} \cdot \hat{\boldsymbol{z}}. \tag{4.63}$$

Only the tangential components of the fields contribute to Eq. (4.63). Therefore, $\langle S_z \rangle$ is continuous, which means that the energy flux across the interface is conserved.

Using the representation of $\boldsymbol{E}_\omega$ and $\boldsymbol{H}_\omega$ as weigthed sums over VPWs according to Eqs. (3.27) and (4.55), we write

$$\begin{aligned}\langle S_z \rangle|_{z=0} &= \frac{1}{2} \sum_{\sigma',\sigma} \sum_{\nu',\nu} \operatorname{Re}\left\{ a_{\nu,\sigma} \boldsymbol{A}_{\nu,\sigma}\big|_{k_{j,\sigma}} \times \left( \frac{-\mathrm{i}\sigma'}{Z_0 Z_j} a_{\nu',\sigma'} \boldsymbol{A}_{\nu',\sigma'}\big|_{k_{j,\sigma'}} \right)^* \right\} \cdot \hat{\boldsymbol{z}} \Bigg|_{z=0} \\ &=: \sum_{\sigma',\sigma} \sum_{\nu',\nu} a^*_{\nu',\sigma'} \Sigma^j_{\nu'\sigma',\nu\sigma} a_{\nu,\sigma},\end{aligned} \tag{4.64}$$

where, for brevity, $\nu$, $\nu'$ represent indices that relate to the wave vector. The second line has the structure of a matrix–vector product, with the matrix

$$\boldsymbol{\Sigma}^j = \frac{\boldsymbol{\Sigma}'^j + \left(\boldsymbol{\Sigma}'^j\right)^{\mathsf{H}}}{2}, \tag{4.65a}$$

where $\boldsymbol{\Sigma}'^j$ has the entries

$$\Sigma'^j_{\nu'\sigma',\nu\sigma} = \frac{\mathrm{i}\sigma'}{2 Z_0 Z_j^*} \left[ \boldsymbol{A}_{\nu,\sigma}\big|_{k_{j,\sigma}} \times \left( \boldsymbol{A}_{\nu',\sigma'}\big|_{k_{j,\sigma'}} \right)^* \right] \cdot \hat{\boldsymbol{z}} \Bigg|_{z=0}. \tag{4.65b}$$

The Hermitian matrix $\boldsymbol{\Sigma}^j$ in Eq. (4.65a) is defined for convenience, accounting for taking the real part in Eq. (4.64).

For the following discussion, we slightly adjust our notation: In the equations above, the index $\nu$ (resp. $\nu'$) represents the normalized wave vector $\hat{\boldsymbol{k}}_\sigma$. Since the tangential components of the wave vector $\boldsymbol{k}_\parallel$ are conserved and the $z$-component of the wave vector satisfies Eq. (4.53), the only degree of freedom left is the sign of the $z$-component, which determines if the direction of propagation (or decay) is towards positive or negative $z$. Consequently,

we denote the $z$-component as $dk^z_{j,\sigma}$, where the sign $d \in \{+1, -1\}$ is the only relevant information contained in the index $\nu$. Moving on, we replace $\nu$ by $d$ and use the symbolic representation $d \in \{\uparrow, \downarrow\}$, with $\uparrow \coloneqq +1, \downarrow \coloneqq -1$. With this adjustment, we find explicit representations for the matrix entries of Eqs. (4.65),

$$\Sigma'^{j}_{d'\sigma',d\sigma} = \frac{1}{4Z_0 Z_j^*}\left[\frac{dk^z_{j,\sigma}}{k_{j,\sigma}} + \sigma\sigma'\left(\frac{d'k^z_{j,\sigma'}}{k_{j,\sigma'}}\right)^*\right], \tag{4.66a}$$

and

$$\Sigma^{j}_{d'\sigma',d\sigma} = \frac{1}{8Z_0\left|Z_j\right|^2}\left[\left(Z_j + \sigma\sigma' Z_j^*\right)\frac{dk^z_{j,\sigma}}{k_{j,\sigma}} + \left(Z_j^* + \sigma\sigma' Z_j\right)\left(\frac{d'k^z_{j,\sigma'}}{k_{j,\sigma'}}\right)^*\right], \tag{4.66b}$$

after inserting the formulas for the VPWs.

We apply the developed formalism to the interface considered before. Assuming a unit amplitude of the incident wave, the other coefficients are directly given by the reflection and transmission coefficients of Eqs. (4.59). Evaluating Eq. (4.64) for $z \to 0$ in the lower halfspace yields

$$\langle S_z\rangle\big|_{z=0} = \underbrace{\Sigma^1_{\uparrow\lambda,\uparrow\lambda}}_{=:\langle S_z\rangle_{\mathrm{i}}} + \underbrace{\sum_{\sigma',\sigma}\mathfrak{r}^*_{\sigma',\lambda}\Sigma^1_{\downarrow\sigma',\downarrow\sigma}\mathfrak{r}_{\sigma,\lambda}}_{=:-\langle S_z\rangle_{\mathrm{r}}} + \underbrace{\sum_{\sigma}\left(\Sigma^1_{\uparrow\lambda,\downarrow\sigma}\mathfrak{r}_{\sigma,\lambda} + \mathfrak{r}^*_{\sigma,\lambda}\Sigma^1_{\downarrow\sigma,\uparrow\lambda}\right)}_{=:\langle S_z\rangle_{\mathrm{ir}}}, \tag{4.67a}$$

and in the upper halfspace

$$\langle S_z\rangle\big|_{z=0} = \sum_{\sigma',\sigma}\mathfrak{t}^*_{\sigma',\lambda}\Sigma^2_{\uparrow\sigma',\uparrow\sigma}\mathfrak{t}_{\sigma,\lambda} =: \langle S_z\rangle_{\mathrm{t}}. \tag{4.67b}$$

The continuity of the tangential field components yields

$$\langle S_z\rangle_{\mathrm{i}} + \langle S_z\rangle_{\mathrm{ir}} - \langle S_z\rangle_{\mathrm{r}} = \langle S_z\rangle_{\mathrm{t}}. \tag{4.68}$$

To interpret the different terms of Eqs. (4.67), we observe that for cross-polarized terms

$$\Sigma^{j}_{d\sigma,d',-\sigma} \propto \mathrm{Im}\{Z_j\}, \tag{4.69a}$$

while the co-polarized co- and counter-propagating matrix elements are

$$\Sigma^j_{\uparrow\sigma,\uparrow\sigma} = -\Sigma^j_{\downarrow\sigma,\downarrow\sigma} = \frac{\operatorname{Re} Z_j}{2Z_0\left|Z_j\right|^2} \operatorname{Re}\left\{\frac{k^z_{j,\sigma}}{k_{j,\sigma}}\right\}, \tag{4.69b}$$

$$\Sigma^j_{\uparrow\sigma,\downarrow\sigma} = -\Sigma^j_{\downarrow\sigma,\uparrow\sigma} = \frac{-\mathrm{i}\operatorname{Re} Z_j}{2Z_0\left|Z_j\right|^2} \operatorname{Im}\left\{\frac{k^z_{j,\sigma}}{k_{j,\sigma}}\right\}. \tag{4.69c}$$

The term associated with the incident field, $\langle S_z\rangle_{\mathrm{i}}$, directly follows from Eq. (4.69b). For the term associated with the reflected field, $\langle S_z\rangle_{\mathrm{r}}$, the involved sums give rise to a co-polarized ($\sigma = \sigma' = \lambda$) and cross-polarized ($\sigma = \sigma' = -\lambda$) term, each proportional to Eq. (4.69b) and $|\mathfrak{r}_{\sigma,\lambda}|^2$. Additionally, there are the mixed terms ($\sigma = -\sigma'$), proportional to Eq. (4.69a). As $\operatorname{Im} Z_j$ vanishes in a lossless medium, the terms of mixed helicity only contribute in an absorbing medium. The same observations hold true for the term associated with the transmitted field, $\langle S_z\rangle_{\mathrm{t}}$, as it is structurally equivalent to $\langle S_z\rangle_{\mathrm{r}}$.

Finally, the interference term between the incident and reflected fields, $\langle S_z\rangle_{\mathrm{ir}}$, also vanishes if medium "1" is lossless: It contains a cross-polarized term (for $\sigma = -\lambda$) that vanishes as $\operatorname{Im} Z_j = 0$ (cf. Eq. (4.69a)). Additionally, it contains a co-polarized term (for $\sigma = \lambda$), proportional to Eq. (4.69c). Since we consider the incident wave to be propagating, $k^z_{1,\lambda} \in \mathbb{R}$, hence, the co-polarized term vanishes as well. In an absorbing medium, the interference term can enter the energy balance in Eq. (4.68) as a positive or negative contribution. For instance, it can reduce the effective absorption in an absorbing medium close to an interface to a lossless medium [124]. As the interference term is conceptually equally related to both the incident and the reflected fields, its allocation is ambiguous. In Ref. [125], it is treated as its own entity, modifying the usual relations of energy conservation. Since in the following chapters we consider lossless media when treating planar systems, such discussion is outside of the scope of this work. We follow the convention used in the software treams [100], which adds the interference term to the incident energy flux. Accordingly, we define the reflectance and

transmittance as the relative energy flux associated with the reflected and transmitted waves, respectively:

$$\mathfrak{R}_\lambda \coloneqq \frac{\langle S_z \rangle_\mathrm{r}}{\langle S_z \rangle_\mathrm{i} + \langle S_z \rangle_\mathrm{ir}}, \tag{4.70a}$$

$$\mathfrak{T}_\lambda \coloneqq \frac{\langle S_z \rangle_\mathrm{t}}{\langle S_z \rangle_\mathrm{i} + \langle S_z \rangle_\mathrm{ir}}. \tag{4.70b}$$

Following this convention, the relation

$$\mathfrak{R}_\lambda + \mathfrak{T}_\lambda = 1, \tag{4.71}$$

an expression of the conservation of energy, holds generally. For lossless media, we obtain the explicit expressions

$$\mathfrak{R}_\lambda = \left|\mathfrak{r}_{\lambda,\lambda}\right|^2 + \frac{k_{1,\lambda}}{k_{1,\lambda}^z} \frac{\operatorname{Re} k_{1,-\lambda}^z}{k_{1,-\lambda}} \left|\mathfrak{r}_{-\lambda,\lambda}\right|^2 =: \mathfrak{R}_{\lambda,\lambda} + \mathfrak{R}_{-\lambda,\lambda}, \tag{4.72a}$$

$$\mathfrak{T}_\lambda = \frac{Z_1}{Z_2} \frac{k_{1,\lambda}}{k_{1,\lambda}^z} \frac{\operatorname{Re} k_{2,+}^z}{k_{2,+}} \left|\mathfrak{t}_{+,\lambda}\right|^2 + \frac{Z_1}{Z_2} \frac{k_{1,\lambda}}{k_{1,\lambda}^z} \frac{\operatorname{Re} k_{2,-}^z}{k_{2,-}} \left|\mathfrak{t}_{-,\lambda}\right|^2 =: \mathfrak{T}_{+,\lambda} + \mathfrak{T}_{-,\lambda}. \tag{4.72b}$$

In lossless media, the transmittances and reflectances are entirely given by terms proportional to the squared moduli of the transmission and reflection coefficients. The proportionality constants account for the different propagation (and, hence, energy flow) directions and, in case of the transmittance, for the contrast in impedance. Note that the adjustment for different propagation directions also affects the cross-polarized reflectance, in line with the discussion of circular birefringence above. Only for an achiral medium "1" (or for normal incidence) is the prefactor equal unity, and the reflectance simplifies to the sum of squared moduli of the reflection coefficient for both helicities.

*Total internal reflection* · For lossless media, the real parts of $k_{j,\sigma}^z$ involved in Eqs. (4.72) distinguish between propagating ($|\boldsymbol{k}_\parallel| < k_{j,\sigma}$) and evanescent ($|\boldsymbol{k}_\parallel| > k_{j,\sigma}$) waves. Only propagating waves contribute to the energy flux. If the medium of incidence "1" is optically denser than medium "2", that is, $k_{2,\pm} < k_{1,\lambda}$, and the angle of incidence is sufficiently large, such that

$k_{2,\pm} \leq |\boldsymbol{k}_\parallel| < k_{1,\lambda}$, we find that $\mathfrak{T}_{\pm,\lambda} = 0$. Hence, all power is reflected. Such situation is referred to as total internal reflection (TIR). On a sidenote, we find that a similar observation can be made for the reflectance in a chiral medium: When considering the medium to be denser for the chosen incident helicity, that is, $k_{1,\lambda} > k_{1,-\lambda}$, then only the incident helicity is propagating for incidence angles in the range $k_{1,-\lambda} \leq |\boldsymbol{k}_\parallel| < k_{1,\lambda}$. Consequently, all reflected power resides in the co-polarized reflectance, $\mathfrak{R}_\lambda = \mathfrak{R}_{\lambda,\lambda}$, and $\mathfrak{R}_{-\lambda,\lambda} = 0$.

### 4.2.3 *Scattering matrix for planar and stratified systems*

In the following, we introduce a general formalism for treating the interaction of planar (i.e., infinitely extended in two dimensions) systems with monochromatic plane waves. The formalism further allows to consider stratified systems, formed by multiple planar systems stacked on top of one another. Without loss of generality, we assume the planar systems to coincide with the $xy$-plane.

Similar to our discussion of the planar interface before, we separately expand the fields in the halfspaces above and below the planar system (filled with media "2" and "1", respectively) in VPWs introduced in Section 3.1. In the case of a homogeneous planar system, such as the interface discussed before, the continuous in-plane translational invariance leads to conservation of the in-plane wave vector component $\boldsymbol{k}_\parallel$. We also consider two-dimensionally periodic structures, that is, lattices, for which the continuous translational invariance is reduced to a discrete one. Considering a system with the periodicity of a two-dimensional lattice $L_2 = \{n_1\boldsymbol{\alpha}_1 + n_2\boldsymbol{\alpha}_2 \,|\, n_1, n_2 \in \mathbb{Z}\}$ with basis vectors $\boldsymbol{\alpha}_i$ in the $xy$-plane, the parallel wave vector components are conserved up to integer multiples of the reciprocal lattice vectors. Accordingly, waves with in-plane wave vector component $\boldsymbol{k}_\parallel + \boldsymbol{G}$ for $\boldsymbol{G} \in L_2^*$, where $L_2^*$ denotes the reciprocal lattice, have to be considered collectively.

As discussed earlier, the wave vector of a VPW is uniquely determined by the in-plane wave vector components $(k_x, k_y)$ and the sign of its $z$-component, $d$. In what follows, we use the in-plane components and $d$ as indices when expressing the fields as superpositions of VPWs according to Eqs. (3.27). We separate the total fields into incoming and outgoing parts with respect to the planar system,

$$\boldsymbol{E}_\omega = \boldsymbol{E}_\omega^{\text{in}} + \boldsymbol{E}_\omega^{\text{out}}, \qquad \boldsymbol{H}_\omega = \boldsymbol{H}_\omega^{\text{in}} + \boldsymbol{H}_\omega^{\text{out}}. \tag{4.73}$$

The incoming part accounts for all VPWs that propagate or decay towards the $xy$-plane ($d = \uparrow$ for $z < 0$ and $d = \downarrow$ for $z > 0$), while the outgoing part accounts for the ones propagating or decaying away from it ($d = \downarrow$ for $z < 0$ and $d = \uparrow$ for $z > 0$). Correspondingly, we write

$$\boldsymbol{E}_\omega^{\text{in}} = \sum_\lambda \sum_{\boldsymbol{G}\in L_2^*} \begin{cases} a_{\boldsymbol{k}_\parallel+\boldsymbol{G},\uparrow,\lambda}\ \boldsymbol{A}_{\boldsymbol{k}_\parallel+\boldsymbol{G},\uparrow,\lambda}\Big|_{k=k_{1,\lambda}} & \text{for } z<0, \\ a_{\boldsymbol{k}_\parallel+\boldsymbol{G},\downarrow,\lambda}\ \boldsymbol{A}_{\boldsymbol{k}_\parallel+\boldsymbol{G},\downarrow,\lambda}\Big|_{k=k_{1,\lambda}} & \text{for } z>0, \end{cases} \tag{4.74a}$$

$$\boldsymbol{E}_\omega^{\text{out}} = \sum_\lambda \sum_{\boldsymbol{G}\in L_2^*} \begin{cases} b_{\boldsymbol{k}_\parallel+\boldsymbol{G},\downarrow,\lambda}\ \boldsymbol{A}_{\boldsymbol{k}_\parallel+\boldsymbol{G},\uparrow,\lambda}\Big|_{k=k_{1,\lambda}} & \text{for } z<0, \\ b_{\boldsymbol{k}_\parallel+\boldsymbol{G},\uparrow,\lambda}\ \boldsymbol{A}_{\boldsymbol{k}_\parallel+\boldsymbol{G},\downarrow,\lambda}\Big|_{k=k_{1,\lambda}} & \text{for } z>0. \end{cases} \tag{4.74b}$$

Collecting all expansion coefficients for a given direction $d$ in a column vector, we write the mapping between the incoming and outgoing coefficients as

$$\begin{pmatrix} \boldsymbol{b}_\uparrow \\ \boldsymbol{b}_\downarrow \end{pmatrix} = \underbrace{\begin{pmatrix} \boldsymbol{S}_{\uparrow\uparrow} & \boldsymbol{S}_{\uparrow\downarrow} \\ \boldsymbol{S}_{\downarrow\uparrow} & \boldsymbol{S}_{\downarrow\downarrow} \end{pmatrix}}_{\boldsymbol{S}} \begin{pmatrix} \boldsymbol{a}_\uparrow \\ \boldsymbol{a}_\downarrow \end{pmatrix}. \tag{4.75}$$

The matrix consisting of the four submatrices $\boldsymbol{S}_{d'd}$ represents the interaction between the planar system and the incoming waves, and we call it the *scattering matrix* or S-matrix. The indices $d'$ and $d$ determine the direction of the outgoing and incoming VSWs, respectively. Entries mapping between the same in-plane wave vector components represent relative reflection (in $\boldsymbol{S}_{\downarrow\uparrow}$ and $\boldsymbol{S}_{\uparrow\downarrow}$) and transmission (in $\boldsymbol{S}_{\uparrow\uparrow}$ and $\boldsymbol{S}_{\downarrow\downarrow}$) coefficients for the incoming waves. Entries mapping between $\boldsymbol{k}_\parallel + \boldsymbol{G}$ and $\boldsymbol{k}_\parallel + \boldsymbol{G}'$ where $\boldsymbol{G} \neq \boldsymbol{G}'$ represent diffraction. We now discuss the explicit appearance of the S-matrix for a few types of systems.

*Planar interface between media* · The S-matrix for a planar interface between two media $j \in \{1, 2\}$ can be readily written down using the results of the previous discussion. Specifically, we obtain the entries

$$\left(\boldsymbol{S}_{\uparrow\uparrow}\right)_{\boldsymbol{k}_\parallel+\boldsymbol{G}',\lambda';\boldsymbol{k}_\parallel+\boldsymbol{G},\lambda} = \delta_{\boldsymbol{G}',\boldsymbol{G}}\ \mathfrak{t}_{\lambda',\lambda}\Big|_{\boldsymbol{k}_\parallel+\boldsymbol{G}}, \tag{4.76a}$$

$$\left(\boldsymbol{S}_{\downarrow\uparrow}\right)_{\boldsymbol{k}_\parallel+\boldsymbol{G}',\lambda';\boldsymbol{k}_\parallel+\boldsymbol{G},\lambda} = \delta_{\boldsymbol{G}',\boldsymbol{G}}\ \mathfrak{r}_{\lambda',\lambda}\Big|_{\boldsymbol{k}_\parallel+\boldsymbol{G}}, \tag{4.76b}$$

which are given by Eqs. (4.59). The $k_{j,\lambda}^z$ contained in the reflection and transmission coefficients follow from Eq. (4.53), replacing $\boldsymbol{k}_\parallel \mapsto \boldsymbol{k}_\parallel + \boldsymbol{G}$. The remaining submatrices $\boldsymbol{S}_{\downarrow\downarrow}$ and $\boldsymbol{S}_{\uparrow\downarrow}$ correspond to incoming waves from the upper halfspace. Their entries are obtained accordingly, accounting for the reversed roles of media "1" and "2". Explicitly, exchanging all media related indices $1 \leftrightarrow 2$ in Eqs. (4.59) and (4.60),

$$\left(\boldsymbol{S}_{\downarrow\downarrow}\right)_{\boldsymbol{k}_\parallel+\boldsymbol{G}',\lambda';\boldsymbol{k}_\parallel+\boldsymbol{G},\lambda} = \delta_{\boldsymbol{G}',\boldsymbol{G}}\, \mathfrak{t}_{\lambda',\lambda}\big|_{\boldsymbol{k}_\parallel+\boldsymbol{G};1\leftrightarrow 2}\,, \tag{4.76c}$$

$$\left(\boldsymbol{S}_{\uparrow\downarrow}\right)_{\boldsymbol{k}_\parallel+\boldsymbol{G}',\lambda';\boldsymbol{k}_\parallel+\boldsymbol{G},\lambda} = \delta_{\boldsymbol{G}',\boldsymbol{G}}\, \mathfrak{r}_{\lambda',\lambda}\big|_{\boldsymbol{k}_\parallel+\boldsymbol{G};1\leftrightarrow 2}\,. \tag{4.76d}$$

All submatrices are diagonal with respect to the in-plane wave vector component due to continuous translational invariance, indicated by the Kronecker delta. That is, no diffraction occurs at a homogeneous interface.

*Propagation in a medium* · The simple relation between the expansion coefficients of the fields at two different planes of reference, both parallel to the $xy$-plane and relatively dislocated by a vector $\boldsymbol{R}$, can as well be expressed by an S-matrix. In this case, the only nonzero entries stem from the phase factors that the VPWs pick up as they traverse the space enclosed between the two reference planes. Hence,

$$\left(\boldsymbol{S}_{\uparrow\uparrow}\right)_{\boldsymbol{k}_\parallel+\boldsymbol{G}',\lambda';\boldsymbol{k}_\parallel+\boldsymbol{G},\lambda} = \delta_{\boldsymbol{G}',\boldsymbol{G}}\delta_{\lambda',\lambda}\mathrm{e}^{\mathrm{i}\left(\boldsymbol{k}_\parallel+\boldsymbol{G}+k_{j,\lambda}^z\hat{\boldsymbol{z}}\right)\cdot\boldsymbol{R}}, \tag{4.77a}$$

$$\left(\boldsymbol{S}_{\downarrow\downarrow}\right)_{\boldsymbol{k}_\parallel+\boldsymbol{G}',\lambda';\boldsymbol{k}_\parallel+\boldsymbol{G},\lambda} = \delta_{\boldsymbol{G}',\boldsymbol{G}}\delta_{\lambda',\lambda}\mathrm{e}^{\mathrm{i}\left(\boldsymbol{k}_\parallel+\boldsymbol{G}-k_{j,\lambda}^z\hat{\boldsymbol{z}}\right)\cdot(-\boldsymbol{R})}, \tag{4.77b}$$

and $\boldsymbol{S}_{\uparrow\downarrow}$ and $\boldsymbol{S}_{\downarrow\uparrow}$ are null matrices. Note that, conceptually, the propagation S-matrix reduces the space between the two reference planes to a two-dimensional system, wherein the passage between them is represented as a phase shift of the considered VPWs. The halfspaces $z > 0$ and $z < 0$ correspond to the spaces above and below the two reference planes, both of which simultaneously correspond to $z = 0$. Alternatively, such S-matrix can be understood as a translation between two different origins of the coordinate system.

*Two-dimensionally periodic arrays of scatterers* · In Section 4.1, we represented a periodic array of scatterers arranged on a lattice by the lattice T-matrix

$\boldsymbol{T}_{L_2,\boldsymbol{k}_\parallel}$ for a given $\boldsymbol{k}_\parallel$. An incident field, expanded in regular VSWS with expansion coefficients $\boldsymbol{a}_0$, interacts with every scatterer in the lattice with a relative phase specified by $\boldsymbol{k}_\parallel$. The total scattered electric field is given by a lattice sum,

$$\boldsymbol{E}_\omega(\boldsymbol{r}) = \sum_{\ell,m,\lambda} \sum_{\boldsymbol{R}\in L_2} p_{\ell m,\lambda} \boldsymbol{A}^{(3)}_{\ell m,\lambda}(\boldsymbol{r}-\boldsymbol{R}) \mathrm{e}^{\mathrm{i}\boldsymbol{k}_\parallel\cdot\boldsymbol{R}}, \tag{4.78}$$

and the vector collecting the expansion coefficients $p^0_{\ell m,\lambda}$ is obtained as

$$\boldsymbol{p}_0 = \boldsymbol{T}_{L_2,\boldsymbol{k}_\parallel} \boldsymbol{a}_0 . \tag{4.79}$$

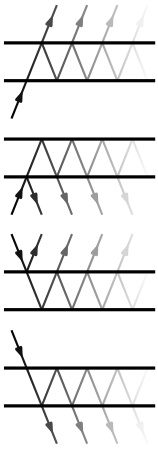

Schematic depiction of the multi-scattering between two planar systems "I" (lower horizontal line) and "II" (upper horizontal line) for incoming waves from the lower (top two panels) and upper (bottom two panels) halfspace, providing a visual representation of Eqs. (4.81). The two systems are depicted here as spatially separated for illustrative purposes only.

Using Eq. (A.66), we obtain the expansion coefficients $a^0_{\ell m,\lambda}(\boldsymbol{k}_\parallel + \boldsymbol{G}, d, \lambda)$, describing a VPW specified by $(\boldsymbol{k}_\parallel + \boldsymbol{G}, d, \lambda)$. Equation (4.79) yields the scattered field coefficients $p^0_{\ell m,\lambda}(\boldsymbol{k}_\parallel + \boldsymbol{G}, d, \lambda)$. We note that the lattice T-matrix $\boldsymbol{T}_{L_2,\boldsymbol{k}_\parallel}$ is the same for all $\boldsymbol{k}_\parallel + \boldsymbol{G}$, $\boldsymbol{G} \in L_2^*$, since the phase relation between different lattice sites is unaffected by linear combinations of the reciprocal lattice vectors. Equation (A.63) finally relates lattice sums of VSWS back to VPWS. Together, these relations complete the mapping between incoming and outgoing VPWS coefficients, constituting an S-matrix. As a last step, an identity matrix has to be added to both $\boldsymbol{S}_{\uparrow\uparrow}$ and $\boldsymbol{S}_{\downarrow\downarrow}$ to account for the unaltered contribution of the incident field to the total field.

*Stacking S-matrices for stratified systems* · Multiple planar systems can be combined into a single stratified system, described via a unified S-matrix. Considering two systems with S-matrices $\boldsymbol{S}^{\mathrm{I}}$ and $\boldsymbol{S}^{\mathrm{II}}$, we define the operation

$$\boldsymbol{S} = \boldsymbol{S}^{\mathrm{I}} \star \boldsymbol{S}^{\mathrm{II}}, \tag{4.80}$$

which yields the S-matrix describing system "II" stacked immediately on top (i.e., at larger $z$) of system "I", The operation in Eq. (4.80) is explicitly defined via the submatrices [99]

$$\boldsymbol{S}_{\uparrow\uparrow} = \boldsymbol{S}^{\mathrm{II}}_{\uparrow\uparrow} \left(\mathbf{1} - \boldsymbol{S}^{\mathrm{I}}_{\uparrow\downarrow} \boldsymbol{S}^{\mathrm{II}}_{\downarrow\uparrow}\right)^{-1} \boldsymbol{S}^{\mathrm{I}}_{\uparrow\uparrow}, \tag{4.81a}$$

$$\boldsymbol{S}_{\downarrow\uparrow} = \boldsymbol{S}^{\mathrm{I}}_{\downarrow\uparrow} + \boldsymbol{S}^{\mathrm{I}}_{\downarrow\downarrow} \boldsymbol{S}^{\mathrm{II}}_{\downarrow\uparrow} \left(\mathbf{1} - \boldsymbol{S}^{\mathrm{I}}_{\uparrow\downarrow} \boldsymbol{S}^{\mathrm{II}}_{\downarrow\uparrow}\right)^{-1} \boldsymbol{S}^{\mathrm{I}}_{\uparrow\uparrow}, \tag{4.81b}$$

$$\boldsymbol{S}_{\uparrow\downarrow} = \boldsymbol{S}^{\mathrm{II}}_{\uparrow\downarrow} + \boldsymbol{S}^{\mathrm{II}}_{\uparrow\uparrow} \boldsymbol{S}^{\mathrm{I}}_{\uparrow\downarrow} \left(\mathbf{1} - \boldsymbol{S}^{\mathrm{II}}_{\downarrow\uparrow} \boldsymbol{S}^{\mathrm{I}}_{\uparrow\downarrow}\right)^{-1} \boldsymbol{S}^{\mathrm{II}}_{\downarrow\downarrow}, \tag{4.81c}$$

$$\boldsymbol{S}_{\downarrow\downarrow} = \boldsymbol{S}^{\mathrm{I}}_{\downarrow\downarrow} \left(\mathbf{1} - \boldsymbol{S}^{\mathrm{II}}_{\downarrow\uparrow} \boldsymbol{S}^{\mathrm{I}}_{\uparrow\downarrow}\right)^{-1} \boldsymbol{S}^{\mathrm{II}}_{\downarrow\downarrow}. \tag{4.81d}$$

The stratified system accounts for the multi-scattering between the two planar systems, constituted by continual reflections between the two systems. Formally, such continual reflections lead to geometric series. If the considered systems are passive and the reflection from at least one of the systems is not perfect, the series converge to the terms $(\mathbf{1} - \cdot)^{-1}$ in the relations above.

As an example, the combination of S-matrices can be used to describe a slab of medium "2" with a finite thickness $D$ embedded in medium "1". Denoting by $\boldsymbol{S}_{\mathrm{int}(j,i)}$ the S-matrix of an interface between media $i$ (lower halfspace) and $j$ (upper halfspace) and by $\boldsymbol{S}_{\mathrm{prop}(\boldsymbol{R},j)}$ the propagation S-matrix between two reference planes in medium $j$ separated by $\boldsymbol{R}$, the S-matrix

$$\boldsymbol{S}_{\mathrm{slab}} = \boldsymbol{S}_{\mathrm{int}(1,2)} \star \boldsymbol{S}_{\mathrm{prop}(\boldsymbol{R},2)} \star \boldsymbol{S}_{\mathrm{int}(2,1)} \tag{4.82}$$

describes the scattering response of the slab. Note that the stacking operation $\star$, also referred to as the Redheffer star product [126], is associative but not commutative. This is consistent with the notion that a different order of layers corresponds to a different system, while the sequence in which adjacent layers are combined is irrelevant. Associativity allows us to write Eq. (4.82) in the presented way.

*Transmittance and reflectance in planar and stratified systems* · Our previous discussion of transmittance and reflectance can be readily transferred to any system represented by an S-matrix. Considering illumination from only one side, which, without loss of generality, we assume to be the lower halfspace (i.e., $\boldsymbol{a}_\downarrow = 0$), we evaluate the reflectance and transmittance according to Eqs. (4.70), dropping the helicity subscript as we may consider mixed helicity illumination. The individual terms follow from

$$\begin{gathered}\langle S_z \rangle_{\mathrm{i}} = \boldsymbol{a}_\uparrow^{\mathsf{H}} \boldsymbol{\Sigma}^1_{\uparrow\uparrow} \boldsymbol{a}_\uparrow, \qquad \langle S_z \rangle_{\mathrm{r}} = \boldsymbol{b}_\downarrow^{\mathsf{H}} \boldsymbol{\Sigma}^1_{\downarrow\downarrow} \boldsymbol{b}_\downarrow, \qquad \langle S_z \rangle_{\mathrm{t}} = \boldsymbol{b}_\uparrow^{\mathsf{H}} \boldsymbol{\Sigma}^2_{\uparrow\uparrow} \boldsymbol{b}_\uparrow, \\ \langle S_z \rangle_{\mathrm{ir}} = \boldsymbol{b}_\downarrow^{\mathsf{H}} \boldsymbol{\Sigma}^1_{\downarrow\uparrow} \boldsymbol{a}_\uparrow + \boldsymbol{a}_\uparrow^{\mathsf{H}} \boldsymbol{\Sigma}^1_{\uparrow\downarrow} \boldsymbol{b}_\downarrow,\end{gathered} \tag{4.83}$$

where we again label the medium in the lower (resp. upper) halfspace as "1" (resp. "2"). The matrices $\boldsymbol{\Sigma}^j_{d'd}$ consist of the entries

$$\left(\boldsymbol{\Sigma}^j_{d'd}\right)_{\boldsymbol{k}_\parallel+\boldsymbol{G}',\lambda';\boldsymbol{k}_\parallel+\boldsymbol{G},\lambda} = \Sigma^j_{d'\lambda',d\lambda}\Big|_{\boldsymbol{k}_\parallel+\boldsymbol{G}} \delta_{\boldsymbol{G}',\boldsymbol{G}}. \tag{4.84}$$

The right-hand side is given by Eq. (4.66b) for the appropriate $k^z_{j,\lambda}(\boldsymbol{k}_\parallel + \boldsymbol{G})$. As indicated by the Kronecker delta, the matrix with entries given by Eq. (4.84) is diagonal with respect to the in-plane wave vector components, which follows from averaging the energy flux over a unit cell of the lattice $L_2$.

For a general S-matrix, $\mathfrak{R}$ and $\mathfrak{T}$ do not necessarily add to unity. Hence, we define the difference to be the absorptance,

$$\mathfrak{A} \coloneqq 1 - \mathfrak{R} - \mathfrak{T}. \tag{4.85}$$

*A note on numerical implementation* · According to the field expansions in Eqs. (4.74), the coefficient vectors $\boldsymbol{a}_d$ and $\boldsymbol{b}_d$, as well as the S-matrix, are infinite-dimensional. We note that the number of VPWs and, correspondingly, the dimensionality of the S-matrix can be truncated, which enables numerical evaluation: Following Eq. (4.53), the imaginary parts of the $z$-components of the wave vectors get larger as $|\boldsymbol{k}_\parallel + \boldsymbol{G}|$ increases,[9] while the real parts fade. Accordingly, the VPWs decay faster in the out-of-plane direction and contribute less to the energy flux towards and away from the system. Usually, it is sufficient to only consider VPWs up to some upper bound for $|\boldsymbol{k}_\parallel + \boldsymbol{G}|$, which is typically a small multiple of the real part of the wavenumber in the medium.

9 In lossless media, this applies as soon as $|\boldsymbol{k}_\parallel + \boldsymbol{G}|$ exceeds the wavenumber, whereupon the $z$-component becomes purely imaginary.

*Chapter summary* · In this chapter, we have investigated the scattering of monochromatic electromagnetic waves. We have separately considered the scattering from localized (i.e., finite-sized) objects and from planar (infinitely extended) systems. For both kinds of systems, this chapter introduces suitable formalisms for their study in detail and derives spectroscopically relevant quantities, laying the groundwork for our further analyses. Below, we briefly review the main results and state their relevance for the following chapters.

For localized scatterers, the key concept is that of the transition matrix, which we introduce in Subsection 4.1.2. The T-matrix of an object maps the coefficients of an incident field expanded in VSWs to the coefficients of the corresponding scattered field, thus providing a representation of the object's linear optical properties. As such, it enables the computation of derived spectroscopic quantities, specifically, the extinction, scattering, and absorption cross-sections. We derive expressions for the helicity-dependent cross-sections with respect to a given illumination direction Eqs. (4.28) as

well as their directional averages in Eqs. (4.32). The T-matrix formalism further extends to clusters of different scatterers (cf. Subsection 4.1.5) and infinitely extended periodic arrays of scatterers (cf. Subsection 4.1.6).

The methods used to compute an object's T-matrix depend on its shape. For spherical particles, including multilayered core-shell geometries, the scattering problem and the computation of T-matrices can be solved analytically. The solution of the general multilayered case is derived in Subsection 4.1.1. For basic spheres embedded in achiral media, the entries of the T-matrix are frequently expressed in terms of Mie coefficients (cf. Eq. (4.23)), which we derive in Eqs. (4.13) and (4.18) for spheres made from achiral and chiral media, respectively. Examining the structure of the Mie coefficients and of their asymptotics for small size parameters gives insight into the optical resonances of small dielectric and metallic particles. For arbitrarily shaped scatterers, the T-matrix may be derived from numerical scattering simulations, using simulation methods such as the FEM. The general procedure including the decomposition of scattered fields into VSWS is sketched in Subsection 4.1.3. As a consequence of the limited precision of scattering simulations, numerically obtained T-matrices can exhibit artificial gain violating energy conservation. In Subsection 4.1.7, we discuss a passivation method for numerically obtained T-matrices that eliminates such artificial gain, removing a potential source of error in subsequent computations.

In Subsection 4.2.3, we introduce the scattering matrix formalism to describe scattering of electromagnetic waves from planar and stratified systems that are infinitely extended in two dimensions. In a similar manner to the T-matrix, the S-matrix maps coefficients of incoming VPWS to the coefficients of outgoing ones, individually considering the halfspaces divided by the planar system. Its entries represent reflection (within each halfspace) and transmission (between the different halfspaces) coefficients, which relate the amplitudes and phases of the VPWS. For periodic systems, the S-matrix further accounts for diffraction. Derived quantities of interest concern the transmittance and reflectance, that is, the relative amounts of transmitted and reflected power (cf. Eq. (4.83) and Eqs. (4.70)).

Of particular importance are S-matrices representing the planar interface between two media and the propagation inside a medium. The latter is given in Eqs. (4.77). S-matrices for planar interfaces are obtained from the results of Subsection 4.2.1, where we analytically derive the corresponding

transmission and reflection coefficients. Individual matrices can be combined per Eqs. (4.81) to describe composite systems. Hence, these S-matrices serve as building blocks and enable the description of slabs and general stratified media. Furthermore, S-matrices describing a periodic array of scatterers can be obtained from the results derived within the T-matrix formalism, Eq. (4.78). Combining all elements, systems such as periodic arrangements of particles on substrates can be consistently treated within the formalism.

The key results of this chapter enable us, in the following chapters, to analyze chiral light–matter interactions with localized objects as well as chiral optical cavities. Chapter 5 makes extensive use of the T-matrix formalism and the derived cross-sections to evaluate CD, a hallmark of chiral optical properties. Furthermore, the T-matrix is used for optimizing the electromagnetic chirality of scatterers. Periodic arrays of these optimized scatterers on a substrate form chiral mirrors. Their investigation in Chapter 6 is facilitated by the S-matrix formalism, and the discussion of helicity-preserving reflections at grazing incidence as well as TIR in Section 4.2 guides us in their design. Finally, these mirrors are assembled into a chiral optical cavity in Chapter 6.

# 5 *Chiral Light–Matter Interaction with Localized Objects*

In the previous chapters, we have laid the groundwork for our investigation of the optical properties of chiral systems. In particular, our emphasis on helicity-specific formalisms provides the most suitable framework for examining the chiral systems that will be the focus of this and the next chapter. In this chapter, we make extensive use of the transition matrix formalism to calculate chiral spectroscopic quantities.

First, we formally introduce the concept of chirality and the associated spectroscopic quantities in the context of chiral light–matter interactions. In particular, we consider circular dichroism (CD), which is the difference in the absorption of light with opposite helicity. In the case of a scattering object of finite size, both its geometric shape and the medium of which it is composed can be a source of chirality. In Section 5.2, we investigate how the chirality of the medium and the chirality of the geometric shape of a given scatterer combine to form its total chiral optical response. We show that the CD spectrum can be separated with regard to the two different origins of chirality. Building on these findings, we discuss efficient approximations of the CD as well as transition matrices for chiral scatterers, made possible by the small chirality parameters of naturally occurring media. Afterward, we consider the CD of chiral arrangements of small, achiral metallic objects. In the final section, we introduce the concept of electromagnetic chirality, which we in turn use to optimize scatterers for a strongly varying optical response in dependence on the helicity of the illumination.

Many of the results discussed in this chapter are published in Refs. [P9, P3, P2]. They expand our understanding of the chiral optical response of microscopic and mesoscopic systems and provide insights and strategies for their design and optimization. The approximation scheme discussed in Section 5.2 builds on some of the published results, in particular those of Ref. [P9], and presents an original contribution to this work. Finally, the electromagnetically chiral scatterers optimized in Section 5.4 serve as building blocks for a chiral optical cavity designed in Chapter 6, extending our discussion from the microscopic and mesoscopic scale to that of macroscopic optical devices.

## 5.1 *Chirality*

The central concept around which this work revolves is chirality. We have already touched on this concept in earlier chapters, for instance in the nomenclature of media classes in Section 2.2, and it has guided our decision to introduce electromagnetic waves and the formalisms for treating their interaction with matter in a helicity-dependent manner. In this section, we provide the formal definition of chirality and briefly discuss the history of its significance for light–matter interactions. We discuss optical rotation (OR) and CD as two spectroscopically relevant manifestations of chiral light–matter interactions. CD, in particular, will be the main quantity of interest in the next to sections.

### 5.1.1 *Geometric concept and molecular chirality*

The concept of chirality is, fundamentally, a geometric one. It is easiest understood from the examination of examples. In Fig. 5.1, we see the eponymous example of hands: The mirror image of a left hand is a right one, and the two cannot be brought to coincide. Considering such objects, Lord Kelvin introduced the term *chirality*[1] to refer to any shape or group of points, which cannot be brought to coincide with its mirror image. Figure 5.1 shows another example by the group of points assuming a helical shape. Much like our hands, the mirror images are distinctly different, and we may use the sense of helical twistedness to assign a sense of left- and right-handedness to one of the groups of points each. If we interpret the points as carbon atoms and the lines connecting them as chemical bonds, the shown molecule corresponds to helicene, one of countless examples of chiral molecules of relevance for the study of chiral optical properties [127]. Much like the shown molecule, the shells of snails and correlations between the directions in which spiral galaxies spin [128] constitute examples of chirality, demonstrating its ubiquity in nature across the length scales.

1 Chirality derives from Ancient Greek χείρ (*cheir*; hand), linking it closely to the notion of handedness.

The discovery of molecular chirality is due to the discovery of OR of light observed in organic liquids by Biot in the 19th century [52]. OR refers to the rotation of the plane of polarization of linearly polarized light, schematically depicted in Fig. 5.2; we discuss it in the next subsection. Molecules and media that exhibit OR are referred to as optically active. Shortly after, the discovery

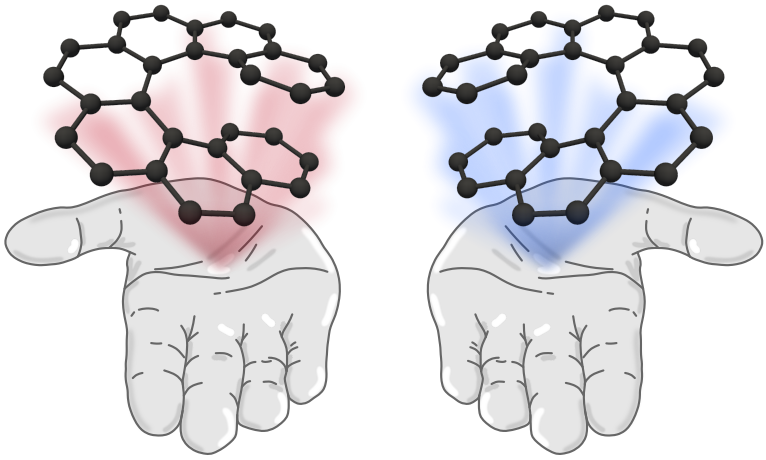

*Figure* 5.1: *Examples of chirality* · A shape or group of points is called chiral if it cannot be brought to coincide with its own mirror image. The eponymous example are our hands: In a mirror, our left hand turns into a right one, the two of which are distinctly different. The shown helical arrangement of points is another example. Interpreting the points as carbon atoms and the lines as chemical bonds, the shown arrangement corresponds to the organic molecule helicene, one of countless examples of chiral molecules. The indicated color scheme is used in parts of this work to distinguish left- and right-handed (i.e., positive and negative helicity) electromagnetic waves, themselves an example of chirality.

of circularly polarized light by Fresnel enabled him to explain OR via different phase velocities for the two different circular polarization handedness (now, more generally, expressed as helicity) [52]. Finally, while studying crystals of sodium ammonium tartrate, Pasteur was able to separate them into two types of crystals that appeared as mirror images of each other [2]. Dissolved in water, these two types gave rise to OR of equal magnitude but opposite sign. It established the link between the chiral optical phenomenon and the two different versions of the molecule, mirror images of each other, called

*enantiomers*. The original crystal, an even mixture of the two enantiomers (called a *racemate* or *racemic* mixture) was optically inactive, retrospectively understood as a result of the cancellation of the two opposite effects [129].

The importance of chirality in molecules is undeniable: Most biochemically relevant compounds are chiral, and the chemistry that enables life exhibits exceptional *homochirality*, meaning that in living organisms, only one of the two enantiomers of a given molecule is present. This applies to amino acids, proteins, and nucleic acids, and the correct pairing of enantiomers is crucial, as chemical reactions depend on the chiral nature of the compounds involved [5, 8]. In enzymatic reactions, for example, the enzyme and the substrate—the molecule on which it acts—must fit together, a concept often referred to as the lock-and-key principle [6, 7]. Mismatched enantiomers are just as hindered in their interaction as an attempt to shake a right hand with a left hand. In other words: "Homochirality is essential for an efficient biochemistry, rather like the universal adoption of right-handed screws in engineering" [129, p. 4]. Homochirality directly transfers to requirements for medical drugs, which interact with the chiral environment of our biochemistry, rendering molecular chirality vital for pharmacology and pharmacy [130, 131]. The adverse effects of exposure to the wrong enantiomer of a drug can be as severe as toxicity, as drastically demonstrated by the thalidomide scandal of the 1960s [9]. Hence, methods are needed for the selective detection of enantiomers and for the targeted synthesis of enantiomerically pure compounds. One central topic of interest in the study of chiral light–matter interactions arises from the question, to which extent such interactions can be utilized for the purposes stated above. This question informs our motivation for the chiral optical cavity discussed in Chapter 6. We now discuss OR and CD. The latter will be examined further in the next sections.

### 5.1.2 *Optical rotation and circular dichroism*

OR and CD are two phenomena of chiral light–matter interactions that can be explained by examining the propagation of electromagnetic waves in a chiral medium. In particular, we consider the role of helicity. To explain OR, we consider a linearly polarized monochromatic plane wave of unit amplitude in a lossless achiral medium. For simplicity, we consider $\hat{\boldsymbol{k}} = \hat{z}$

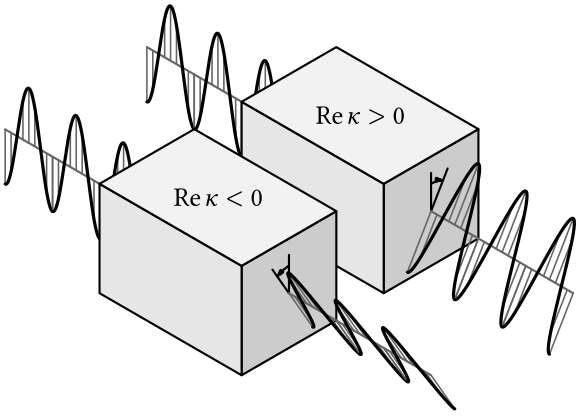


*Figure* 5.2: *Schematic depiction of optical rotation* · A linearly polarized plane wave propagating through a chiral medium (gray box) exhibits a rotation of the direction of linear polarization, called optical rotation. The linearly polarized wave can be expressed as a superposition of a left- and a right-handed circularly polarized plane wave. The difference in the phase velocities of left- and right-handed waves in a chiral medium leads to a phase shift between the two, accumulating over the propagation and resulting in the optical rotation. The direction of rotation depends on the sign of the real part of the chirality parameter $\kappa$.

and the polarization to be in the $x$-direction. We can express such linearly polarized wave as a superposition of a left-handed (positive helicity) and right-handed (negative helicity) circularly polarized wave. Using Eq. (3.18),

$$\hat{\boldsymbol{x}}\mathrm{e}^{\mathrm{i}kz} = \frac{-1}{\sqrt{2}}\left(\hat{\boldsymbol{e}}_{+}(\hat{\boldsymbol{z}}) + \hat{\boldsymbol{e}}_{-}(\hat{\boldsymbol{z}})\right)\mathrm{e}^{\mathrm{i}kz}, \tag{5.1}$$

with the wavenumber in the achiral medium, $k$, and $\hat{\boldsymbol{e}}_{\pm}(\hat{\boldsymbol{z}}) = -(\hat{\boldsymbol{x}} \pm \mathrm{i}\hat{\boldsymbol{y}})/\sqrt{2}$. These descriptions are equivalent, and the polarization direction is the same for all $z$. Now, we consider the same wave to propagate through a chiral medium, as schematically depicted in Fig. 5.2. For the purpose of this discussion, we ignore any reflections at interfaces between media and

simply focus on the evolution of the wave during its propagation in the chiral medium. As explained in Chapter 3, the behavior of a plane wave of a given helicity $\lambda$ in a chiral medium characterized by the Pasteur parameter $\kappa$ is determined by the helicity-dependent refractive index $n_\pm = \sqrt{\varepsilon\mu} \pm \kappa$. Correspondingly, the wavenumbers of the two circularly polarized plane waves in Eq. (5.1), $k_\pm = k_0 n_\pm$, differ, yielding[2]

$$\begin{aligned}\frac{-1}{\sqrt{2}}\left(\hat{\boldsymbol{e}}_+(\hat{\boldsymbol{z}})\mathrm{e}^{\mathrm{i}k_+ z} + \hat{\boldsymbol{e}}_-(\hat{\boldsymbol{z}})\mathrm{e}^{\mathrm{i}k_- z}\right) &= \frac{1}{2}\left((\hat{\boldsymbol{x}} + \mathrm{i}\hat{\boldsymbol{y}})\mathrm{e}^{\mathrm{i}k_0\kappa z} + (\hat{\boldsymbol{x}} - \mathrm{i}\hat{\boldsymbol{y}})\mathrm{e}^{-\mathrm{i}k_0\kappa z}\right)\mathrm{e}^{\mathrm{i}k_0\sqrt{\varepsilon\mu}z} \\ &= (\hat{\boldsymbol{x}}\cos(k_0\kappa z) - \hat{\boldsymbol{y}}\sin(k_0\kappa z))\,\mathrm{e}^{\mathrm{i}k_0\sqrt{\varepsilon\mu}z}.\end{aligned} \tag{5.2}$$

2 The different exponential factors of the separate terms in Eq. (5.2) demonstrate that linearly polarized waves are not well-suited for a description of waves in chiral media, suggesting the use of a circular polarization (helicity) based description.

After propagating a distance $\Delta z$ inside the chiral medium, we find that the polarization direction has rotated around the axis of propagation by an angle of $k_0\,\mathrm{Re}\{\kappa\}\Delta z$. The direction of the rotation of the polarization—the OR— depends on the sign of $\mathrm{Re}\,\kappa$. Hence, the different enantiomers of a chiral molecule, corresponding to different signs of $\kappa$, manifest themselves in opposite directions of the OR.[3]

3 The term *optical rotatory dispersion* used in Chapter 1 refers to the dispersion of optical rotation as characterized by its spectral dependence.

We have found that a nonvanishing real part of the chirality parameter $\kappa$ causes OR. We consider the effect of a nonvanishing imaginary part next. To this end, we examine separately the evolution of the amplitudes of a left- and a right-handed circularly polarized plane wave, propagating through an absorbing chiral medium as depicted in Fig. 5.3. From Eq. (3.18), we find that the electric field amplitude of a plane wave decreases as

$$\boldsymbol{A}_{\hat{\boldsymbol{k}},\pm}(\boldsymbol{r}) \propto \mathrm{e}^{\mathrm{i}\,\mathrm{Re}\{k_\pm\}\hat{\boldsymbol{k}}\cdot\boldsymbol{r}}\mathrm{e}^{-\mathrm{Im}\{k_\pm\}\hat{\boldsymbol{k}}\cdot\boldsymbol{r}}. \tag{5.3}$$

Consequently, the wave's intensity decays exponentially as well, which is nothing but a statement of the Beer–Lambert law [132, 133]. Since the intensity is proportional to the squared modulus of the field amplitude, its decay rate is twice that of the amplitude, and we define the *attenuation coefficient*

$$\alpha_\pm := 2\,\mathrm{Im}\,k_\pm = 2k_0\,\mathrm{Im}\,n_\pm. \tag{5.4}$$

Comparing the attenuation coefficients for different helicity, we find that they differ by

$$\alpha_+ - \alpha_- = 4k_0\,\mathrm{Im}\,\kappa. \tag{5.5}$$

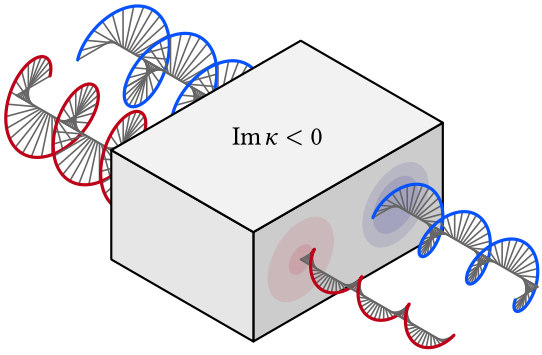


*Figure* 5.3: *Schematic depiction of circular dichroism* · A chiral medium (gray box) exhibits different attenuation coefficients for light of positive and negative helicity, such as left-handed (blue) and right-handed (red) circularly polarized plane waves. The different attenuation coefficients lead to a difference of the amplitudes of the transmitted waves, which is called circular dichroism. Which of the two polarization handedness is attenuated more strongly depends on the sign of the imaginary part of the chirality parameter $\kappa$.

Hence, left- and right-handed circularly polarized light is absorbed differently by a chiral medium with nonvanishing $\operatorname{Im}\kappa$. Which handedness is absorbed more strongly depends on the sign of $\operatorname{Im}\kappa$.

This difference in absorption depending on the incident helicity is called CD [134, 135]. Its measurement provides a powerful spectroscopic technique for probing the chirality of an object. As such, it is crucial for applications such as sensing [136–140] and imaging [141, 142] of chiral compounds. The precise definition of CD in terms of the measured quantities can differ depending on context. For instance, if an extended system or medium is considered, one might measure and compare the absorbed intensity (i.e., the absorptance, cf. Section 4.2) for left- and right-handed circularly polarized light. The CD is then evaluated as their relative difference,

$$\mathrm{CD} \coloneqq \frac{\mathfrak{A}_+ - \mathfrak{A}_-}{\mathfrak{A}_+ + \mathfrak{A}_-}. \tag{5.6}$$

In many experimental setups, however, the quantity being actually measured is the transmitted power or transmittance. Accordingly, a *transmission* CD is defined as

$$\mathrm{TCD} \coloneqq \frac{\mathfrak{T}_+ - \mathfrak{T}_-}{\mathfrak{T}_+ + \mathfrak{T}_-}. \tag{5.7}$$

Another occasionally used definition of transmission CD is

$$\begin{aligned}\mathrm{TCD} &= \arctan\left(\frac{\sqrt{\mathfrak{T}_-} - \sqrt{\mathfrak{T}_+}}{\sqrt{\mathfrak{T}_-} + \sqrt{\mathfrak{T}_+}}\right) \\ &= \frac{1}{2}\frac{\mathfrak{T}_- - \mathfrak{T}_+}{\mathfrak{T}_- + \mathfrak{T}_+} + \frac{1}{12}\left(\frac{\mathfrak{T}_- - \mathfrak{T}_+}{\mathfrak{T}_- + \mathfrak{T}_+}\right)^3 + O\left(\left(\frac{\mathfrak{T}_- - \mathfrak{T}_+}{\mathfrak{T}_- + \mathfrak{T}_+}\right)^5\right),\end{aligned} \tag{5.8}$$

where in the second line we have expanded the expression for small relative differences of the helicity-dependent transmission, showcasing that for small differences, this definition is approximately equal to the one given before with an additional prefactor of one half. The transmission CD of Eq. (5.8) is usually expressed in units of millidegree, the corresponding value is obtained by multiplying the right-hand side by $(180/\pi) \times 10^3$ mdeg rad$^{-1}$. To distinguish the original definition of CD—which considers absorption—from the transmission CD, the former is occasionally referred to retroactively as *absorption* CD.

So far, we have discussed the CD considering the properties of bulk media. For localized scatterers, we consider CD as a property of the scatterer. To compare its absorption of light of different helicity, we evaluate its directionally averaged absorption cross-section according to Eqs. (4.32) and define

$$\mathrm{CD} \coloneqq \frac{\langle C_{\mathrm{abs},+}\rangle_{\hat{\boldsymbol{k}}} - \langle C_{\mathrm{abs},-}\rangle_{\hat{\boldsymbol{k}}}}{\langle C_{\mathrm{abs},+}\rangle_{\hat{\boldsymbol{k}}} + \langle C_{\mathrm{abs},-}\rangle_{\hat{\boldsymbol{k}}}}. \tag{5.9}$$

This is the definition that we work with in the next section. Considering the chiral nature of a localized scatterer, we realize that the overall chiral optical response can now be due to two causes. The chirality of the material, characterized by $\kappa$, causes a chiral response just as in the case of a bulk medium. However, the shape of the scatterer itself may be chiral as well, contributing to the overall chiral response. In the next section, we address these two origins of a scatterer's chiral response and discuss their separate contribution to the CD.

## 5.2 *Geometric and Material Origins of Circular Dichroism*

Different causes lead to an object's chiral optical response. On the one hand, an object can be made from chiral media, represented by a nonvanishing chirality parameter $\kappa$. On the other hand, the geometric shape of the object itself can break inversion and mirror symmetries, causing a chiral optical response as well. Hence, there can be a material and a geometric contribution to the chiral response. These are alternatively referred to as constitutional and configurational causes, respectively. An exemplary object combining a chiral medium and chiral geometry is depicted in Fig. 5.4. The effect of a chiral medium relies on its constituents—molecules—to be chiral [143]. The chirality parameter $\kappa$ provides an effective description for this aspect. Therefore, both material and geometric contributions are fundamentally related to geometry. While the chirality of the material is apparent on the microscopic length scales of molecules, typically on the order of $10^{-1}$ to 1 nm, the object's geometric shape manifests on a mesoscopic scale on the order of $10^2$ to $10^3$ nm. Thus, a separate consideration of material and geometric contributions to an object's chiral response corresponds essentially to a separation of length scales.

In this section, we study the contributions of constitutional and configurational chirality to the chiral optical response of an object, specifically, with regard to its CD. First, we examine objects, whose overall optical response is predominantly determined by their medium, which means that no considerable resonances induced by the object's finite size and the details of its shape are present. We will henceforth refer to such geometrically induced resonances as the *optical* resonances of an object. We demonstrate that the CD of an object that exhibits no significant optical resonances is, within close approximation, determined by the sum of two independent terms, which separately account for the material and the geometric contribution, respectively. Second, we address objects exhibiting optical resonances that strongly influence their optical response. Particularly for shapes with mildly broken symmetries, we demonstrate a similar separability of their CD. The main results discussed in these subsections are published in Ref. [P9]. We then go further and explore efficient approximations of CD spectra and T-matrices based on the smallness of $\kappa$. We provide a summary of the main results and discuss prospects in a final subsection.

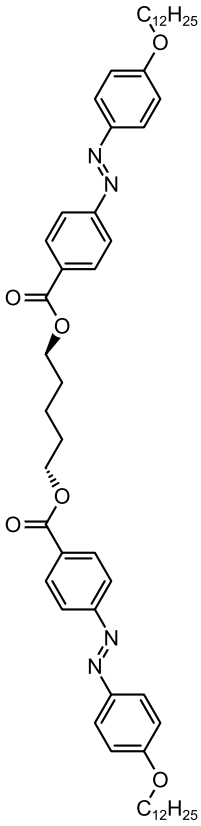


Skeletal formula of 12OAzo5AzoO12.

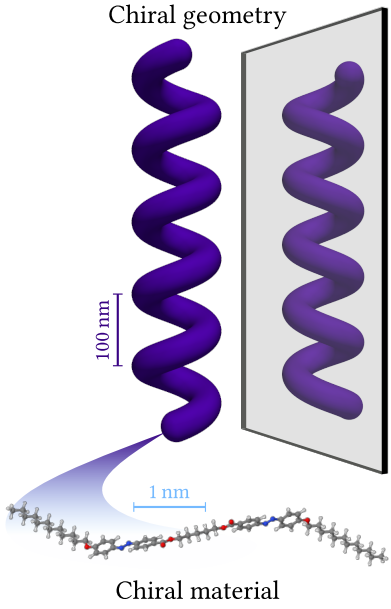


*Figure 5.4: Object combining a chiral geometry and a chiral medium ·* Schematic depiction of an object with a chiral geometry made from a chiral medium. Its shape, a right-handed helix, does not coincide with its left-handed mirror image, rendering the object geometrically chiral. Simultaneously, the helix' medium consists of the chiral organic molecule 12OAzo5AzoO12. Both geometric and material chirality cause the object to exhibit a chiral optical response. These two causes of the overall chiral response reside on length scales that differ by orders of magnitude. Molecule and general layout reproduced with permission from Ref. [P9]. © 2024 American Chemical Society.

### 5.2.1 *Separation in the absence of optical resonances*

The geometry of the object in Fig. 5.4 is inspired by Ref. [P6], which studies helical nanotubes forming from an organic thin film. The thin films are formed by the organic molecule 12OAzo5AzoO12, an aromatic azo dimer that assembles into helically shaped ribbons and lends itself to the study of chiral optical properties of thin films [144–147]. The molecule is depicted in the lower part of Fig. 5.4 and on the side. Consequently, we use material parameters modeling this compound for our analysis. To this end, the molecular properties of 12OAzo5AzoO12 are determined from quantum chemical simulations, specifically, density functional theory and time-dependent density functional theory [148]. These simulations were performed by Marjan Krstić. Afterward, the molecular properties are used to obtain effective material parameters, representing a homogeneous, bi-isotropic medium formed

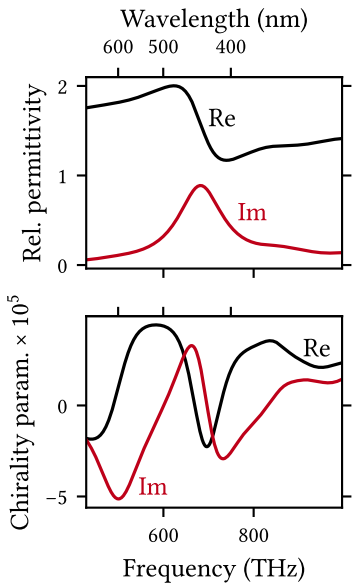


*Figure 5.5: Effective material parameters for 12OAzo5AzoO12* · The spectrally resolved relative permittivity (upper panel) and chirality parameter (lower panel) model a medium formed by the organic compound 12OAzo5AzoO12, assuming a molecular concentration of $3 \times 10^{26}\,\mathrm{m}^{-3}$. The real and imaginary parts of the parameters are represented by solid black and red lines, respectively. The $x$-axis scales linearly with frequency; the upper axis displays the corresponding vacuum wavelength for reference on a non-linear scale. Data originally published in Ref. [P9].

by unordered (i.e., randomly oriented) molecules. Specifically, we obtain a frequency-dependent scalar relative permittivity $\varepsilon(\omega)$ and chirality parameter $\kappa(\omega)$, determining the optical properties of the medium as per the constitutive relations in Eq. (2.38). The effective material parameters depend on the molecular concentration, which we choose to be $3 \times 10^{26}\,\mathrm{m}^{-3}$. This value is inspired by studies employing a similar multi-scale approach involving an effective description of organic compounds and yields reasonable material parameters [149, 150]. The effective material parameters were computed by Benedikt Zerulla.

The frequency dependence of the relative permittivity and the chirality parameter modeling 12OAzo5AzoO12 are shown in Fig. 5.5. The considered spectral range covers vacuum wavelengths from 300 to 700 nm, extending from the edge of the ultraviolet to the visible. Notably, the relative permittivity exhibits a resonance centered around 440 nm, indicated by the maximum of the imaginary part and a strong dispersion (i.e., a strong dependence

on frequency) of the real part. The feature is due to the excitation of an electronic state of the molecule. For further discussions, we refer to the Supporting Information of Ref. [P9]. The resonant response of the medium predominantly determines the absorption properties of the helix, as we will see below. The nonvanishing chirality parameter reveals the chiral nature of the molecule 12OAzo5AzoO12 and its corresponding medium, reaching magnitudes on the order of $10^{-5}$.

We remark that by the same procedure, a relative permeability describing the medium is obtained. Its difference from unity is negligible as the molecule exhibits no notable magnetic response. According to Eq. (2.41), approximating the permeability as unity, and, hence, its imaginary part as zero, breaks the conservation of energy, since the imaginary part of $\kappa(\omega)$ is nonzero. However, since the imaginary part of the relative permittivity exceeds that of the chirality parameter by four orders of magnitude, the gain introduced by such approximation is imperceptible.[4]

4 Passivity demands $\operatorname{Im}\mu \geq (\operatorname{Im}\kappa)^2/|\operatorname{Im}\varepsilon|$, cf. Eq. (2.41). For the material parameters in Fig. 5.5, it corresponds to a lower bound for $\operatorname{Im}\mu$ on the order of $10^{-8}$ and lower.

With an effective description of the chiral medium via the material parameters available, we continue with the computation of the optical properties of the helix. In [P9], the entire multi-scale workflow is sketched out, including the computation of molecular properties discussed above. Here, we focus on the steps concerning the optical properties of the mesoscopic helix as shown in Fig. 5.6. We compute the T-matrix of the helix separately for each considered frequency. Four parameters specify the geometry of the helix: The radius of the tube forming the helix is $r_{\text{tube}} = 21.25\,\text{nm}$, the helical windings themselves are specified by a radius $r_{\text{helix}} = 41.25\,\text{nm}$ and a pitch $p = 100\,\text{nm}$, and the total number of turns described by the helix is $n_{\text{turns}} = 5$. These geometric parameters have been chosen in line with experimental observations in Ref. [P6]. T-matrices of the helix are computed from FEM scattering simulations following our discussion in Section 4.1. The FEM simulations were performed using the software JCMsuite [115, 151]. The multipolar degree for truncation of the T-matrices has been chosen to be $\ell_{\text{max}} = 8$, which is amply sufficient for the convergence of the spectroscopic quantities under consideration.

At each considered frequency, we evaluate the helix' absorption of light of a given helicity $\lambda$ as given by the directionally averaged absorption cross-sections in Eqs. (4.32) from the respective T-matrix. Subsequently, we calculate the CD as the relative difference of the absorption cross-sections with

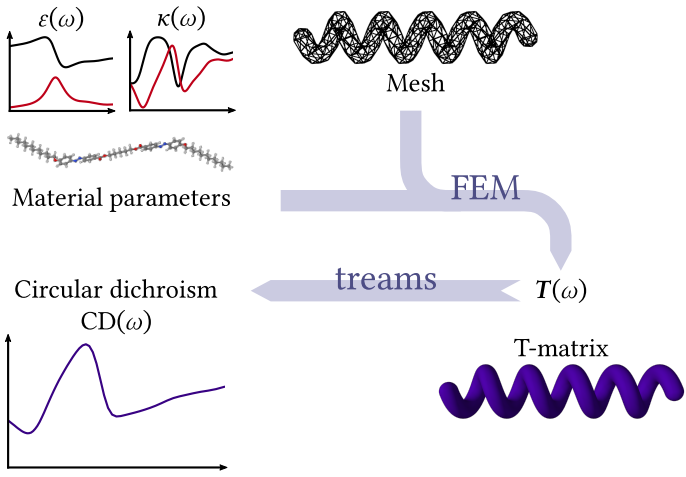


*Figure* 5.6: *Simulation workflow for obtaining circular dichroism spectra* · The presented simulation workflow provides the optical response of the helix made from a chiral organic material. Combining the material parameters (detailed graphs shown in Fig. 5.5), which model the organic molecule 12OAzo5AzoO12, and a description of the helical geometry in form of a mesh, we compute transition matrices via full-wave scattering simulations using the finite element method. Afterward, the in-house software treams [100] allows for the efficient computation of spectroscopic quantities of interest, such as the circular dichroism. Molecule reproduced with permission from Ref. [P9]. © 2024 American Chemical Society.

regard to positive and negative helicity illumination as defined in Eq. (5.9). All computations involving T-matrices were carried out using the in-house software treams [100]. The CD for the chiral helix made from a chiral medium is plotted in Fig. 5.7 represented by the indigo curve. As expected by the connection between the helicity-dependent absorption and $\operatorname{Im}\kappa$, the main features of the CD spectrum resemble those of the imaginary part of $\kappa(\omega)$ (cf. Fig. 5.5).

We are interested in the interplay of geometric and material contributions

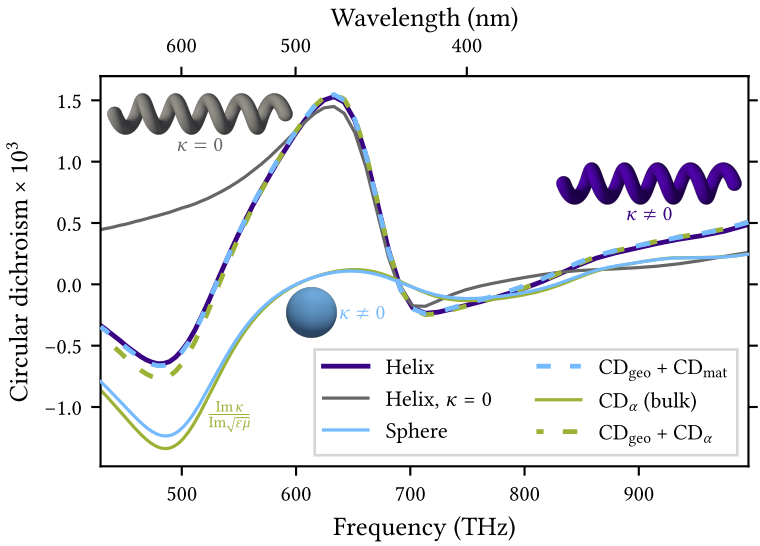


*Figure* 5.7: *Circular dichroism of the chiral helix and reference objects* · The indigo curve represents the circular dichroism spectrum of a helix made from the chiral medium in Fig. 5.5. The total spectrum can be separated into a geometric and a material contribution. The isolated geometric contribution $\mathrm{CD}_{\mathrm{geo}}$ is computed from the same helix with $\kappa = 0$ identically (gray curve). The isolated material contribution $\mathrm{CD}_{\mathrm{mat}}$ is evaluated using a sphere (light blue, solid). The sum of the geometric and the material contribution (light blue, dashed) excellently matches the total circular dichroism spectrum. The attenuation coefficients of the chiral bulk medium yield another approximation of the isolated material contribution (light green, solid). Its superposition with the geometric contribution closely matches the total circular dichroism as well (light green, dashed). Data originally published in Ref. [P9].

to the overall chiral optical response. Thus, we compare the CD spectrum to that of two reference objects that separately capture the two contributions.

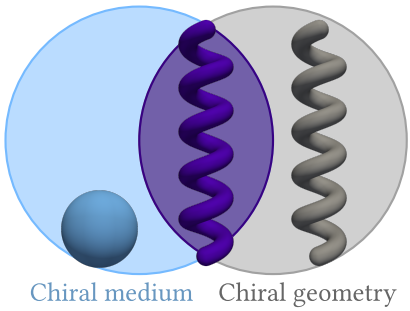


*Figure 5.8: Schematic of the chiral helix and reference objects* · The original helix combining a chiral geometry and a chiral medium is shown in the middle. The same helix but with its chirality parameter $\kappa$ set to zero isolates the effect of the chiral geometry (right). For an isolated consideration of the medium's chirality, a sphere of matching volume is considered (left).

The reference objects and their relation to the original helix are shown in Fig. 5.8. To isolate the effect of the chiral geometry, we compute T-matrices for the same helix, however, in these simulations we set $\kappa(\omega) = 0$ identically for all frequencies.[5] The CD spectrum obtained from these T-matrices is represented by the solid gray curve in Fig. 5.7. As it is entirely caused by the chiral geometry of the helix, we denote it $\mathrm{CD}_{\mathrm{geo}}$. It differs considerably from the CD spectrum of the original helix (indigo), particularly toward lower frequencies, and even assumes opposite signs. The observed difference highlights that the original CD spectrum is a joint effect of the chiral geometry and the chiral medium.

5 The relative permittivity and permeability remain unchanged. The achiral medium with $\kappa = 0$ identically represents a racemic mixture of the two enantiomers of 12OAzo5AzoO12.

To study the material contribution to the CD, we consider another reference object made from the same medium. The chosen reference object needs to be geometrically achiral to isolate the chiral effect of the medium. Here, we simply choose a sphere. The total absorption of light by a scatterer depends, in crude approximation, on the volume of the scatterer, as it determines the amount of the absorbing medium that is present. For the scatterers considered currently, such approximation is legitimized by the absence of strong geometrically induced resonances, as we discuss below. Consequently, we choose a reference sphere with a radius of 76.54 nm to match the volume of the helix. T-matrices for the sphere made from the chiral medium are readily obtained from the analytic expressions discussed in Section 4.1, Eq. (4.23). The resulting CD spectrum is shown in Fig. 5.7

by the solid light blue curve. Since it entirely depends on the chirality of the medium, we denote it $\mathrm{CD}_{\mathrm{mat}}$. As in the case of the isolated geometric contribution, we find it to differ considerably from the original spectrum.

Adding the isolated contributions $\mathrm{CD}_{\mathrm{mat}}$ and $\mathrm{CD}_{\mathrm{geo}}$ together yields the dashed light blue curve in Fig. 5.7. It matches the original spectrum obtained for the helix combining the medium's and its geometry's chirality to an excellent degree. Hence, we find that the total CD is well approximated by a linear superposition of an independent geometric and a material contribution,

$$\mathrm{CD}(\omega) \approx \mathrm{CD}_{\mathrm{geo}}(\omega) + \mathrm{CD}_{\mathrm{mat}}(\omega). \tag{5.10}$$

We intuitively relate the fact that these contributions show marginal interference to the difference in length scales on which both origins of chirality manifest.

*Absorption and circular dichroism of bulk chiral medium* · As a consequence of the approximate separability discussed above, we find that the medium's contribution to the CD spectra is nearly identical for the helix and the sphere. Hence, the spectra are in good approximation independent of the geometric shape of the considered object, even though the considered shapes differ considerably. This approximate independence is due to the fact that the overall absorption characteristic of both considered objects, the helix and the sphere, are predominantly determined by the absorption characteristic of the medium. To illustrate this aspect, we consider the attenuation coefficients for plane waves inside of the bulk chiral medium. As given in Eq. (5.4), the intensity decays at a rate of $\alpha_\pm = 2k_0 \operatorname{Im} n_\pm$, with the vacuum wavenumber $k_0 = c_0^{-1}\omega$ and the helicity-dependent refractive index of the chiral medium $n_\pm = \sqrt{\varepsilon\mu} \pm \kappa$. We further define the helicity-averaged attenuation coefficient

$$\alpha := \frac{\alpha_+ + \alpha_-}{2} = 2k_0 \operatorname{Im}\{\sqrt{\varepsilon\mu}\}. \tag{5.11}$$

To show that the absorption characteristics of the helix and the sphere are predominantly due to the absorption characteristic of the chiral medium, we compare the helicity-averaged attenuation coefficient of the bulk medium with the helicity-averaged absorption cross-sections of both objects in Fig. 5.9. The attenuation coefficient is represented by the solid green curve.

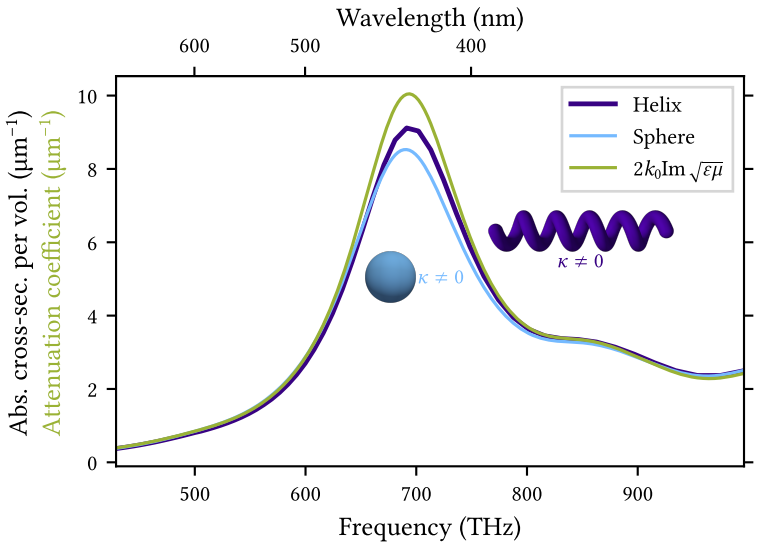


*Figure* 5.9: *Absorption spectra for the scatterers and bulk medium* · The main features of the directionally and helicity-averaged absorption cross-sections of the helix (indigo) and the sphere (light blue) closely follow the absorption characteristic of the bulk medium as given by its attenuation coefficient (light green). No significant influence of optical resonances on the objects' absorption spectra is observed. Data originally published in Ref. [P9].

In line with Eq. (5.11), its main features follow from the relative permittivity of the medium, noticeable by the absorption peak related to the electronic resonance visible in Fig. 5.5. The cross-sections have dimensions of area while the attenuation coefficient has the dimension of inverse length; for a comparison, we normalize the objects' cross-sections to their volume. The resulting absorption cross-sections per unit volume are shown by the indigo and the light blue curve for the helix and the sphere, respectively. Indeed, the absorption characteristic of both objects closely follows that of the medium. Neither object exhibits features associated with optical (i.e., geometrically

induced) resonances that would considerably alter their absorption spectra in the examined frequency range. Such optical resonances are expected to occur at higher frequencies for the considered objects.

Inspired by the observation that the scatterers' absorption spectra are in first approximation independent of their geometry, we consider the CD associated with the chiral bulk medium. To this end, we define the CD of bulk medium as the relative difference of the helicity-dependent attenuation coefficients,

$$\mathrm{CD}_{\alpha}(\omega) \coloneqq \frac{\alpha_{+}(\omega) - \alpha_{-}(\omega)}{\alpha_{+}(\omega) + \alpha_{-}(\omega)} = \frac{\mathrm{Im}\{\kappa(\omega)\}}{\mathrm{Im}\left\{\sqrt{\varepsilon(\omega)\mu(\omega)}\right\}}. \tag{5.12}$$

The definition of $\mathrm{CD}_{\alpha}$ follows the same structure as Eq. (5.9) and is entirely independent of geometric aspects. Evaluating $\mathrm{CD}_{\alpha}$ for the given material parameters yields the light green curve in Fig. 5.7. It closely matches the CD spectrum of the sphere confirming the sphere's spectrum to be directly related to the medium's chirality. Adding $\mathrm{CD}_{\alpha}$ to the isolated geometry contribution $\mathrm{CD}_{\mathrm{geo}}$ yields the dashed green curve, which again closely matches the original total CD spectrum of the chiral helix made from the chiral medium. Accordingly, we find that the entirely geometry-independent term $\mathrm{CD}_{\alpha}$, associated with the chiral bulk medium, is a viable approximation of the material-dependent contribution $\mathrm{CD}_{\mathrm{mat}}$, allowing for a separate consideration of the two contributions via Eq. (5.10).

*The influence of a finite volume* · The superposition of the isolated geometric contribution $\mathrm{CD}_{\mathrm{geo}}$ and the geometry-independent term based on the attenuation coefficients $\mathrm{CD}_{\alpha}$ provides a good approximation for the helix combining the medium's and its geometry's chirality. The agreement between the spectra is, however, slightly worse compared to the approximation using the sphere's CD as the material contribution. Turning toward the helicity-averaged absorption spectra in Fig. 5.9, on closer inspection, we find that the cross-sections of the helix and the sphere exhibit a closer match between themselves than compared to the mere attenuation coefficient. Note that the volume of both objects was chosen to be the same, hence, the similarity of the shown cross-sections is unaffected by the normalization. We conclude that the restriction to a finite absorptive volume affects the material

contribution to the CD, since it introduces optical resonances, which alter an object's response. However, as the effect of such resonances is not very pronounced in the considered spectral range for the scatterers investigated above, the details of their shapes appear virtually irrelevant.

The presence of optical resonances in objects modulates the material contribution to their CD spectra as well as their absorption spectra in comparison to the pure bulk attenuation coefficient. Hence, the material contribution to the CD is only expected to match for objects that also share a similar absorption characteristic. For the sphere and the helix, this condition is satisfied due to their joint closeness to the medium's absorption characteristic, that is, due to the weak manifestation of optical resonances. When such resonances are strongly present, however, the similarity of the absorption spectra of two objects of different shape but same volume is far from guaranteed. Furthermore, the entirely geometry-independent approximation $\mathrm{CD}_{\mathrm{mat}} \approx \mathrm{CD}_{\alpha}$ is certainly no longer valid. In the next subsection, we extend the current discussion to objects featuring pronounced optical resonances in the considered spectral region.

### 5.2.2 *Separation in the presence of optical resonances*

To address the impact of optical resonances on the conclusions drawn in the previous subsection, we consider objects supporting such resonances while featuring both material-related and geometric chirality. As we show below, the presence of optical resonances vastly changes an object's absorption characteristic, resulting in spectra that differ significantly from the pure absorption spectrum of the medium. The optical resonances are inherent properties of a given scatterer and are sensitive to the details of the scatterer's geometry. Hence, scatterers with fundamentally different shapes, such as the sphere and the helix studied before, do generally not feature similar optical resonances, and their absorption spectra differ accordingly.

The separate consideration of the material and the geometric contribution to the total CD spectrum of a scatterer requires us to evaluate both contributions in isolation. This is easily done for the geometric contribution, simply by considering the same scatterer but using the material parameters of the achiral medium, that is, setting $\kappa(\omega) = 0$ identically. Since $|\kappa(\omega)| \ll \left|\sqrt{\varepsilon(\omega)\mu(\omega)}\right|$ for ordinary media in the infrared to ultraviolet spectral

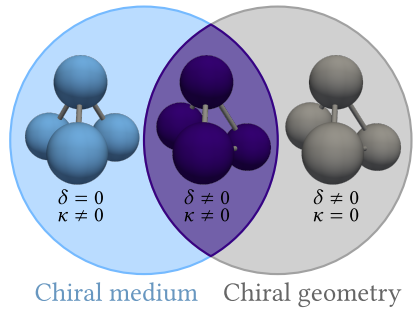


*Figure* 5.10: *Schematic of tetrahedral arrangements of spheres* · On the left, the geometrically achiral tetrahedron ($\delta = 0$) exhibits a chiral response due to the chiral medium ($\kappa \neq 0$). On the right, the distorted tetrahedron ($\delta \neq 0$) made from an achiral medium ($\kappa = 0$) is chiral due to its geometry. In the middle, we find the fully chiral tetrahedron combining both its geometry's and the medium's chirality ($\delta \neq 0$ and $\kappa \neq 0$). Connecting rods between the spheres are displayed for reference.

region, such change of the material parameters leaves the major (helicity-averaged) features of the scatterer's response intact. In particular, it results in virtually identical optical resonances and resulting absorption spectra. By contrast, the isolated material contribution is more difficult to obtain. Using a simple reference object with achiral geometry, such as the sphere considered before, is unworkable, as it does not feature similar optical resonance; as a result, its overall optical properties differ greatly from those of a differently shaped object.

The considerations above illustrate the importance of choosing suitable object geometries to ensure the similarity of their material-related chiral response. Our solution starts by considering a symmetric geometry, specifically, four identical spheres placed on the vertices of a regular tetrahedron. This tetrahedral arrangement is mirror symmetric with respect to any plane containing two of the vertices and the tetrahedron's centroid. Hence, the structure is geometrically achiral. By a continuous transformation that breaks the symmetries, we obtain a related chiral geometry. To this end, we pick one of the spheres as a reference point. Of the three center-to-center lines connecting it to the other spheres, we leave one unchanged, while the second (resp. third) is contracted (resp. stretched) by a relative factor

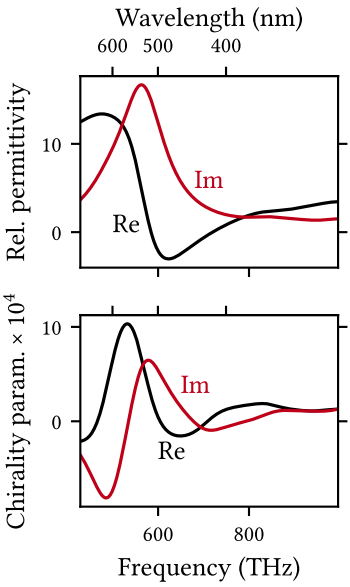


*Figure 5.11: Effective material parameters for an increased concentration of 12OAzo5AzoO12* · The spectrally resolved relative permittivity (upper panel) and chirality parameter (lower panel) model a medium formed by the organic compound 12OAzo5AzoO12. Compared to Fig. 5.5, the molecular concentration was increased to $12 \times 10^{26}\,\mathrm{m}^{-3}$. The real and imaginary parts of the parameters are represented by solid black and red lines, respectively. The $x$-axis scales linearly with frequency; the upper axis displays the corresponding vacuum wavelength for reference on a non-linear scale. Data originally published in Ref. [P9].

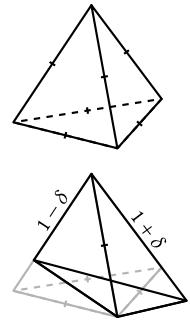


Wireframe of a tetrahedron. The regular tetrahedron (upper panel) is mirror symmetric w.r.t. any plane containing two vertices and the tetrahedron's centroid. The small ticks on the lines mark all side lengths as equal. Stretching one leg and contracting another breaks all mirror symmetries and yields a chiral, irregular (distorted) tetrahedron (lower panel).

of $1 - \delta$ (resp. $1 + \delta$; cf. the sketch on the side). The relative orientation of the connecting lines remains unchanged. The continuous transformation, parametrized by the scaling factor $\delta$, breaks the mirror symmetries and results in a geometrically chiral, distorted tetrahedral arrangement of spheres. We find that for reasonable yet considerable values of $\delta$ (here, $\delta = 20\,\%$) the absorption spectrum is only weakly perturbed. Hence, we have found a suitable geometrically chiral ($\delta \neq 0$) object and its achiral reference object ($\delta = 0$) that we examine in the following. The parameter $\delta$ represents the geometry's chirality, with $\delta = 0$ recovering the achiral arrangement. The different geometry and material combinations used in the following discussion are shown in Fig. 5.10.

To ensure that the tetrahedral arrangements exhibit optical resonances without having to increase their size compared to the wavelength significantly, we adjust the material parameters. The material parameters used so far model an organic compound, and the resulting refractive index is in a

similar range to that of conventional polymers. Consequently, it does not provide a strong refractive index contrast to the surrounding free space. For the discussion below, we use material parameters corresponding to the same molecule at a higher concentration of $12 \times 10^{26}\,\mathrm{m}^{-3}$. The spectrally resolved relative permittivity and chirality parameter are plotted in Fig. 5.11. As a result of the higher concentration, both parameters exhibit strong dispersion and span ranges approximately one order of magnitude larger than before. We stress that these parameters, while useful for obtaining resonant scatterers, do not realistically represent the optical properties of the organic compound as it would appear naturally, for instance, in the thin films of Ref. [P6]. For the remainder of this subsection, they are merely used as model parameters. The qualitative results discussed below and the conclusion drawn therefrom are independent of this particular choice of material parameters.

T-matrices for the tetrahedral arrangements of spheres are readily obtained from the expressions for a single sphere, Eq. (4.23), together with Eq. (4.38), describing the cluster of four spheres. To evaluate the directionally averaged absorption cross-sections in Eq. (5.9), we utilize the global description of the objects' T-matrix as per Eq. (4.41). We choose the radius of the spheres to $r = 80\,\mathrm{nm}$ and the edge length of the regular tetrahedron—the center-to-center distance between the spheres—to 220 nm. The truncation multipolar degree is $\ell_{\max} = 4$ for the individual spheres and $\ell_{\max} = 8$ for the global T-matrix of the tetrahedral arrangement, yielding sufficiently converged quantities of interest. For the geometrically chiral arrangement, we set $\delta = 20\,\%$. This results in a minimum center-to-center distance of 176 nm, ensuring that none of the spheres overlap.

The presence of optical resonances and the similarity of the absorption spectra of the geometrically chiral ($\delta \neq 0$) and achiral ($\delta = 0$) tetrahedral arrangement are demonstrated in Fig. 5.12. The helicity-averaged attenuation coefficient of the bulk medium is shown for comparison, represented by the green curve. The main features of the absorption cross-sections of the chiral (indigo) and achiral (light blue) arrangements differ significantly from the attenuation coefficient of the medium (green), unveiling the presence of optical resonances. Conversely, both tetrahedral arrangements exhibit similar spectra. As discussed above, the resonances innately depend on the details of the scatterer. This includes the coupling between the spheres, hence, the different geometries corresponding to different distances between

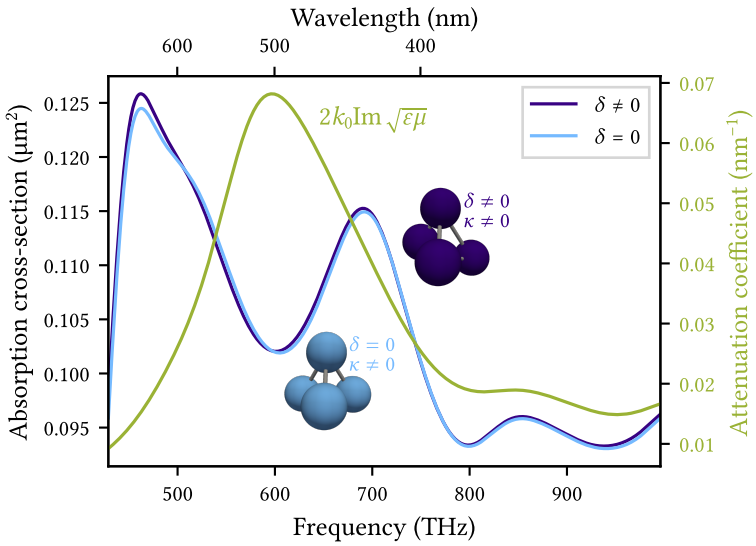


*Figure* 5.12: *Absorption spectra of tetrahedral arrangements and bulk medium* · The directionally and helicity-averaged absorption cross-sections for the regular, achiral tetrahedral arrangement ($\delta = 0$; light blue) and the distorted, chiral arrangement ($\delta = 20\,\%$; indigo) are plotted with reference to the left y-axis. Both spectra exhibit distinct spectral features as compared to the helicity-averaged attenuation coefficient of the medium (light green; right y-axis) as a consequence of optical resonances. The cross-sections of both tetrahedral arrangements are similar, slight differences hint at the geometric origin of the observed features. Data originally published in Ref. [P9].

the spheres lead to slight deviations between the two spectra. Yet, the two spectra are similar enough to merit a comparison of their CD spectra.

The CD spectra of the different arrangements are shown in Fig. 5.13. In place of the helix made from a chiral medium before, we plot the CD spectrum for the chiral arrangement made from a chiral medium ($\delta \neq 0$ and $\kappa(\omega) \neq 0$), shown as the indigo curve. The isolated geometric contribution is evaluated

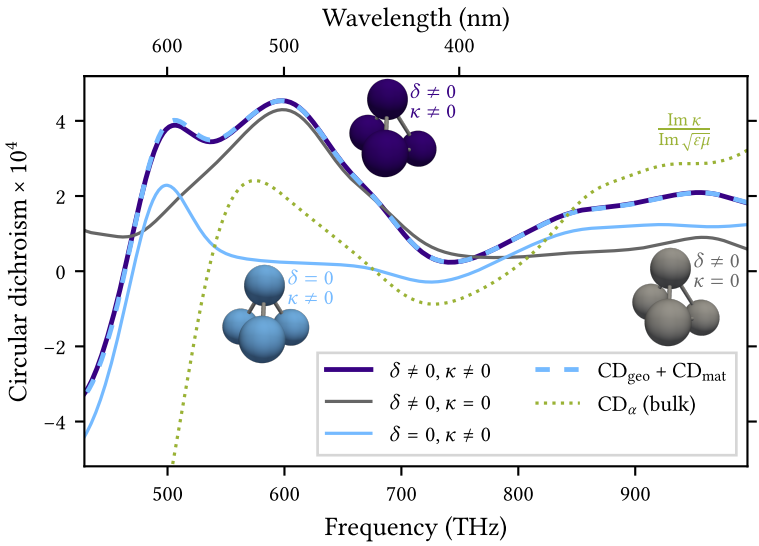


*Figure* 5.13: *Circular dichroism of tetrahedral arrangements of spheres* · The total circular dichroism of a chiral arrangement made from a chiral medium ($\delta \neq 0, \kappa \neq 0$) is displayed by the indigo curve. The spectrum for the chiral arrangement with an achiral medium ($\delta \neq 0, \kappa = 0$; gray) represents the isolated geometric contribution $\mathrm{CD}_{\mathrm{geo}}$. For an achiral arrangement, we find the material-related contribution $\mathrm{CD}_{\mathrm{mat}}$ caused by the nonvanishing chirality of the medium ($\delta = 0, \kappa \neq 0$; light blue). The superposition of the isolated geometric and material contribution (dashed light blue) closely matches the total spectrum. Due to optical resonances, $\mathrm{CD}_{\mathrm{mat}}$ differs significantly from the bulk term $\mathrm{CD}_{\alpha}$. Data originally published in Ref. [P9].

for the chiral arrangement for an achiral medium ($\delta \neq 0$ and $\kappa(\omega) = 0$) and shown in gray. Finally, the spectrum for the achiral arrangement with chiral medium ($\delta = 0$ and $\kappa(\omega) \neq 0$) is shown in light blue. Since a nonvanishing CD is necessarily due to the chirality of the medium in this latter case, we interpret it as the medium's contribution $\mathrm{CD}_{\mathrm{mat}}$.

We evaluate the superposition of the isolated material and geometric contributions to postdict the total chiral response of the fully chiral arrangement. The sum of the two spectra yields the dashed light blue curve, which we find to excellently agree with the indigo curve. Hence, we recover Eq. (5.10): The total CD of a chiral object is constituted by contributions associated with the chirality of its geometry and the chirality of its medium, and these contributions may be considered independently. Simply combining them as $\mathrm{CD} \approx \mathrm{CD}_{\mathrm{geo}} + \mathrm{CD}_{\mathrm{mat}}$ recovers the total chiral response in excellent approximation. This finding holds even in the presence of optical resonances.

Within the scope of this study, the presence of optical resonances mainly causes the isolated material contribution to be less straightforward to obtain. The approach presented here relies on finding a geometrically achiral reference object that exhibits a similar absorption spectrum to the geometrically chiral object. We demonstrate the importance of a similar absorption characteristic by reintroducing $\mathrm{CD}_{\alpha}$ from Eq. (5.12), representing the CD of the bulk medium. It corresponds to the dotted green curve in Fig. 5.13. Evidently, it does not align with the material contribution evaluated for the tetrahedral arrangement at $\delta = 0$ (light blue). Hence, $\mathrm{CD}_{\alpha}$ does not provide a useful description of the medium's contribution to the CD in the presence of optical resonances. Relatedly, the slight deviations between the absorption characteristics of the different tetrahedral arrangements observed in Fig. 5.12 limit the quality of the approximation as compared to the non-resonant case. As an outlook, a fundamental consideration of the optical resonances of objects [S2] with a focus on their relation between geometrically chiral and achiral shapes presents a promising opportunity to expand the scope of the work presented here.

### 5.2.3 *Efficient approximation of circular dichroism spectra for varying chirality parameters*

In the previous subsections, we have shown the separability of the medium's and the geometry's contribution to the CD of chiral scatterers, valid even in the presence of optical resonances. The isolated computation of the material contribution, however, required finding a suitable reference object, complicating the analysis in the presence of resonances. In the following, we show how to exploit the separability to approximate the chiral optical response of

scatterers for different dispersive chirality parameters. The proposed scheme does not rely on finding a reference object and hence can be readily applied to generic scatterers. We find that the quality of the approximation is related to the smallness of the chirality parameter as compared to the other material parameters and, hence, is expected to be excellent for ordinary media. Provided that the optical response of an object for suitably chosen material parameters, that is, its T-matrix, is known, approximating the response for different chirality parameters is computationally cheap. In the next subsection, we expand the proposed approximation scheme and show that it can be deployed directly on the level of the object's T-matrix. This extends its use to the entire linear optical response of the object. The results discussed in this and the next subsection present original contributions that have not yet been published. They present an extension to the work published in Ref. [P9] that was covered in the previous subsections.

The basis for the following discussion is Eq. (5.10), the separability of an object's CD spectrum into a geometric and a material contribution. Here, we define the material contribution to an object's CD as

$$\mathrm{CD}_{\mathrm{mat}}\big(\omega,\kappa(\omega)\big) \coloneqq \mathrm{CD}\big(\omega,\kappa(\omega)\big) - \mathrm{CD}(\omega,0), \tag{5.13}$$

where $\mathrm{CD}(\omega,\kappa(\omega))$ refers to the total CD of a given object made from a medium featuring a dispersive chirality parameter $\kappa(\omega)$. $\mathrm{CD}(\omega,0)$ denotes the CD of the same object made from the achiral medium (racemate) that is obtained by setting $\kappa(\omega) = 0$ identically. This is precisely the isolated geometry contribution $\mathrm{CD}_{\mathrm{geo}}$ discussed before. By definition, the material contribution of Eq. (5.13) and the isolated geometry contribution sum up to be exactly equal the total CD.

In what follows, we show that $\mathrm{CD}_{\mathrm{mat}}(\omega,\kappa(\omega))$ depends, within good approximation, linearly on the chirality parameter. This is a consequence of the relative smallness of the chirality parameter (specifically, $|\kappa| \ll |\sqrt{\varepsilon\mu}|$) and is at the heart of the proposed approximation scheme. Accordingly, we write

$$\begin{aligned}\mathrm{CD}_{\mathrm{mat}}\big(\omega,\kappa(\omega)\big) \approx \underbrace{\mathrm{CD}_{\mathrm{mat}}(\omega,0)}_{=0} &+ \mathrm{Re}\{\kappa(\omega)\}\frac{\partial}{\partial\kappa_{\mathrm{r}}}\mathrm{CD}_{\mathrm{mat}}(\omega,0) \\ &+ \mathrm{Im}\{\kappa(\omega)\}\frac{\partial}{\partial\kappa_{\mathrm{i}}}\mathrm{CD}_{\mathrm{mat}}(\omega,0),\end{aligned} \tag{5.14}$$

and expect the error incurred by the approximation to scale with the second power of the chirality parameter.[6] The vanishing of the first term on the right-hand side of Eq. (5.14) follows directly from the definition in Eq. (5.13). The second and third term involve derivatives with respect to the real and imaginary part of the chirality parameter, denoted as $\partial/\partial\kappa_\mathrm{r}$ and $\partial/\partial\kappa_\mathrm{i}$, respectively. Since $\mathrm{CD}_\mathrm{mat}(\omega, \kappa(\omega))$ is a real-valued function of the complex parameter $\kappa(\omega)$, we consider separately its dependence on the real and imaginary parts. The expression above lends itself to numerical implementation; formally, Eq. (5.14) may be equivalently expressed using the Wirtinger derivatives $\partial/\partial\kappa$, $\partial/\partial\kappa^*$ [152, 153].

6 For a geometrically achiral scatterer, the total CD is entirely equal to the material contribution and is odd w.r.t. a sign change of $\kappa$. In that case, the error scales with the third power of $\kappa$, corresponding to an even closer approximation.

Together, Eqs. (5.13) and (5.14) allow us to readily approximate the CD spectrum of a given object for any reasonably sized dispersive chirality parameter $\kappa(\omega)$, provided the geometry contribution $\mathrm{CD}_\mathrm{geo}(\omega) = \mathrm{CD}(\omega, 0)$ and the derivatives with respect to $\kappa_\mathrm{r}$ and $\kappa_\mathrm{i}$ in Eq. (5.14) are known. We illustrate the procedure with a numerical example. For simplicity, we adopt the setup of the previous subsection, that is, we consider a distorted tetrahedral arrangement of spheres, made from the material parameters shown in Fig. 5.11. As before, we choose the radius of the spheres to be 80 nm and the side length of the reference tetrahedron to be 220 nm, with two of the center-to-center distances scaled according to $\delta = 20\,\%$. The total CD spectrum of this object, combining both the medium's and its geometry's chirality, is shown as the indigo curve in the upper panel of Fig. 5.14. The isolated geometric contribution is shown in gray. These two curves are the same as in Fig. 5.13. If only the first term on the right-hand side of Eq. (5.14) were to be considered, then $\mathrm{CD}_\mathrm{mat} = 0$ and our approximation of the total CD would be entirely determined by the isolated geometric contribution. Hence, the geometric contribution $\mathrm{CD}(\omega, 0)$ represents the zeroth order approximation within the proposed scheme.

We numerically determine the derivatives in Eq. (5.14) as finite differences. To this end, we compute two additional T-matrices per considered angular frequency $\omega$. For these T-matrices, we set the chirality parameter to two constant (non-dispersive) values, namely,

$$\boldsymbol{T}_\mathrm{r}(\omega) = \boldsymbol{T}(\omega)\big|_{\kappa=c_\mathrm{r}}\,, \qquad \boldsymbol{T}_\mathrm{i}(\omega) = \boldsymbol{T}(\omega)\big|_{\kappa=c_\mathrm{i}}\,. \tag{5.15}$$

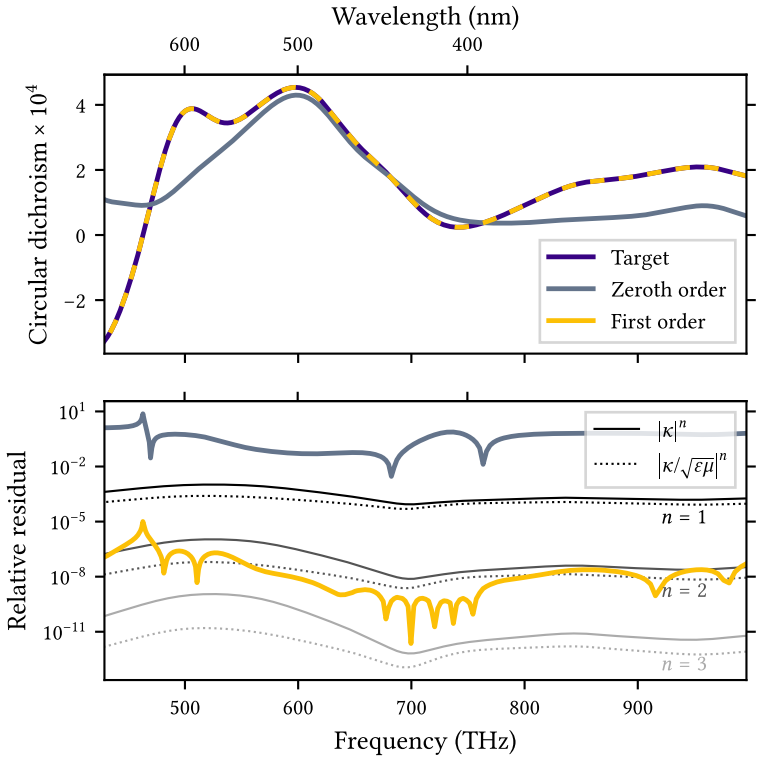


*Figure* 5.14: *Target and approximated circular dichroism spectra* · Upper panel: The target circular dichroism spectrum of a geometrically chiral scatterer made from a chiral medium is shown by the indigo curve. The circular dichroism of the same object made from the achiral medium ($\kappa = 0$) provides the zeroth order term of the approximation (gray). If the first order term is included in the approximation, the resulting spectrum (yellow, dashed) is visually indistinguishable from the target. Lower panel: Relative residuals of the zeroth and first order approximations with respect to the target. The solid (resp. dotted) reference lines correspond to the $n$th powers of the small parameter $|\kappa|$ (resp. $|\kappa/\sqrt{\varepsilon\mu}|$) for $n \in \{1, 2, 3\}$. The relative residual of the first order approximation appears upper-bounded by the second power of $|\kappa|$.

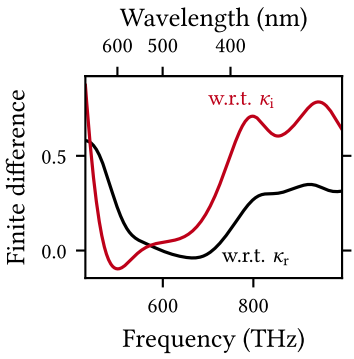


*Figure 5.15: Derivatives of the circular dichroism with respect to the chirality parameter* · The derivative of the circular dichroism with respect to the real (resp. imaginary) part of the chirality parameter, approximated as a finite difference, is shown by the solid black (resp. red) curve. The $x$-axis scales linearly with frequency; the upper axis displays the corresponding vacuum wavelength for reference on a non-linear scale.

Here, we choose $c_\mathrm{r} = 10^{-5}$ and $c_\mathrm{i} = 10^{-5}\mathrm{i}$. Subsequently, we compute CD spectra via Eq. (5.9),

$$\mathrm{CD}(\omega, \kappa = c_\mathrm{r}) = \mathrm{CD}\{\boldsymbol{T}_\mathrm{r}(\omega)\}, \qquad \mathrm{CD}(\omega, \kappa = c_\mathrm{i}) = \mathrm{CD}\{\boldsymbol{T}_\mathrm{i}(\omega)\}. \tag{5.16}$$

From these, we obtain the finite differences

$$\frac{\partial}{\partial \kappa_\mathrm{r}} \mathrm{CD}_\mathrm{mat}(\omega, 0) \approx \frac{\mathrm{CD}(\omega, c_\mathrm{r}) - \mathrm{CD}(\omega, 0)}{c_\mathrm{r}}, \tag{5.17a}$$

$$\frac{\partial}{\partial \kappa_\mathrm{i}} \mathrm{CD}_\mathrm{mat}(\omega, 0) \approx \frac{\mathrm{CD}(\omega, c_\mathrm{i}) - \mathrm{CD}(\omega, 0)}{\mathrm{i}c_\mathrm{i}^*}. \tag{5.17b}$$

The spectrally resolved finite differences are shown in Fig. 5.15. In Section 5.1, we discussed that the CD of a homogeneous chiral medium is determined by the imaginary part of the chirality parameter, as the difference of the helicity-dependent attenuation coefficients is proportional to $\mathrm{Im}\,\kappa$ (cf. Eq. (5.5)). For finite objects, their optical properties, particularly optical resonances, cause a more complex dependence of the material properties. Hence, both real and imaginary parts of $\kappa$ influence the full chiral optical response. This is apparent by both finite difference curves in Fig. 5.15 exhibiting similar orders of magnitude. Interestingly, the two derivatives do not behave uniformly, which means that the CD reacts disproportionally to changes of either $\mathrm{Re}\,\kappa$ or $\mathrm{Im}\,\kappa$ at different frequencies.

Finally, we evaluate Eq. (5.14) for the dispersive chirality parameter $\kappa(\omega)$ of Fig. 5.11 using the finite differences obtained above. Combining it with the geometric contribution as per Eq. (5.13), we obtain a first order approximation of the total CD of the distorted tetrahedral arrangement. The resulting spectrum, represented by the dashed yellow curve in the upper panel of Fig. 5.14, is visually indistinguishable from the original spectrum, which is the target of the approximation. The lower panel of Fig. 5.14 shows the relative residuals between the approximated spectra and the target. The first order approximation matches the target up to a relative residual on the order of $10^{-7}$ to $10^{-9}$ across the considered frequency range.[7] For comparison, first, second, and third powers of the magnitude of $\kappa$ (resp. $\kappa/\sqrt{\varepsilon\mu}$) are displayed as solid (resp. dotted) reference lines. The relative residual of the first order approximation appears upper-bounded by $|\kappa(\omega)|^2$, roughly following the shape of the reference line. Such relation is expected, since we neglected quadratic and higher order terms in the approximation. The smallness of the chirality parameter is responsible for the excellent agreement between the approximation and the target spectrum.

7 The spike in the relative residual occurring at approximately 450 THz is due to a zero-crossing of the target CD.

The zeroth order term, which only accounts for the isolated geometric contribution, yields a significantly worse approximation with relative deviations on the order of one. In general, the error of a zeroth order approximation is expected to scale with the first power of the small parameter. However, for chiral optical properties such as the CD, the effect of the otherwise small chirality parameter is disproportionately accentuated, leading to a contribution to the total spectrum on the same order of magnitude as that of the chiral geometry. Thus, taking the chirality parameter into account is indispensable for the accurate prediction of chiral optical properties.

In summary, we have demonstrated that the CD spectrum of a chiral object made from a dispersive chiral medium can be efficiently approximated by exploiting the relative smallness of the chirality parameter. Per frequency, three T-matrices need to be computed, one each for the constant values $\kappa(\omega) \in \{0, c_\mathrm{r}, c_\mathrm{i}\}$. If different dispersive chirality parameters are to be considered for a given object, the scheme described above can eliminate the need for the costly computation of T-matrices for every frequency and material parameter configuration. Instead, the CD spectrum is obtained directly from Eq. (5.14) after substituting the fitting prefactors for the derivatives. In this regard, we note that the tetrahedral arrangement was chosen for the dis-

cussion above out of convenience, as the required T-matrices are easy to compute. However, unlike before, there is no longer a need for a geometrically achiral reference object, which was the main reason for the original choice of this geometry. Consequently, any geometry can be considered, such as the helix from the penultimate subsection. For such—more complex—geometric shapes, the approximation scheme is particularly useful, as it can reduce the amount of computationally expensive full-wave scattering simulations.

Although the approximation of specific spectroscopic quantities is of practical interest, the underlying principle applies to the entire optical response of the object. Therefore, in the next subsection, we discuss how the same approximation scheme can be applied directly to T-matrices.

### 5.2.4 *Direct approximation of transition matrices*

In the following, we demonstrate that T-matrices for chiral objects made from chiral dispersive media can be approximated using the same approach described above. The scheme enables the efficient computation of all quantities related to the object's linear optical response. Naturally, the approach is particularly relevant when considering an object's chiral optical response. However, we find that the approximation also yields excellent results for general quantities such as cross-sections.

Following the principles outlined in the previous subsection, we approximate the T-matrix of an object made from a dispersive chiral medium as

$$\boldsymbol{T}(\omega, \kappa(\omega)) \approx \boldsymbol{T}(\omega, 0) + \mathrm{Re}\{\kappa(\omega)\}\frac{\partial}{\partial \kappa_\mathrm{r}}\boldsymbol{T}(\omega, 0) + \mathrm{Im}\{\kappa(\omega)\}\frac{\partial}{\partial \kappa_\mathrm{i}}\boldsymbol{T}(\omega, 0). \quad (5.18)$$

We expect the residual to scale with the second power of the smallness of the chirality parameter. For illustration, we consider the same tetrahedral arrangement as in the previous subsection and obtain the derivatives of the T-matrix entry-wise as finite differences with constants $c_\mathrm{r} = 10^{-5}$, $c_\mathrm{i} = 10^{-5}\mathrm{i}$, analogously to Eqs. (5.17). We assess the quality of the approximation in Fig. 5.16. The upper right panel shows the absolute values of the entries of the original (target) T-matrix of the chiral arrangement of spheres with the media parameters shown in Fig. 5.11, evaluated at an angular frequency of $\omega \approx 2\pi \times 996\,\mathrm{THz}$, and with $\ell_\mathrm{max} = 8$.[8] The four distinctly visible quadrants

8 We choose the highest frequency in the considered spectral range (corresponding to the shortest wavelength), since this makes the higher-degree contributions to the T-matrix stand out relatively most clearly and emphasizes the quality of the approximation across all multipolar degrees.

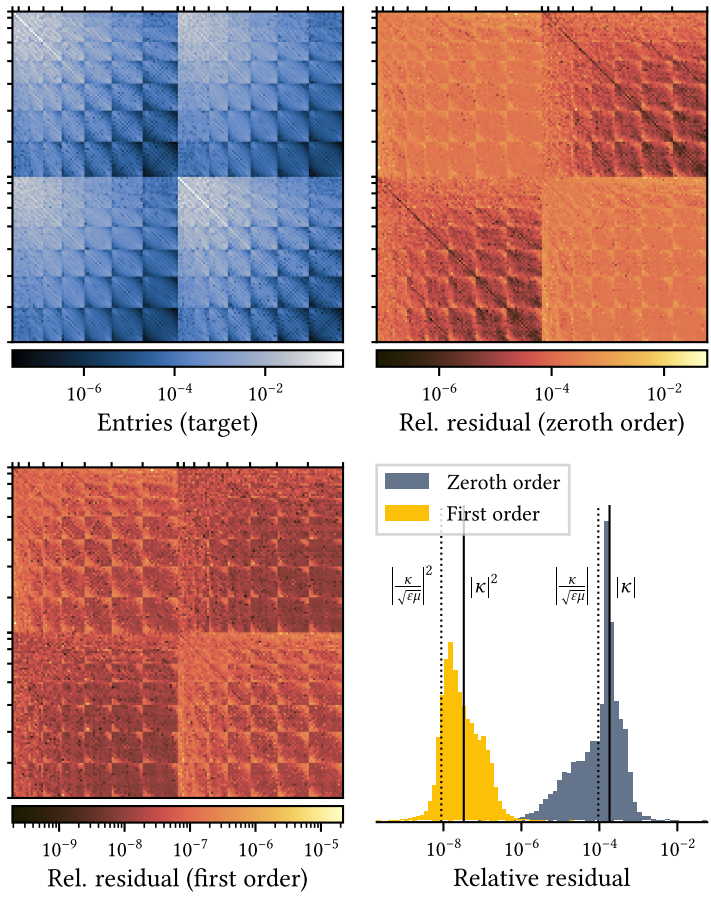


*Figure* 5.16: *Comparison of target and approximated transition matrices* · Upper left panel: moduli of entries of the target T-matrix. Entry-wise relative residuals for the zeroth (upper right) and first order (lower left) approximation are jointly displayed in the histogram in the lower right panel. Note the different data limits, as indicated by their respective colorbars. Solid (resp. dotted) reference lines in the histogram show the first and second power of the magnitude of the chirality parameter (resp. its ratio to the helicity-averaged refractive index). Colormaps from Refs. [154, 155].

of the T-matrix correspond to the helicity-dependent submatrices $\boldsymbol{T}_{\lambda'\lambda}$, with $\lambda'$ (rows), $\lambda$ (columns) $\in \{+1, -1\}$. Within each submatrix, entries are ordered in blocks of increasing multipolar degree $\ell \in \{1, \ldots, \ell_{\max}\}$. The outlines of these blocks are marked by the ticks on the right and upper axes. Within a block for a given $\ell$, entries are ordered according to an increasing multipolar order $m \in \{-\ell, \ldots, \ell\}$. The upper right and lower left panels of Fig. 5.16 show the entry-wise relative residuals,

$$\delta\tilde{T}_{\ell' m' \lambda', \ell m \lambda} := \frac{\left| T_{\ell' m' \lambda', \ell m \lambda} - \tilde{T}_{\ell' m' \lambda', \ell m \lambda} \right|}{\left| T_{\ell' m' \lambda', \ell m \lambda} \right|}, \tag{5.19}$$

between the target T-matrix $\boldsymbol{T}$ and $\tilde{\boldsymbol{T}}$, denoting either the zeroth or first order approximation obtained from Eq. (5.18). The zeroth order approximation corresponds to the first term on the right-hand side of Eq. (5.18), $\boldsymbol{T}(\omega, 0)$. With regard to chiral aspects of the optical response of a given object, it may be interpreted as isolating the effects of a chiral geometry, in line with our discussions before. The first order approximation corresponds to the full right-hand side of Eq. (5.18). It closely matches the target, reaching relative residuals predominantly on the order of $10^{-7}$ to $10^{-8}$. To compare the two approximations, the entry-wise relative residuals are collected in a histogram in the lower right panel. As expected, we find that the relative residuals of the zeroth and first order approximation assume values complying with the first and second power of the magnitude of the chirality parameter, respectively. An interesting feature is observed in the zeroth order approximation, where the relative residuals of the co-polarized (i.e., the on-diagonal quadrants) are significantly larger than those of the cross-polarized (i.e., the off-diagonal quadrants) submatrices. The corresponding histogram (gray) shows a bimodal distribution, suggesting that the co-polarized and cross-polarized entries depend differently on the chirality parameter. We return to this observation below.

The derivatives of the T-matrix with respect to the real and imaginary parts of the chirality parameter are again calculated using finite differences. As an example, we show the derivative with respect to the real part in Fig. 5.17. Qualitatively, the derivative with respect to the imaginary part appears similar; hence, we limit our discussion to one of the two terms.

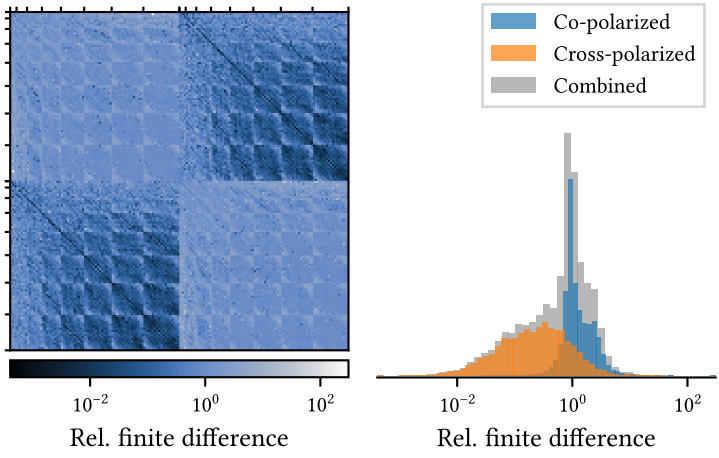


*Figure* 5.17: *Relative finite differences of transition matrix entries* · Left panel: entry-wise magnitude of the entries of $\frac{\partial}{\partial \kappa_r} \boldsymbol{T}(\omega, 0)$ relative to the entries of $\boldsymbol{T}(\omega, 0)$, corresponding to the relative instantaneous change of each entry with respect to a change of the real part of $\kappa$. The co-polarized (diagonal quadrants) and cross-polarized (off-diagonal quadrants) submatrices depend differently on such change, as apparent in the separate histograms in the right panel. The combined histogram of all entries correspondingly exhibits a bimodal distribution. Each histogram is displayed using 50 bins. The derivatives of the matrix entries are approximated as a finite differences. Colormap from Refs. [154, 155].

The left panel shows the absolute values of the entries of the derivative normalized to the corresponding entries of the constant (zeroth order) term,

$$\left| \frac{\frac{\partial}{\partial \kappa_r} T_{\ell' m' \lambda', \ell m \lambda}(\omega, 0)}{T_{\ell' m' \lambda', \ell m \lambda}(\omega, 0)} \right|,$$

approximating an entry-wise logarithmic derivative. It corresponds to the relative instantaneous change of each entry with respect to a change of the real part of $\kappa$.

Related to our observation before, the co-polarized entries exhibit a stronger dependence on the chirality parameter than the cross-polarized ones, apparent by the overall lighter and darker shades of the corresponding quadrants. The histogram in the right panel of Fig. 5.17 shows the distributions of the normalized derivatives for co-polarized and cross-polarized entries separately. It confirms the observed difference and reveals an overall bimodal distribution similar to that seen in the residuals of the zeroth order approximation in Fig. 5.16. To gain intuition for this behavior, we consider the T-matrix of a simple chiral sphere, Eq. (4.23), determined by the chiral Mie coefficients. As follows from Eqs. (4.18), the coefficients $\mathfrak{a}_\ell$ and $\mathfrak{b}_\ell$ are symmetric with respect to an exchange of the helicity eigenvalues $+ \leftrightarrow -$. Since the sphere is geometrically achiral, exchanging the eigenvalues of helicity is equivalent to changing the sign of the chirality parameter. Consequently, $\mathfrak{a}_\ell$ and $\mathfrak{b}_\ell$ cannot depend linearly on the chirality parameter. By constrast, $\mathfrak{c}_\ell$ is antisymmetric with respect to a sign change in the chirality parameter. Hence, within first order approximation, only $\mathfrak{c}_\ell$ depends on the chirality parameter, with corrections for the other coefficients determined by the second order. As per Eq. (4.23), $\mathfrak{c}_\ell$ only contributes to the co-polarized parts of the T-matrix, while the cross-polarized parts depend only on $\mathfrak{a}_\ell$ and $\mathfrak{b}_\ell$. Therefore, only co-polarized entries depend linearly on $\kappa$, resulting in a contrast between the co-polarized and cross-polarized components similar to that observed above.

An interesting question is to which types of objects this observation can be generalized. In general, the cross-polarized parts of the T-matrix are related by a reciprocity [117, Eq. (36)][106]. In connection with the fact that, for a geometrically achiral scatterer, a sign change in $\kappa$ is equivalent to an exchange of the helicity eigenvalues, a similar distinction between co-polarized and cross-polarized T-matrix entries might arise with respect to the parity (even or odd) of the powers of $\kappa$ on which they can depend. However, we do not attempt to answer this question within the scope of the present discussion.

The entry-wise comparison of the target and the approximated T-matrices in Fig. 5.16 provides a detailed assessment of the validity of the approximation. For a similar assessment covering the entire spectral region, we directly

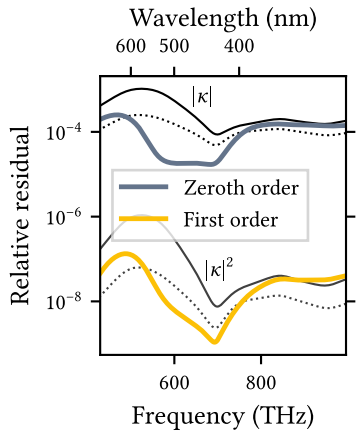


*Figure* 5.18: *Relative residual of approximated transition matrices* · The relative residuals in the Hilbert–Schmidt norm of the zeroth order (gray) and first order (yellow) approximation with respect to the target T-matrix are plotted. Solid (resp. dotted) reference lines show the first and second power of the magnitude of $\kappa$ (resp. of $\kappa/\sqrt{\varepsilon\mu}$). The $x$-axis scales linearly with frequency; the upper axis displays the corresponding vacuum wavelength for reference on a non-linear scale.

evaluate relative residuals of approximated T-matrices $\tilde{\boldsymbol{T}}$ with respect to the target $\boldsymbol{T}$ in the Hilbert–Schmidt norm,

$$\delta\tilde{\boldsymbol{T}} \coloneqq \frac{\|\boldsymbol{T} - \tilde{\boldsymbol{T}}\|_{\mathrm{HS}}}{\|\boldsymbol{T}\|_{\mathrm{HS}}}. \tag{5.20}$$

The Hilbert–Schmidt norm is chosen as it directly relates to spectroscopically accessible quantities, namely the scattering cross-section. According to Eq. (4.33a), the directionally and helicity-averaged scattering cross-section of an object in an achiral embedding is proportional to the squared Hilbert–Schmidt norm of the T-matrix. Therefore, the squared norm quantifies an object's optical response and is occasionally referred to as the object's *interaction cross-section*. Correspondingly, the squared numerator of Eq. (5.20) can be interpreted as a spurious interaction cross-section, relating the residual of the approximation to an erroneous optical response. In Fig. 5.18, we plot the spectrally resolved relative residuals of the approximated T-matrices in zeroth and first order. As expected, the residuals roughly follow the first and second power of $|\kappa(\omega)|$, respectively, corresponding to the higher orders neglected in each approximation. Again, the smallness of $\kappa(\omega)$ permits an excellent approximation of T-matrices in first order, matching the true T-matrix up to relative residuals on the order of $10^{-7}$ to $10^{-9}$.

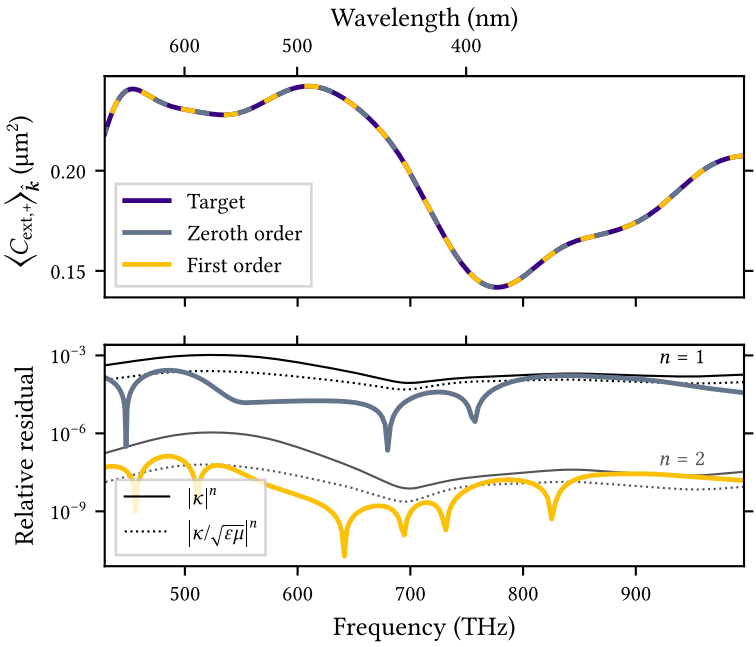


*Figure* 5.19: *Extinction cross-section evaluated from approximated transition matrices* · Upper panel: directionally averaged extinction cross section for positive helicity illumination, evaluated from the target T-matrices (indigo) as well as from the zeroth (gray) and first order (yellow) approximations. Lower panel: relative residuals for the zeroth and first order approximation. Solid (resp. dotted) reference lines correspond to the first and second power of the magnitude of $\kappa$ (resp. $\kappa/\sqrt{\varepsilon\mu}$).

The direct approximation of T-matrices is evidently even more powerful than the approximation of CD spectra discussed in the previous subsection. Comprising the full description of an object's linear optical response, it enables the subsequent evaluation of all other spectroscopically relevant quantities. This includes the CD, which, if evaluated from the approximated T-

matrices described above, yields virtually identical results to the ones shown in the previous subsection. Other quantities are approximated equally well, as shown in Fig. 5.19. There, we compare as an example the directionally averaged extinction cross-section for positive helicity illumination. Unlike the CD, the extinction cross-section is not a quantity that immediately highlights an object's chiral optical response. Accordingly, the spectra obtained from the target (indigo) and approximated zeroth and first order T-matrices (gray and yellow) are not easily distinguished in the upper panel of Fig. 5.19. Yet, the quality of the approximation is consistent with our previous discussions, as shown by the relative residuals in the lower panel. As remarked before, the proposed scheme is arguably more relevant when dealing with chiral optical properties; in case of the CD, the necessity of including the first order term became immediately apparent upon comparing resulting spectra in the upper panel of Fig. 5.14. Nonetheless, the first order approximation achieves excellent agreement for other quantities as well, such as the extinction cross-section, and represents a significant improvement over the zeroth order term, as illustrated by the relative residuals on the order of $10^{-7}$ to $10^{-9}$ shown in the lower panel of Fig. 5.19.

In conclusion, we have found that the smallness of typical chiral material parameters allows for an efficient and powerful approximation of T-matrices for varying dispersive chiral media. It extends the applicability of the approximation presented in the previous subsection to all spectroscopic quantities of interest that are determined by the linear optical response of an object. Below, we summarize our results and discuss their potential for further applications.

### 5.2.5 *Summary and outlook*

In the preceding subsections, we employed a multiscale modeling approach combining quantum chemical simulations of the optical properties of molecules with FEM based scattering simulations and the transition matrix formalism. It allowed us to investigate and understand the origin of the CD spectrum of objects exhibiting both a geometric and a medium-induced chirality. In Subsections 5.2.1 and 5.2.2, we studied two different setups, considering separately scatterers that feature optical (geometrically induced) resonances and those that do not. For both kinds of scatterers, we found

that the total CD can be decomposed into two contributions, one attributed to the chirality of the geometric shape and the other to the chiral medium. These results were originally published in Ref. [P9].

In the absence of optical resonances, the material contribution to the chiral response is, within good approximation, independent of the geometric shape of the scatterer, as demonstrated by the comparison of a helix and a sphere of equal volume in Subsection 5.2.1. In such cases, the material contribution can even be well approximated from the properties of bulk medium without any consideration of geometry; for this purpose, we defined the CD of the medium in terms of its attenuation coefficients. For objects that support optical resonances, the CD remains decomposable, however, the isolated contribution of the medium is generally more difficult to obtain. It required a suitable reference object that is geometrically achiral and exhibits a similar overall absorption characteristic (i.e., similar optical resonances) as the original object whose CD spectrum we want to decompose. In Subsection 5.2.2, we met this condition by considering a irregular, chiral tetrahedral arrangement of spheres, which, through continuous deformations, yielded the required achiral reference geometry. This choice allowed us to conclude that, in both resonant and non-resonant cases, the total CD can be separated into independent contributions due to the chiral geometry and the chiral medium.

Our results suggest that the shape and the medium of a mesoscopic scatterer can be considered as separate factors influencing an object's chiral optical response, essentially differentiating the length scales on which chirality manifests. Since full-wave simulations of an object's response can be costly, approximating the material contribution in a simpler object offers a computationally cheaper alternative for obtaining spectra for different values of the material chirality. Such approximation is possible in the absence of optical resonances or, in the resonant case, if a suitable achiral reference object can be constructed. Apart from the potential savings in computational time and effort, our results open up the prospect of tailoring chiral optical responses. To this end, the geometry and the medium are treated as separate degrees of freedom, enabling an optimization of the total chiral response. Finally, the pairing of geometrically chiral and achiral reference objects used in the resonant analysis could be reconsidered from the perspective of a pole expansion of the T-matrix [S2]. Such poles of the T-matrix correspond

directly to the resonances of an object, hence, the comparability of the absorption characteristic of separate objects could be evaluated on this basis. Investigating how the resonances of an object depend on the chirality of its medium promises an insightful continuation of the presented study.

Building on our insight that geometric and material-related contributions can be separated, we discussed the approximation of CD as well as the direct approximation of T-matrices in Subsections 5.2.3 and 5.2.4 made possible by the small chirality parameters. The results and the discussion presented in these subsections extends the work of Ref. [P9] and constitute an original contribution of this thesis.

The approximation of CD spectra is based on the observation, that, in a series expansion of the total spectrum with respect to the chirality parameter, the isolated geometric contribution and the material contribution correspond to the zeroth order term and the sum of all higher order terms, respectively. Since the chirality parameter for naturally occurring media is small in the ultraviolet to infrared range (relative to the helicity-averaged refractive index, $|\kappa| \ll |\sqrt{\varepsilon\mu}|$), the material contribution is, to a good approximation, determined by the linear (first order) term of the series, with a residual on the order of the square of the small chirality parameter. For the example discussed above, this approximation reproduces the target spectrum with a relative residual on the order of $10^{-6}$ to $10^{-8}$. For a geometrically achiral object, we expect the approximation to be even more accurate: Since the CD spectrum is entirely due to the medium, it has to be odd with respect to a sign change of $\kappa$. Hence, only odd orders contribute, leading to even smaller residuals determined by the third power of $\kappa$.

Finally, we saw in Subsection 5.2.4 that the approximation of the chiral medium's influence can be applied directly to an object's T-matrix. As the relative residual of the approximation is again related to higher powers of the chirality parameter, the approximation yields equally good results. Hence, the proposed approximation scheme is applicable to any spectroscopic quantity of interest and not limited to the evaluation of CD spectra. Evidently, the scheme is mostly relevant when considering chiral or helicity-resolved aspects of an object's optical response.

If the T-matrix of an object with $\kappa = 0$ and its derivatives with respect to the chirality parameter are known, T-matrices for different values of $\kappa$ can be approximated swiftly and cheaply. The ability to perform such rapid calcula-

tions of (chiral) optical responses for varying dispersive chirality parameters makes them well-suited for studies of media consisting of chiral molecules at different enantiomeric ratios. In such case, the permittivity and permeability are independent of the enantiomeric ratio, while the chirality parameter varies continuously between the two extremal values determined by the enantiomerically pure (i.e., containing only one of the enantiomers) media. In a racemic mixture, that is, when both enantiomers are present in equal concentrations, the chirality parameter vanishes identically. Consequently, T-matrices for a given object made from a chiral medium can be easily calculated as the enantiomeric ratio varies, using the proposed approximation. Similarly, chiral inclusions consisting of chiral particles embedded in an achiral host could be considered [156–161]. For such inclusions, the chirality parameter depends entirely on the particles used in the inclusion, while permittivity and permeability are firstly determined by the host medium and may depend on the general presence of the inclusion than on its specific properties. Therefore, at not too high concentrations, inclusions of different particles in the same host medium could be modeled as a simple exchange of the dispersive chirality parameter, while maintaining a similar modified permittivity and permeability of the host medium. The optical properties of objects made from different inclusions using the same host medium could then be readily approximated according to the scheme developed above.

With regard to possible extensions of the results presented, we highlight the differing behavior of co-polarized and cross-polarized submatrices of the T-matrix, as observed in the approximation. For a simple sphere, we have shown that such pattern results directly from the Mie coefficients, with only the co-polarized submatrices depending linearly on the chirality parameter. For more complex shapes, we suspect that the observed pattern can be explained by reciprocity relating different submatrices [106, 117].

Furthermore, we approximated the derivatives of the T-matrix with respect to the chirality parameter as finite differences. The use of automatic differentiation when computing T-matrices [162–166] offers great potential for the proposed approximation scheme. It would eliminate the need for additional T-matrix computations used to assemble the derivatives as finite differences, which would save additional computation time.

## 5.3 *Circular Dichroism of Helically Arranged Metallic Nanoparticles*

In this section, we consider chiral spatial arrangements of metallic nanoparticles and their chiral optical response. In contrast to the systems considered previously, all involved media are achiral, and the individual nanoparticles are also achiral. Hence, the chiral optical response is entirely an emergent feature of the spatially distributed particle cluster due to the geometric chirality of its arrangement. We examine the optical response of individual particles, which is characterized by plasmonic resonances. We investigate the coupling between these resonances in the arrangement and demonstrate that it is the decisive factor for the observed strongly pronounced CD and its characteristic bisignate spectral shape.

Chiral optical responses of small metallic structures and assemblies thereof have attracted considerable attention due to the strength they can exhibit, as well as their potential to enhance the chiral response of molecules—both of which are enabled by the presence of plasmonic resonances in these systems [167–170]. The system we discuss below numerically models assemblies that were characterized in experiments conducted as part of a collaborative project led by the group of Wiktor Lewandowski [P3]. In these experiments, CD spectra of chiral arrangements of gold nanoparticles were analyzed. The arrangements form in liquid-crystal thin films of an organic oleylimine compound. A transmission electron micrograph of one of the measured systems can be seen in the upper left corner of Fig. 5.20. After doping the thin films with a chiral organic compound and thermal treatment, the liquid-crystal molecules self-assemble into helically twisted nanofilaments—morphologically chiral supramolecular structures. These helical nanofilaments serve as guides for surface-activated gold nanoparticles, which attach themselves to the edges of the nanofilaments, resulting in the arrangement of nanoparticles along a helical curve. A stylized representation of the system is shown in the lower left corner of Fig. 5.20. In Ref. [P3], various configurations of nanoparticles and organic thin films are investigated to explore the possibilities for engineering the system's specific chiral optical response.

In the following, we present results and conclusions from numerical modeling of helical arrangements of nanoparticles, based on our results that were

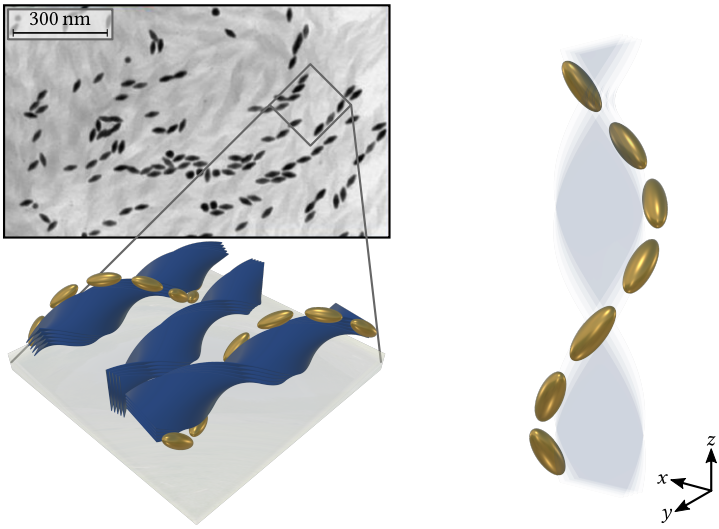


*Figure* 5.20: *Formation of helical arrangements of metallic nanoparticles and the structure considered for modeling* · Upper left: transmission electron micrograph of an organic thin film forming helically twisted nanofilaments with embedded gold nanoparticles. The gold nanoparticles accumulate at the edges of the nanofilaments, arranging themselves into helical structures. The lower left shows a stylized representation of the helically twisted nanofilaments with attached gold nanoparticles. Right panel: example of an idealized helical arrangement considered for numerical modeling, consisting of seven evenly distributed nanoparticles aligned tangentially to a helical curve. In the modeling, the organic thin film is treated as a homogeneous embedding; the morphology of the nanofilaments is considered negligible. Transmission electron micrograph reproduced from Ref. [P3], CC BY 4.0.

originally published jointly with the experimental findings in Ref. [P3]. Our model focuses on individual, idealized helical arrangements and a specific parameter, namely the distance between adjacent nanoparticles, as this is directly related to the coupling between the particles. Assuming that the

response of the complete system investigated in the experiments is largely determined by an ensemble average of the properties of various nanoparticle arrangements, our modeling provides insight into their fundamental properties. An example of the modeled system is shown on the right in Fig. 5.20. Since the optical response of such arrangements is predominantly due to the response of nanoparticles, we treat the presence of the organic thin film as a homogeneous background medium but consider its morphology to have negligible effect (apart from providing the scaffold for the nanoparticles, which determines the geometry of the arrangements). First, we study individual gold nanoparticles and their resonant response. In this context, we discuss the effect of small sizes on the optical response of small metallic particles and introduce a correction to the permittivity of the medium to account for this effect. We then examine the optical response of helical arrangements of nanoparticles and its dependence on the distance between adjacent nanoparticles. We highlight the coupling between the resonances of the particles as the primary cause of the chiral optical response of the arrangements. This emphasizes the nature of the chiral optical response as an emergent feature of the composite system. We conclude with a note on the importance of higher multipolar degrees when modeling systems such as the one investigated here, followed by a summary and an outlook.

### 5.3.1 *Single-particle response and size correction to permittivity*

Physically, the permittivity of metals arises from the response of free electrons with additional contributions from interband transitions [171]. The free electron contribution is treated by the Drude model [172, 173]. In the Drude model, the conductivity of metals is explained by the free movement of electrons that is frequently interrupted when the electrons scatter from the relatively stationary metal ions and from each other. The distance between successive scattering events corresponds to a mean free path length for the electrons. When combined with the interband contributions, the Drude model provides a sound estimate of the permittivity of bulk metals. However, when the size of a given metallic particle becomes similar to the electron mean free path length, collisions with the particle boundary play a significant role, effectively limiting the distance between scattering events. In gold, for instance, the mean free path of the electrons works out to ap-

proximately 13 nm [cf. 171, Eq. (5) and Tab. 1]. For particles of comparable dimensions, we take this finite-size effect into account as a correction to the permittivity [171, Eqs. (7) and (8)],

$$\varepsilon(\omega) = \varepsilon_{\text{bulk}}(\omega) + \frac{\omega_\text{p}^2}{\omega^2 + \mathrm{i}\Gamma_{\text{bulk}}\omega} - \frac{\omega_\text{p}^2}{\omega^2 + \mathrm{i}\Gamma\omega}, \tag{5.21a}$$

where

$$\Gamma = \Gamma_{\text{bulk}} + A\frac{v_\text{F}}{r_1}. \tag{5.21b}$$

Here, $\omega_\text{p}$ and $v_\text{F}$ are the plasma frequency and the Fermi velocity of the metal, respectively. $\Gamma_{\text{bulk}}$ is the damping constant of the electron motion and is inversely proportional to the mean free path length. For gold, the explicit values are $\omega_\text{p} \approx 13.8 \times 10^{15}\,\text{s}^{-1}$, $v_\text{F} \approx 1.39 \times 10^{6}\,\text{m}\,\text{s}^{-1}$, and $\Gamma_{\text{bulk}} \approx 1.08 \times 10^{14}\,\text{s}^{-1}$ [119, 171, 174]. Equation (5.21b) gives the size-corrected damping constant, where the radius $r_1$ characterizes the size of the particle and $A$ is a constant that depends on the shape of the particle and is usually close to unity. The correction term scales with the inverse particle size, reflecting that the ratio between the particle's surface and its volume determines the relative impact of additional collisions [175]. We follow Ref. [171] and set $A = 1$ in subsequent calculations.

Figure 5.21 shows the effect of the size correction for gold nanoparticles. The permittivity for gold was determined experimentally in [176]. Next to these values for bulk material, we show the result of the correction in Eqs. (5.21) for various particle radii $r_1$ ranging from 1 to 10 nm. As the radius increases, the curves gradually approach the original bulk permittivity, consistent with the idea that the finite-size effect is insignificant for particle sizes considerably larger than the mean free path length. The effect appears generally more pronounced in the imaginary part of the permittivity, indicating that the increased rate of collisions results in an increase in absorption losses.

We proceed with the computation of optical properties of the individual gold nanoparticles. We model the nanoparticle as a prolate spheroid with semiaxes 6.5 nm and 16.5 nm; a visual representation is shown in the lower panel of Fig. 5.22. Material parameters for gold are determined by the permittivity shown in Fig. 5.21, corrected for a small particle radius of

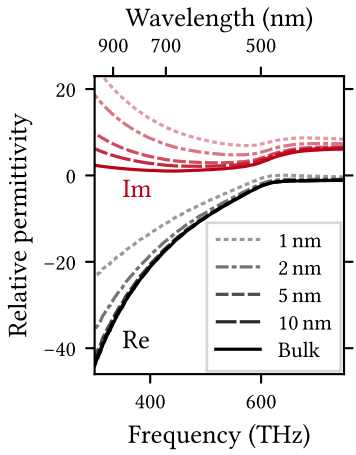


*Figure 5.21: Small particle correction to relative permittivity* · Relative permittivity of gold for bulk medium, as well as corrected for small particle sizes, as represented by the radii specified in the legend. The real and imaginary parts of the relative permittivity are represented by black and red lines, respectively. The $x$-axis scales linearly with frequency; the upper axis displays the corresponding vacuum wavelength for reference on a non-linear scale. Bulk permittivity interpolated from data in Ref. [176] as provided by Ref. [177].

$r_1 = 8.9\,\mathrm{nm}$, which corresponds to the geometric mean of the three semi-axes of the spheroid. Following a workflow similar to that described in the previous section (cf. Fig. 5.6), we compute the T-matrix of the spheroid up to $\ell_{\max} = 4$ at various frequencies in the visible to near-infrared region using FEM simulations. The rotational symmetry of the spheroid about its major axis, which we choose to be parallel to $\hat{z}$, makes it possible to restrict the FEM simulations to a two-dimensional mesh with appropriate boundary conditions, thus reducing the computational effort. Furthermore, doing so yields more accurate T-matrices: For an object with rotational symmetry about the $z$-axis, the T-matrix is diagonal with respect to the multipolar order $m$ [117, Eq. (30)],

$$T_{\ell' m' \lambda', \ell m \lambda} = \delta_{m m'} T_{\ell' m \lambda', \ell m \lambda}. \tag{5.22}$$

In T-matrices obtained from simulations considering the full three-dimensional geometry, entries vanishing due to Eq. (5.22) are still affected by numerical imprecision. By explicitly involving the rotational symmetry, this source of error is eliminated. To account for the organic thin film in which the particles are embedded in the experiment, we use a non-dispersive re-

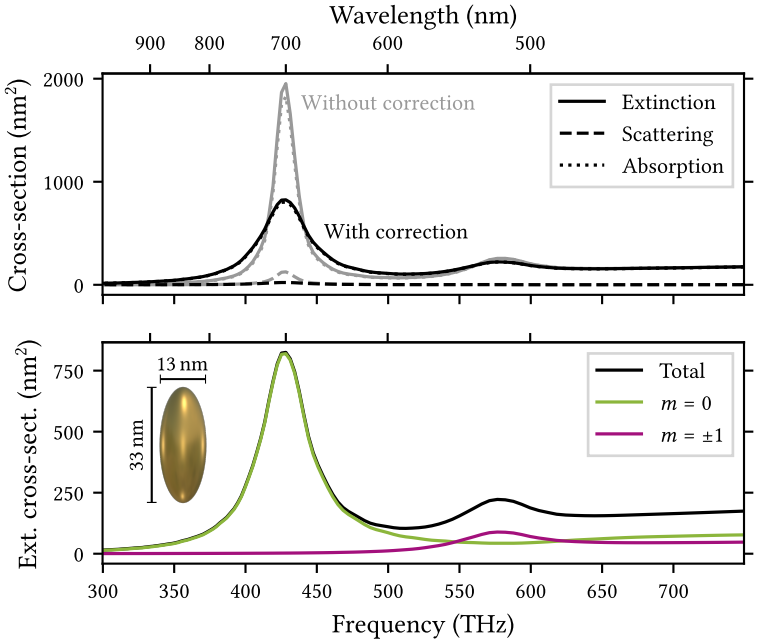


*Figure* 5.22: *Cross-sections of a gold spheroid* · The helicity- and direction-averaged extinction (solid lines), scattering (dashed), and absorption (dotted) cross-sections of a prolate gold spheroid (inset in the lower panel) are shown in the upper panel. The spheroid is modeled with a permittivity as shown in Fig. 5.21, separately with (gray) and without (black) size correction at $r_1 = 8.9\,\text{nm}$. The embedding is modeled with a non-dispersive refractive index of 1.6. The size correction visibly decreases and broadens the two peaks observed in the spectra. The lower panel shows the total extinction cross-section including size correction (black; identical to the solid black curve in the upper panel), as well as individual electric dipolar contributions. The main peak located at around 430 THz is dominated by the dipolar contribution with order $m = 0$ (green), which corresponds to an orientation parallel to the major axis of the spheroid. The secondary peak at around 580 THz is due to the two-fold degenerate dipolar resonance parallel to the spheroid's equatorial plane ($m = \pm 1$; purple).

fractive index of 1.6 for the embedding in the simulations. Subsequently, spectroscopic quantities are computed from the T-matrices using the software treams [100, 101].

The upper panel of Fig. 5.22 shows the helicity- and direction-averaged extinction, scattering, and absorption cross-sections for the spheroid (black curves). The total optical response of the spheroid as represented by the extinction cross-section is predominantly due to absorption, as is evident from the nearly overlapping respective curves. Cross-sections computed from T-matrices obtained for the same spheroid without size correction for the permittivity are shown for comparison. As a result of the correction, the two peaks observed in the spectra decrease and broaden, consistent with our earlier comment regarding increased absorption losses. For the remainder of this section, we only consider quantities computed with the size correction applied.

The computed spectra exhibit two distinct peaks that qualitatively reproduce the features of the extinction spectra experimentally recorded for nanoparticles in Ref. [P3]. The origins of the two peaks can be traced back to the particle's electric dipolar resonances. To this end, we consider the averaged extinction cross-section as given in Eq. (4.33b), which is determined by the trace of the T-matrix. The trace corresponds to a sum over individual contributions for each combination of multipolar degree $\ell$, order $m$, and helicity $\lambda$. The particle shape and all involved media are achiral, which further allows us to use Eq. (C.23) to represent the same expression in terms of multipolar contributions of well-defined parity, that is, multipolar contributions of electric and magnetic character. Evaluating the individual contribution associated with an electric dipole ($\ell = 1$) of order $m = 0$—which corresponds to an orientation parallel to $\hat{z}$, the major axis of the spheroid—yields the green curve of Fig. 5.22. It accounts for up to 99.4 % of the total extinction cross-section and causes the main peak at around 430 THz. Similarly, the electric dipolar contributions for $m = \pm 1$ are responsible for the secondary peak at around 580 THz. They correspond to linear combinations of dipolar reponses parallel to the equatorial plane of the spheroid and are degenerate due to its rotational symmetry. Physically, these resonances are due to collective oscillations of the free electrons in the particle and are referred to as localized surface plasmon resonances. The spectral separation of the two resonances is determined by the aspect ratio of the prolate spheroid:

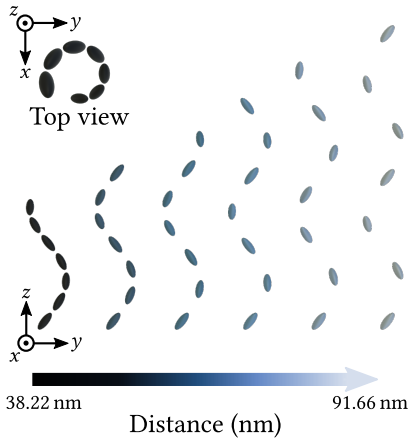


*Figure* 5.23: *Helical arrangements of metallic nanoparticles* · Examples of helically arranged metallic nanoparticles are shown, corresponding to different turn numbers of the helical curve connecting the particles, ranging from 0.79 to 2.0. The corresponding center-to-center distances between adjacent particles range from 38.22 to 91.66 nm. A top view of the leftmost arrangement is included for reference. Adapted from Ref. [P3], CC BY 4.0. Colormap from Refs. [154, 155].

The nonspherical geometry results in different dimensions for the oscillations and alters the restoring force exerted by the accumulated surface charges, depending on whether the mode is excited along the major axis or one of the minor axes [cf. 178, Chapter 7].[9] According to this orientation, the resonances are frequently referred to as longitudinal and transverse plasmon resonances, respectively. The coupling of the longitudinal plasmon resonance between multiple nanoparticles is the primary cause of the chiral optical response of the helically arranged nanoparticles, which we discuss next.

9 Following these considerations, we expect that the size correction computed for a single particle radius $r_1$ results in the finite-size effect being slightly overestimated for the longitudinal resonance and slightly underestimated for the transverse one. Nevertheless, it provides a reasonable estimate.

### 5.3.2 *Composite response and the influence of coupling between particles*

As a model for the chiral clusters of nanoparticles, we assemble seven nanoparticles on a helical curve with their major axes aligned tangentially to the curve (cf. the right panel of Fig. 5.20). The parameters specifying the helical curve are based on experimentally obtained geometric properties of the twisted organic nanofilaments that guide the formation of the chiral clusters in Ref. [P3]. Specifically, these are a pitch of 230 nm and a radius of 29 nm, equal to the sum of half the width of the nanofilaments

and the semi-minor axis of the spheroids. The setup describes an idealized arrangement of nanoparticles that are evenly attached to one edge of the nanofilament. We consider several such arrangements for various distances between the particles; Fig. 5.23 shows a few examples. To this end, we vary the total number of turns of the helical curve between the centers of the outermost nanoparticles from 0.79 to 2.0, corresponding to distances between adjacent nanoparticles of 38.22 to 91.66 nm, center to center. In each helical arrangement, the seven nanoparticles are spaced at equal intervals.

The optical properties of helical arrangements are obtained from Eq. (4.38), describing the T-matrix of a cluster of particles. T-matrices for the individual spheroids upon reorientation (for tangential alignment to the helical curve) follow from the rotation of VSWS, see Eq. (A.50). Subsequently, we compute cross-sections from Eqs. (4.42) and obtain the resulting CD. To account for the fact that the nanofilaments and the resulting chiral clusters of nanoparticles observed in the experiments are oriented flat in the thin film, we consider directional cross-sections with illumination directions oriented radially to the helical curve. Furthermore, the azimuthal orientation of the helical arrangement (i.e., the relative orientation w.r.t. to rotations around the central axis of the helical curve) is not controlled in the experiment. Therefore, we average the cross-sections for two orthogonal radial illumination directions, namely, $\hat{\boldsymbol{k}} = -\hat{\boldsymbol{x}}$ and $\hat{\boldsymbol{k}} = -\hat{\boldsymbol{y}}$, which is sufficient to eliminate any dependence on the azimuthal orientation. Correspondingly, we also evaluate the CD from the resulting helicity-dependent radially averaged directional absorption cross-sections, by replacing the fully directionally averaged cross-sections in Eq. (5.9) accordingly.

Figure 5.24 shows the helicity-averaged radial extinction cross-sections of the helical arrangements at different distances between adjacent particles in the spectral region focused on the longitudinal plasmon resonance of a single particle. The spectra exhibit a similar resonance line shape arising from a collective response of the coupled resonances of the individual particles. As the particle distance decreases, the effect of the coupling between the resonances becomes more evident, leading to a spectral shift accompanied by a broadening and a decrease in amplitude of the resonant line shape. However, we remark that even at the smallest particle distance considered—which corresponds to a tip-to-tip distance of merely 5 nm, approximately—no splitting of the resonant feature is observable. Such splitting is often considered

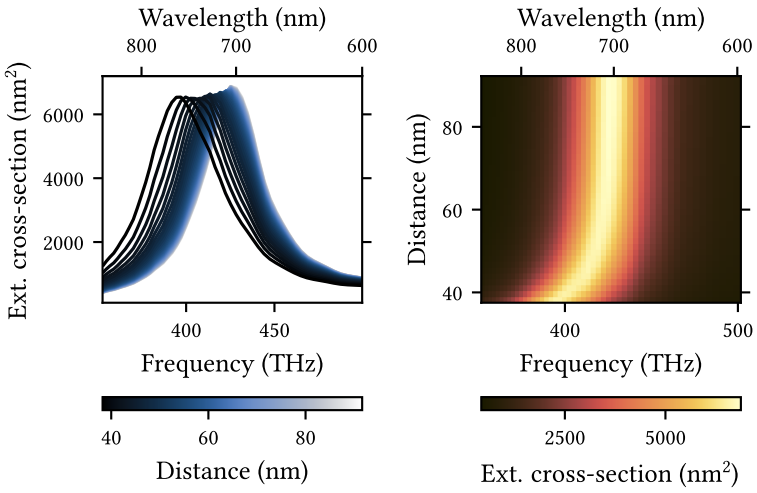


*Figure* 5.24: *Extinction cross-section of helically arranged nanoparticles dependent on particle distance* · The left panel shows the line shapes of the main resonance in the helicity-averaged extinction cross-section of helical arrangements of nanoparticles for radial illumination at various distances between adjacent particles. Across the considered distance range, a single peak is observed. For small particle distances, the amplitude of the peak decreases slightly and it broadens as it shifts toward lower frequencies. The right panel displays a heatmap of the same data, which illustrates the trajectory of the peak's central position across varying distances. Colormaps from Refs. [154, 155].

an experimental hallmark for the detection of the coupling of resonances. Here, it is hidden by the broad nature of the single-particle resonance.[10] Similarly, the spectral shift of the resonance position is considered as another marker for coupling, yet the right panel of Fig. 5.24 unveils that the spectral position of the resonance of the coupled nanoparticle arrangement quickly approaches that of the single particle, differing only marginally relative to the spectral linewidth for particle distances of approximately

10 In spectra obtained without applying a size correction to the permittivity, resonance splitting begins to appear for the smallest particle distances considered; see Fig. 5c of Ref. [P3].

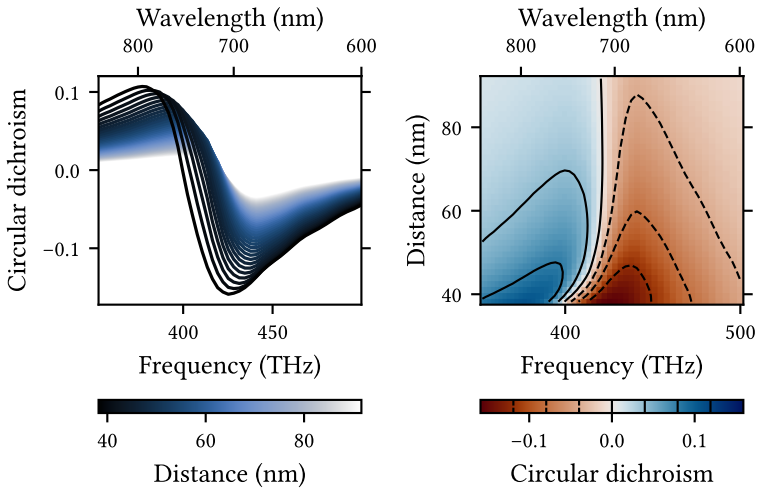


*Figure* 5.25: *Circular dichroism of helically arranged nanoparticles dependent on particle distance* · The left panel shows the circular dichroism of helical arrangements of nanoparticles for radial illumination at various distances between adjacent particles. It exhibits a bisignate feature centered around the main resonance of the arrangements' optical response. For small particle distances, the extent of the bisignate feature grows and it shifts toward lower frequencies. The right panel displays a heatmap of the same data with overlaid contours. The contours outline the strength of the circular dichroism, which grows toward small distances. The central contour, which marks the zero-crossing of the bisignate feature, illustrates the spectral trajectory of the feature across varying distances. Colormaps from Refs. [154, 155].

50 nm and upward. Even though both of these markers are hardly detectable for the majority of the simulated arrangements, coupling between the particles' resonances remains the primary cause for the chiral response of the nanoparticle arrangements, as we will show below.

The CD spectra of the helical arrangements evaluated from the helicity-

dependent absorption cross-sections for radial illumination are shown in Fig. 5.25. They exhibit a strong bisignate feature with a zero-crossing located near the central frequency of the resonance seen in the extinction cross-sections of Fig. 5.24. The total extent of the feature—the difference between its extremal values—increases for decreasing particle distances, hinting at the relevance of the coupling between the particles' resonances for the general presence of the feature. As can be seen in the right panel of Fig. 5.25, the zero-crossing follows a similar trajectory as the peak of the collective resonance line shape in Fig. 5.24.

The bisignate line shape of the spectra resembles that of signatures found in CD spectra of molecules near absorption bands. In that context, the emergence of such bisignate features is referred to as the Cotton effect [179–181] and is associated with the coupling of transition dipole moments arranged in a chiral fashion [182–184]. Much in the same way, we interpret the Cotton-like signature in the spectra of Fig. 5.25 as a consequence of the coupling of the dipolar resonances of the chirally arranged nanoparticles. Similar conclusions were drawn in Refs. [185, 186]. Simply put, the coupling between the resonances leads to spectrally separated absorption maxima for the two helicities, depending on the chirality of the spatial arrangement of the individual particles. As we scan the spectral region occupied by the resonances, the absorption for one helicity dominates, leading to a nonzero CD. As we approach the central frequency of the resonance feature, we pass the maximum absorption for one helicity and approach that of the other. At a certain point between the two maxima, the absorption is balanced, and the CD exhibits a zero-crossing. From that point onward, the other helicity is absorbed more strongly, which corresponds to a sign reversal of the CD. Taken together, this produces the characteristic Cotton-like signature of the CD spectrum. Evidently, dependencies on parameters such as the distance between the particles are more readily apparent from the zero-crossing of the CD than from the separation of the absorption maxima, whose direct visibility may be obscured [187].

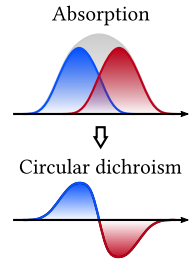


Sketch of spectrally separated absorption maxima for positive (blue) and negative (red) helicity, leading to a bisignate Cotton-like line shape of the corresponding circular dichroism spectrum. Spectral separation exaggerated for illustrative purposes.

The experimental determination of the coupling between the particles based on the observed extinction spectra depends on markers, which we have seen to be either masked by the broad linewidths of the resonant response or to be clearly pronounced only for small particle distances. Combined with the fact that the experimentally observed spectra arise as a collective

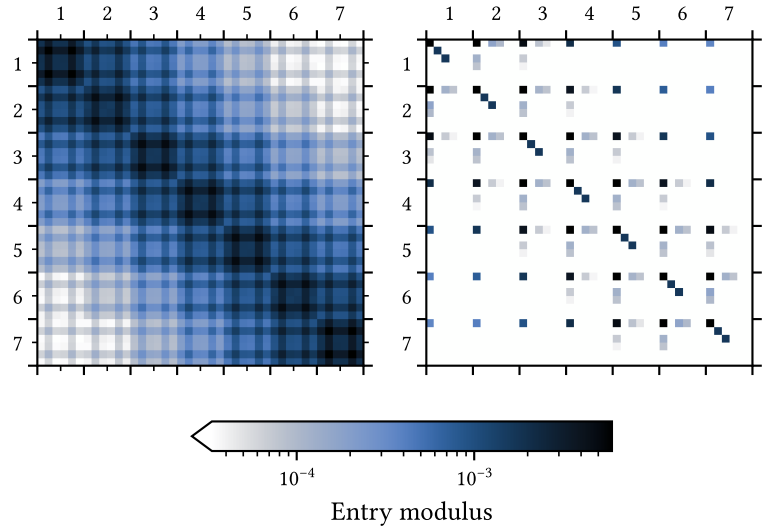


*Figure 5.26: Cluster transition matrix and particle-wise singular value decomposition* · The left panel shows the modulus of entries of the T-matrix for a helical arrangement of nanoparticles with a particle distance of 38.22 nm at a frequency of 439 THz. The T-matrix is expressed in a local basis comprising particle-specific expansion centers. Labels on the right and upper axis index the nanoparticles in order of appearance along the helical curve, beginning at the particle with the lowest $z$-coordinate. Only dipolar ($\ell = 1$) entries are shown. Every block for given particle indices, outlined by the major axis ticks, is separated into four submatrices of size $3 \times 3$ by the minor ticks, corresponding to the helicity-dependent submatrices. Entries in the off-diagonal blocks represent the coupling between different particles. The right panel shows the result of a particle-wise singular value decomposition of the T-matrix, applied to the full T-matrix truncated at $\ell_{\mathrm{max}} = 4$. Only the six largest entries for each block on the diagonal are shown to match the shape of the dipolar matrix on the left. Colormaps from Refs. [154, 155].

response of various arrangements with different configurations as well as isolated particles (cf. the transmission electron micrograph in Fig. 5.20),

observing a clear coupling signature in extinction spectra of the system under consideration becomes a challenge. In our numerical modeling, on the other hand, these aspects are directly accessible. Specifically, to evaluate the coupling between particles, we examine the T-matrix $\boldsymbol{T}_{\mathrm{loc}}$ of the cluster of helically arranged nanoparticles. The left panel of Fig. 5.26 shows the dipolar entries of the T-matrix at a frequency of 439 THz, close to the resonance peak observed in the spectra, for the smallest particle distance considered. We remind ourselves of the structure of a T-matrix described in a local basis (i.e., accounting for multiple VSW expansion centers centered on each particle) as determined by Eqs. (4.36) and (4.38). The blocks on the diagonal correspond to the T-matrices of the individual particles, modified by the multi-scattering between the particles. They represent each particle's individual optical response with the modification of the incident field due to the presence of other particles and their scattered fields taken into account. Entries in off-diagonal blocks, by contrast, determine the scattered field that originates from a particle $j$ as a result of a field incident onto a different particle $i$. These entries arise purely as a consequence of sequential scattering from different particles (specifically, any sequence of scattering events starting at particle $i$ and ending at particle $j$) and encode the coupling between the particles' individual responses. Therefore, we use the information contained in the off-diagonal entries to evaluate the coupling of the particles' resonances.

We extract the coupling between the resonances of the individual particles by employing a singular value decomposition (SVD) of their T-matrices. As can be seen in the left panel of Fig. 5.26, the T-matrices of the individual particles are densely populated. One reason for this is the spatial orientation of the particles in the helical arrangement; as a consequence, the longitudinal resonance no longer corresponds to the pure electric dipolar contribution for $m = 0$. An SVD of an $n \times n$ matrix $\boldsymbol{T}$ factorizes it as

$$\boldsymbol{T} = \boldsymbol{U}\boldsymbol{\Sigma}\boldsymbol{V}^{\mathrm{H}}, \tag{5.23}$$

where $\boldsymbol{U}$ and $\boldsymbol{V}$ are unitary matrices and $\boldsymbol{\Sigma} = \mathrm{diag}(\sigma_1, \dots, \sigma_n)$ is a diagonal matrix containing the real, non-negative singular values $\sigma_s$ of $\boldsymbol{T}$ in non-increasing order: $\sigma_1 \geq \cdots \geq \sigma_n \geq 0$. The columns of $\boldsymbol{U}$ and $\boldsymbol{V}$ form two sets of orthonormal bases and are called left- and right-singular vectors, respectively. Accordingly, the SVD represents the matrix as a sequence of a unitary change of basis ($\boldsymbol{V}^{\mathrm{H}}$), followed by a scaling ($\boldsymbol{\Sigma}$), and a final basis change, returning

to the VSW basis used for scattered fields ($\boldsymbol{U}$). The SVD is a generalization of the eigendecomposition and exists for any real or complex matrix [188]. In particular, for T-matrices, reciprocity establishes a relationship between the left- and right-singular vectors (cf. Subsection S3.3 of Ref. [S2]), and the modes defined by the SVD are recognized as the proper modes of an object's optical response, with the singular values $\sigma_s$ denoting their strength—or significance—in the interaction [189].

For our purposes, we perform a particle-wise SVD of the local T-matrix of the helical arrangement. For each on-diagonal block $i \in \{1, \dots, 7\}$ of the local T-matrix $\boldsymbol{T}_{\mathrm{loc}}$, which corresponds to the T-matrix of particle $i$ including its modification due to multi-scattering, we compute the SVD and obtain the unitary matrices $\boldsymbol{U}_i$ and $\boldsymbol{V}_i$. We then evaluate

$$\boldsymbol{\Sigma}_{\mathrm{loc}} \coloneqq \operatorname{diag}(\boldsymbol{U}_1, \dots, \boldsymbol{U}_7)^{\mathrm{H}} \boldsymbol{T}_{\mathrm{loc}} \operatorname{diag}(\boldsymbol{V}_1, \dots, \boldsymbol{V}_7), \tag{5.24}$$

multiplying the local T-matrix by block-diagonal matrices composed of the individual unitary matrices $\boldsymbol{U}_i$ and $\boldsymbol{V}_i$. The on-diagonal blocks of $\boldsymbol{\Sigma}_{\mathrm{loc}}$ are the diagonal matrices $\boldsymbol{\Sigma}_i$, which contain the individual singular values of each particle. Each particle's singular values correspond to the singular modes of the respective particle in the coupled cluster. The entries of $\boldsymbol{\Sigma}_{\mathrm{loc}}$ are shown in the right panel of Fig. 5.26. For each particle, only the first six rows and columns are shown, which contain the six largest singular values of each T-matrix in non-increasing order. The off-diagonal blocks, whose entries are ordered accordingly, now represent the coupling due to multi-scattering between the singular modes of each particle.

Since rotations, translations, and the change between helicity- and parity-based descriptions of the T-matrix are represented by unitary transformations, the SVD may be interpreted as a combination including these transformations. The singular modes are linear combinations of the VSWs that form the bases of the original T-matrix. As we perform the SVD per particle, its singular modes only combine VSWs centered on that particle. An analysis of the singular vectors of the unitary matrices $\boldsymbol{U}_i$ and $\boldsymbol{V}_i$ shows that the three singular modes of each particle with the largest singular values correspond to linear combinations of electric dipolar (i.e., $\ell = 1$) contributions to the T-matrix, with insignificant contributions from higher multipolar degrees. These modes recover the dipolar resonances of each particle, with the largest singular value corresponding to the longitudinal plasmon resonance as it

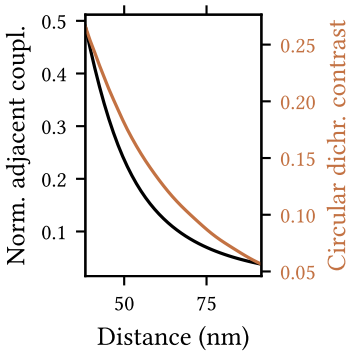


*Figure 5.27: Normalized adjacent coupling and circular dichroism contrast* · The average coupling between the leading singular modes of the nanoparticles in the helical arrangement, normalized to the average of their respective singular values, decreases as the distance between the particles increases (black; left axis). The circular dichroism contrast (i.e., the difference between the maximal and the minimal values reached) follows a similar trend, albeit with a different scaling (coral; right axis).

occurs in the coupled system. The next three smaller singular values shown for each matrix are predominantly mixtures of magnetic dipolar and electric quadrupolar contributions.[11] As is evident from the diagonal entries shown in Fig. 5.26, they contribute very little to the total response.

Inspecting the off-diagonal blocks of $\Sigma_{\text{loc}}$ in Fig. 5.26, we see that each block exhibits one significant entry in its upper-left corner. For each pair of particles $(i, j)$, this entry in the respective off-diagonal block represents the strength of the coupling between the longitudinal resonances of the two particles. To evaluate the overall coupling in the arrangement, we focus on the entries relating adjacent particles, which are found in the blocks on the first off-diagonal. As a measure of the coupling strength, we calculate the average of the absolute values of the entries relating the longitudinal resonances of adjacent particles and normalize it to the average of the largest singular value of each particle—the strength of its longitudinal resonance. Doing so for all considered helical arrangements with varying particle distances, at a fixed frequency of 439 THz near the longitudinal resonance of the arrangement, yields the black curve in Fig. 5.27. Notably, it increases as the distance decreases, indicating that the coupling between particles depends on the distance between them.

To relate the normalized coupling between adjacent particles to the emer-

11 Notably, the composition of the singular modes follows a hierarchy similar to that encountered in the microscopic origins of a medium's optical response—including chiral aspects—which we discussed in Section 2.2. In particular, electric quadrupolar and magnetic dipolar contributions must be considered jointly.

gence of the observed bisignate feature in the CD spectra, we evaluate the total contrast of the CD signals, which we define as the difference between the maximum and minimum values (i.e., the peak-to-peak range). The resulting curve, which shows the CD contrast as a function of distance, is also shown in Fig. 5.27. The CD contrast correlates strongly with the coupling strength and increases nonlinearly as the particle distance decreases. The trajectory of the two curves differ slightly, suggesting a different functional dependence of both quantities on the particle distance. We conclude that the coupling between achiral nanoparticles in chiral spatial arrangements is a crucial aspect for evaluating and tailoring the chiral optical response of plasmonic systems such as the one investigated here, and that the coupling between plasmonic resonances is the primary cause of the strong CD signal and its Cotton-like appearance observed in the experiments of Ref. [P3].

### 5.3.3 *A note on multipolar degree and truncation*

In our analysis above, we have mentioned that the dipolar resonances of the nanoparticles present the major contribution to the overall optical response of the coupled chiral arrangements. This is consistent with the single-particle spectra, which are dominated by the plasmonic resonances of dipolar character shown in Fig. 5.22, as well as with the leading singular mode of the particles in the coupled arrangement, which correspond to the same resonance, as discussed in connection with Fig. 5.26. The predominance of dipolar responses in plasmonic nanoparticles is frequently noted in the literature and is often the focus of theoretical considerations [167, 190–193].

In the following, we use the results discussed above to highlight a subtlety of the dipolar nature of the response of coupled plasmonic systems. In particular, we note that while the resulting response of a coupled arrangement of nanoparticles is well approximated by the dipolar response of the nanoparticles, the accurate modeling of the overall response and the coupling between the particles requires the inclusion of higher multipolar degrees in the analysis. To illustrate this aspect, we compare the spectroscopic quantities of interest of a helical arrangement of gold nanoparticles—namely, the extinction cross-section and the CD—obtained from three separate calculations. The helical arrangement is identical to the one presented in the previous subsection, with a particle distance of 38.22 nm. We consider the quantities

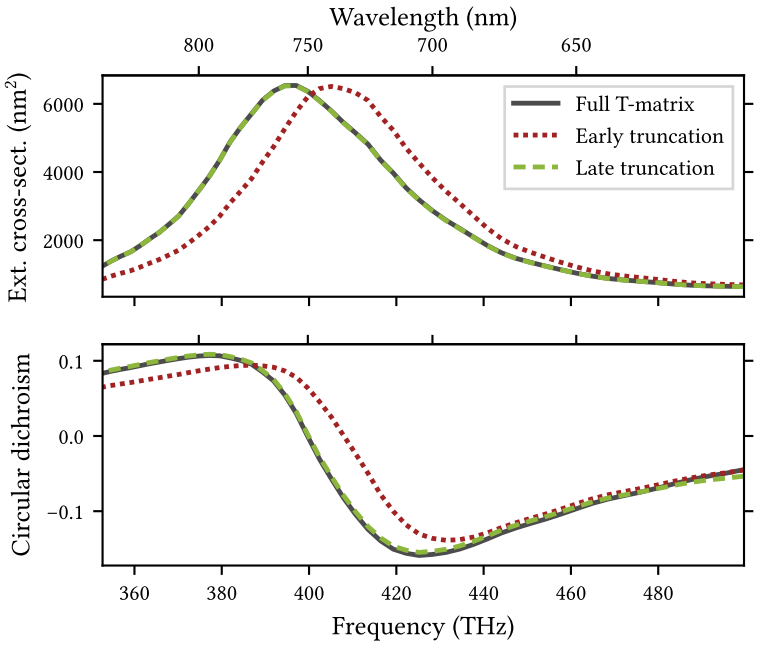


*Figure* 5.28: *Effect of transition matrix truncation on spectroscopic quantities* · The helicity-averaged radial extinction cross-section and the circular dichroism of a helical arrangement of gold nanoparticles at a particle distance of 38.22 nm are shown in the upper and the lower panel, respectively. Spectra derived from a local T-matrix, which was computed from a single-particle T-matrix truncated at $\ell_{\mathrm{max}} = 4$, are represented by solid gray curves. The same spectra, derived from a local T-matrix computed using a single-particle T-matrix truncated at $\ell_{\mathrm{max}} = 1$, are represented by dotted red curves (labeled "early truncation"). They differ significantly from the spectra calculated from the full T-matrix. If the full local T-matrix is truncated at $\ell_{\mathrm{max}} = 1$ *after* the interaction between particles has been calculated (labeled "late truncation"), the full spectra are still recovered with excellent approximation (dashed green).

evaluated from the arrangement's full local T-matrix—which was derived from the T-matrices of the individual particles, truncated at $\ell_{\mathrm{max}} = 4$—to be the most accurate description provided by our modeling. The resulting spectra, which are identical to those shown for the same particle distance in Figs. 5.24 and 5.25, are represented by the dark gray curves in Fig. 5.28. We compare it with the spectra from two different calculations: First, we further truncate the single-particle T-matrix by discarding all entries except the dipolar ones ($\ell = 1$), *before* we compute the local T-matrix of the particle cluster, thus only taking dipolar contributions into account for the multi-scattering (hereafter referred to as *early* truncation). Second, we compute the local T-matrix of the cluster from the full single-particle T-matrices up to $\ell_{\mathrm{max}} = 4$ and *then* truncate the resulting local T-matrix at $\ell = 1$, again discarding everything except dipolar entries. In this second case, the multi-scattering considers the full available information about the particles' isolated response, and only the final T-matrix of the cluster is truncated (we refer to this as *late* truncation).

The spectra evaluated from the respective T-matrices of both approaches, together with the original spectra obtained from the full T-matrix, are shown in Fig. 5.28. The dotted red and dashed green curves represent the results of early and late truncation, respectively. As is apparent from a comparison of the curves, early truncation, in which only dipolar terms are considered throughout the analysis, introduces considerable errors. The curves for late truncation agree notably better with the most accurate spectra. Hence, the assumption that the response of each particle in the coupled arrangement is predominantly dipolar is evidently a valid approximation. However, for the computation of the particle response in the coupled arrangement, the consideration of higher-degree contributions is far more important.[12] The spectra obtained with early truncation not only underestimate the strength of the chiral optical response of the nanoparticle composite, but also predict an inaccurate spectral position of the resonance, as indicated in the upper panel of Fig. 5.28. Overall, limiting the analysis to dipolar responses of individual particles and their interaction leads to an underestimation of the coupling between the particles. The effect becomes more pronounced the closer the particles are to each other. From a physical perspective, a smaller distance between the particles confines the strong near-fields resulting from

12 A similar finding was reported in Ref. [194] in the context of the homogenization of materials based on the transition matrix formalism. In essence, effective material parameters that describe a medium constituted by small scatterers can be derived from the dipolar part of a T-matrix, which considers the interaction between the scatterers. However, to obtain the dipolar part of the T-matrix accurately, higher-degree contributions must be taken into account.

the particles' resonant response to smaller volumes, which in turn requires higher-degree VSWs for an accurate representation.

In summary, we emphasize that while the overall response of the investigated chiral plasmonic arrangement can be well represented as collective dipolar responses of the individual particles, the full picture requires a differentiated view, as higher-degree contributions contribute disproportionately to the coupling between the modes. We presume that these results are not specific to the system under consideration and also apply to other composite plasmonic systems. We conclude this section with a brief overview of the main results presented so far.

### 5.3.4 *Summary and outlook*

In the preceding subsections, we modeled the chiral optical response of chiral arrangements of plasmonic nanoparticles using the formalisms introduced in the previous chapters. Our results provide fundamental insights into the optical properties of the system under consideration and highlight the potential of chirality as an emergent feature in a mesoscopic structure. Below, we summarize the key findings, highlight possible continuations, and place the study within the context of the investigation of chiral aspects in this thesis.

We investigated the optical response of individual nanoparticles, taking their microscopic size into account. Their spectra are dominated by two plasmonic resonances, which are spectrally separated due to the geometric anisotropy of the prolate spheroidal nanoparticles. Afterward, we examined the optical response of helical arrangements of these nanoparticles, focusing in particular on CD. Based on the T-matrix description in local basis, we evaluated the coupling between the resonances of the particles, employing an SVD to determine the contributions of the proper resonances in the coupled arrangement. We find that the singular modes follow a hierarchy similar to that discussed in the microscopic treatment of media in electrodynamics in Section 2.2. The strength of the CD response scales inversely to the distance between adjacent particles, as does the coupling between the particles. Finally, we noted the significance of higher-degree contributions to the T-matrix for accurate modeling, which contrasts with the initial observation that the particles' response is predominantly dipolar.

This apparent contradiction is resolved by the fact that higher-degree contributions disproportionately affect the calculation of the multi-scattering and thus the coupling between particles, while the resulting response ultimately manifests itself largely in dipolar contributions.

Our modeling shows good qualitative agreement with the spectra observed in spectroscopic experiments on organic thin films containing chirally assembled plasmonic nanoparticles. Importantly, the coupling between particles is highlighted as the primary cause of the large CD response found in chiral plasmonic assemblies, as well as of the characteristic bisignate line shape in the spectra, akin to the Cotton effect observed in chiral molecules. It arises as a consequence of the spectrally separated absorption maxima for light of opposite helicity, resulting from the coupling of resonances. We demonstrated that while typical markers of resonance coupling in the measured spectroscopic quantities are masked or easily missed, the characteristic and strong response is nevertheless to be understood as a consequence of coupling. This finding is consistent with earlier models that predict the CD of plasmonic systems. In this context, the significance of higher-degree contributions is of particular interest, since the dipolar part, although predominant in the response of individual particles, is generally insufficient to accurately predict the optical response. Accordingly, our modeling approach based on the transition matrix formalism appears well-suited for the investigation of systems such as the one presented in this section.

With a view to possible continuation of the work presented here, we examine the shape of CD spectra in closer detail. It appears that the asymmetry of the bisignate line shape, which can be appreciated in Fig. 5.25, depends on the dimensions of the chiral system under study [195]. At the time of writing, an in-depth investigation of this aspect is in progress. A particular question concerns whether this relationship can be utilized as a gauge for determining the dimensions of the assembly. Another topic of interest is the study of binary assemblies in which different nanoparticles are combined to tailor the chiral optical response. Experimental results were already included in Ref. [P3]. Measurements show the appearance of more detailed CD spectra, which offer further degrees of freedom for tailoring the system response—a finding also confirmed by preliminary results derived from our modeling approach applied to these systems. A joint research effort guided by experimental possibilities and leveraging the predictive power

of the modeling approach holds promise for the tailoring of chiral optical responses and the continuation of this work.

The central conclusion of the preceding study in the context of this dissertation is that chiral optical properties can arise solely from mesoscopic arrangement, even when no intrinsic chirality is present at smaller length scales. This leads to a key question for the remainder of this the thesis, namely how chiral properties of individual constituents translate into the optical response of the composite system. In the next section, we examine metallic particles with an intrinsically chiral shape and optimize their geometry for a maximized chiral optical response. In Chapter 6, these optimized scatterers are then incorporated into a chiral optical cavity, where the collective behavior of the microscopic constituents gives rise to chirality at the macroscopic level. Taken together, these results demonstrate how chiral optical functionality can be generated and propagated across length scales through the design of the overall arrangement.

## 5.4 *Electromagnetic Chirality*

So far, in this chapter, we have examined the material and geometric influences on the chiral optical response of an object and investigated the strong chiral response of clusters of small metallic particles, arising purely from their chiral spatial arrangement. The final section is devoted to optimizing a single scatterer to achieve the most chiral response possible within the limits of the system under consideration. To this end, we introduce the *electromagnetic chirality*, which holistically quantifies an object's differential response to light of opposite helicity. The electromagnetic chirality serves as the objective function for our optimization. The resulting optimized scatterer provides the building block that we use in Chapter 6 to construct a chiral optical cavity. Main results regarding the chiral scatterer were originally published in Ref. [P2].

### 5.4.1 *Definition of electromagnetic chirality*

We discussed the geometric concept of chirality in Section 5.1. A related question concerns whether the chirality of a particular geometry or object can be quantified. This question proves to be surprisingly difficult and cannot

be answered in a universally applicable way [196]. Proposed measures of chirality face fundamental difficulties: For instance, when attempting to quantify the chirality of irregular tetrahedra, one can construct equivalent measures that identify any given chiral tetrahedron as the most chiral one, regardless of how close it is to an achiral configuration [197]. Furthermore, if one attempts to construct bisignate measures of chirality that distinguish enantiomers of molecules or mirror images of the same object by values with opposite signs—which can be interpreted as a notion of left- and right-handedness—another challenge arises in the form of chiral connectedness: Chiral three-dimensional shapes can be continuously deformed into their respective mirror images without having to pass through a geometrically achiral configuration. Any continuous real-valued function that assigns opposite values to the two mirror images must necessarily cross zero during the continuous deformation and thus assigns the value 0 to a chiral object, thereby incorrectly labeling it as achiral.

In this work, we focus on the chiral interaction between light and matter; therefore, we do not attempt to quantify an object's chirality based on geometrical considerations, but rather examine the chirality of its optical response. Although spectroscopic quantities such as the previously discussed CD and OR provide information about an object's chiral response, they capture only certain aspects and do not consider the chiral response holistically. In Ref. [198], a different measure of an object's chiral optical response was proposed, namely the *electromagnetic chirality*. It quantifies the difference in an object's interaction with light of positive and negative helicity and is formulated in terms of the object's T-matrix, taking into account the object's complete linear optical response. Let $\boldsymbol{\sigma}_{\lambda'\lambda}$ be the column vector containing the singular values of the submatrix $\boldsymbol{T}_{\lambda'\lambda}$ of an object's T-matrix (cf. Eq. (4.22)) in non-increasing order. The electromagnetic chirality, or em-chirality in short, is then defined as[13]

$$\chi_{\mathrm{em}} \coloneqq \sqrt{\|\boldsymbol{\sigma}_{++} - \boldsymbol{\sigma}_{--}\|_2^2 + \|\boldsymbol{\sigma}_{-+} - \boldsymbol{\sigma}_{+-}\|_2^2}\,. \tag{5.25}$$

By comparing the singular values of the T-matrix for positive and negative incident helicity, in both the co-polarized and cross-polarized parts, the em-chirality is sensitive to any differences in an object's chiral optical response

13 The definition used here differs by a factor of two from the definition introduced in Ref. [198]. This difference is inconsequential for the arguments presented below.

as a function of incident helicity. The em-chirality is non-negative and upper-bounded by the square root of the object's total interaction cross-section,

$$0 \leq \chi_{\mathrm{em}} \leq \|\boldsymbol{T}\|_{\mathrm{HS}}. \tag{5.26}$$

For achiral objects, the em-chirality assumes the value 0. The upper bound may be intuitively understood as follows: The imbalance of an objects interaction with light of positive and negative helicity can at most encompass the entirety of its interaction. As discussed in Ref. [198], if a reciprocal object reaches the maximal value $\chi_{\mathrm{em}} = \|\boldsymbol{T}\|_{\mathrm{HS}}$, it responds exclusively to light of one helicity, while being completely transparent to the opposite helicity.

In Refs. [199, 200], a different, equivalent expression for the em-chirality is given, which allows the quantity to be related back to a geometric interpretation. To this end, it was shown that [cf. 199, Eq. (59)]

$$\|\boldsymbol{\sigma}_{++} - \boldsymbol{\sigma}_{--}\|_2 = \min_{\boldsymbol{U},\boldsymbol{V}} \left\|\boldsymbol{T}_{++} - \boldsymbol{U}\boldsymbol{T}_{--}\boldsymbol{V}^{\mathrm{H}}\right\|_{\mathrm{HS}}, \tag{5.27}$$

and the analogue for the second term on the right-hand side of Eq. (5.25), where the minimization runs over all pairs of unitary matrices $\boldsymbol{U}$ and $\boldsymbol{V}$. Since rotations and translations acting on the T-matrix are represented by unitary matrices, they, as well as their combinations, are included in the minimization. Therefore, the em-chirality computes the minimal difference in an object's interaction cross-section with respect to the incident helicity, which in turn represents the intrinsic chirality of its optical response. In the next subsection, we use the em-chirality normalized to $\|\boldsymbol{T}\|_{\mathrm{HS}}$ as an objective function to optimize the chiral optical response of a scatterer.

### 5.4.2 *Optimizing electromagnetically chiral scatterers*

Below, we optimize the geometry of a scatterer to achieve a strongly chiral optical response. We have previously discussed the potential of small metallic structures to exhibit a strong chiral optical response. Accordingly, we select a small metallic scatterer for our optimization. As a prime example of the concept of chirality, we choose a scatterer in the form of a helix. The potential of small metallic helices for strong chiral responses has already been demonstrated numerically [201], and their fabrication and experimental characterization is the subject of numerous recent studies [202–206].

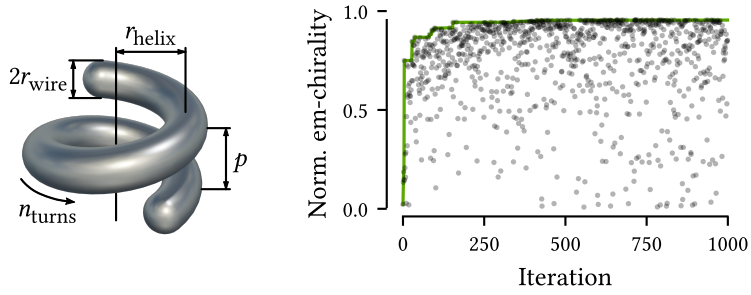


*Figure* 5.29: *Optimization of an electromagnetically chiral helix* · Left panel: representation of a silver helix with the four parameters that specify its geometry. Right panel: normalized electromagnetic chirality of silver helices considered in each iteration of the optimization. The green curve represents the cumulative maximum of the electromagnetic chirality throughout the optimization. The optimal configuration is found for the parameters $r_{\text{helix}} \approx 183.0\,\text{nm}$, $r_{\text{wire}} \approx 53.3\,\text{nm}$, $p \approx 168.6\,\text{nm}$, and $n_{\text{turns}} \approx 1.407$, achieving a normalized electromagnetic chirality of 0.955 at the target frequency. Helix reproduced from Ref. [P2], .

For our optimization of em-chiral helices, we follow a procedure similar to that described in Refs. [201, 207]. To this end, we consider a silver helix embedded in a homogeneous embedding with relative permittivity $\varepsilon_{\text{emb}} = 1.8912$. The permittivity of silver is interpolated from the measurement data in [208, 209] as provided by [177]. The geometry of the helix is specified by four parameter: the radius $r_{\text{helix}}$, the pitch $p$, and the total number of turns $n_{\text{turns}}$ of the helical windings, as well as the radius of the silver wire forming the helix, $r_{\text{wire}}$. The silver wire terminates in hemispherical end caps. A schematic example can be seen on the left side of Fig. 5.29.

The objective of our optimization is to find the parameter configuration that maximizes the em-chirality of the helix, specifically at a target frequency of 44.21 THz. The target frequency and the relative permittivity of the embedding are chosen with regard to the integration of the helices into a chiral cavity in Chapter 6 and are addressed there. Following Ref. [201],

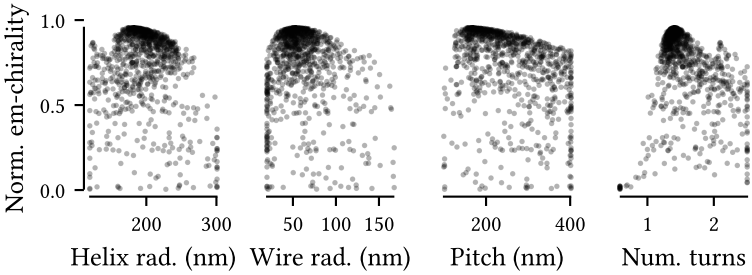


*Figure* 5.30: *Helix parameters sampled during optimization* · The objective value (i.e., the normalized electromagnetic chirality) and the geometric parameters of each sample of the optimization are plotted, separately for the four parameters that specify the geometry of the helix. The clusters of data points visible at the top of each plot provide an estimate of the sensitivity of the electromagnetic chirality to variations in the geometric parameters. Adapted from Ref. [P2], .

we use Bayesian optimization with Gaussian processes as implemented in the "Analysis and Optimization Toolkit" of JCMsuite [114], which has been shown to be a favorable optimization approach for tasks such as the one considered here [210]. At each iteration of the optimization, a parameter tuple that specifies the helix geometry is suggested. Using FEM simulations, the T-matrix of the corresponding helix is computed. From this T-matrix, we evaluate the em-chirality, as defined in Eq. (5.25), using the software treams [100]. The em-chirality is then fed back into the optimization and influences the next suggestion for the geometric parameters. We terminate the optimization after 1 000 iterations; the maximal em-chirality found during the optimization is shown in Fig. 5.29. High values for the normalized em-chirality are reached early on, with occasional minor improvements occurring after the first few hundred iterations. The most em-chiral helix resulting from the optimization exhibits $\chi_{\mathrm{em}} \approx 0.955$ at the target frequency, that is, close to 96 % of the theoretical maximum. The corresponding parameters are $r_{\mathrm{helix}} \approx 183.0\,\mathrm{nm}$, $r_{\mathrm{wire}} \approx 53.3\,\mathrm{nm}$, $p \approx 168.6\,\mathrm{nm}$, and $n_{\mathrm{turns}} \approx 1.407$.

The representation of a helix depicted on the left in Fig. 5.29 matches these proportions.

Figure 5.30 shows the normalized em-chirality of all samples considered in the optimization, plotted against each of the four geometric parameters. While the samples generally differ simultaneously across all parameters, the dome-like shape resulting from the data points clustered at higher values provides an estimate of the sensitivity of the em-chirality to variations in the individual parameters. Since these regions are rather broad, we conclude that the em-chirality of the optimized silver helix is quite stable against parameter variations—an important observation in view of a potential fabrication. For the helix radius, wire radius, and pitch, a single maximum is observed in the data; for the number of turns, a secondary, smaller maximum appears at values slightly greater than 2. However, it corresponds to smaller values of the em-chirality and appears to be less stable against variations in the parameter, making it less desirable for our purposes.

The optimization targets a single frequency. To assess the response of the helix in a broader spectral region, we evaluate the em-chirality for frequencies around the target value. To this end, we compute T-matrices for the optimized silver-helix in a frequency range surrounding the target frequency, up to sufficiently high $\ell_{\mathrm{max}} = 4$. We evaluate the em-chirality at each frequency, as well as the helicity- and direction-averaged cross-sections, which quantify the optical response of the helix. The data are presented in Fig. 5.31. The green curve shows that the em-chirality of the helix is a relatively broad spectral feature. Although its value decreases when the frequency deviates from the target, this occurs at a moderate pace; for example, values of $\chi_{\mathrm{em}} \geq 0.8$ are achieved in a spectral window spanning 5.25 THz. This property is beneficial for the use of the optimized helix in the chiral cavity discussed in Chapter 6, as it provides a considerable spectral window in which the strongly chiral response of the helices can be utilized. The cross-sections reveal that the helix exhibits an optical resonance centered on the target optimization frequency, and hence the high em-chirality is a resonant feature of the helix. The helix is strongly absorptive, with the absorption cross-section exceeding the scattering cross-section by a factor of approximately 3 across most of the considered frequency range. Overall, the response of the helix is largely dipolar in character, as can be seen from an individual examination of the multipolar contributions to its extinction

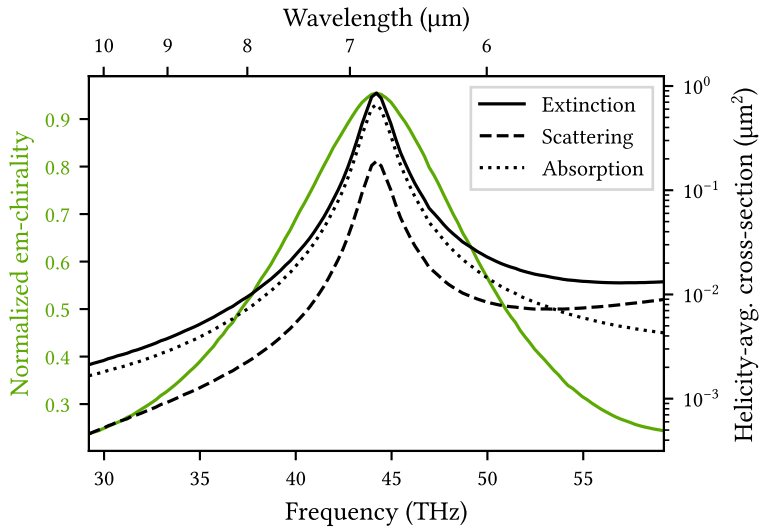


*Figure* 5.31: *Electromagnetic chirality and cross-sections of the optimized helix* · The normalized electromagnetic chirality of the optimized helix is represented by the green curve (left axis). The helicity- and direction-averaged cross-sections (black; right axis) show that the high electromagnetic chirality is related to a resonance of the helix. Across most of the shown spectral range, the absorption cross-section considerably exceeds the scattering cross-section.

cross-section in Eq. (4.33b) (cf. our discussion in the previous section). Across the frequency range under consideration, dipolar contributions (i.e., $\ell = 1$) account for $> 99.7\,\%$ of the total extinction cross-section, which is to be expected given the small dimensions of the helix relative to the illumination wavelength. Upon closer examination, the resonance at the target frequency manifests itself predominantly in the dipolar contribution for positive helicity and multipolar order $m = 0$, which corresponds to a dipolar orientation parallel to the $z$-axis. At the target frequency, this contribution alone accounts for $98.5\,\%$ of the total extinction cross-section. These observations are

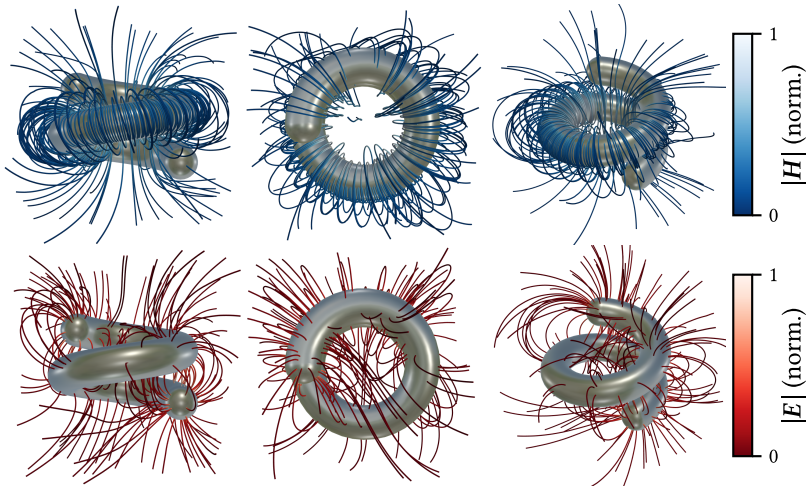


*Figure* 5.32: *Field lines of the electromagnetically chiral helix at resonance* · Near field data obtained from a resonant state computation of the electromagnetically chiral helix using the finite element method. Upper row: side, top, and diagonal views of the magnetic field lines, showing that the helix acts as an electrical coil. Lower row: side, top, and diagonal views of the electric field lines, evaluated one quarter of an oscillation cycle later, illustrating the capacitive effect of adjacent windings. Near-field data computed using code kindly provided by Jan David Fischbach.

consistent with an analysis of the helix's resonances using a pole expansion, a method discussed in [S2].

The response of the helix can be intuitively understood as that of a coupled system consisting of an electric dipole antenna and an electrical coil with a winding number of $n_{\text{turns}}$. Charges moving from one tip to the other give rise to an electric dipolar response. As they move from one tip to the other, they follow the helical windings of the coil, thereby generating a magnetic dipolar response. The phase relation between the electric and magnetic dipolar response is determined by the handedness of the helix and is optimally near $\pm\pi/2$. In that case, the response of the helix approaches that

of a helical dipole, an idealized source consisting of an electric and a magnetic dipole moment, $\boldsymbol{d}$ and $\boldsymbol{m}$, respectively, located at the same point in space and satisfying the relation $\boldsymbol{m} = \mp \mathrm{i} Z_0 Z \boldsymbol{d}$ [52, Chapter 6]. A helical dipole radiates waves of pure helicity.[14] Accordingly, the optimization yields the geometric parameters for which the helix's response most closely matches this idealized configuration. Figure 5.32 shows the magnetic and electric field lines associated with the helix's resonance, which are determined from a resonant state computation using FEM simulations. The magnetic field lines shown in the upper row demonstrate that the helix acts as an electrical coil, giving rise to a magnetic dipolar response. The electric field lines, evaluated one quarter of an oscillation cycle later and shown in the lower row, illustrate the capacitive effect of the helix, and field lines that begin and end at the hemispherical end caps highlight its electric dipolar response.

14 In Ref. [52], combinations of electric and magnetic dipoles that satisfy the given relation are referred to as the canonical sources of radiation in chiral media.

The resulting contrast in the helix's response to light with opposite helicity is demonstrated in Fig. 5.33. Blue and red curves represent the directionally averaged extinction, scattering, and absorption cross-sections of the helix for positive and negative helicity illumination, respectively. Cross-sections for both helicity eigenvalues exhibit the resonance at the target frequency, showing that the helix's resonance is not perfectly matched to only one helicity. However, the values of the cross-sections for illumination with positive and negative helicity differ substantially, as is to be expected for the highly em-chiral helix: For a perfectly em-chiral scatterer, transparency to one helicity would mean that the cross-sections for that helicity would vanish entirely. For our scatterer at the target frequency, the contrast between the cross-sections for positive and negative helicity exceeds two orders of magnitude.

Due to the strong helicity-dependent contrast in the response of the helix, and since it is strongly absorbing, it exhibits strong CD. We evaluate the CD in Fig. 5.34, which allows us to represent the helix's chiral optical response by an experimentally accessible spectroscopic quantity. As expected, the CD of the optimized helix is strongly pronounced and reaches nearly perfect values of up to 0.988 close to the target frequency. As already suggested in [201], the strong helicity-dependent absorption contrast makes the optimized helices suitable for application as direction-independent circular polarization filters in the form of a solid suspension of randomly oriented helices.

Since the strong chiral response of the helix is largely related to a dipolar

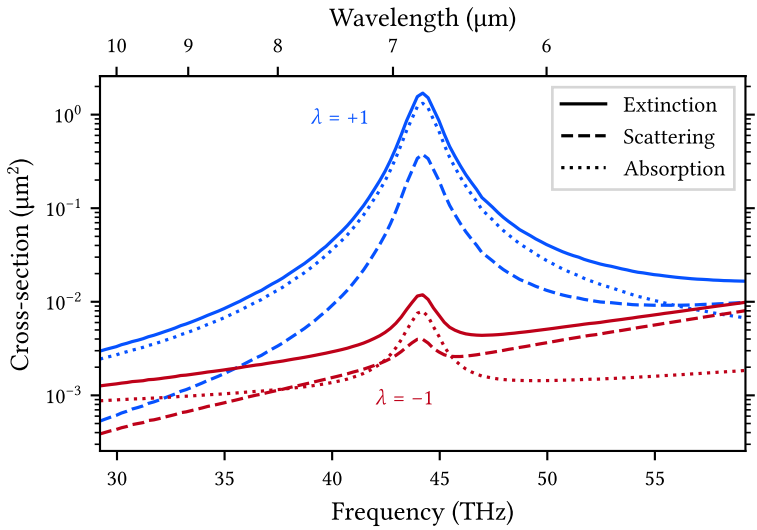


*Figure* 5.33: *Helicity-dependent cross-sections of the optimized helix* · The directionally averaged cross-sections for positive (blue curves) and negative (red) helicity demonstrate how strongly the response of the optimized helix depends on the helicity of the illumination. The contrast between the cross-sections for positive and negative helicity reaches two orders of magnitude in the vicinity of the target frequency of the optimization.

response oriented along the $z$-axis, the response exhibits a corresponding directionality. This directionality is illustrated in Fig. 5.35, where the directional extinction cross-section is shown for positive and negative helicity illumination. The upper and lower panel of Fig. 5.35 show the extinction cross-section for illumination directions $\hat{\boldsymbol{k}}$ sampled over the entire unit sphere in a Mollweide projection. The data on the equator represent illumination of the helix along the radial direction, while the data for axial illumination are shown at the poles. The strong contrast in the cross-sections between positive and negative helicity illumination is highlighted by the markedly different shades of the data in the two panels. In particular, for

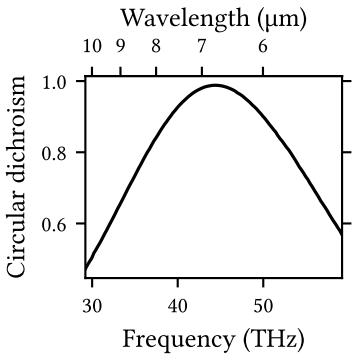


*Figure* 5.34: *Circular dichroism of the optimized helix* · Circular dichroism of the optimized electromagnetically chiral helix evaluated in the spectral region surrounding the target frequency. At the target frequency of the optimization, the circular dichroism is approximately equal to 0.988, thus approaching the maximum possible value.

data corresponding to positive helicity, it is evident that the response is stronger under radial illumination than under axial illumination. This is consistent with the idea that the oscillations of charges in the helix—which, as previously explained, cause it to act as an antenna and coil—are excited by an electric field oriented parallel to the axis of the helix. Such a field orientation occurs when the illuminating circularly polarized plane wave propagates in radial direction. When illuminated along axial direction, the electric field oscillates in the $xy$-plane, thereby diminishing the resulting response of the helix. This directional dependence of the helix's response is considered in Chapter 6 for its orientation in the chiral optical cavity.

As for directions of illumination within the $xy$-plane (i.e., radial illumination), the helix's response varies only mildly, as can be seen primarily in the differently shaded areas in the plot for negative helicity in Fig. 5.35. To mitigate the effect of such a dependence even further, structures with (discrete) rotational symmetry about the $z$-axis can be considered. An example in the form of a three-stranded silver helix and its corresponding spectra are shown in Fig. 5.36. It exhibits an overall optical response similar to that of the single-stranded helix considered so far, although a secondary resonance occurs in the spectral range at higher frequencies. At the target frequency of 44.21 THz, the three-stranded helix exhibits an em-chirality normalized to its total interaction cross-section of 0.949, thus performing comparably well to the single-stranded helix. For the results presented in

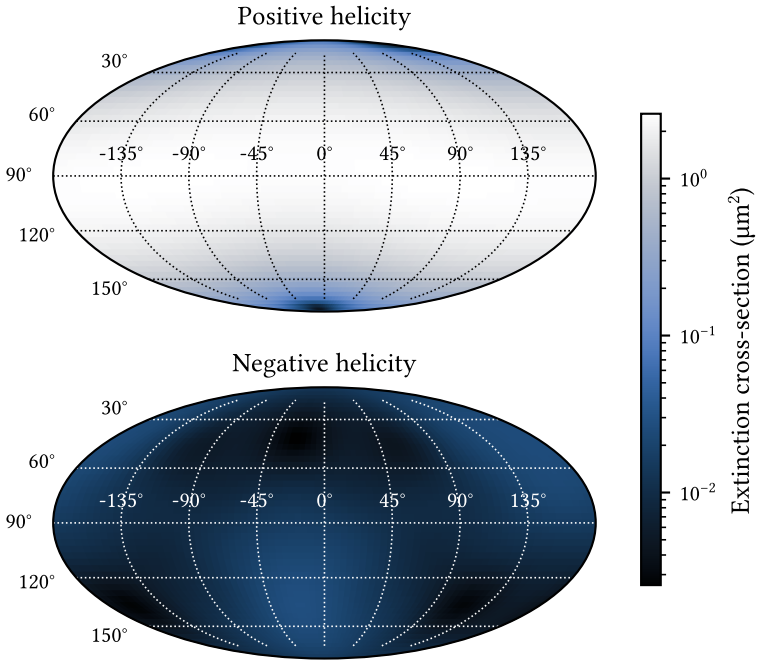


*Figure* 5.35: *Directional helicity-dependent extinction cross-section of the optimized helix* · Extinction cross-section for positive (upper panel) and negative (lower panel) helicity depending on the illumination direction. The data is shown in a Mollweide projection, with lines of equal latitude corresponding to the azimuthal angle and lines of equal longitude corresponding to the polar angle of the illumination direction $\hat{\boldsymbol{k}}$ in a spherical coordinate system. Data on the equator corresponds to radial illumination of the helix, and data at the poles corresponds to axial illumination of the helix. For positive helicity, the helix responds more strongly to radial illumination, as seen in the upper panel. Overall, the extinction cross-section for positive helicity exceeds that for negative helicity by two orders of magnitude. Colormap from Refs. [154, 155].

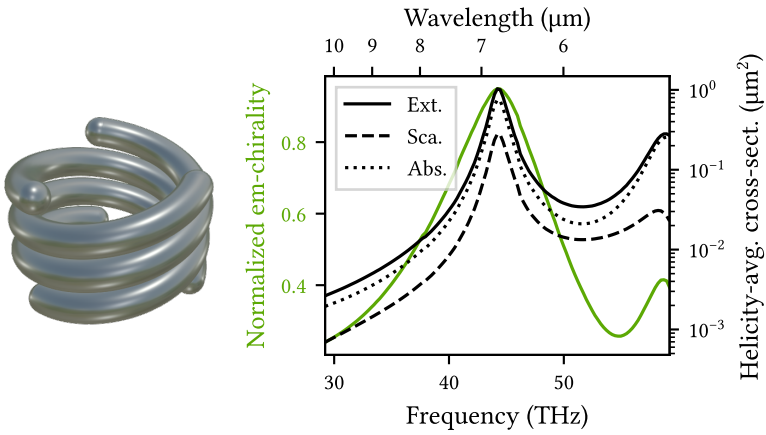


*Figure* 5.36: *Electromagnetic chirality and cross-sections of a three-stranded helix* · The green curve (left axis) shows the normalized electromagnetic chirality of a three-stranded silver helix. Black curves (right axis) show the helicity- and direction-averaged cross-sections. The scatterer consists of three intertwined helices, which are specified by the parameters $r_{\text{helix}} \approx 194.8\,\text{nm}$, $r_{\text{wire}} \approx 35.70\,\text{nm}$, $p \approx 257.1\,\text{nm}$, and $n_{\text{turns}} \approx 0.989$, which were determined by optimization. At the target frequency of 44.21 THz, the three-stranded helix exhibits a normalized electromagnetic chirality of 0.949.

Chapter 6, the mild directional dependence for radial illumination of the single-stranded helix does not appear to be detrimental, which is why we use the single-stranded version in that context. In particular, the larger wire radius of the single-stranded helix should make the proposed structure more feasible for potential fabrication.

In summary, we have presented the results of a shape optimization of small silver helices, with the objective of maximizing their chiral optical response, quantified by the em-chirality at a given target frequency. We have found that the helix resulting from the optimization exhibits a strongly chiral response, facilitated by a resonance that combines both an electric and a magnetic dipolar response into a nearly perfect helical response.

The resulting contrast in the helicity-dependent cross-sections exceeds two orders of magnitude. With regard to the potential fabrication of the scatterers discussed here, we remark that helices of comparable sizes as well as lattices made from them have been fabricated and characterized in the literature [201–206]. With regard to potential applications, we note that the optimized helices discussed above, adapted to a different embedding, were also used in [P1, P4] for considerations regarding chiral thermal emissions. In the context of the present work, the optimized helix serves as a highly chiral building block for the design of a chiral optical cavity in the next chapter.

*Chapter summary* · In this chapter, we have investigated chiral interactions between light and localized objects. We have explored fundamental aspects of the origin of chiral optical responses and demonstrated how the shape of a scatterer can be optimized to maximize its chiral optical response. Below, we briefly summarize the most important findings.

Following an initial introduction to the geometric concept of chirality and the spectroscopic quantities used to determine it, we focused on the CD of scatterers. In particular, we investigated how the chirality of a scatterer's geometric shape and the chirality of its medium combine to form its CD. We found that the total spectrum can be expressed as the sum of two contributions, attributed to the geometry of the scatterer and its medium, respectively. This insight led us to an approximation scheme that enables the efficient computation of a scatterer's linear optical response, represented by its T-matrix, as well as of derived spectroscopic quantities for variations of the dispersive chirality parameter of the scatterer's medium. The scheme lends itself well to the analysis of scatterers made from chiral media, where different enantiomeric ratios of the molecular constituents are to be considered, or for chiral inclusions within the same host material. The analysis of the derivatives of an object's T-matrix with respect to the chirality parameter further follows a pattern that distinguishes between co-polarized and cross-polarized entries, which appears to be a promising starting point for continuing the work discussed in that section.

In Section 5.3, we studied the optical response of chiral spatial arrangements of small, achiral metallic particles. Our modeling of these systems complements experimental studies on such systems and provides fundamental insights into the spectral features observed in the experiments. In

particular, we emphasize the significance of the coupling between the plasmonic resonances of the scatterers for the emergence of a strong CD and its characteristic bisignate line shape. Accordingly, the chiral response is entirely an emergent feature of the assembly of scatterers, arising from their chiral spatial arrangement. With regard to the numerical modeling of systems such as the one considered in Section 5.3, we have highlighted the importance of higher multipolar contributions to the object's optical response, in contrast to the observation that the individual particles can be well described within dipolar approximation. While the response of the particles in the coupled arrangement, in turn, manifests itself largely in their dipolar contributions, the accurate computation of these contributions, accounting for the multi-scattering between the particles, depends disproportionately on the inclusion of higher-degree contributions. Prospects for continuing the work presented in Section 5.3 are outlined in the corresponding outlook and include a thorough investigation of the length-dependent asymmetry of the bisignate CD signature.

Finally, we discussed the optimization of a silver helix with the objective of maximizing its chiral optical response. To this end, we introduced the electromagnetic chirality as a holistic measure of an object's linear chiral optical response. The optimization yields scatterers with an electromagnetic chirality that is close to its theoretical upper bound. We discussed the optical properties of the helix and explained the origin of the strong chiral response in terms of a resonance that largely corresponds to a helical dipole radiating nearly pure helicity.

In the final thematic chapter of this dissertation, we discuss a chiral optical cavity that utilizes the optimized electromagnetically chiral silver helices described earlier. The macroscopic electromagnetic environment inside the cavity, which strongly favors one helicity of light, is enabled by the chiral properties of the optimized microscopic scatterers. This demonstrates the propagation of chiral properties across length scales.

# 6 *Chiral Optical Cavities*

In the previous chapter, we discussed various aspects of chiral interactions between light and localized objects. It led us to the shape optimization of a silver helix to maximize its chiral optical response. Below, we utilize the strongly chiral response of these helices to design a chiral optical cavity that supports modes of nearly pure helicity, with one helicity being strongly favored.

In Section 5.1, we mentioned the vital importance of molecular chirality, particularly in a pharmaceutical and pharmacological context. It teaches us about the necessity of sensing and selecting the enantiomeric composition of a given chiral compound. In the study of chiral light–matter interactions, the development of solutions to these tasks by optical means is an active area of research, for instance with the goal of separating the two enantiomers in a mixture of chiral molecules [211–214] or larger chiral objects [215, 216]. Chiral optical cavities can provide the chiral electromagnetic environment—resonant modes with a preference for a given helicity—on which such applications depend [37, 217]. In particular, given the inherently weak chiral optical response of molecules [22, 23], the resonant enhancement of the chiral light with which these molecules can interact appears to be an indispensable advantage of such devices. Moreover, experimentally observed changes in chemical reactivity within optical cavities [218–220] suggest the use of chiral optical cavities to induce a bias toward one of the enantiomers already during their chemical synthesis [39]. While establishing a theoretical framework to explain and predict such chemical reactivities remains challenging [221, 222], we expect such effects to depend on how pronounced the chirality of the electromagnetic environment provided by the cavity is. Other applications for chiral optical cavities involve the manipulation of the helicity of radiation, for instance in circularly polarized lasers [223, 224] or for the enhancement of chiral luminescent emissions [225]. Again, their performance appears to be intrinsically related to the degree of chirality of the optical cavity.

In the following, we consider a cavity formed by two planar mirrors into which the optimized electromagnetically chiral silver helices discussed in the previous chapter are integrated. Our aim is to utilize the strong chiral

response of the helices to achieve a similarly pronounced chirality in the electromagnetic environment inside the cavity by imprinting the helicity-selective interaction of the scatterers onto the large-scale properties of the cavity. Throughout our analysis, we make extensive use of the scattering matrix formalism that we introduced in Section 4.2. First, we examine the planar mirrors constructed using a diffractive array of electromagnetically chiral scatterers. We then proceed with the description of the chiral cavity formed by two such mirrors and analyze the eigenmodes supported in its interior. The main results discussed in this chapter were originally published in [P2], and our discussion in this chapter largely follows the one presented therein.

## 6.1 *Mirrors Made from Electromagnetically Chiral Scatterers*

Various designs of chiral optical cavities have been described in the literature [36, 226–231]. Such cavities are based on helicity-preserving or chiral mirrors, for which several variants have likewise been proposed [232–236]. Often, the aim is helicity-preserving reflection at normal incidence, which enables cavity modes of nearly pure helicity in a typical Fabry–Perot setup.

In Section 4.2, we discussed that planar systems exhibit perfect helicity-preserving reflection in the limiting case of grazing incidence. The effectiveness of utilizing the helicity-preserving reflection at large oblique angles of incidence for helicity-preserving cavities was demonstrated in Refs. [237, 238]. The experimental realization and characterization of such cavities for enhanced chiral spectroscopy is actively being researched [161, 239]. We follow a similar principle in the design of our cavity. However, the cavities reported in Refs. [161, 237] are themselves achiral so as not interfere with the chiral signal of a molecular analyte that the cavity is intended to amplify. By contrast, our aim is to maximize the chirality of the cavity itself, which in turn may be used to actively manipulate chiral compounds injected into the cavity. With a view toward potential enantioselective applications, we have chosen the target frequency of 44.21 THz for our optimization in Section 5.4: In particular, this frequency corresponds to a vibronic resonance of the chiral organic compound BINOL—a common representative of chiral molecules for studies such as the present one [161]. The results discussed below primarily illustrate the working principles of the chiral cavity. For studies targeting

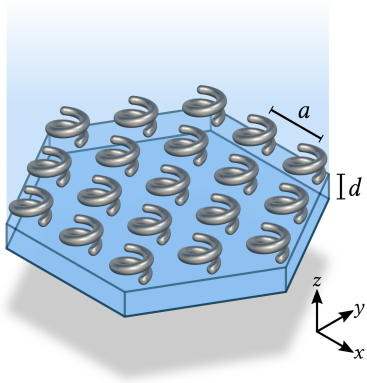


*Figure 6.1: Schematic representation of the chiral mirror* · Schematic representation of a chiral mirror consisting of a hexagonal periodic array of electromagnetically chiral helices on a substrate. The system is considered to be infinitely extended in the $xy$-plane. The substrate thickness $d$, the lattice constant $a$ of the hexagonal array, and the silver helices are not shown to scale. Adapted from Ref. [P2], .

other chiral molecules, our proposed design can be adjusted by optimizing the helix for a particular frequency of interest.

The mirrors used for our cavity are constructed as follows: A single mirror consists of a periodic array of the em-chiral silver helices optimized in Section 5.4 arranged on a hexagonal lattice on a thin substrate. For our modeling, the mirror is considered to be infinitely extended in the $xy$-plane. A schematic representation can be seen in Fig. 6.1. The space above the mirror (i.e., the upper halfspace), which will later correspond to the interior of the cavity, is occupied by a non-dispersive medium with a relative permittivity of $\varepsilon = 1.8912$. We choose a permittivity different from that of vacuum, as the cavity is designed with potential applications in mind where the interior of the cavity is filled, for example, with a solution of chiral molecules; hence, the relative permittivity of the cavity interior can be interpreted to represent the solvent of the analyte. As discussed in Section 5.4, we have already taken this relative permittivity into account during the optimization of the em-chiral helices.

The substrate on which the array of helices is situated has a thickness $d$, which we choose as to ensure an optimal helicity-preserving reflection, as explained below. For simplicity, we choose a substrate whose refractive index is matched to the interior of the cavity and model it with the same relative permittivity as specified above. By matching the refractive index of the cavity

interior to that of the substrate, the influence of the upper interface of the substrate directly beneath the array of helices is suppressed. We emphasize, however, that refractive index matching is not strictly necessary, provided that the refractive index of the cavity interior does not exceed that of the substrates; otherwise, TIR (cf. Section 4.2) occurs at the interface between the substrate and the interior, which in turn affects our analysis of the cavity's working principles. The halfspace below the substrate is modeled as vacuum.

The array of helices is constructed with a hexagonal geometry for two reasons: First, a hexagonal lattice allows for the densest packing of the emchiral helices for a fixed lattice constant, thereby accentuating the chiral interaction of light with the helices. Second, the high degree of rotational symmetry[1] mitigates the effect of a possible directional dependence of the response of the mirror. The distance between the helices, the lattice constant $a$, determines the wave vector components of the plane waves diffracted at the lattice and thus the angle at which these waves propagate. To take advantage of the nearly helicity-preserving reflection at large oblique angles, we choose the lattice constant accordingly: For $a \approx 5.74\,\mu\text{m}$, the first diffraction orders relative to normal incidence enclose an angle of 83° with the surface normal at 44.21 THz in the halfspace above the mirror. We stress that the lattice is only diffracting within cavity interior, since the lattice constant is subwavelength relative to the vacuum wavelength, rendering all diffraction orders in the lower halfspace evanescent. Similar to the design of a helicity-preserving cavity in Ref. [237], this construction enables the coupling of plane waves incident normally onto the mirror to plane waves propagating with a large in-plane wave vector component, which is associated with a reflection with high degree of helicity-preservation.

1 The sixfold rotational symmetry of the lattice is broken by the silver helices, which are not rotationally symmetric. However, because the helices respond nearly uniformly with respect to rotations around their own axis (cf. Fig. 5.35), the response of the lattice nonetheless largely follows the sixfold rotational symmetry.

To determine the optimal substrate thickness, we examine the helicity-preserving (i.e., co-polarized) reflectance (cf. Eqs. (4.72) and the discussion of Eq. (4.83)) from the chiral mirror as a function of the substrate thickness. For this purpose, we consider illumination with a plane wave from above at 44.21 THz with an incidence angle of 83°, aligned with one of the first diffraction orders. The overall dependence of the reflectance on the substrate thickness is determined by the interference of the waves reflected from the helix array and the bottom surface of the substrate. The effect is most pronounced for positive helicity, to which the helices respond the most. The highest helicity-preserving reflectance is obtained for negative helicity at a

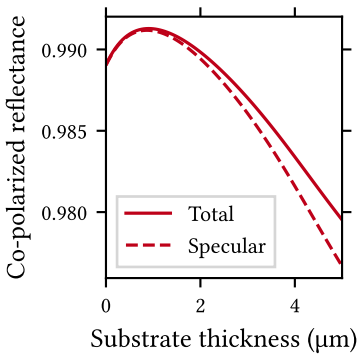


*Figure 6.2: Co-polarized reflectance for negative helicity as a function of substrate thickness* · The solid curve shows the total helicity-preserving (i.e., co-polarized) reflectance from the chiral mirror at 44.21 THz as a function of the substrate thickness. The incident plane wave has negative helicity and propagates at an angle of 83° to the surface normal, aligned with one of the first diffraction orders. The dashed line represents the contribution of specular reflection, the non-diffraction-related part of the reflectance.

substrate thickness of $d \approx 0.9\,\mu\text{m}$, as shown in Fig. 6.2. The dashed curve shows the specular reflectance, that is, the fraction of reflected power that preserves the in-plane wave vector. The solid curve shows the total helicity-preserving reflectance, including the power reflected into other diffraction orders. Both quantities reach their maximum at approximately the same substrate thickness of 0.9 μm.

In accordance with the maximum of the total helicity-preserving reflectance, we choose $d \approx 0.9\,\mu\text{m}$ in the following. For the resulting mirror, we examine the helicity-preserving reflectance as a function of the incidence angle to obtain a comprehensive picture of the directionality of the mirror's performance. To this end, we consider wave vectors in the $k_x k_z$-plane with $k_y = 0$. Although the mirror is not rotationally symmetric (the mirror exhibits approximately sixfold discrete rotational symmetry), the resulting reflectance characteristic, shown in Fig. 6.3, does not depend substantially on the direction of the illumination within the $xy$-plane. The reflectances shown can be considered representative for any azimuthal angle of illumination. Larger angles of incidence are of particular interest, as they represent the mirror's ability to sustain cavity modes with large in-plane wave vectors through successive reflections, harnessing the nearly helicity-preserving

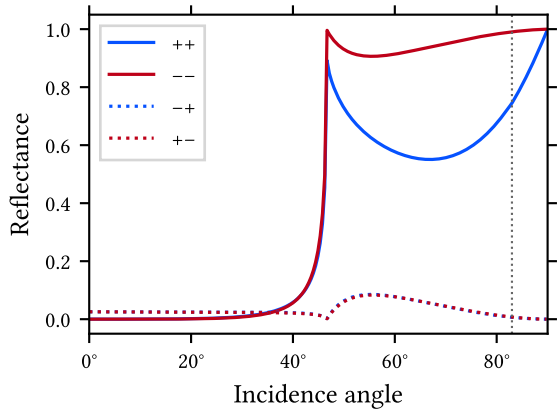


*Figure* 6.3: *Angle-dependent reflectance of the chiral mirror* · Co-polarized (solid curves) and cross-polarized (dotted) reflectance for illumination with positive (blue) and negative (red) helicity at 44.21 THz as a function of the incidence angle. An incidence angle of approximately 46.6° marks the onset of the total internal reflection at the lower interface between the substrate and vacuum. For larger incidence angles, a high degree of helicity-preserving reflectance is maintained for incident waves with negative helicity. In contrast, the reflectance for positive helicity is suppressed, an effect of the array of electromagnetically chiral helices. The dotted gray vertical line indicates an incidence angle of 83°. Adapted from Ref. [P2], CC BY 4.0.

nature of these reflections. The helicity-preserving reflectances shown by the solid curves in Fig. 6.3 exhibit a sudden increase at approximately 45°. This behavior is due to the onset of TIR at the lower interface of the substrate to vacuum. Specifically, TIR occurs at an angle of $\arcsin\left(1/\sqrt{\varepsilon}\right) \approx 46.6°$. For incidence angles greater than this value, a high degree of helicity-preserving reflectance is maintained. Crucially for our purposes, a significant contrast arises between the reflectances for positive and negative helicity, spanning the entire angle range between the onset of TIR and grazing incidence. This contrast is a manifestation of the array of em-chiral helices: For light of

positive helicity, with which the helices strongly interact, the absorptive nature of the helices takes effect. Furthermore, light incident on the array at oblique angles greater than the TIR threshold of the substrate–vacuum interface is partially diffracted into waves that propagate at smaller angles of incidence, thus bypassing the TIR. Since the em-chiral helices—and, consequently, the entire diffracting lattice—interact much less with light of negative helicity, these effects barely impact the reflection of negative helicity light. Thus, the array of helices introduces a loss channel that is highly helicity-selective. It reduces the helicity-preserving reflectance for positive helicity, in the most extreme case to values below 60 %, as seen in Fig. 6.3. At the same time, the helicity-preserving reflectance for negative helicity remains above 90 % across the entire range. The significance of TIR for the mirror's response is the reason for our earlier statement that the refractive index of the cavity interior should not exceed that of the substrate. Otherwise, the upper interface of the substrate would act as an additional cause of TIR, which would significantly affect the response of the mirror and render the previously performed optimization of the substrate thickness ineffective. Helicity-converting, or cross-polarized, reflectances are small for all incidence angles. Together, these characteristics enable the build-up of resonant modes of nearly pure helicity supported by continual reflections off the mirrors in the chiral cavity. We proceed with that discussion in the next section.

## 6.2 *Eigenmodes of the Chiral Optical Cavity*

Finally, we consider a cavity constructed from two of the chiral mirrors composed of an array of helices on a substrate, which we discussed in the previous section, facing each other. A schematic representation of the cavity is shown Fig. 6.4. As before, the mirrors—and thus the cavity—are considered to be infinitely extended in the $xy$-plane. The cavity interior is modeled using the relative permittivity of $\varepsilon = 1.8912$ introduced above, with the prospect of a cavity filled with, for example, an aqueous solution of molecules. The space above and below the cavity is considered as free space. We refer to the distance between the two mirrors as measured between the midplanes of the helix arrays, which determines the height of the cavity interior, as the cavity length $L$.

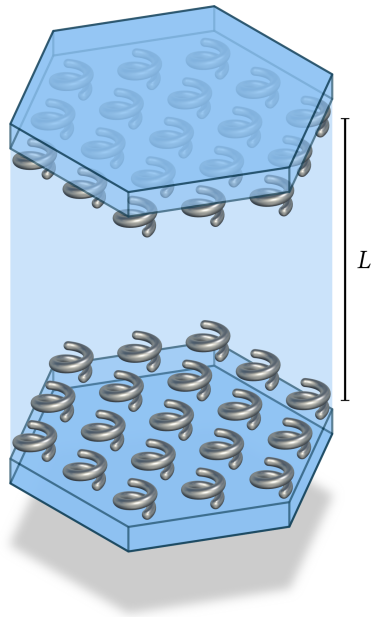


*Figure 6.4: Schematic representation of the chiral optical cavity* · Chiral optical cavity formed by two facing planar chiral mirrors. Each mirror consists of an array of electromagnetically chiral helices on a substrate and is considered to be infinitely extended in the $xy$-plane, see Fig. 6.1. The mirrors are separated by a distance $L$, measured between the midplanes of the helix arrays, which we call the cavity length. We vary the cavity length to tune different eigenmodes of the cavity into and out of resonance. Adapted from Ref. [P2], .

To model the cavity, we leverage the S-matrix formalism of Section 4.2. Specifically, we consider three different elements forming the cavity: The first two, namely, the upper and lower mirror, correspond to one S-matrix each, which we denote by $\boldsymbol{S}^{\mathrm{upr}}$ and $\boldsymbol{S}^{\mathrm{lwr}}$, respectively. Each S-matrix is computed as a stack of the elemental S-matrices introduced in Section 4.2, which represent the optical properties of the periodic array of helices and the substrate. The resulting combined S-matrix, as described in Eq. (4.80) and the related discussion, represents the chiral mirror. We used such S-matrices already for the computation of the reflectance of the single mirror in the previous section. The third S-matrix represents the cavity interior. It accounts for the phases picked up by the plane waves as they propagate across the space between the two mirrors, see Eqs. (4.77), and we denote it by $\boldsymbol{S}^{\mathrm{prop}}$.

Using the S-matrices that represent the mirrors and the cavity interior,

we can describe a roundtrip of an electromagnetic wave inside the cavity. We recall that an S-matrix maps the amplitudes and phases of a set of VPWs between the halfspaces surrounding the planar system it represents. As discussed in Section 4.2, the in-plane (i.e., parallel to the planar structure) wave vector components of VPWs interacting with the infinitely extended cavity are conserved up to multiples of the reciprocal unit vectors of the hexagonal lattice, that is, up to diffraction by the array of helices. In what follows, we consider an initial in-plane vector of $k_x = k_y = 0$, equivalent to normal incidence, and the VPWs corresponding to the associated diffraction orders. We further truncate this set, since VPWs with an in-plane vector exceeding the wavenumber become evanescent. For the helix arrays in Section 6.1, we chose a lattice constant close to the wavelength in the medium; as a result, the first diffraction orders associated with normal incidence at 44.21 THz propagate at an angle of 83° to the surface normal. Consequently, already the second diffraction orders are strongly evanescent and, hence, negligible in the interaction between the upper and lower mirror which will be separated by cavity lengths on the order of tens of microns in the following. Therefore, we consider only VPWs that are propagating in the cavity interior for modeling a roundtrip inside the cavity.[2] At a frequency of 44.21 THz, which we consider first, this corresponds to seven different wave vectors (one for normal incidence plus six for the associated first diffraction orders of the hexagonal lattice). For each wave vector, two circularly polarized VPWs are included in the analysis, one with positive helicity and one with negative helicity. Accordingly, the matrices that we work with below are of dimension $14 \times 14$.

The S-matrix based representation of a cavity roundtrip is given by the term

$$S^{\mathrm{rt}} := S^{\mathrm{lwr}}_{\uparrow\downarrow} S^{\mathrm{prop}}_{\downarrow\downarrow} S^{\mathrm{upr}}_{\downarrow\uparrow} S^{\mathrm{prop}}_{\uparrow\uparrow}. \tag{6.1}$$

The subscripts of the S-matrices on the right-hand side indicate the common propagation direction of the considered VPWs before (right index; incoming waves) and after (left index; outgoing waves) the interaction with the respective element of the cavity (cf. Eq. (4.75)). Starting at the lower mirror, the right-hand side of Eq. (6.1) (read from right to left) represents: propagation of the VPWs through the cavity interior toward the upper mirror, reflection from the upper mirror, propagation downward through the interior, and reflection from the lower mirror, completing one full roundtrip.

2 Evanescent waves were included when computing the S-matrices for the individual mirrors, which involve smaller spatial separations between their various parts. In those computations, we chose an upper bound of $2.51k$ for the magnitude of the in-plane component of the wave vector, where $k$ is the wavenumber in the homogeneous medium of the cavity interior.

We obtain the eigenmodes of the chiral cavity from an eigendecomposition of the roundtrip matrix $\boldsymbol{S}^{\mathrm{rt}}$. Each eigenvector $\boldsymbol{v}_i$ specifies a linear combination of the 14 VPWS whose composition remains unchanged after a roundtrip (i.e., an eigenmode), and the associated eigenvalue $w_i$ represents the relative change of the common amplitude and phase of the eigenmode after one roundtrip. An excited eigenmode experiences an indefinite series of consecutive roundtrips as a result of the waves being reflected back and forth between the two mirrors. Formally, this process corresponds to a geometric series in the roundtrip matrix $\boldsymbol{S}^{\mathrm{rt}}$,

$$\sum_{r=0}^{\infty} \left(\boldsymbol{S}^{\mathrm{rt}}\right)^r = \left(\mathbf{1} - \boldsymbol{S}^{\mathrm{rt}}\right)^{-1}, \tag{6.2}$$

where convergence to the term on the right-hand side is guaranteed since the chiral mirrors are passive and exhibit nonvanishing (absorptive and radiative) losses. Equation (6.2) describes the resonant enhancement (resp. suppression) of eigenmodes due to the constructive (resp. destructive) interference of the contributions after each roundtrip. Importantly, the eigenvectors $\boldsymbol{v}_i$ of $\boldsymbol{S}^{\mathrm{rt}}$ are also eigenvectors of Eq. (6.2), and the geometric series can be evaluated directly on the level of the eigenvalues $w_i$. Thus, the relative (internal) enhancement of a given eigenmode's amplitude and its relative phase are determined by $1/(1 - w_i)$. The corresponding internal intensity enhancement, proportional to the squared modulus of the eigenmode amplitude, is given by

$$\mathrm{IE}_i := \left| \frac{1}{1 - w_i} \right|^2. \tag{6.3}$$

We consider the internal intensity enhancement as a measure for how well the various eigenmodes are supported by the cavity.

The internal intensity enhancement of the cavity eigenmodes is shown in Fig. 6.5, evaluated as a function of the cavity length. Varying the cavity length changes the phases accumulated by the waves during a roundtrip and thus influences if the contributions of consecutive roundtrips in Eq. (6.2) interfere constructively or destructively. It allows us to tune the various eigenmodes of the cavity into and out of resonance, thereby providing a comprehensive picture of the modal landscape of the cavity.

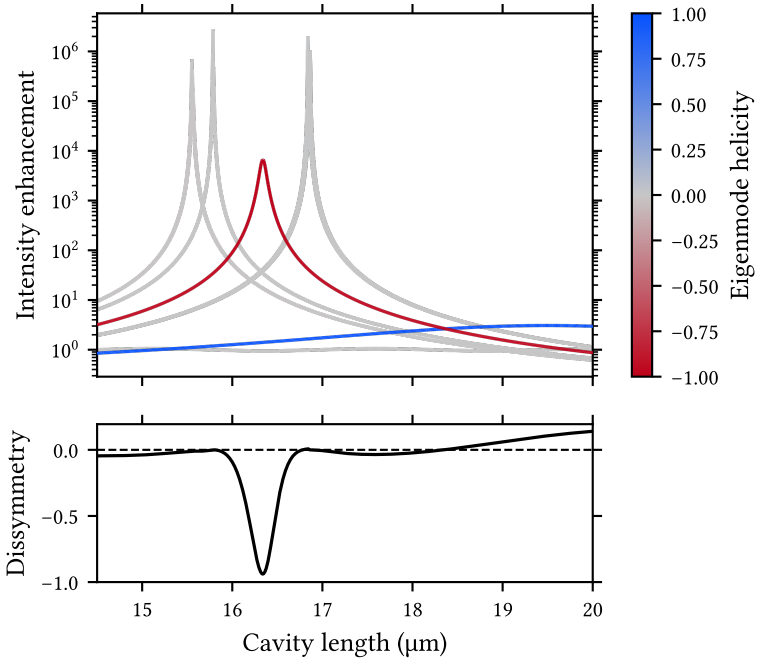


*Figure* 6.5: *Internal intensity enhancement of cavity eigenmodes as a function of cavity length* · Curves in the upper panel show the internal intensity enhancement of the eigenmodes of the chiral cavity at 44.21 THz. Different eigenmodes are tuned into and out of resonance as the cavity length changes. The curves are colored according to the helicity of the respective eigenmode, individually for every cavity length. Since the eigenmode helicity varies only very little as a function of the cavity length, the curves appear uniformly colored. Two eigenmodes stand out as being of nearly pure helicity. Compared at their respective resonance, the negative helicity eigenmode exhibits a substantially larger intensity enhancement. Taken together, the cavity exhibits a high dissymmetry, up to −0.94 at a cavity length of 16.34 μm (lower panel). Adapted from Ref. [P2], .

Since our goal is to create a chiral cavity that is biased with regard to helicity, we evaluate the helicity of the eigenmodes. To this end, we use that each eigenmode is represented via their eigenvector $\boldsymbol{v}_i$ by a linear combination of the basis VPWs, which we chose to be of well-defined helicity. Therefore, we evaluate the helicity of an eigenmode as the average of the VPWs' helicity weighted by the squared moduli of the respective coefficients contained in $\boldsymbol{v}_i$,

$$\Lambda(\boldsymbol{v}_i) \coloneqq \frac{\sum_{j=1}^{14} \left|(v_i)_j\right|^2 \lambda_j}{\|\boldsymbol{v}_i\|_2^2}. \tag{6.4}$$

Here, $\lambda_j \in \{+1, -1\}$ denotes the helicity of the VPWs $j$. Due to the normalization, Eq. (6.4) is limited to $-1 \leq \Lambda(\boldsymbol{v}_i) \leq 1$, where the extreme values correspond to an eigenmode composed of waves of a specific helicity, that is, the eigenmode itself is an eigenfunction of helicity. A value of $\Lambda(\boldsymbol{v}_i) = 0$, on the other hand, indicates a balanced composition of positive and negative helicity VPW, hence, the eigenmode is not biased toward either handedness. To display the helicity of each eigenmode as given by Eq. (6.4), we color the curves representing the modes' intensity enhancements in Fig. 6.5 according to the colormap shown on the side. The eigenmode helicity is evaluated separately at every considered cavity length, however, it varies only negligibly as a function of the cavity length, resulting in a uniformly colored appearance of the curves.

Two eigenmodes stand out as being of almost pure helicity, and the maximal intensity enhancements reached on resonance of the two modes differs substantially. The first of these modes, represented by the red curve in Fig. 6.5, evaluates to $\Lambda \approx -0.987$ and exhibits an internal intensity enhancement of up to $6.6 \times 10^3$ on resonance at a cavity length of $L \approx 16.34\,\mu\text{m}$, while the mode represented by the blue curve, with $\Lambda \approx 0.987$, exhibits an intensity enhancement of 3.1 on resonance at $L \approx 19.49\,\mu\text{m}$. To probe the chiral nature of the fields associated with the two eigenmodes, we evaluate the optical chirality density (or, equivalently for the monochromatic fields, the helicity density) as given in Eq. (3.39). Figure 6.6 shows the optical chirality density for the negative helicity eigenmode (left panel) and the positive helicity eigenmode (right panel) in the cavity interior. The shown slice extends from the helix array of the lower mirror (situated at $z = 0$) to the array of the upper mirror (at $z = L$). In the direction parallel to the mirrors, the fields

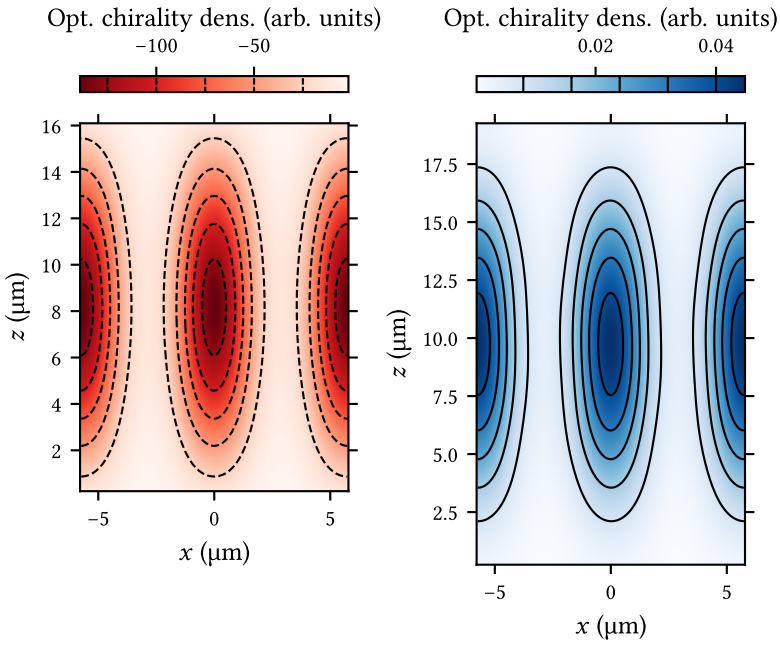


*Figure* 6.6: *Optical chirality density inside the cavity* · Both panels show a slice ($y = 0$) of the optical chirality density of the resonantly enhanced fields of an eigenmode, evaluated inside the cavity at 44.21 THz. The left and right panels show the negative and positive helicity eigenmodes, respectively. Both modes are tuned into resonance, corresponding to cavity lengths of 16.34 µm and 19.49 µm, respectively, and are excited with unit amplitude. Note the contrast of four orders of magnitude between the optical chirality densities in each plot, indicated by the limits of their associated colorbar, which demonstrates the substantially different resonant intensity enhancements of both modes (cf. Fig. 6.5). Data originally published in Ref. [P2].

conform to the periodicity of the array. The optical chirality density is calculated using the resonantly enhanced fields of each eigenmode arising from

an excitation with a unit amplitude from within the cavity. Both modes are evaluated on resonance, that is, for cavity lengths of 16.34 µm and 19.49 µm, respectively. Nevertheless, the resulting values for the two modes are separated by four orders of magnitude, as indicated by the different colorbar limits of the respective plots, which demonstrates the bias of the chiral cavity toward negative helicity. Importantly, the resonant cavity lengths of the two modes are separated, allowing us to choose the resonant cavity length of the negative helicity eigenmode to maximize the bias.

To express the bias of the cavity toward one helicity—its chirality—which is seen across the properties of its eigenmodes, by a single quantity, we compute a weighted average of the helicity of all eigenmodes, where the intensity enhancements act as weights. This quantity represents the helicity bias arising in the combination of all resonantly enhanced eigenmodes, assuming for simplicity that they are all excited equally. We refer to it as the *dissymmetry*,

$$\gamma := \frac{\sum_i \Lambda(\boldsymbol{\nu}_i)\mathrm{IE}_i}{\sum_i \mathrm{IE}_i}. \tag{6.5}$$

The dissymmetry is limited as $-1 \leq \gamma \leq 1$, where, similar to before, extremal values indicate a chiral cavity that exclusively supports eigenmodes of a given helicity. Its dependence on the cavity length is shown in the lower panel of Fig. 6.5. Related to the resonance of the negative helicity eigenmode, the dissymmetry assumes large values; at $L \approx 16.34\,\mu\mathrm{m}$, it reaches $\gamma \approx 0.94$.

Choosing the cavity length at 16.34 µm, we consider the frequency dependence of the cavity next. So far, we have considered a frequency of 44.21 THz, corresponding to the target frequency of the optimization of the silver helices in Section 5.4. Since the silver helices exhibit their most chiral and overall strongest response at that frequency (cf. Fig. 5.31), we can also expect the cavity to be most chiral there. T-matrices of the helix used to model the periodic arrays of the mirrors are interpolated from the T-matrices evaluated at various frequencies, which were used in Section 5.4. The interpolation is based on a pole expansion of the T-matrices of the helix [S2] and allows us to sample the T-matrix at finely spaced frequencies at relatively low computational cost. The pole expansion itself was carried out by Jan David Fischbach. The interpolated T-matrices are passivated following the procedure explained in Subsection 4.1.7.[3] Although the passivation

3 Data shown in Figs. 6.5 and 6.6 were computed using a passivated T-matrix as well.

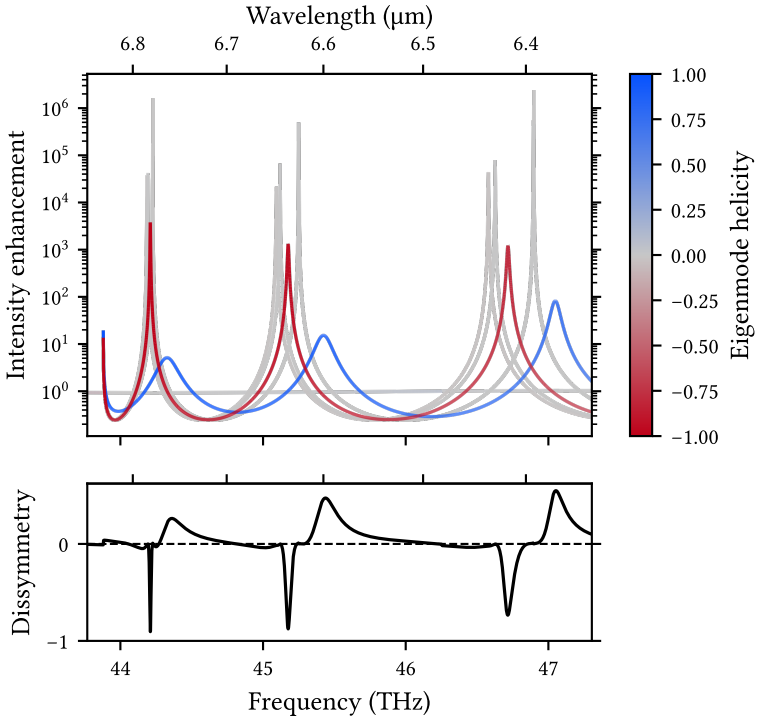


*Figure 6.7: Internal intensity enhancement of cavity eigenmodes as a function of frequency* · Upper panel: internal intensity enhancement of the eigenmodes of the chiral cavity with $L = 16.34\,\mu\text{m}$ as a function of frequency, showing multiple resonances. The curves are colored according to the helicity of the respective eigenmode, individually for every frequency. Below 43.88 THz, the first diffraction orders of the helix array become evanescent. As we move away from the optimization frequency of 44.21 THz toward higher frequencies, the response of the silver helix becomes less chiral (cf. Fig. 5.31). Accordingly, the contrast between the resonant intensity enhancements of the negative and positive helicity eigenmodes decreases to one order of magnitude. The dissymmetry of the cavity (lower panel) exhibits broader features with less extreme values for higher frequencies.

alters the T-matrices relatively on an order of $10^{-2}$ to $10^{-3}$, evaluated as per Eq. (5.20), it considerably affects the intensity enhancements. For example, the intensity enhancement of the negative helicity eigenmode on resonance at 44.21 THz is approximately twice as large if evaluated using a T-matrix without passivation.

The chiral cavity exhibits resonances of the eigenmodes with preference for a given helicity at multiple frequencies, as can be seen in Fig. 6.7. Toward lower frequencies, the first diffraction orders of the helix array propagate at ever larger angles to the surface normal, until they become evanescent at frequencies below 43.88 THz, rendering the array non-diffractive. The eigenmodes with strong helicity preference can be seen to vanish at that point, since they largely rely on the first diffraction orders, associated with near-grazing incidence angles and their reflection with a high degree of helicity-preservation. Toward higher frequencies, the contrast between the peak intensity enhancements of the positive and negative helicity eigenmodes decreases to about one order of magnitude. Simultaneously, the helicity preferences of both modes as given by Eq. (6.4) decrease, from approximately $\pm 0.989$ at the onset of diffraction down to $-0.696$ and 0.697, respectively, at a frequency of 47.30 THz. This can be seen by the colors of the two respective curves in Fig. 6.7, which fade toward higher frequencies. Consequently, the dissymmetry, shown in the lower panel, reaches less extreme negative values and is shaped by broader features resulting from the broader resonances of the negative helicity eigenmode. This behavior is consistent with our expectation based on the properties of the silver helices, namely, that they respond more weakly and less chiral at frequencies away from the target frequency at which they have been optimized, which in turn affects the performance of the chiral mirrors.

Although the effect of the decreasing electromagnetic chirality of the helices for higher frequencies is discernible in the data shown in Fig. 6.7, the cavity eigenmodes remain collectively biased toward negative helicity in the considered range. To demonstrate this fact and to connect the analyses of Figs. 6.5 and 6.7, we evaluate the dissymmetry as a function of both the cavity length and frequency. The data is shown in Fig. 6.8. Dotted lines mark the parameter ranges considered in Figs. 6.5 and 6.7, respectively. Repeated lines of pronounced positive and negative dissymmetry are visible, following the trajectory of the positive and negative helicity eigenmodes.

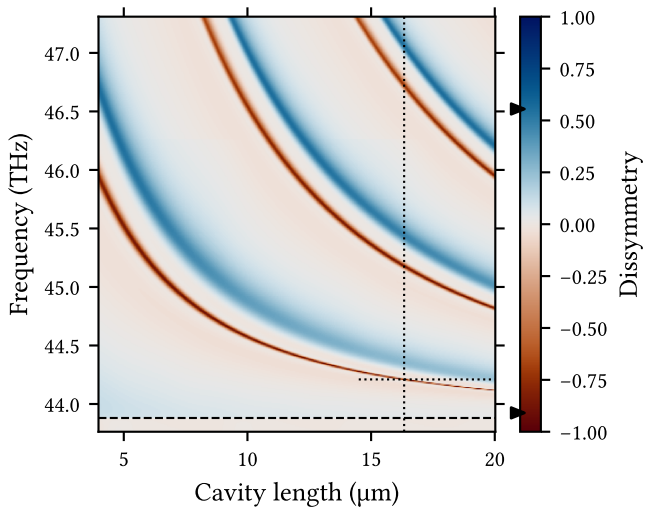


*Figure* 6.8: *Dissymmetry of the cavity eigenmodes* · Dissymmetry of the eigenmodes of the chiral optical cavity under variation of the cavity length and the frequency. High and low values of the dissymmetry follow the resonances of the eigenmodes with largely positive and negative helicity. The dashed horizontal line at 43.88 THz marks the onset of diffraction. The dotted horizontal and vertical lines indicate the parameter ranges presented in Figs. 6.5 and 6.7, respectively. Arrowheads on the colorbar show the minimum and maximum dissymmetry in the investigated parameter space. Colormap from [154, 155].

The inverse relationship between the frequency and the cavity length of the resonances is consistent with the resonance condition for the first diffraction order inside a planar cavity or slab; for details, we refer to Eq. (7) and the related discussion in [237]. For large cavity lengths, the curves asymptotically approach the onset of diffraction, marked by the black dashed line. Markers on the colorbar indicate the largest dissymmetries of either sign encountered in the considered parameter space. They demonstrate the overall bias of

the chiral optical cavity toward negative helicity. If targeting a narrow frequency range, the cavity length can be tuned to utilize the maximum possible dissymmetry.

*Chapter summary* · In this chapter, we have discussed the design of a chiral optical cavity, which was originally published in Ref. [P2]. The cavity combines helices optimized for a strongly chiral optical response with the preservation of helicity associated with reflections at large angles of incidence. Together, this combination gives rise to cavity eigenmodes that are approximately eigenfunctions of helicity and biases the cavity toward one sign of helicity. Below, we briefly summarize and discuss the most important results.

First, we discussed mirrors composed of arrays of optimized electromagnetically chiral helices on a substrate. TIR at the bottom of the substrate results in a strong, helicity-preserving reflectance, and the helix arrays create a significant contrast between the reflectances for positive and negative helicity by introducing a helicity-selective loss channel. By using diffractive arrays of chiral helices, the cavity targets modes with large in-plane wave vector components, whose potential in terms of helicity preservation has been discussed in previous publications. This choice distinguishes the cavity from other planar chiral cavities discussed in the literature, which are often designed for normal incidence.

We then examined the cavity formed by two of the chiral mirrors facing each other. We utilized the S-matrix formalism to model the resonant build-up of waves inside the cavity and analyzed the resulting eigenmodes of the cavity. In particular, we calculated the internal intensity enhancement of the fields associated with the eigenmodes, as well as their composition in terms of helicity. The cavity supports eigenmodes with nearly pure helicity and is strongly biased toward negative helicity, resulting in a contrast of three orders of magnitude between the intensity enhancements of the two modes at their respective resonance. Near the resonance of the negative helicity eigenmode, the chiral cavity is characterized by a dissymmetry that reaches 94 % of its theoretical limit, where 100 % corresponds to a perfect preference for negative helicity. We presume that this strong dissymmetry will be advantageous for potential enantioselective applications or for the manipulation of chiral light.

With regard to future work building on the results presented here, we first point out aspects to be considered in the theoretical modeling: First, the free-space excitation of the cavity's eigenmodes is hindered, which we found to be a consequence of the absorptive properties of the electromagnetically chiral helices. This does not pose a limitation for applications that do not rely on external excitation, such as when considering emitters within the cavity that directly excite the cavity modes. For applications that rely on external excitation, we propose excitation via evanescent coupling, or frustrated TIR. Second, the analysis of the eigenmodes presented above considers waves incident normally to the mirrors, as well as the associated diffraction orders. An extension to other propagation directions and an investigation of the angular dependence of the cavity provide a natural continuation of the presented analysis.

In a next step, solutions of chiral molecules injected into the cavity and their interaction with the cavity eigenmodes could be incorporated in the modeling, with the goal of developing enantioselective applications. A combination of our representation of the macroscopic cavity with quantum chemical simulations of chiral molecules in a multiscale approach similar to that in Section 5.2 holds promise for a comprehensive description of such systems. Finally, verifying the applicability of the proposed design requires experimental realization and characterization of the cavity. Regarding feasibility, we again refer to the fabrication of helices with comparable dimensions described in the literature [201–206], as well as to the ongoing experimental characterization of a structurally similar, helicity-preserving cavity [161, 239]. Additionally, Ref. [240] discusses the free-form optimization of electromagnetically chiral scatterers, and objects with an em-chirality comparable to that of the helices, with larger dimensions, have been identified. Such objects could ease the fabrication of the chiral optical cavity, which in turn would enable the experimental testing of the cavity's potential for enantioselective applications.

In the final chapter of this dissertation, we recapitulate the most important aspects of our various investigations into chirality in the interaction between light and matter, in which we examined microscopic and mesoscopic objects with different causes for their chiral response, extending up to a macroscopic optical device in the form of a chiral optical cavity.

# 7 *Conclusions and Outlook*

In this dissertation, we explored chirality in the interaction between light and matter through theoretical and numerical analysis. We collected the results of investigations of various chiral aspects, part of which we previously published in the literature, and we provided the fundamental concepts enabling their explanation and the formalisms used for their modeling. Original contributions to this thesis augment and extend these investigations. Here, in the concluding chapter of this dissertation, we take the opportunity to revisit our central findings and their implications, and to comment on possible future work extending the scope of this thesis.

*Summary* · In Chapter 2, we introduce the description of linear optical media in electrodynamics via constitutive relations. The constitutive relations link the auxiliary fields to the fundamental electromagnetic fields, providing an effective representation of the macroscopic properties of a medium arising from the properties of its microscopic, molecular constituents. The structure of the constitutive relations is used for a classification of linear media. The chirality of a medium, which derives from its chiral molecular compounds, in particular is represented by a designated chirality parameter that is related to the cross-coupling between electric and magnetic fields in the medium. We present two perspectives to motivate such cross-coupling, one related to the microscopic origins of Maxwell's equations, and a second considering an effective description of nonlocal optical responses. The latter of these perspectives emphasizes the finite spatial extent that electromagnetic fields need to resolve to possibly appreciate the chirality of a microscopic object.

In Chapter 3, we discuss electromagnetic waves in chiral media. The magnetic–electric cross-coupling affects the wave equations, which can no longer be decoupled for electric and magnetic fields as is the case in achiral media. Instead, the equations are decoupled for appropriate linear combinations of the fields, which turn out to be the eigenfunctions of helicity—a generalization of circular polarization handedness. Vector spherical waves and vector plane waves of well-defined helicity are discussed as two sets of solutions to the resulting Helmholtz equation. These solutions conform to the geometries of spatially localized and planar, infinitely extended sys-

tems, respectively, and facilitate the formalisms that we use to model such systems. We recognize the relevance of considering electromagnetic waves in the presence of chiral media with helicity in mind, linking the concepts of helicity and chirality.

Chapter 4 introduces the formalisms that combine our formulation of chiral media and that of electromagnetic waves and helicity presented in the preceding two chapters to describe their interaction. The study of waves scattering from spatially localized objects is facilitated by the transition matrix formalism, which provides a full representation of the objects linear optical response. For spherical particles, the scattering is solved analytically, and for particles with arbitrary shape, we resort to scattering simulations based on the finite element method. For the latter case, we introduce a passivation scheme that eliminates artificial gain arising from the limited precision of numerical simulations. Relations for the cross-sections enable us to evaluate spectroscopically relevant quantities from the transition matrix. For scattering from planar systems, we introduce scattering matrices, which can represent elements such as interfaces between media or periodic arrays of localized scatterers. When representing an interface, the entries of the scattering matrix correspond to the reflection and transmission coefficients characterizing the interaction of a plane electromagnetic wave impinging on the interface. We derive these coefficients for the general case of an interface between two chiral media analytically, as well as the related power transmission and reflection coefficients—the transmittance and reflectance—which also represent spectroscopically relevant quantities. Different scattering matrices can be combined to model complex stratified media including periodic arrays of scatterers. Together, these formalisms enable our various investigations of chiral light–matter interactions.

The chiral optical response of microscopic and mesoscopic systems is the central theme of Chapter 5. Our focus lies in particular on the different causes of the chiral optical response of such systems and their interplay. In this regard, we first consider scatterers with a chiral geometry and made of chiral media, and we illustrate using circular dichroism that the chiral response of such scatterers arises from a combination of the two causes [P9]. We demonstrate that the total circular dichroism is correspondingly given, within excellent approximation, by a superposition of two independent terms, which separately represent a material and a geometric contribution.

We discuss the isolation of these two contributions, where we particularly take optical resonances of the objects into account. Pronounced optical resonances require particular consideration as they affect how the chirality of the medium manifests in the response of the finite scatterer. Our results highlight an intriguing realization: Fundamentally, the chirality of a geometric shape and of the molecules constituting a chiral medium is in either case just a symptom of the lack of spatial inversion and mirror symmetries. Nevertheless, the contrast in the length scales associated with these two aspects and their different representation within our formalism enables a meaningful separation of their contributions to the total chiral response. Taken a step further, this realization proposes the utilization of geometric and material contributions as individual degrees of freedom to tailor chiral optical responses.

Extending these findings, we demonstrate the efficient approximation of transition matrices and of derived spectroscopic quantities for scatterers under variation of the material chirality parameter. The results and their discussion present a major original contribution to this dissertation. The approximation is made feasible by the relative smallness of the chirality parameters of naturally occurring media. Despite this smallness, spectroscopic quantities such as the circular dichroism strongly depend on the chirality parameter: In our earlier investigation of the separate causes of a chiral response, the medium and the geometry give rise to contributions on the same order of magnitude. This renders the approximation of chiral quantities disproportionately effective. Although we consider the possibility of such approximation most useful for chirality-related spectroscopic quantities, the approximation of quantities such as cross-sections yields equally excellent results. For example, in scenarios where different ratios of the enantiomeric composition of a chiral medium are considered, the approximation can substantially reduce the amount of costly transition matrix computations necessary. The evaluation of derivatives of the transition matrix with respect to the chirality parameter as part of the approximation leads to another interesting observation: We observe a pattern that distinguishes co-polarized from cross-polarized entries of the transition matrix. This pattern hints at intricacies of how chiral causes manifest themselves in the transition matrix and, thus, the chiral optical response, suggesting an avenue for promising future work.

Next, we consider the chiral response of arrangements of small, achiral metallic nanoparticles. The results of our modeling accompany the experimental investigation of corresponding systems [P3]. They lead us to the consideration of chirality as an emergent feature on mesoscopic scales, arising solely from the chiral spatial arrangement of inherently achiral constituents. At the same time, the chiral response exhibited by such systems can be highly pronounced: Coupling between plasmonic resonances of the nanoparticles facilitates strong circular dichroism signals and further lends it a characteristic, bisignate spectral shape, akin to the signature of the Cotton effect. We illustrate these aspects using helical arrangements of nanoparticles, considering various distances between the particles. Changing the distance between the particles changes the coupling between their resonances, the effect of which we not only see in our analysis of spectroscopic quantities but that we also evaluate directly based on a singular value decomposition of the transition matrix. The strong chiral response and its dependence on the configuration of the spatial arrangement provide yet another promising platform for tailoring chiral optical responses. With regard to the accurate numerical modeling of these and similar systems, we demonstrate the significance of contributions of higher multipolar degrees of the individual particles. Although the response of the nanoparticles in isolation, as well as in the coupled arrangement, predominantly manifests in dipolar contributions, the inclusion of higher multipolar degrees is essential for computing the multi-scattering between the particles and, thus, for the accurate prediction of the response in the coupled arrangement.

In the final section of Chapter 5, we demonstrate the optimization of a small silver helix to maximize its chiral optical response. With a remark on fundamental difficulties in quantifying chirality, we introduce the concept of electromagnetic chirality, which represents a holistic measure of an object's chiral optical response and serves as an objective function for the optimization. We explain the chiral response of the silver helix by its simultaneous action as an electric dipole antenna and an electrical coil. A perfectly electromagnetically chiral scatterer is characterized by being fully transparent to light of one helicity and interacting exclusively with the other helicity. Our optimized helix exhibits an electromagnetic chirality of 95 % of this theoretical upper limit, providing us with a strongly chiral building block for our next and final investigation treated in this dissertation.

In Chapter 6, the final thematic chapter, we leverage the optimized electromagnetically chiral helices to design a chiral cavity, imprinting their strongly chiral response onto the properties of a macroscopic optical device. The cavity is formed by planar mirrors consisting of a diffractive array of these helices on a substrate. Total internal reflection at near grazing incidence by the substrate facilitates a high, helicity-preserving reflectance, and diffraction and absorption by the helix array introduce a helicity-selective loss channel. As a result, the chiral cavity supports eigenmodes of nearly pure helicity, but is strongly biased toward a specific helicity, characterized by a contrast of three orders of magnitude between the intensity enhancements experienced by the two eigenmodes at their respective resonance. Expressed as a comprehensive dissymmetry, the chiral cavity reaches values as large as 94 %, where perfect dissymmetry corresponds to a total preference for a specific helicity. The proposed chiral cavity demonstrates how the chiral optical response of a macroscopic structure can be shaped by the deliberate design of its constituents. It provides the chiral electromagnetic environment that could facilitate the enantioselective processes relevant to pharmaceutic applications.

*Future work* · The study of chiral light–matter interactions constitutes an ongoing contemporary research effort. Our findings contribute in this effort by illuminating how different causes of chirality—separated by length scales in reality and distinguished by their conceptual representation within the formalism—influence the total chiral response of a given object. Furthermore, they contribute by giving examples of how the chiral response of microscopic objects and macroscopic devices can be maximized. Several aspects highlighted throughout our various studies provide starting points for an extension of our findings in future work. We discussed these aspects in the dedicated concluding parts of each thematic segment. Below, we consolidate the lines of continuation that we deem most worthwhile.

We have demonstrated the approximate independence of geometric and material contributions to the circular dichroism of a given object, and investigated the strong chiral responses in chiral, resonant assemblies depending on their spatial arrangement. Together, these findings propose individual degrees of freedom to be utilized for tailoring chiral optical responses. With regard to numerical modeling, such studies are expedited by the efficient

approximation of transition matrices accounting for the effect of different dispersive material chirality parameters. Future studies could explore the limitations of such an approach and utilize it for the intentional design of chiral systems, building, for instance, on the work on nanoparticle assemblies combining different shapes that was initiated in Ref. [P3]. A related investigation, which—following the opposite direction—explores how to interpret an observed chiral response to gain insights into the geometric composition of certain systems, is in progress at the time of writing.

Focused on the approximation scheme, aspects for future work are twofold: First, testing its limitations and exploring potential refinements pose a natural extension of the work conducted here. Automatic differentiation is expected to yield a more precise evaluation of the derivatives with respect to the chirality parameter, which we approximated as finite differences, and could decrease the amount of necessary full-wave simulations even further. Since the quality of the proposed approximation is tied to the smallness of the material chirality parameter, an investigation of its applicability for media and systems with large manufactured chirality could consolidate the approach with the conceptual research on, among others, strongly chiral metamaterials [241–244]. Second, our observation of a pattern distinguishing co-polarized and cross-polarized entries with regard to their dependence to the chirality parameter proposes a comprehensive analysis of how different causes of chirality manifest themselves in the transition matrix and, thereby, shape the optical response of an object.

Several ideas for future work arise when considering the pole expansion of transition matrices introduced in [S2]. The pole expansion provides direct access to the resonances of an object and their properties. Enabled with such explanatory power, we might revisit the isolation computation of material and geometric contributions to an object's circular dichroism, in particular focusing on the influence of pronounced optical resonances. Doing so might eliminate the need for a geometrically achiral reference object, which we relied on in the respective part of the analysis, and is especially relevant given the lack of a general constructive recipe to obtain such reference. Moreover, the pole expansion allows us to characterize the resonance underlying the strong electromagnetically chiral response of the helices optimized in Chapter 5. Preliminary findings in this regard—not included in this thesis—could be expanded to the fundamental explanation of resonant chiral

optical responses and facilitate the rational design of scatterers such as the ones investigated here. The design of such scatterers not only enables the highly helicity-biased chiral cavity reported in Chapter 6, but also serves as a chiral unit in other studies that lie outside the scope of this dissertation. Two such studies, exploring, in particular, chiral thermal emissions were already published in Refs. [P1, P4].

In Chapter 6, we focused on the conceptual development of a chiral optical cavity that leverages the strong chiral response of the helices targeted in our optimization. Accordingly, our discussion considered the bare cavity and a fundamental investigation of the electromagnetic environment constituted by the cavity's eigenmodes. The natural next step includes an experimental realization and characterization of the proposed cavity. Although we provided general considerations regarding the feasibility of fabrication by referring to structurally comparable elements realized previously, the actual fabrication of the proposed cavity will certainly face challenges that are not considered in the idealized numerical modeling. Overcoming these challenges will necessarily be the objective of initial work following that direction. If the cavity has been successfully realized, the clear goal is to explore its real-world potential for enantioselective applications. Ultimately, this provided the initial motivation for our investigation. To aid this goal in a joint research effort combining experiments and numerical simulations, the inclusion of chiral molecules inside the cavity and their interaction with the cavity eigenmodes needs to be incorporated into the numerical model. In our study of chiral organic helices in Chapter 5, we introduced a multi-scale approach that unifies the quantum chemical simulation of molecular properties with the formalisms describing electromagnetic scattering of mesoscopic or macroscopic structures, similar to the approach developed in [245]. Such multi-scale modeling presents the natural approach for the comprehensive numerical consideration of chiral molecular compounds interacting with the chiral cavity, enabling the conceptual development of enantioselective applications with relevance in pharmacy and pharmacology.

The works collected in this dissertation reflect an ongoing engagement with chiral interactions between light and matter. Throughout the various investigations into chiral aspects and the examination of their underlying principles, a fascination remained for how an unassuming geometric concept that is as easily explained as observing your own hands in a mirror can exert

an influence as profound as shaping the chemistry of life itself. Curiosity and vital applications—aimed, for example, at the manufacturing and control of medical drugs—alike drive us in our continued effort to understand and manipulate chiral light–matter interactions. It is my sincere hope that the investigations presented in this dissertation will prove a lasting, meaningful contribution to this collective effort, and that this work, in some measure, reflects the impact that engaging with these research questions has had on me.

# A *Vector Spherical Waves and Related Functions*

This appendix collects useful relations for vector spherical waves (VSWS) and the related functions that constitute them. VSWS arise as solutions to the vector Helmholtz equation expressed in spherical coordinates. Following Ref. [67], they can be derived from the solutions to the scalar Helmholtz equation,

$$\left(\nabla^2 + k^2\right) f(\boldsymbol{r}) = 0,$$

which, in spherical coordinates, reads

$$\frac{1}{r^2}\frac{\partial}{\partial r}\left(r^2 \frac{\partial}{\partial r} f(\boldsymbol{r})\right) + \frac{1}{r^2 \sin\theta}\frac{\partial}{\partial \theta}\left(\sin\theta \frac{\partial}{\partial \theta} f(\boldsymbol{r})\right) + \frac{1}{r^2 \sin^2\theta}\frac{\partial^2}{\partial \varphi^2} f(\boldsymbol{r}) + k^2 f(\boldsymbol{r}) = 0. \quad \text{(A.1)}$$

The separation ansatz $f(\boldsymbol{r}) = R(r)\Theta(\theta)\Phi(\varphi)$ yields the differential equations

$$\frac{\mathrm{d}^2}{\mathrm{d}\varphi^2}\Phi(\varphi) + m^2\Phi(\varphi) = 0, \quad \text{(A.2a)}$$

$$\frac{1}{\sin\theta}\frac{\mathrm{d}}{\mathrm{d}\theta}\left(\sin\theta \frac{\mathrm{d}}{\mathrm{d}\theta}\Theta(\theta)\right) + \left(\ell(\ell+1) - \frac{m^2}{\sin^2\theta}\right)\Theta(\theta) = 0, \quad \text{(A.2b)}$$

$$\frac{\mathrm{d}}{\mathrm{d}r}\left(r^2 \frac{\mathrm{d}}{\mathrm{d}r} R(r)\right) + \left(k^2 r^2 - \ell(\ell+1)\right) R(r) = 0, \quad \text{(A.2c)}$$

where the separation constants $\ell$ and $m$ have been introduced [93, Section 4.1]. Solutions to Eq. (A.2a) are readily found as

$$\Phi_m(\varphi) = \mathrm{e}^{\mathrm{i}m\varphi}. \quad \text{(A.3)}$$

Solutions to Eq. (A.2b) are given by the associated Legendre polynomials, and, together, $\Theta(\theta)\Phi(\varphi)$ form the spherical harmonics, see Section A.2. Equation (A.2c) is solved by spherical Bessel and Hankel functions, which are discussed in Section A.1. Joining these parts, the separation ansatz yields the solutions given in Eq. (3.10).

## A.1 *Spherical Bessel and Hankel Functions*

$j_\ell(x)$ and $y_\ell(x)$ are alternatively referred to as spherical Bessel functions of first and second kind.

The spherical Bessel and Neumann functions, given by [92, Eq. (10.49.14)]

$$j_\ell(x) = x^\ell \left(-\frac{1}{x}\frac{\mathrm{d}}{\mathrm{d}x}\right)^\ell \left(\frac{\sin x}{x}\right), \tag{A.4a}$$

$$y_\ell(x) = -x^\ell \left(-\frac{1}{x}\frac{\mathrm{d}}{\mathrm{d}x}\right)^\ell \left(\frac{\cos x}{x}\right), \tag{A.4b}$$

Equation (A.2c) turns into Eq. (A.5) upon change of variables; $kr = x$.

for nonnegative integer $\ell$, are solutions to

$$\left[\frac{\mathrm{d}^2}{\mathrm{d}x^2} + 2x\frac{\mathrm{d}}{\mathrm{d}x} + x^2 - \ell(\ell+1)\right] z_\ell^{(n)}(x) = 0. \tag{A.5}$$

For real $x$, $j_\ell(x)$ and $y_\ell(x)$ are real-valued. Their complex-valued combinations, the spherical Hankel functions of first and second kind,

$$h_\ell^{(1)}(x) = j_\ell(x) + \mathrm{i}y_\ell(x), \tag{A.6a}$$

$$h_\ell^{(2)}(x) = j_\ell(x) - \mathrm{i}y_\ell(x), \tag{A.6b}$$

also solve Eq. (A.5). For a joint notation, we define $z_\ell^{(n)}$ as

$$z_\ell^{(1)} = j_\ell, \qquad z_\ell^{(2)} = y_\ell, \qquad z_\ell^{(3)} = h_\ell^{(1)}, \qquad z_\ell^{(4)} = h_\ell^{(2)}. \tag{A.7}$$

These functions satisfy the recurrence relation

$$z_{\ell-1}^{(n)}(x) + z_{\ell+1}^{(n)}(x) = \frac{2\ell+1}{x} z_\ell^{(n)}(x). \tag{A.8}$$

Their derivative can be found to be

$$\frac{\mathrm{d}}{\mathrm{d}x} z_\ell^{(n)}(x) = z_{\ell-1}^{(n)}(x) - \frac{\ell+1}{x} z_\ell^{(n)}(x), \tag{A.9a}$$

$$\frac{\mathrm{d}}{\mathrm{d}x} z_\ell^{(n)}(x) = -z_{\ell+1}^{(n)}(x) + \frac{\ell}{x} z_\ell^{(n)}(x). \tag{A.9b}$$

The asymptotic behavior of the spherical Bessel and Neumann functions for small (complex) arguments is given by

$$j_\ell(x) \sim \frac{x^\ell}{(2\ell+1)!!} \quad (\text{as } x \to 0), \tag{A.10a}$$

$$y_\ell(x) \sim -\frac{(2\ell-1)!!}{x^{\ell+1}} \quad (\text{as } x \to 0). \tag{A.10b}$$

The asymptotic behavior of $h_\ell^{(1)}$ and $h_\ell^{(2)}$ for small arguments is dominated by Eq. (A.10b). For large arguments,

$$h_\ell^{(1)}(x) \sim \frac{(-\mathrm{i})^{\ell+1}}{x} \mathrm{e}^{\mathrm{i}x} \quad (\text{as } x \to \infty), \tag{A.11a}$$

$$h_\ell^{(2)}(x) \sim \frac{\mathrm{i}^{\ell+1}}{x} \mathrm{e}^{-\mathrm{i}x} \quad (\text{as } x \to \infty). \tag{A.11b}$$

## A.2 *Scalar and Vector Spherical Harmonics*

In the following, we introduce the associated Legendre polynomials, which are subsequently used to construct the (scalar) spherical harmonics as well as the vector spherical harmonics (VSHs).

### A.2.1 *Associated Legendre polynomials*

*Definition* · The associated Legendre polynomials $P_\ell^m$ are solutions to the associated Legendre equation,

$$\left[\left(1-x^2\right)\frac{\mathrm{d}^2}{\mathrm{d}x^2} - 2x\frac{\mathrm{d}}{\mathrm{d}x} + \ell(\ell+1) - \frac{m^2}{1-x^2}\right] P_\ell^m(x) = 0. \tag{A.12}$$

Equation (A.2b) turns into Eq. (A.12) for $x \in [-1, 1]$ upon change of variables; $\cos\theta = x$.

For $m \geq 0$, they can be written in terms of the (regular) Legendre polynomials $P_\ell$ (solutions of Eq. (A.12) for $m = 0$; $P_\ell = P_\ell^0$) as

$$P_\ell^m(x) = (-1)^m \left(1-x^2\right)^{\frac{m}{2}} \frac{\mathrm{d}^m}{\mathrm{d}x^m} P_\ell(x), \tag{A.13a}$$

which, by using Rodrigues' formula, leads to the explicit expression

$$P_\ell^m(x) = \frac{(-1)^m}{2^\ell \ell!} \left(1-x^2\right)^{\frac{m}{2}} \frac{\mathrm{d}^{\ell+m}}{\mathrm{d}x^{\ell+m}} \left(x^2-1\right)^\ell. \tag{A.13b}$$

Consistent with [42, Eqs. (3.49–50)], [101, Eq. (B.2)], [246, Eq. (A.3)], [247, Eq. (15.80)], [92, Eqs. (14.7.8) and (14.7.10)]. Differs by $(-1)^m$ from [89, p. 401], [93, Eq. (4.25)].

Equation (A.13b) is valid for $-\ell \leq m \leq \ell$. Above definition of the associated Legendre polynomials includes the Condon–Shortley phase $(-1)^m$ [248, Chapter 3]. While Eq. (A.12) is indifferent to the sign of $m$, Eq. (A.13b) establishes the proportionality between the solutions for negative and positive $m$ to

$$P_\ell^{-m}(x) = (-1)^m \frac{(\ell - m)!}{(\ell + m)!} P_\ell^m(x), \tag{A.14}$$

which also allows to obtain $P_\ell^m$ for negative $m$ from those for positive $m$.

*Orthogonality and normalization* · For a fixed $m$, $P_\ell^m$ satisfy the orthogonality and normalization relation

$$\int_{-1}^{1} \mathrm{d}x\, P_{\ell'}^m(x) P_\ell^m(x) = \frac{2}{2\ell + 1} \frac{(\ell + m)!}{(\ell - m)!} \delta_{\ell\ell'}. \tag{A.15}$$

*Parity* · The symmetry of $P_\ell^m$ with respect to $x = 0$ is given by

$$P_\ell^m(-x) = (-1)^{\ell - m} P_\ell^m(x). \tag{A.16}$$

### A.2.2 *Spherical harmonics*

Consistent with [42, Eq. (3.53)], [101, Eq. (B.1)], [246, Eq. (A.2)], [247, Eq. (15.137)], [92, Eq. (14.30.1)].

*Definition* · The spherical harmonics $Y_{\ell m}$ are defined as

$$Y_{\ell m}(\theta, \varphi) \coloneqq \sqrt{\frac{2\ell + 1}{4\pi} \frac{(\ell - m)!}{(\ell + m)!}} P_\ell^m(\cos\theta) \mathrm{e}^{\mathrm{i}m\varphi}. \tag{A.17}$$

From Eq. (A.14), we find a relation between positive and negative $m$,

$$Y_{\ell,-m}(\theta, \varphi) = (-1)^m Y_{\ell m}^*(\theta, \varphi). \tag{A.18}$$

*Orthogonality and normalization* · The spherical harmonics satisfy the orthogonality and normalization relation

$$\iint \mathrm{d}\Omega\, Y_{\ell' m'}^*(\theta, \varphi) Y_{\ell m}(\theta, \varphi) = \delta_{\ell\ell'} \delta_{mm'}, \tag{A.19}$$

where we have introduced the shorthand notation $\iint \mathrm{d}\Omega \equiv \int_0^{2\pi} \mathrm{d}\varphi \int_0^{\pi} \sin\theta \,\mathrm{d}\theta$ and $\delta_{ij}$ is the Kronecker delta.

*Completeness* · The completeness relation for the spherical harmonics is

$$\sum_{\ell=0}^{\infty}\sum_{m=-\ell}^{\ell} Y^*_{\ell m}(\theta',\varphi')Y_{\ell m}(\theta,\varphi) = \delta(\varphi-\varphi')\delta(\cos\theta-\cos\theta'). \tag{A.20}$$

*Parity* · From Eq. (A.16) follows the behavior of $Y_{\ell m}$ under parity as

$$Y_{\ell m}(\pi-\theta,\varphi+\pi) = (-1)^l Y_{\ell m}(\theta,\varphi). \tag{A.21}$$

### A.2.3 *Vector spherical harmonics*

*Definition* · In Eq. (3.21a), we defined, for $\ell \geq 1$,

$$\begin{aligned} \boldsymbol{X}_{\ell m}(\theta,\varphi) &\coloneqq \frac{1}{\sqrt{\ell(\ell+1)}}\frac{1}{\mathrm{i}}\boldsymbol{r}\times\boldsymbol{\nabla}Y_{\ell m}(\theta,\varphi) \\ &= \mathrm{i}\gamma_{\ell m}\left(\mathrm{i}\pi^m_\ell(\cos\theta)\hat{\boldsymbol{\theta}} - \tau^m_\ell(\cos\theta)\hat{\boldsymbol{\varphi}}\right)\mathrm{e}^{\mathrm{i}m\varphi}. \end{aligned} \tag{A.22a}$$

Consistent with [42, Eq. (9.119)], [101, Eq. (11a)]; $\boldsymbol{X}_{\ell m} = \boldsymbol{Y}_{\ell\ell m}$ [247, Eq. (16.88)]; $\boldsymbol{X}_{\ell m} = \mathrm{i}\gamma_{\ell m}\boldsymbol{C}_{m\ell}$, $\boldsymbol{V}_{\ell m} = \mathrm{i}\gamma_{\ell m}\boldsymbol{B}_{m\ell}$, $\boldsymbol{W}_{\ell m} = \mathrm{i}\gamma_{\ell m}\sqrt{\ell(\ell+1)}\boldsymbol{P}_{m\ell}$ [246, Eqs. (C.16–18)].

We further define

$$\begin{aligned} \boldsymbol{V}_{\ell m}(\theta,\varphi) &\coloneqq \frac{\mathrm{i}}{\sqrt{\ell(\ell+1)}} r\boldsymbol{\nabla}Y_{\ell m}(\theta,\varphi) \\ &= \hat{\boldsymbol{r}}\times\boldsymbol{X}_{\ell m}(\theta,\varphi), \end{aligned} \tag{A.22b}$$

and, for $\ell \geq 0$,

$$\boldsymbol{W}_{\ell m}(\theta,\varphi) \coloneqq \mathrm{i}Y_{\ell m}(\theta,\varphi)\hat{\boldsymbol{r}}. \tag{A.22c}$$

We recognize the right-hand sides of Eqs. (A.22b) and (A.22c) in Eq. (3.21b). For the second line of Eq. (A.22a), we introduced

$$\gamma_{\ell m} \coloneqq \sqrt{\frac{2\ell+1}{4\pi\ell(\ell+1)}\frac{(\ell-m)!}{(\ell+m)!}}, \tag{A.23}$$

$$\pi^m_\ell(x) \coloneqq \frac{mP^m_\ell(x)}{\sqrt{1-x^2}}, \tag{A.24}$$

$$\tau^m_\ell(x) \coloneqq \frac{\partial}{\partial\theta}P^m_\ell(\cos\theta)\bigg|_{\cos\theta=x}. \tag{A.25}$$

Collectively, $\boldsymbol{X}_{\ell m}$, $\boldsymbol{V}_{\ell m}$, and $\boldsymbol{W}_{\ell m}$ are called VSHs. On a given spherical surface, parametrized by the angles $(\theta,\varphi)$, $\boldsymbol{X}_{\ell m}$ and $\boldsymbol{V}_{\ell m}$ are tangential to the surface

and mutually orthogonal, while $\boldsymbol{W}_{\ell m}$ is normal to the surface. Together, they form a complete basis for vector fields on the unit sphere.

From Eq. (A.18) follow

$$\boldsymbol{X}_{\ell,-m}(\theta,\varphi) = (-1)^{m+1}\boldsymbol{X}^*_{\ell m}(\theta,\varphi), \tag{A.26a}$$
$$\boldsymbol{V}_{\ell,-m}(\theta,\varphi) = (-1)^{m+1}\boldsymbol{V}^*_{\ell m}(\theta,\varphi), \tag{A.26b}$$
$$\boldsymbol{W}_{\ell,-m}(\theta,\varphi) = (-1)^{m+1}\boldsymbol{W}^*_{\ell m}(\theta,\varphi). \tag{A.26c}$$

*Orthogonality and normalization* · The VSHS satisfy the orthogonality and normalization relations

$$\iint \mathrm{d}\Omega\, \boldsymbol{X}^*_{\ell' m'}(\theta,\varphi)\cdot\boldsymbol{X}_{\ell m}(\theta,\varphi) = \delta_{\ell\ell'}\delta_{mm'}, \tag{A.27a}$$
$$\iint \mathrm{d}\Omega\, \boldsymbol{V}^*_{\ell' m'}(\theta,\varphi)\cdot\boldsymbol{V}_{\ell m}(\theta,\varphi) = \delta_{\ell\ell'}\delta_{mm'}, \tag{A.27b}$$
$$\iint \mathrm{d}\Omega\, \boldsymbol{W}^*_{\ell' m'}(\theta,\varphi)\cdot\boldsymbol{W}_{\ell m}(\theta,\varphi) = \delta_{\ell\ell'}\delta_{mm'}, \tag{A.27c}$$
$$\iint \mathrm{d}\Omega\, \boldsymbol{X}^*_{\ell' m'}(\theta,\varphi)\cdot\boldsymbol{V}_{\ell m}(\theta,\varphi) = 0, \tag{A.27d}$$

and, identically for all $(\theta,\varphi)$, the even stricter

$$\boldsymbol{X}^*_{\ell' m'}\cdot\boldsymbol{W}_{\ell m} = \boldsymbol{X}_{\ell' m'}\cdot\boldsymbol{W}_{\ell m} = 0, \tag{A.27e}$$
$$\boldsymbol{V}^*_{\ell' m'}\cdot\boldsymbol{W}_{\ell m} = \boldsymbol{V}_{\ell' m'}\cdot\boldsymbol{W}_{\ell m} = 0, \tag{A.27f}$$

for all $\ell, \ell', m, m'$. Equation (A.27c) follows immediately from Eq. (A.19); Eqs. (A.27e) and (A.27f) follow from the fact that $\boldsymbol{X}_{\ell m} \perp \hat{\boldsymbol{r}}$ and $\boldsymbol{V}_{\ell m} \perp \hat{\boldsymbol{r}}$ by construction, which also allows to derive Eq. (A.27b) directly from Eqs. (A.27a) and (A.27d).

*Parity* · From Eq. (A.21), we find that $\boldsymbol{X}_{\ell m}$ has opposite parity as compared to the other two VSHS:

$$\boldsymbol{X}_{\ell m}(\pi-\theta,\varphi+\pi) = (-1)^{\ell}\boldsymbol{X}_{\ell m}(\theta,\varphi), \tag{A.28a}$$

whereas

$$\boldsymbol{V}_{\ell m}(\pi-\theta,\varphi+\pi) = (-1)^{\ell+1}\boldsymbol{V}_{\ell m}(\theta,\varphi), \tag{A.28b}$$
$$\boldsymbol{W}_{\ell m}(\pi-\theta,\varphi+\pi) = (-1)^{\ell+1}\boldsymbol{W}_{\ell m}(\theta,\varphi). \tag{A.28c}$$

*Divergence and curl* · For vector fields given by one of the VSHs scaled radially with some scalar function $f(r)$, their divergence is given by

$$\boldsymbol{\nabla} \cdot [f(r)\boldsymbol{X}_{\ell m}(\theta,\varphi)] = 0, \tag{A.29a}$$

$$\boldsymbol{\nabla} \cdot [f(r)\boldsymbol{V}_{\ell m}(\theta,\varphi)] = -\mathrm{i}\sqrt{\ell(\ell+1)}\frac{1}{r}f(r)Y_{\ell m}(\theta,\varphi), \tag{A.29b}$$

$$\boldsymbol{\nabla} \cdot [f(r)\boldsymbol{W}_{\ell m}(\theta,\varphi)] = \mathrm{i}\left(\frac{\mathrm{d}}{\mathrm{d}r}f(r) + \frac{2}{r}f(r)\right)Y_{\ell m}(\theta,\varphi), \tag{A.29c}$$

and their curl by

$$\begin{aligned}\boldsymbol{\nabla} \times [f(r)\boldsymbol{X}_{\ell m}(\theta,\varphi)] = &\left(\frac{\mathrm{d}}{\mathrm{d}r}f(r) + \frac{1}{r}f(r)\right)\boldsymbol{V}_{\ell m}(\theta,\varphi) \\ &+ \sqrt{\ell(\ell+1)}\frac{1}{r}f(r)\boldsymbol{W}_{\ell m}(\theta,\varphi),\end{aligned} \tag{A.30a}$$

$$\boldsymbol{\nabla} \times [f(r)\boldsymbol{V}_{\ell m}(\theta,\varphi)] = -\left(\frac{\mathrm{d}}{\mathrm{d}r}f(r) + \frac{1}{r}f(r)\right)\boldsymbol{X}_{\ell m}(\theta,\varphi), \tag{A.30b}$$

$$\boldsymbol{\nabla} \times [f(r)\boldsymbol{W}_{\ell m}(\theta,\varphi)] = \sqrt{\ell(\ell+1)}\frac{1}{r}f(r)\boldsymbol{X}_{\ell m}(\theta,\varphi). \tag{A.30c}$$

## A.3 *Vector Spherical Waves*

In this section, we introduce the VSWs, solutions to the vector Helmholtz equation expressed in spherical coordinates, which feature the VSHs discussed in the previous section. We also provide relations linking spherical and plane waves.

### A.3.1 *Definition and useful relations*

*Definition* · We define the VSWs

$$\boldsymbol{M}^{(n)}_{\ell m}(\boldsymbol{r}) = z^{(n)}_{\ell}(kr)\boldsymbol{X}_{\ell m}(\theta,\varphi), \tag{A.31a}$$

$$\begin{aligned}\boldsymbol{N}^{(n)}_{\ell m}(\boldsymbol{r}) = &\left(\frac{1}{k}\frac{\mathrm{d}}{\mathrm{d}r}z^{(n)}_{\ell}(kr) + \frac{z^{(n)}_{\ell}(kr)}{kr}\right)\boldsymbol{V}_{\ell m}(\theta,\varphi) \\ &+ \sqrt{\ell(\ell+1)}\frac{z^{(n)}_{\ell}(kr)}{kr}\boldsymbol{W}_{\ell m}(\theta,\varphi),\end{aligned} \tag{A.31b}$$

Consistent with [101, Eqs. (11)].
$\boldsymbol{M}^{(1)}_{\ell m} = \mathrm{i}\mathrm{Rg}\mathbf{M}_{\ell m}$, $\boldsymbol{M}^{(3)}_{\ell m} = \mathrm{i}\mathbf{M}_{\ell m}$, and analogous relations for $\boldsymbol{N}^{(n)}_{\ell m}$ [246, Eqs. (C.14–15)], [117, Eqs. (7–8)].
$\boldsymbol{M}^{(n)}_{\ell m} = (-1)^{\frac{m+|m|}{2}}\left(\boldsymbol{M}^{(n)}_{\mathrm{e}|m|\ell} + \mathrm{i}\,\mathrm{sgn}(m)\boldsymbol{M}^{(n)}_{\mathrm{o}|m|\ell}\right)\mathrm{i}^{\ell}Y_{\ell|m|}$, and analogous relations for $\boldsymbol{N}^{(n)}_{\ell m}$ [93, p. 87ff.].

which solve the vector Helmholtz equation, $\left(\nabla^2 + k^2\right) \boldsymbol{F}(\boldsymbol{r}) = 0$, conveniently expressed in spherical coordinates. Additionally, we have the solutions

$$\boldsymbol{A}^{(n)}_{\ell m,\pm}(\boldsymbol{r}) = \frac{1}{\sqrt{2}} \left( \boldsymbol{N}^{(n)}_{\ell m}(\boldsymbol{r}) \pm \boldsymbol{M}^{(n)}_{\ell m}(\boldsymbol{r}) \right), \tag{A.32}$$

which are Beltrami fields,

$$\boldsymbol{\nabla} \times \boldsymbol{A}^{(n)}_{\ell m,\pm}(\boldsymbol{r}) = \pm k \boldsymbol{A}^{(n)}_{\ell m,\pm}(\boldsymbol{r}). \tag{A.33}$$

*Parity and helicity* · $\boldsymbol{M}^{(n)}_{\ell m}$ and $\boldsymbol{N}^{(n)}_{\ell m}$ are eigenfunctions of the parity operation, or spatial inversion, and Eqs. (A.28) yield

$$\boldsymbol{M}^{(n)}_{\ell m}(-\boldsymbol{r}) = (-1)^{\ell} \boldsymbol{M}^{(n)}_{\ell m}(\boldsymbol{r}), \tag{A.34a}$$

$$\boldsymbol{N}^{(n)}_{\ell m}(-\boldsymbol{r}) = (-1)^{\ell+1} \boldsymbol{N}^{(n)}_{\ell m}(\boldsymbol{r}). \tag{A.34b}$$

As a consequence of $\boldsymbol{M}^{(n)}_{\ell m}$ having opposite parity from $\boldsymbol{N}^{(n)}_{\ell m}$, the linear combinations $\boldsymbol{A}^{(n)}_{\ell m,+}$ and $\boldsymbol{A}^{(n)}_{\ell m,-}$ are not eigenfunctions of parity, as spatial inversion ($\boldsymbol{r} \mapsto -\boldsymbol{r}$) relates the two:

$$\boldsymbol{A}^{(n)}_{\ell m,+}(-\boldsymbol{r}) = (-1)^{\ell+1} \boldsymbol{A}^{(n)}_{\ell m,-}(\boldsymbol{r}). \tag{A.35}$$

Instead, they are eigenfunctions of the helicity operator with eigenvalues $\pm 1$, which follows from Eq. (A.33) after division by $k$,

$$\frac{1}{k} \boldsymbol{\nabla} \times \boldsymbol{A}^{(n)}_{\ell m,\pm}(\boldsymbol{r}) = \pm \boldsymbol{A}^{(n)}_{\ell m,\pm}(\boldsymbol{r}). \tag{A.36}$$

Accordingly, Eq. (A.35) demonstrates a result of spatial inversion and helicity anticommuting.

### A.3.2 *Far field pattern and radiation condition*

*Far field* · We use Eq. (A.11a) to derive the asymptotic behavior of the VSWS far from the origin, $kr \to \infty$.

$$\boldsymbol{M}^{(3)}_{\ell m}(\boldsymbol{r}) \sim (-\mathrm{i})^{\ell+1} \boldsymbol{X}_{\ell m}(\theta, \varphi) \frac{\mathrm{e}^{\mathrm{i}kr}}{kr} \quad (\text{as } kr \to \infty), \tag{A.37a}$$

$$\boldsymbol{N}^{(3)}_{\ell m}(\boldsymbol{r}) \sim (-\mathrm{i})^{\ell} \boldsymbol{V}_{\ell m}(\theta, \varphi) \frac{\mathrm{e}^{\mathrm{i}kr}}{kr} \quad (\text{as } kr \to \infty). \tag{A.37b}$$

We call the angular dependence in front of the common $\mathrm{e}^{\mathrm{i}kr}/kr$ factor the *far field pattern* of the vector fields. For the helicity eigenfunctions, we obtain

$$\boldsymbol{A}^{(3)}_{\ell m,\pm}(\boldsymbol{r}) \sim \frac{(-\mathrm{i})^{\ell+1}}{\sqrt{2}} \left[\mathrm{i}\boldsymbol{V}_{\ell m}(\theta,\varphi) \pm \boldsymbol{X}_{\ell m}(\theta,\varphi)\right] \frac{\mathrm{e}^{\mathrm{i}kr}}{kr} \quad (\text{as } kr \to \infty). \tag{A.38}$$

With

$$\boldsymbol{X}_{\ell m} = X^{\theta}_{\ell m}\hat{\boldsymbol{\theta}} + X^{\varphi}_{\ell m}\hat{\boldsymbol{\varphi}}, \tag{A.39a}$$

where

$$X^{\theta}_{\ell m}(\theta,\varphi) = -\gamma_{\ell m}\pi^{m}_{\ell}(\cos\theta)\mathrm{e}^{\mathrm{i}m\varphi}, \qquad X^{\varphi}_{\ell m}(\theta,\varphi) = -\mathrm{i}\gamma_{\ell m}\tau^{m}_{\ell}(\cos\theta)\mathrm{e}^{\mathrm{i}m\varphi},$$

and

$$\boldsymbol{V}_{\ell m} = X^{\theta}_{\ell m}\hat{\boldsymbol{\varphi}} - X^{\varphi}_{\ell m}\hat{\boldsymbol{\theta}}, \tag{A.39b}$$

Eq. (A.38) reads

$$\boldsymbol{A}^{(3)}_{\ell m,\pm}(\boldsymbol{r}) \sim \underbrace{\frac{-1}{\sqrt{2}}\left(\hat{\boldsymbol{\theta}} \pm \mathrm{i}\hat{\boldsymbol{\varphi}}\right)}_{=\hat{\boldsymbol{e}}_{\pm}(\hat{\boldsymbol{r}})} (-\mathrm{i})^{\ell-1}\left(-\mathrm{i}X^{\varphi}_{\ell m}(\theta,\varphi) \pm X^{\theta}_{\ell m}(\theta,\varphi)\right) \frac{\mathrm{e}^{\mathrm{i}kr}}{kr} \quad (\text{as } kr \to \infty) \tag{A.40}$$

and we recognize the circular polarization vectors defined in Eq. (3.18). Thus, we find that, while the polarization of the helicity eigenfunctions $\boldsymbol{A}^{(n)}_{\ell m,\pm}$ is not generally easily described, in the far field the waves appear circularly polarized again, locally at every $(\theta,\varphi)$.

*Radiation condition* · Equations (A.37) and Eq. (A.38) allow us to verify that the VSWS satisfy the Silver–Müller radiation condition [249, Eq. (7.90)]. For a solution to the vector Helmholtz equation $\boldsymbol{F}(\boldsymbol{r})$, it reads

$$\lim_{r\to\infty} r\left[\hat{\boldsymbol{r}} \times \left[\boldsymbol{\nabla} \times \boldsymbol{F}(\boldsymbol{r})\right] + \mathrm{i}k\boldsymbol{F}(\boldsymbol{r})\right] = 0, \tag{A.41}$$

or, equivalently, in little-o notation,

$$\hat{\boldsymbol{r}} \times \left[\boldsymbol{\nabla} \times \boldsymbol{F}(\boldsymbol{r})\right] + \mathrm{i}k\boldsymbol{F}(\boldsymbol{r}) = o\left(r^{-1}\right). \tag{A.42}$$

Recalling Eqs. (3.12c) and (3.13) and inserting Eqs. (A.37), which represent the $O\left(r^{-1}\right)$ contributions to the fields, we find that all terms cancel out.

Using the same arguments, we find that $\boldsymbol{M}^{(4)}_{\ell m}$, $\boldsymbol{N}^{(4)}_{\ell m}$, and $\boldsymbol{A}^{(4)}_{\ell m,\pm}$ satisfy the modified radiation condition for incoming radiation, which is obtained by replacing $k \mapsto -k$ in Eq. (A.41) or Eq. (A.42).

### A.3.3 *Translation coefficients*

A VSW can be expressed in terms of VSWS evaluated at a different position, expanding it in VSWS centered around a different origin. For matching superscript $n$ [101, Eq. (C.2)],

$$\boldsymbol{A}^{(n)}_{\ell m,\pm}(\boldsymbol{r}) = \sum_{\ell'=1}^{\infty} \sum_{m'=-\ell'}^{\ell'} \left( A^{(1)}_{\ell' m',\ell m}(\boldsymbol{r}-\boldsymbol{r}') \pm B^{(1)}_{\ell' m',\ell m}(\boldsymbol{r}-\boldsymbol{r}') \right) \boldsymbol{A}^{(n)}_{\ell' m',\pm}(\boldsymbol{r}'). \tag{A.43}$$

Additionally, outwards radiating fields ($n = 3$) can be expanded in regular ($n = 1$) fields by [101, Eq. (C.3)]

$$\boldsymbol{A}^{(3)}_{\ell m,\pm}(\boldsymbol{r}) = \sum_{\ell'=1}^{\infty} \sum_{m'=-\ell'}^{\ell'} \left( A^{(3)}_{\ell' m',\ell m}(\boldsymbol{r}-\boldsymbol{r}') \pm B^{(3)}_{\ell' m',\ell m}(\boldsymbol{r}-\boldsymbol{r}') \right) \boldsymbol{A}^{(1)}_{\ell' m',\pm}(\boldsymbol{r}'). \tag{A.44}$$

Note that these expansions do not mix VSWS of opposite helicity eigenvalues, a consequence of the fact that helicity is invariant under translations. For both relations, the translation coefficients for VSWS [250, 251] are given in Eqs. (C1) of Ref. [101] as

$$\begin{aligned} A^{(n)}_{\ell' m',\ell m}(\boldsymbol{r}) &= (-1)^m \mathrm{i}^{\ell'-\ell} \sqrt{\pi \frac{2\ell'+1}{\ell'(\ell'+1)} \frac{2\ell+1}{\ell(\ell+1)}} \\ &\times \sum_p \mathrm{i}^p \sqrt{2p+1} z^{(n)}_p(kr) Y_{p,m-m'}(\theta,\varphi) \begin{pmatrix} \ell & \ell' & p \\ m & -m' & -m+m' \end{pmatrix} \\ &\times \begin{pmatrix} \ell & \ell' & p \\ 0 & 0 & 0 \end{pmatrix} \left[ \ell(\ell+1) + \ell'(\ell'+1) - p(p+1) \right], \end{aligned} \tag{A.45a}$$

and

$$B^{(n)}_{\ell' m',\ell m}(\boldsymbol{r}) = (-1)^m \mathrm{i}^{\ell'-\ell} \sqrt{\pi \frac{2\ell'+1}{\ell'(\ell'+1)} \frac{2\ell+1}{\ell(\ell+1)}}$$
$$\times \sum_p \mathrm{i}^p \sqrt{2p+1} z^{(n)}_p(kr) Y_{p,m-m'}(\theta,\varphi) \begin{pmatrix} \ell & \ell' & p \\ m & -m' & -m+m' \end{pmatrix} \tag{A.45b}$$
$$\times \begin{pmatrix} \ell & \ell' & p-1 \\ 0 & 0 & 0 \end{pmatrix} \sqrt{\left[(\ell+\ell'+1)^2 - p^2\right]\left[p^2 - (\ell-\ell')^2\right]},$$

with the sums running over all values $p$ for which the Wigner $3j$ symbols [252][92, Section 34.2] are nonzero [101]. For convenience, we define the translation matrices $\boldsymbol{C}^{(n)}(\boldsymbol{r})$ with entries

$$C^{(n)}_{\ell' m' \lambda',\ell m \lambda}(\boldsymbol{r}) \coloneqq \delta_{\lambda\lambda'} \left( A^{(n)}_{\ell' m',\ell m}(\boldsymbol{r}) + \lambda B^{(n)}_{\ell' m',\ell m}(\boldsymbol{r}) \right). \tag{A.46}$$

For $n = 1$, the translation coefficients in Eqs. (A.45) satisfy

$$A^{(1)}_{\ell' m',\ell m}(\boldsymbol{r}=0) = \delta_{\ell\ell'}\delta_{mm'}, \qquad B^{(1)}_{\ell' m',\ell m}(\boldsymbol{r}=0) = 0. \tag{A.47}$$

Hence, Eq. (A.43) is trivially satisfied for $\boldsymbol{r} = \boldsymbol{r}'$. Additionally, we find their behavior with regard to parity for real wavenumbers $k$ to

$$A^{(1)}_{\ell' m',\ell m}(-\boldsymbol{r}) = \left( A^{(1)}_{\ell m,\ell' m'}(\boldsymbol{r}) \right)^*, \qquad B^{(1)}_{\ell' m',\ell m}(-\boldsymbol{r}) = \left( B^{(1)}_{\ell m,\ell' m'}(\boldsymbol{r}) \right)^*. \tag{A.48}$$

Equations (A.47) and (A.48) follow from the explicit expressions in Eqs. (A.45) using Eqs. (A.18) and (A.21) for the spherical harmonics and Eq. (A.10a) for the spherical Bessel functions, together with properties of the Wigner $3j$ symbols found in Sections 34.2 and 34.3 of Ref. [92]. For the matrix $\boldsymbol{C}^{(1)}(\boldsymbol{r})$, Eqs. (A.47) and (A.48) yield

$$\boldsymbol{C}^{(1)}(\boldsymbol{r}=0) = \mathbf{1}, \qquad \boldsymbol{C}^{(1)}(-\boldsymbol{r}) = \left( \boldsymbol{C}^{(1)}(\boldsymbol{r}) \right)^{\mathsf{H}}. \tag{A.49}$$

### A.3.4 *Rotations of vector spherical waves*

Rotations of VSWS are expressed in terms of Wigner-D-matrices [253, 254]. We represent a general rotation by the three Euler angles $\alpha$, $\beta$, and $\gamma$. These

correspond to three consecutive rotations around the axes of the unaffected coordinate system (i.e., extrinsic rotations) following the sequence $z$-$y$-$z$. Applied to a VSW, such rotation is represented by [91, Eq. (2.66)]

$$\boldsymbol{R}(\alpha,\beta,\gamma)\boldsymbol{A}^{(n)}_{\ell m,\pm}\big(\boldsymbol{R}^{-1}(\alpha,\beta,\gamma)\boldsymbol{r}\big) = \sum_{m'=-\ell}^{\ell} D^{\ell}_{mm'}(\alpha,\beta,\gamma)\boldsymbol{A}^{(n)}_{\ell m',\pm}(\boldsymbol{r}), \tag{A.50}$$

where

$$\boldsymbol{R}(\alpha,\beta,\gamma) = \boldsymbol{R}_z(\alpha)\boldsymbol{R}_y(\beta)\boldsymbol{R}_z(\gamma) \tag{A.51a}$$

and

$$\boldsymbol{R}_z(\alpha) = \begin{pmatrix} \cos\alpha & -\sin\alpha & 0 \\ \sin\alpha & \cos\alpha & 0 \\ 0 & 0 & 1 \end{pmatrix}, \quad \boldsymbol{R}_y(\alpha) = \begin{pmatrix} \cos\beta & 0 & -\sin\beta \\ 0 & 1 & 0 \\ \sin\beta & 0 & \cos\beta \end{pmatrix}. \tag{A.51b}$$

Note that the order in which the three elemental rotations are applied is determined by Eq. (A.51a) from right to left, that is, the first rotation is about an angle of $\gamma$, the second about $\beta$, and the final one about $\alpha$. As can be seen from Eq. (A.50), rotations only mix VSWS of different multipolar order $m$, while the multipolar degree $\ell$ and the helicity eigenvalue remain invariant.

### A.3.5 *Conversions between spherical and plane waves*

*Integral representations of spherical waves* · From Refs. [255, 256] we get the integral representations for the regular VSWS,

$$\boldsymbol{M}^{(1)}_{\ell m}(\boldsymbol{r}) = \frac{1}{4\pi \mathrm{i}^{\ell}} \iint \mathrm{d}\Omega_{\boldsymbol{k}}\, \boldsymbol{X}_{\ell m}(\theta_{\boldsymbol{k}},\varphi_{\boldsymbol{k}})\mathrm{e}^{\mathrm{i}\boldsymbol{k}\cdot\boldsymbol{r}}, \tag{A.52a}$$

$$\boldsymbol{N}^{(1)}_{\ell m}(\boldsymbol{r}) = \frac{1}{4\pi \mathrm{i}^{\ell-1}} \iint \mathrm{d}\Omega_{\boldsymbol{k}}\, \boldsymbol{V}_{\ell m}(\theta_{\boldsymbol{k}},\varphi_{\boldsymbol{k}})\mathrm{e}^{\mathrm{i}\boldsymbol{k}\cdot\boldsymbol{r}}, \tag{A.52b}$$

where $\boldsymbol{k} = k\hat{\boldsymbol{k}}$, with $k$ being the wavenumber implicit in the VSWS (the parameter appearing in the vector Helmholtz equation) and $\hat{\boldsymbol{k}}$ the radial unit

vector corresponding to $(\theta_{\boldsymbol{k}}, \varphi_{\boldsymbol{k}})$. Recalling their definition in Eqs. (3.17), we can hence express the VSWS in terms of the vector plane waves (VPWS),

$$\boldsymbol{M}^{(1)}_{\ell m}(\boldsymbol{r}) = \iint \mathrm{d}\Omega_{\boldsymbol{k}} \left( \frac{-X^{\theta}_{\ell m}(\theta_{\boldsymbol{k}}, \varphi_{\boldsymbol{k}})}{4\pi \mathrm{i}^{\ell}} \boldsymbol{N}_{\hat{\boldsymbol{k}}}(\boldsymbol{r}) + \frac{X^{\varphi}_{\ell m}(\theta_{\boldsymbol{k}}, \varphi_{\boldsymbol{k}})}{4\pi \mathrm{i}^{\ell-1}} \boldsymbol{M}_{\hat{\boldsymbol{k}}}(\boldsymbol{r}) \right), \tag{A.53a}$$

$$\boldsymbol{N}^{(1)}_{\ell m}(\boldsymbol{r}) = \iint \mathrm{d}\Omega_{\boldsymbol{k}} \left( \frac{X^{\varphi}_{\ell m}(\theta_{\boldsymbol{k}}, \varphi_{\boldsymbol{k}})}{4\pi \mathrm{i}^{\ell-1}} \boldsymbol{N}_{\hat{\boldsymbol{k}}}(\boldsymbol{r}) + \frac{-X^{\theta}_{\ell m}(\theta_{\boldsymbol{k}}, \varphi_{\boldsymbol{k}})}{4\pi \mathrm{i}^{\ell}} \boldsymbol{M}_{\hat{\boldsymbol{k}}}(\boldsymbol{r}) \right). \tag{A.53b}$$

For the radiating VSWS, the integral representations are given, for $z > 0$, as

$$\boldsymbol{M}^{(3)}_{\ell m}(\boldsymbol{r}) = \frac{1}{2\pi \mathrm{i}^{\ell}} \iint_{\mathbb{R}^2} \frac{\mathrm{d}k_x \, \mathrm{d}k_y}{\zeta k} \, \boldsymbol{X}_{\ell m}(\theta_{\boldsymbol{k}}, \varphi_{\boldsymbol{k}}) \mathrm{e}^{\mathrm{i}\boldsymbol{k}\cdot\boldsymbol{r}}, \tag{A.54a}$$

$$\boldsymbol{N}^{(3)}_{\ell m}(\boldsymbol{r}) = \frac{1}{2\pi \mathrm{i}^{\ell-1}} \iint_{\mathbb{R}^2} \frac{\mathrm{d}k_x \, \mathrm{d}k_y}{\zeta k} \, \boldsymbol{V}_{\ell m}(\theta_{\boldsymbol{k}}, \varphi_{\boldsymbol{k}}) \mathrm{e}^{\mathrm{i}\boldsymbol{k}\cdot\boldsymbol{r}}. \tag{A.54b}$$

For $z < 0$, Eqs. (A.34) may be used. Here, $\boldsymbol{k} = k\hat{\boldsymbol{k}} = (k_x, k_y, \mathrm{sgn}(z)\zeta)^{\mathsf{T}}$ in Cartesian coordinates, where $\zeta := \sqrt{k^2 - k_x^2 - k_y^2}$ with $\arg\zeta \in [0, \pi)$. The angles $(\theta_{\boldsymbol{k}}, \varphi_{\boldsymbol{k}})$ are determined by

$$\cos\theta_{\boldsymbol{k}} = \frac{\mathrm{sgn}(z)\zeta}{k}, \qquad \varphi_{\boldsymbol{k}} = \mathrm{atan2}\big(k_y, k_x\big). \tag{A.55}$$

The combination $\mathrm{sgn}(z)\zeta$ ensures that only waves, which exponentially decay with increasing distance to the $xy$-plane, contribute in the respective half-spaces $z \gtrless 0$. For positive $z$, the integral measure of Eqs. (A.54) is alternatively expressed as

$$\iint_{\mathbb{R}^2} \frac{\mathrm{d}k_x \, \mathrm{d}k_y}{\zeta k} \equiv \mathrm{sgn}(z) \int_0^{2\pi} \mathrm{d}\varphi_{\boldsymbol{k}} \int_0^{\frac{\pi}{2} - \mathrm{i}\infty} \sin\theta_{\boldsymbol{k}} \mathrm{d}\theta_{\boldsymbol{k}} \,, \tag{A.56}$$

with the integration contour for $\theta_{\boldsymbol{k}}$ shown on the side. For $z < 0$, the bounds of integration for $\theta_{\boldsymbol{k}}$ are $(\pi, \frac{\pi}{2} + \mathrm{i}\infty)$, the corresponding contour again passing through $\frac{\pi}{2}$. Note that functions depending on $\theta_{\boldsymbol{k}}$ have to be evaluated in terms of their analytic continuation, since the angle is now generally complex. The

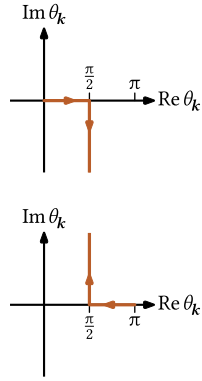


Integration contours for $z > 0$ (upper panel) and $z < 0$ (lower panel).

unit vectors in Eq. (3.16) behave accordingly. Writing Eqs. (A.54) in terms of VPWS yields

$$\boldsymbol{M}^{(3)}_{\ell m}(\boldsymbol{r}) = \iint_{\mathbb{R}^2} \frac{\mathrm{d}k_x\,\mathrm{d}k_y}{\zeta k} \left( \frac{-X^{\theta}_{\ell m}(\theta_{\boldsymbol{k}}, \varphi_{\boldsymbol{k}})}{2\pi \mathrm{i}^{\ell}} \boldsymbol{N}_{\hat{\boldsymbol{k}}}(\boldsymbol{r}) + \frac{X^{\varphi}_{\ell m}(\theta_{\boldsymbol{k}}, \varphi_{\boldsymbol{k}})}{2\pi \mathrm{i}^{\ell-1}} \boldsymbol{M}_{\hat{\boldsymbol{k}}}(\boldsymbol{r}) \right), \tag{A.57a}$$

$$\boldsymbol{N}^{(3)}_{\ell m}(\boldsymbol{r}) = \iint_{\mathbb{R}^2} \frac{\mathrm{d}k_x\,\mathrm{d}k_y}{\zeta k} \left( \frac{X^{\varphi}_{\ell m}(\theta_{\boldsymbol{k}}, \varphi_{\boldsymbol{k}})}{2\pi \mathrm{i}^{\ell-1}} \boldsymbol{N}_{\hat{\boldsymbol{k}}}(\boldsymbol{r}) + \frac{-X^{\theta}_{\ell m}(\theta_{\boldsymbol{k}}, \varphi_{\boldsymbol{k}})}{2\pi \mathrm{i}^{\ell}} \boldsymbol{M}_{\hat{\boldsymbol{k}}}(\boldsymbol{r}) \right), \tag{A.57b}$$

for $z \gtrless 0$. Figure A.1 shows the result and discusses the limitations of using Eqs. (A.57) to numerically approximate VSWS by superpositions of VPWS. For their corresponding Beltrami fields, Eqs. (A.53) and (A.57) give

$$\boldsymbol{A}^{(1)}_{\ell m,\pm} = \iint \mathrm{d}\Omega_{\boldsymbol{k}} \left( \frac{X^{\varphi}_{\ell m}(\theta_{\boldsymbol{k}}, \varphi_{\boldsymbol{k}})}{4\pi \mathrm{i}^{\ell-1}} \pm \frac{-X^{\theta}_{\ell m}(\theta_{\boldsymbol{k}}, \varphi_{\boldsymbol{k}})}{4\pi \mathrm{i}^{\ell}} \right) \boldsymbol{A}_{\hat{\boldsymbol{k}},\pm}(\boldsymbol{r}) \tag{A.58}$$

and

$$\boldsymbol{A}^{(3)}_{\ell m,\pm} = \iint_{\mathbb{R}^2} \frac{\mathrm{d}k_x\,\mathrm{d}k_y}{\zeta k} \left( \frac{X^{\varphi}_{\ell m}(\theta_{\boldsymbol{k}}, \varphi_{\boldsymbol{k}})}{2\pi \mathrm{i}^{\ell-1}} \pm \frac{-X^{\theta}_{\ell m}(\theta_{\boldsymbol{k}}, \varphi_{\boldsymbol{k}})}{2\pi \mathrm{i}^{\ell}} \right) \boldsymbol{A}_{\hat{\boldsymbol{k}},\pm}(\boldsymbol{r}). \tag{A.59}$$

For completeness, we also give the integral representation for the scalar spherical waves, defined in Eq. (3.10), [256, Eqs. (3) and (19)]

$$f^{(1)}_{\ell m}(\boldsymbol{r}) = \frac{1}{4\pi \mathrm{i}^{\ell}} \iint \mathrm{d}\Omega_{\boldsymbol{k}}\, Y_{\ell m}(\theta_{\boldsymbol{k}}, \varphi_{\boldsymbol{k}}) \mathrm{e}^{\mathrm{i}\boldsymbol{k}\cdot\boldsymbol{r}}, \tag{A.60a}$$

$$f^{(3)}_{\ell m}(\boldsymbol{r}) = \frac{1}{2\pi \mathrm{i}^{\ell}} \iint_{\mathbb{R}^2} \frac{\mathrm{d}k_x\,\mathrm{d}k_y}{\zeta k} Y_{\ell m}(\theta_{\boldsymbol{k}}, \varphi_{\boldsymbol{k}}) \mathrm{e}^{\mathrm{i}\boldsymbol{k}\cdot\boldsymbol{r}}, \qquad z > 0. \tag{A.60b}$$

*Two-dimensional lattice sums* · We can expand the combined field of a two-dimensional periodic arrangement of singular VSWS in VPWS based on Eqs. (A.57). As discussed in Fig. A.1, numerically approximating a single VSW suffers from artifacts due to the discrete evaluation of the integrand in Eqs. (A.57). However, the naturally arising pattern of such discretization is precisely that of periodically repeated VSWS. The expressions given here are equivalent to Eqs. (34) and (E.5) of Ref. [101].

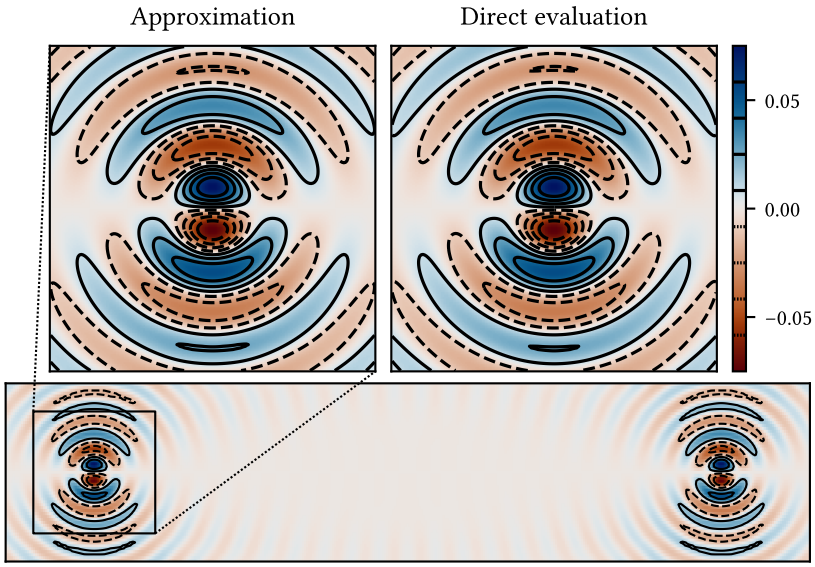


*Figure* A.1: *Approximation of a vector spherical wave using plane waves* · The plots show $\mathrm{Re}\, \boldsymbol{N}_{\ell m}^{(3)} \cdot \hat{\boldsymbol{y}}$, the real part of the out-of-plane component, evaluated in the $xz$-plane for $\ell = 2$ and $m = -1$. The bottom panel and the detail view in the top left panel show the result of using Eq. (A.57b) to numerically approximate the vector spherical wave. The integral is approximated as a Riemann sum, sampling the integrand at 10 201 points; 101 points equidistantly distributed in the range $[-2.15k, 2.15k]$ for $k_x$ and $k_y$ each. A comparison with the directly evaluated vector spherical wave shown in the top right panel highlights the excellent agreement of the fields obtained near the origin. However, as a result of the equidistant sampling of $k_x$, $k_y$, the approximated field repeats periodically in the $xy$-plane with periodicities $2\pi/\Delta k_i$, where $\Delta k_i$, $i \in \{x, y\}$, are the sampling step sizes. Such an artifact of the approximation is visible on the right of the extended bottom panel as a perfect replica of the spherical wave pattern. Colormap from Refs. [154, 155].

We consider a two-dimensional lattice $L_2 = \{n_1\boldsymbol{a}_1 + n_2\boldsymbol{a}_2 \,|\, n_1, n_2 \in \mathbb{Z}\}$ with basis vectors $\boldsymbol{a}_i$ in the $xy$-plane. We denote its corresponding reciprocal lattice as $L_2^*$. The derivation makes use of the Poisson summation formula [101, Eq. (E.3)],

$$\sum_{\boldsymbol{R}\in L_2} \mathrm{e}^{\mathrm{i}\boldsymbol{k}\cdot\boldsymbol{R}} = \frac{(2\pi)^2}{A} \sum_{\boldsymbol{G}\in L_2^*} \delta^{(2)}(\boldsymbol{k}-\boldsymbol{G}), \tag{A.61}$$

with $A$ being the area of a unit cell. Lattice sums over periodically repeated singular VSWS then become

$$\sum_{\boldsymbol{R}\in L_2} \boldsymbol{M}^{(3)}_{\ell m}(\boldsymbol{r}-\boldsymbol{R})\mathrm{e}^{\mathrm{i}\boldsymbol{k}_\parallel\cdot\boldsymbol{R}} = \frac{2\pi}{\mathrm{i}^\ell A} \sum_{(k_x,k_y)\in L_2^*+\{\boldsymbol{k}_\parallel\}} \frac{1}{\zeta k}\Big(-X^\theta_{\ell m}(\theta_{\boldsymbol{k}},\varphi_{\boldsymbol{k}})\boldsymbol{N}_{\hat{\boldsymbol{k}}}(\boldsymbol{r}) + \mathrm{i}X^\varphi_{\ell m}(\theta_{\boldsymbol{k}},\varphi_{\boldsymbol{k}})\boldsymbol{M}_{\hat{\boldsymbol{k}}}(\boldsymbol{r})\Big), \tag{A.62a}$$

$$\sum_{\boldsymbol{R}\in L_2} \boldsymbol{N}^{(3)}_{\ell m}(\boldsymbol{r}-\boldsymbol{R})\mathrm{e}^{\mathrm{i}\boldsymbol{k}_\parallel\cdot\boldsymbol{R}} = \frac{2\pi}{\mathrm{i}^\ell A} \sum_{(k_x,k_y)\in L_2^*+\{\boldsymbol{k}_\parallel\}} \frac{1}{\zeta k}\Big(\mathrm{i}X^\varphi_{\ell m}(\theta_{\boldsymbol{k}},\varphi_{\boldsymbol{k}})\boldsymbol{N}_{\hat{\boldsymbol{k}}}(\boldsymbol{r}) - X^\theta_{\ell m}(\theta_{\boldsymbol{k}},\varphi_{\boldsymbol{k}})\boldsymbol{M}_{\hat{\boldsymbol{k}}}(\boldsymbol{r})\Big), \tag{A.62b}$$

and

$$\sum_{\boldsymbol{R}\in L_2} \boldsymbol{A}^{(3)}_{\ell m,\pm}(\boldsymbol{r}-\boldsymbol{R})\mathrm{e}^{\mathrm{i}\boldsymbol{k}_\parallel\cdot\boldsymbol{R}} = \frac{2\pi}{\mathrm{i}^\ell A} \sum_{(k_x,k_y)\in L_2^*+\{\boldsymbol{k}_\parallel\}} \frac{1}{\zeta k} \times \Big(\mathrm{i}X^\varphi_{\ell m}(\theta_{\boldsymbol{k}},\varphi_{\boldsymbol{k}}) \mp X^\theta_{\ell m}(\theta_{\boldsymbol{k}},\varphi_{\boldsymbol{k}})\Big)\boldsymbol{A}_{\hat{\boldsymbol{k}},\pm}(\boldsymbol{r}). \tag{A.63}$$

In the equations above, $\boldsymbol{k}_\parallel$ is a vector in the $xy$-plane, which determines the relative phase between different unit cells by means of the exponential on the left-hand side, akin to a Bloch phase. The sum for $\left(k_x, k_y\right)$ runs over

$$L_2^* + \left\{\boldsymbol{k}_\parallel\right\} = \left\{\boldsymbol{G} + \boldsymbol{k}_\parallel \,\middle|\, \boldsymbol{G}\in L_2^*\right\}. \tag{A.64}$$

$\left(k_x, k_y\right)$ determine $\boldsymbol{k}$ and $\zeta$ as defined right before Eq. (A.55).

*Spherical wave expansion of plane waves* · Using the expansion coefficients of plane waves given in Ref. [117, Eqs. (16) and (17)] allows us to write the VPWS for real $\boldsymbol{k}$ in terms of VSWS, after adjusting for differences in notation,

$$\boldsymbol{M}_{\hat{\boldsymbol{k}}}(\boldsymbol{r}) = 4\pi \sum_{\ell=1}^{\infty} \sum_{m=-\ell}^{\ell} \mathrm{i}^{\ell} \left( -\mathrm{i} X_{\ell m}^{\theta *}(\theta_{\boldsymbol{k}}, \varphi_{\boldsymbol{k}}) \boldsymbol{N}_{\ell m}^{(1)}(\boldsymbol{r}) + X_{\ell m}^{\varphi *}(\theta_{\boldsymbol{k}}, \varphi_{\boldsymbol{k}}) \boldsymbol{M}_{\ell m}^{(1)}(\boldsymbol{r}) \right), \tag{A.65a}$$

$$\boldsymbol{N}_{\hat{\boldsymbol{k}}}(\boldsymbol{r}) = 4\pi \sum_{\ell=1}^{\infty} \sum_{m=-\ell}^{\ell} \mathrm{i}^{\ell} \left( X_{\ell m}^{\varphi *}(\theta_{\boldsymbol{k}}, \varphi_{\boldsymbol{k}}) \boldsymbol{N}_{\ell m}^{(1)}(\boldsymbol{r}) - \mathrm{i} X_{\ell m}^{\theta *}(\theta_{\boldsymbol{k}}, \varphi_{\boldsymbol{k}}) \boldsymbol{M}_{\ell m}^{(1)}(\boldsymbol{r}) \right). \tag{A.65b}$$

Consequently, we find

$$\boldsymbol{A}_{\hat{\boldsymbol{k}},\pm}(\boldsymbol{r}) = 4\pi \sum_{\ell=1}^{\infty} \sum_{m=-\ell}^{\ell} \mathrm{i}^{\ell} \left( X_{\ell m}^{\varphi *}(\theta_{\boldsymbol{k}}, \varphi_{\boldsymbol{k}}) \mp \mathrm{i} X_{\ell m}^{\theta *}(\theta_{\boldsymbol{k}}, \varphi_{\boldsymbol{k}}) \right) \boldsymbol{A}_{\ell m,\pm}^{(1)}(\boldsymbol{r}), \tag{A.66}$$

which is equivalent to Eq. (31) of Ref. [101]. Note that the VPWS are regular everywhere and, accordingly, only the regular (superscript (1)) VSWS are suitable for the expansion.

For completeness, we add the expansion of a scalar plane wave, known as the Rayleigh expansion,

$$\begin{aligned} \mathrm{e}^{\mathrm{i}\boldsymbol{k}\cdot\boldsymbol{r}} &= 4\pi \sum_{\ell=0}^{\infty} \sum_{m=-\ell}^{\ell} \mathrm{i}^{\ell} j_{\ell}(kr) Y_{\ell m}^{*}(\theta_{\boldsymbol{k}}, \varphi_{\boldsymbol{k}}) Y_{\ell m}(\theta, \varphi) \\ &= 4\pi \sum_{\ell=0}^{\infty} \sum_{m=-\ell}^{\ell} \mathrm{i}^{\ell} Y_{\ell m}^{*}(\theta_{\boldsymbol{k}}, \varphi_{\boldsymbol{k}}) f_{\ell m}^{(1)}(\boldsymbol{r}). \end{aligned} \tag{A.67}$$

# B *On Different Expressions of Electromagnetic Helicity*

In Section 3.2, we discuss the helicity of electromagnetic fields. Two different expressions for the electromagnetic helicity are given, one obtained as the Noether charge associated with the duality symmetry of Maxwell's equations, Eq. (3.30), and the other obtained as the expectation value of the helicity operator using the conformally invariant scalar product for free electromagnetic fields, Eq. (3.37). Here, we derive the equivalence of the two different expressions. Such equivalence was already reported in Ref. [83], starting from the expression of the expectation value and considering complex fields (i.e., their positive frequency restriction, or analytic signal) in particular. The transition between fields and potentials followed after introducing their relationship involving time derivatives. Here, we approach the demonstration of equivalence the other way, starting from the Noether charge involving real-valued fields. We relate the potentials to the fields via their curl, the operator deeply embedded in the dynamical consideration of helicity, and make use of the Helmholtz decomposition. The first step was already made in Eq. (3.32) and we continue in Section B.2. In the process, we identify the representation of the helicity operator acting on plane wave components, which we introduce first. We consider the fields in vacuum and note that a homogeneous, isotropic, achiral, nondispersive, and lossless background medium can be accommodated for by replacing the constants of vacuum, $\varepsilon_0$, $\mu_0$, and $c_0$, accordingly.

## B.1 *Preliminaries*

Solutions to the vector Helmholtz equation can be represented by continuous superpositions of monochromatic plane waves. We introduce such representation for real-valued solutions and define the plane wave components of the fields. We briefly comment on complex-valued fields in Section B.2, for which these considerations could be readily extended.

*Plane wave components of real-valued solutions to the Helmholtz equation*

We consider the Fourier transform $\tilde{\boldsymbol{F}}(\boldsymbol{r},\omega)$ of a real-valued field $\boldsymbol{F}(\boldsymbol{r},t)$, related by Eqs. (2.9). For suitable functions, we express such fields via their three-dimensional Fourier transform with respect to the spatial variable $\boldsymbol{r}$ as[1]

$$\tilde{\boldsymbol{F}}(\boldsymbol{r},\omega) = \frac{1}{\sqrt{2\pi}^3} \iiint_{\mathbb{R}^3} \mathrm{d}^3k\, \underline{\boldsymbol{F}}(\boldsymbol{k},\omega) \mathrm{e}^{\mathrm{i}\boldsymbol{k}\cdot\boldsymbol{r}}. \tag{B.1}$$

1 For the spatial Fourier transform, we choose the opposite sign convention for the exponential functions as compared to Eqs. (2.9).

For fields that satisfy the vector Helmholtz equation in free space, where the wavenumber $k = \omega/c_0$ in Eq. (3.8), we have

$$\left(\nabla^2 + \frac{\omega^2}{c_0^2}\right) \tilde{\boldsymbol{F}}(\boldsymbol{r},\omega) = \frac{1}{\sqrt{2\pi}^3} \iiint_{\mathbb{R}^3} \mathrm{d}^3k \left(-|\boldsymbol{k}|^2 + \frac{\omega^2}{c_0^2}\right) \underline{\boldsymbol{F}}(\boldsymbol{k},\omega) \mathrm{e}^{\mathrm{i}\boldsymbol{k}\cdot\boldsymbol{r}} \stackrel{!}{=} 0. \tag{B.2}$$

$\underline{\boldsymbol{F}}(\boldsymbol{k},\omega)$ may be nonzero only for $c_0|\boldsymbol{k}| = |\omega|$. Consequently, we restrict[2]

$$\underline{\boldsymbol{F}}(\boldsymbol{k},\omega) = \sqrt{\frac{\pi}{2}} \left[\delta(\omega - c_0|\boldsymbol{k}|)\boldsymbol{F}(\boldsymbol{k}) + \delta(\omega + c_0|\boldsymbol{k}|)\boldsymbol{F}^*(-\boldsymbol{k})\right], \tag{B.3}$$

2 The restriction imposed by $c_0|\boldsymbol{k}| = |\omega|$ is called the *on-shell* condition. For fixed $\omega$, it restricts the domain of integration in Eq. (B.1) to a sphere of radius $\omega/c_0$.

where the prefactor has been chosen for convenience. The form of the right-hand side above is fixed by the conjugate symmetry of $\tilde{\boldsymbol{F}}(\boldsymbol{r},\omega)$ with respect to $\omega$, which is a consequence of the field being real-valued in time domain. After applying the inverse Fourier transform to Eq. (B.1) and inserting Eq. (B.3), we obtain the original field as

$$\begin{aligned}
\boldsymbol{F}(\boldsymbol{r},t) &= \frac{1}{2\sqrt{2\pi}^3} \int_{-\infty}^{\infty} \mathrm{d}\omega \iiint_{\mathbb{R}^3} \mathrm{d}^3k \big[\delta(\omega - c_0|\boldsymbol{k}|)\boldsymbol{F}(\boldsymbol{k}) \\
&\qquad + \delta(\omega + c_0|\boldsymbol{k}|)\boldsymbol{F}^*(-\boldsymbol{k})\big] \mathrm{e}^{\mathrm{i}\boldsymbol{k}\cdot\boldsymbol{r} - \mathrm{i}\omega t} \\
&= \frac{1}{2\sqrt{2\pi}^3} \iiint_{\mathbb{R}^3} \mathrm{d}^3k \left(\boldsymbol{F}(\boldsymbol{k})\mathrm{e}^{-\mathrm{i}c_0|\boldsymbol{k}|t} + \boldsymbol{F}^*(-\boldsymbol{k})\mathrm{e}^{\mathrm{i}c_0|\boldsymbol{k}|t}\right) \mathrm{e}^{\mathrm{i}\boldsymbol{k}\cdot\boldsymbol{r}} \\
&= \frac{1}{2}\left(\frac{1}{\sqrt{2\pi}^3} \iiint_{\mathbb{R}^3} \mathrm{d}^3k\, \boldsymbol{F}(\boldsymbol{k}) \mathrm{e}^{\mathrm{i}\boldsymbol{k}\cdot\boldsymbol{r} - \mathrm{i}c_0|\boldsymbol{k}|t} + \text{c.c.}\right).
\end{aligned} \tag{B.4}$$

The shorthand notation "c.c." is introduced to denote the complex conjugate of the term preceding it and $\mathrm{Re}\{\cdot\} = \frac{1}{2}(\cdot + \text{c.c.})$. Without taking the real part, the integral in the last line yields the analytic signal of $\boldsymbol{F}(\boldsymbol{r},t)$ [68, Section 10.2]. Identifying the exponential as monochromatic plane waves with wave vector $\boldsymbol{k}$ and nonnegative angular frequency $c_0|\boldsymbol{k}|$, we call $\boldsymbol{F}(\boldsymbol{k})$ the plane wave components of $\boldsymbol{F}(\boldsymbol{r},t)$.

## B.2 *Demonstration of Equivalence*

Equations (3.30) and (3.32) give the helicity of the free electromagnetic field

$$\begin{aligned} h_{\mathrm{em}} &= \frac{\varepsilon_0}{2} \iiint_{\mathbb{R}^3} \mathrm{d}^3 r \left( c_0 \boldsymbol{A}(\boldsymbol{r},t) \cdot \boldsymbol{B}(\boldsymbol{r},t) - c_0^{-1} \boldsymbol{C}(\boldsymbol{r},t) \cdot \boldsymbol{E}(\boldsymbol{r},t) \right) \\ &= \frac{\varepsilon_0}{8\pi} \iiint_{\mathbb{R}^3} \mathrm{d}^3 r \iiint_{\mathbb{R}^3} \mathrm{d}^3 r' \left( c_0 \frac{\boldsymbol{B}(\boldsymbol{r},t) \cdot [\boldsymbol{\nabla}' \times \boldsymbol{B}(\boldsymbol{r}',t)]}{|\boldsymbol{r}-\boldsymbol{r}'|} \right. \\ &\qquad \left. + c_0^{-1} \frac{\boldsymbol{E}(\boldsymbol{r},t) \cdot [\boldsymbol{\nabla}' \times \boldsymbol{E}(\boldsymbol{r}',t)]}{|\boldsymbol{r}-\boldsymbol{r}'|} \right). \end{aligned} \tag{B.5}$$

To obtain the second line, we use the Helmholtz decomposition of the vector potentials in Eqs. (3.31). Focusing on the part of the integrand containing $\boldsymbol{B}(\boldsymbol{r},t)$, we introduce the plane wave components using Eq. (B.4).

$$\begin{aligned} \boldsymbol{B}(\boldsymbol{r},t) \cdot [\boldsymbol{\nabla}' \times \boldsymbol{B}(\boldsymbol{r}',t)] = \frac{1}{4(2\pi)^3} \iiint_{\mathbb{R}^3} \mathrm{d}^3 k \iiint_{\mathbb{R}^3} \mathrm{d}^3 k' \Big\{ \\ \left( \boldsymbol{B}(\boldsymbol{k}) \mathrm{e}^{\mathrm{i}\boldsymbol{k}\cdot\boldsymbol{r} - \mathrm{i}c_0|\boldsymbol{k}|t} + \mathrm{c.c.} \right) \cdot \left( \mathrm{i}\boldsymbol{k}' \times \boldsymbol{B}(\boldsymbol{k}') \mathrm{e}^{\mathrm{i}\boldsymbol{k}'\cdot\boldsymbol{r}' - \mathrm{i}c_0|\boldsymbol{k}'|t} + \mathrm{c.c.} \right) \Big\}, \end{aligned} \tag{B.6}$$

where we have applied the curl. In Eq. (B.5), $h_{\mathrm{em}}$ was obtained as the conserved Noether charge associated with the duality symmetry. As such, it is time-independent, that is, $\frac{\mathrm{d}}{\mathrm{d}t} h_{\mathrm{em}} = 0$. This allows us to significantly simplify the product inside the curly braces of Eq. (B.6), as only terms without the time-dependent exponential may contribute. In the derivation this may be enforced by averaging $h_{\mathrm{em}}$ over time, which, for a constant, does not change its value. The time average removes all time-dependent terms from the integrand and only allows contributions for $|\boldsymbol{k}| = |\boldsymbol{k}'|$. Furthermore, only two of the four terms obtained after expanding the dot product in the second line of Eq. (B.6) are time-independent, and we find them to be complex conjugates of one another. For the term inside the curly braces, this yields

$$\Big\{ \ldots \Big\} = \boldsymbol{B}^*(\boldsymbol{k}) \cdot [\mathrm{i}\boldsymbol{k}' \times \boldsymbol{B}(\boldsymbol{k}')] \, \mathrm{e}^{\mathrm{i}\boldsymbol{k}'\cdot\boldsymbol{r}' - \mathrm{i}\boldsymbol{k}\cdot\boldsymbol{r}} + \mathrm{c.c.} \tag{B.7}$$

After inserting Eqs. (B.6) and (B.7) and analogous terms for the $\boldsymbol{E}$-part of the integrand into Eq. (B.5) and changing the order of integration, we find that $h_{\mathrm{em}}$ depends on

$$\iiint_{\mathbb{R}^3} \mathrm{d}^3 r \iiint_{\mathbb{R}^3} \mathrm{d}^3 r' \, \frac{\mathrm{e}^{\mathrm{i}\boldsymbol{k}'\cdot\boldsymbol{r}'-\mathrm{i}\boldsymbol{k}\cdot\boldsymbol{r}}}{|\boldsymbol{r}-\boldsymbol{r}'|} = \iiint_{\mathbb{R}^3} \mathrm{d}^3 r \, \mathrm{e}^{\mathrm{i}(\boldsymbol{k}'-\boldsymbol{k})\cdot\boldsymbol{r}} \iiint_{\mathbb{R}^3} \mathrm{d}^3 r'' \, \frac{1}{|\boldsymbol{r}''|} \mathrm{e}^{\mathrm{i}\boldsymbol{k}'\cdot\boldsymbol{r}''} , \tag{B.8}$$

where the right-hand side follows after a change of variables, $\boldsymbol{r}'' = \boldsymbol{r}' - \boldsymbol{r}$. The first integral on the right-hand side yields $(2\pi)^3\delta^{(3)}(\boldsymbol{k}-\boldsymbol{k}')$, and we recognize the second one as the three-dimensional Fourier transform of the function $1/|\boldsymbol{r}|$ (up to prefactors), which can be readily solved in spherical coordinates:

$$\iiint_{|\boldsymbol{r}|\leq R} \mathrm{d}^3 r \, \frac{1}{|\boldsymbol{r}|} \mathrm{e}^{\mathrm{i}\boldsymbol{k}'\cdot\boldsymbol{r}} = \frac{4\pi}{|\boldsymbol{k}'|^2} \left[1 - \cos(|\boldsymbol{k}'|R)\right] . \tag{B.9}$$

Inside Eq. (B.5), we let $R \to \infty$ and use the Riemann–Lebesgue lemma to drop the cosine term. Collecting all terms, we find

$$\begin{aligned} h_{\mathrm{em}} &= \frac{\varepsilon_0}{16(2\pi)^4} \iiint_{\mathbb{R}^3} \mathrm{d}^3 k \iiint_{\mathbb{R}^3} \mathrm{d}^3 k' \, \frac{2(2\pi)^4\delta^{(3)}(\boldsymbol{k}-\boldsymbol{k}')}{|\boldsymbol{k}'|^2} \Big\{ \\ &\qquad c_0 \boldsymbol{B}^*(\boldsymbol{k}) \cdot [\mathrm{i}\boldsymbol{k}' \times \boldsymbol{B}(\boldsymbol{k}')] + c_0^{-1} \boldsymbol{E}^*(\boldsymbol{k}) \cdot [\mathrm{i}\boldsymbol{k}' \times \boldsymbol{E}(\boldsymbol{k}')] \Big\} + \mathrm{c.c.} \\ &= \frac{\varepsilon_0}{8} \iiint_{\mathbb{R}^3} \frac{\mathrm{d}^3 k}{c_0|\boldsymbol{k}|} \left\{ c_0^2 \boldsymbol{B}^*(\boldsymbol{k}) \cdot \left[ \frac{\mathrm{i}\boldsymbol{k}}{|\boldsymbol{k}|} \times \boldsymbol{B}(\boldsymbol{k}) \right] + \boldsymbol{E}^*(\boldsymbol{k}) \cdot \left[ \frac{\mathrm{i}\boldsymbol{k}}{|\boldsymbol{k}|} \times \boldsymbol{E}(\boldsymbol{k}) \right] \right\} + \mathrm{c.c.} \end{aligned} \tag{B.10}$$

Finally, we express $\tilde{\boldsymbol{G}}_{\pm}(\boldsymbol{r},\omega)$, the fields defined in Eq. (3.3), via their spatial Fourier transforms according to Eq. (B.1). We use that $\boldsymbol{B} = \mu_0 \boldsymbol{H}$ in free space. After expressing both $\underline{\boldsymbol{B}}$ and $\underline{\boldsymbol{E}}$ as given in Eq. (B.3), we find

$$\underline{\boldsymbol{G}}_{\pm}(\boldsymbol{k},\omega) = \sqrt{\frac{\pi}{2}} \left[ \delta(\omega - c_0|\boldsymbol{k}|) \boldsymbol{G}_{\pm}(\boldsymbol{k}) + \delta(\omega + c_0|\boldsymbol{k}|) \boldsymbol{G}_{\mp}^*(-\boldsymbol{k}) \right] , \tag{B.11a}$$

with

$$\boldsymbol{G}_{\pm}(\boldsymbol{k}) = \sqrt{\frac{\varepsilon_0}{2}} \left[ \boldsymbol{E}(\boldsymbol{k}) \pm \mathrm{i} c_0 \boldsymbol{B}(\boldsymbol{k}) \right] . \tag{B.11b}$$

Note that $\underline{G}_{\pm}(\boldsymbol{k},\omega)$ itself does not follow the structure given by Eq. (B.3), as $\tilde{\boldsymbol{G}}_{\pm}(\boldsymbol{r},\omega)$ by construction does not preserve the conjugate symmetry (w.r.t. $\omega$) of the Hermitian functions $\tilde{\boldsymbol{B}}$ and $\tilde{\boldsymbol{E}}$. If needed, Eq. (B.4) has to be adjusted accordingly. We find that

$$\sum_{\lambda=\pm1} \boldsymbol{G}_\lambda^*(\boldsymbol{k}) \cdot \left[\mathrm{i}\hat{\boldsymbol{k}} \times \boldsymbol{G}_\lambda(\boldsymbol{k})\right] = \varepsilon_0 \left(\boldsymbol{E}^*(\boldsymbol{k}) \cdot \left[\mathrm{i}\hat{\boldsymbol{k}} \times \boldsymbol{E}(\boldsymbol{k})\right] + c_0^2 \boldsymbol{B}^*(\boldsymbol{k}) \cdot \left[\mathrm{i}\hat{\boldsymbol{k}} \times \boldsymbol{B}(\boldsymbol{k})\right]\right), \tag{B.12}$$

where $\hat{\boldsymbol{k}} = \boldsymbol{k}/|\boldsymbol{k}|$. All mixed terms involving both $\boldsymbol{E}(\boldsymbol{k})$ and $\boldsymbol{B}(\boldsymbol{k})$ cancel in the sum over $\lambda$. Hence, we rewrite Eq. (B.10);

$$h_{\mathrm{em}} = \frac{1}{8} \sum_{\lambda=\pm1} \iiint_{\mathbb{R}^3} \frac{\mathrm{d}^3k}{c_0|\boldsymbol{k}|}\, \boldsymbol{G}_\lambda^*(\boldsymbol{k}) \cdot \left[\mathrm{i}\hat{\boldsymbol{k}} \times \boldsymbol{G}_\lambda(\boldsymbol{k})\right] + \text{c.c.} \tag{B.13}$$

The structure of $\underline{\boldsymbol{G}}_{\pm}$ hints at the intricate relation between the sign of frequency and the sign of helicity [cf. 257, Section III].

Lastly, we recall Eq. (3.6a) and note

$$\begin{aligned} &\frac{c_0\boldsymbol{\nabla}}{\omega} \times \tilde{\boldsymbol{G}}_{\pm}(\boldsymbol{r},\omega) = \pm\tilde{\boldsymbol{G}}_{\pm}(\boldsymbol{r},\omega) \\ \iff &\frac{\mathrm{i}c_0\boldsymbol{k}}{\omega} \times \underline{\boldsymbol{G}}_{\pm}(\boldsymbol{k},\omega) = \pm\underline{\boldsymbol{G}}_{\pm}(\boldsymbol{k},\omega) \\ \iff &\mathrm{i}\hat{\boldsymbol{k}} \times \boldsymbol{G}_{\pm}(\boldsymbol{k}) = \pm\boldsymbol{G}_{\pm}(\boldsymbol{k}). \end{aligned} \tag{B.14}$$

We identify $\mathrm{i}\hat{\boldsymbol{k}}\times$ as the representation of the helicity operator $\boldsymbol{\Lambda}$, given in Eq. (3.34), acting on plane wave components. We use the last line above to transform Eq. (B.13) into

$$\begin{aligned} h_{\mathrm{em}} &= \frac{1}{8} \sum_{\lambda=\pm1} \iiint_{\mathbb{R}^3} \frac{\mathrm{d}^3k}{c_0|\boldsymbol{k}|}\, \lambda|\boldsymbol{G}_\lambda(\boldsymbol{k})|^2 + \text{c.c.} \\ &= \frac{1}{4} \iiint_{\mathbb{R}^3} \frac{\mathrm{d}^3k}{c_0|\boldsymbol{k}|} \left(|\boldsymbol{G}_+(\boldsymbol{k})|^2 - |\boldsymbol{G}_-(\boldsymbol{k})|^2\right). \end{aligned} \tag{B.15}$$

Going from the first to the second line, we notice that the integrand is purely real and the addition of the complex conjugated term equates to a multiplication by a factor of two. We retrospectively understand the same to be true for the expression in Eq. (B.13). Hence, we find the expressions for the electromagnetic helicity $h_{\mathrm{em}}$ in Eqs. (B.13) and (B.15) to be equivalent to the first and second line of Eq. (3.37) with an additional prefactor of $1/4$.

Ultimately, we have recovered the equivalence between Eq. (3.30), the conserved Noether charge associated with the duality symmetry of Maxwell's equations, and Eq. (3.37), the expectation value of the helicity operator derived using the conformally invariant scalar product for free electromagnetic fields.

# C *Cross-Sections in Electromagnetic Scattering*

In the following, we derive the formulas for the extinction, scattering, and absorption cross-sections of a scatterer represented by a transition matrix, used in Section 4.1. We first derive the directional cross-sections for a given illumination direction. Afterward, we average with respect to the illumination direction to obtain the formulas for orientationally averaged cross sections. We provide explicit expressions for spheres in an achiral embedding in terms of Mie coefficients and discuss directional cross-sections for clusters of scatterers.

*Extinction, scattering, and absorption cross-sections*

Following the setup used to introduce the transition matrix (T-matrix) in Subsection 4.1.2, we consider an object (scatterer) located near the origin and its interaction with a monochromatic electromagnetic wave. The total electric and magnetic fields outside of the region occupied by the scatterer itself are given by the sum of the incident and the scattered fields,

$$\boldsymbol{E}_\omega = \boldsymbol{E}_\omega^{\mathrm{inc}} + \boldsymbol{E}_\omega^{\mathrm{sca}}, \qquad \boldsymbol{H}_\omega = \boldsymbol{H}_\omega^{\mathrm{inc}} + \boldsymbol{H}_\omega^{\mathrm{sca}}. \tag{C.1}$$

The incident and scattered fields are expanded in vector spherical waves (VSWS) (cf. Eqs. (3.27)),

$$\boldsymbol{E}_\omega^{\mathrm{inc}}(\boldsymbol{r}) = \sum_{\ell=1}^{\infty} \sum_{m=-\ell}^{\ell} \sum_{\lambda\in\{+,-\}} a_{\ell m,\lambda}\, \boldsymbol{A}^{(1)}_{\ell m,\lambda}(\boldsymbol{r})\Big|_{k=k_\lambda}, \tag{C.2a}$$

$$\boldsymbol{H}_\omega^{\mathrm{inc}}(\boldsymbol{r}) = \frac{-\mathrm{i}}{Z_0 Z} \sum_{\ell=1}^{\infty} \sum_{m=-\ell}^{\ell} \sum_{\lambda\in\{+,-\}} \lambda a_{\ell m,\lambda}\, \boldsymbol{A}^{(1)}_{\ell m,\lambda}(\boldsymbol{r})\Big|_{k=k_\lambda}, \tag{C.2b}$$

and

$$\boldsymbol{E}_\omega^{\mathrm{sca}}(\boldsymbol{r}) = \sum_{\ell=1}^{\infty} \sum_{m=-\ell}^{\ell} \sum_{\lambda\in\{+,-\}} p_{\ell m,\lambda}\, \boldsymbol{A}^{(3)}_{\ell m,\lambda}(\boldsymbol{r})\Big|_{k=k_\lambda}, \tag{C.3a}$$

$$\boldsymbol{H}_\omega^{\mathrm{sca}}(\boldsymbol{r}) = \frac{-\mathrm{i}}{Z_0 Z} \sum_{\ell=1}^{\infty} \sum_{m=-\ell}^{\ell} \sum_{\lambda\in\{+,-\}} \lambda p_{\ell m,\lambda}\, \boldsymbol{A}^{(3)}_{\ell m,\lambda}(\boldsymbol{r})\Big|_{k=k_\lambda}. \tag{C.3b}$$

Here, $k_\lambda$ is the helicity-dependent wavenumber in the generally chiral, homogeneous and isotropic embedding medium, which is considered to fill all of space outside of the region occupied by the scatterer; $Z$ is the corresponding relative impedance. We consider the embedding to be lossless, restricting $k_\lambda$ and $Z$ to be real. In line with the incident field being finite everywhere, the expansion uses regular VSWS ($n = 1$). Conversely, the scattered field describes a wave radiating away from the scatterer and has to satisfy the outgoing radiation condition; hence, singular ($n = 3$) VSWS are used in the expansion. The incident (resp. scattered) fields are represented by the expansion coefficients $a_{\ell m,\lambda}$ (resp. $p_{\ell m,\lambda}$). The coefficients for different values of $\ell$ and $m$ are frequently collected in column vectors, $\boldsymbol{a}_\lambda$ and $\boldsymbol{p}_\lambda$, with $\lambda \in \{+1, -1\}$.[1] As the scattered fields are due to the (assumed to be linear) optical response of the scatterer upon being illuminated by the incident fields, the scattered field coefficients are determined by the incident ones and the properties of the scatterer. Hence, the linear mapping between the incident and scattered field coefficients represents the (linear) optical properties of the scatterer. It takes the form of a matrix–vector product,

1 When specifying helicity-related indices, we interchangeably use the eigenvalues of the helicity operator, +1 and −1, or simply their sign, + and −.

$$p_{\ell m,\lambda} = \sum_{\ell',m',\lambda'} T_{\ell m\lambda,\ell' m'\lambda'} a_{\ell' m',\lambda'}\,, \tag{C.4}$$

and we call the matrix $\left(T_{\ell m\lambda,\ell' m'\lambda'}\right)$ the scatterer's T-matrix. The bounds for the summation over $\ell'$, $m'$, and $\lambda'$ in the expression above are the same as for the field expansions in Eqs. (C.2) and (C.3). For the purposes of numerical evaluation, the field expansions are truncated by setting an upper bound $\ell_{\max}$ for the summation over the multipolar degree $\ell$. Correspondingly, we work with a truncated representation of the T-matrix, only containing entries $T_{\ell m\lambda,\ell' m'\lambda'}$ for $\ell, \ell' \leq \ell_{\max}$.

We now consider the energy flux out of a volume enclosing the scatterer, that is, the total power leaving the volume, which we call $W$. To this end, we integrate the normal component of the temporally averaged Poynting vector over the surface specified by $|r| = R$, a sphere with radius $R$ centered around the origin. We choose $R$ large enough such that the scatterer is contained inside the sphere. Inserting the fields according to Eq. (C.1), we find terms

related exclusively to the incident and scattered fields as well as a mixed contribution,

$$W \coloneqq \iint R^2 \mathrm{d}\Omega\, \hat{\boldsymbol{r}} \cdot \langle \boldsymbol{S} \rangle = \frac{1}{2} \iint R^2 \mathrm{d}\Omega\, \hat{\boldsymbol{r}} \cdot \mathrm{Re}\left\{ \boldsymbol{E}_\omega^{\mathrm{inc}} \times \boldsymbol{H}_\omega^{\mathrm{inc}\,*} \right\} + \frac{1}{2} \iint R^2 \mathrm{d}\Omega\, \hat{\boldsymbol{r}} \cdot \mathrm{Re}\left\{ \boldsymbol{E}_\omega^{\mathrm{sca}} \times \boldsymbol{H}_\omega^{\mathrm{sca}\,*} \right\} + \frac{1}{2} \iint R^2 \mathrm{d}\Omega\, \hat{\boldsymbol{r}} \cdot \mathrm{Re}\left\{ \boldsymbol{E}_\omega^{\mathrm{inc}} \times \boldsymbol{H}_\omega^{\mathrm{sca}\,*} + \boldsymbol{E}_\omega^{\mathrm{sca}} \times \boldsymbol{H}_\omega^{\mathrm{inc}\,*} \right\}. \quad \text{(C.5)}$$

We insert the expansion Eqs. (C.2) and (C.3) and express $W$ in terms of matrix–vector products involving the coefficient vectors:

$$W = \sum_{\ell',m',\lambda'} \sum_{\ell,m,\lambda} \left( a^*_{\ell'm',\lambda'} \Sigma^{11}_{\ell'm'\lambda',\ell m\lambda} a_{\ell m,\lambda} + p^*_{\ell'm',\lambda'} \Sigma^{33}_{\ell'm'\lambda',\ell m\lambda} p_{\ell m,\lambda} + a^*_{\ell'm',\lambda'} \Sigma^{13}_{\ell'm'\lambda',\ell m\lambda} p_{\ell m,\lambda} + p^*_{\ell'm',\lambda'} \Sigma^{31}_{\ell'm'\lambda',\ell m\lambda} a_{\ell m,\lambda} \right). \quad \text{(C.6)}$$

Here, we have introduced the matrices (we follow a similar procedure in the discussion of transmittance and reflectance for a planar interface in Section 4.2)

$$\boldsymbol{\Sigma}^{n'n} = \frac{\boldsymbol{\Sigma}'^{n'n} + \left( \boldsymbol{\Sigma}'^{nn'} \right)^{\mathsf{H}}}{2}, \quad \text{(C.7)}$$

where $\boldsymbol{\Sigma}'^{n'n}$ has the entries

$$\Sigma'^{n'n}_{\ell'm'\lambda',\ell m\lambda} = \frac{1}{2} \iint R^2 \mathrm{d}\Omega\, \hat{\boldsymbol{r}} \cdot \left[ \boldsymbol{A}^{(n)}_{\ell m,\lambda}(\boldsymbol{r}) \Big|_{k=k_\lambda} \times \left( \frac{-\mathrm{i}\lambda'}{Z_0 Z}\, \boldsymbol{A}^{(n')}_{\ell'm',\lambda'}(\boldsymbol{r}) \Big|_{k=k_{\lambda'}} \right)^* \right]. \quad \text{(C.8)}$$

The real part of these entries corresponds to the energy flux through the spherical surface for a given pair of unit amplitude VSWs. Inserting the definitions of the VSWs, Eq. (3.22) and Eqs. (3.21), and utilizing the orthogonality relations for the vector spherical harmonics (VSHs), Eqs. (A.27), we find

$$\Sigma'^{n'n}_{\ell'm'\lambda',\ell m\lambda} = \delta_{\ell\ell'} \delta_{mm'} \frac{\mathrm{i}R^2}{4Z_0 Z} \left[ \lambda\lambda' z^{(n)}_\ell(k_\lambda R) \left( \frac{z^{(n')}_\ell(k_{\lambda'} R)}{k_{\lambda'} R} + z^{(n')\prime}_\ell(k_{\lambda'} R) \right)^* - \left( z^{(n')}_\ell(k_{\lambda'} R) \right)^* \left( \frac{z^{(n)}_\ell(k_\lambda R)}{k_\lambda R} + z^{(n)\prime}_\ell(k_\lambda R) \right) \right], \quad \text{(C.9)}$$

where $z_\ell^{(n)\prime}(k_\lambda R)$ denotes the derivative of $z_\ell^{(n)}(k_\lambda R)$ with respect to its argument.

The construction of the matrix in Eq. (C.7) accounts for taking the real parts in Eq. (C.5) and guarantees that the power $W$ in Eq. (C.6) is real. It is further simplified by the relation

$$\Sigma'^{n'n}_{\ell'm'\lambda',\ell m\lambda} = \lambda\lambda' \left(\Sigma'^{nn'}_{\ell m\lambda,\ell'm'\lambda'}\right)^*, \tag{C.10}$$

which follows from the right-hand side of Eq. (C.8), considering that $Z$ is real. Hence, the only nonzero entries of the Hermitian matrix $\boldsymbol{\Sigma}^{n'n}$ are those for matching helicity,

$$\begin{aligned}
\Sigma^{n'n}_{\ell'm'\lambda',\ell m\lambda} &= \frac{1+\lambda\lambda'}{2}\Sigma'^{n'n}_{\ell'm'\lambda',\ell m\lambda} \\
&= \delta_{\ell\ell'}\delta_{mm'}\delta_{\lambda\lambda'}\frac{\mathrm{i}R^2}{4Z_0 Z}\Big[z_\ell^{(n)}(k_\lambda R)\left(z_\ell^{(n')\prime}(k_\lambda R)\right)^* \\
&\qquad\qquad - \left(z_\ell^{(n')}(k_\lambda R)\right)^* z_\ell^{(n)\prime}(k_\lambda R)\Big] \\
&= \delta_{\ell\ell'}\delta_{mm'}\delta_{\lambda\lambda'}\frac{\mathrm{i}R^2}{4Z_0 Z}\mathcal{W}\left\{z_\ell^{(n)}(k_\lambda R), \left(z_\ell^{(n')\prime}(k_\lambda R)\right)^*\right\},
\end{aligned} \tag{C.11}$$

where we identify the Wronskian of spherical Bessel and Hankel functions in the last line. Using $\left(h_\ell^{(1)}\right)^* = h_\ell^{(2)}$ for real arguments and [92, Eq. (10.50.1)]

$$\mathcal{W}\left\{h_\ell^{(1)}(x), h_\ell^{(2)}(x)\right\} = 2\mathcal{W}\left\{j_\ell(x), h_\ell^{(2)}(x)\right\} = 2\mathcal{W}\left\{h_\ell^{(1)}(x), j_\ell(x)\right\} = \frac{-2\mathrm{i}}{x^2}, \tag{C.12}$$

we find

$$\Sigma^{11}_{\ell'm'\lambda',\ell m\lambda} = 0, \tag{C.13a}$$

$$\Sigma^{33}_{\ell'm'\lambda',\ell m\lambda} = 2\Sigma^{13}_{\ell'm'\lambda',\ell m\lambda} = 2\Sigma^{31}_{\ell'm'\lambda',\ell m\lambda} = \delta_{\ell\ell'}\delta_{mm'}\delta_{\lambda\lambda'}\frac{1}{2Z_0 Z k_\lambda{}^2}. \tag{C.13b}$$

We insert these results into Eq. (C.6) and note the following: First, the power associated with the incident field, the first term on the right-hand side of Eq. (C.6), vanishes identically. Physically, it is a consequence of the fact that the incident energy flux enters and leaves any volume surrounding the

scatterer at the same rate. This conclusion can also be reached considering that the regular VSWS ($n = 1$) in a lossless medium can be written as balanced superpositions of the outwards ($n = 3$) and inwards ($n = 4$) radiating VSWS, providing the same energy flux towards and away from the origin. Second, there is no explicit dependence on the radius $R$ of the spherical integration surface. As the embedding is lossless, all energy radiated by the waves is conserved outside the scatterer, hence, the energy flux out of any spherical surface enclosing the scatterer has to be the same. Even further, the shape of the enclosing surface is irrelevant, which we discuss later, considering the divergence of the Poynting vector.

As the energy flux into the region occupied by the scatterer associated with the incident field is net zero, the value of $W$ in Eq. (C.6) is entirely determined by the power that the scatterer absorbs. Hence, $W \leq 0$ and we define the nonnegative[2] absorbed power as $W_{\text{abs}} := -W$. The case $W_{\text{abs}} = 0$ signifies a lossless scatterer, where all energy contained in the electromagnetic fields is conserved and only redistributed between the incident and the scattered field. The second term on the right-hand side of Eq. (C.6) is the power radiated by the scattered field; we denote it $W_{\text{sca}}$. The remaining terms of Eq. (C.6) are the mixed terms involving both scattered and incident coefficients. We define the negative of their sum as the extinction power $W_{\text{ext}}$. Rewriting Eq. (C.6) yields

$$W_{\text{ext}} = W_{\text{sca}} + W_{\text{abs}}, \tag{C.14}$$

hence, extinction encapsulates all interaction of the scatterer with the incident field with regard to power exchange, be it through scattering or absorption.

Naturally, the power absorbed and scattered by a scatterer scales with the energy contained in the incident field. As we are most interested in the relation between the two, we define the relative quantities [93]

$$C_{\text{ext}} = \frac{W_{\text{ext}}}{I_{\text{inc}}}, \qquad C_{\text{sca}} = \frac{W_{\text{sca}}}{I_{\text{inc}}}, \qquad C_{\text{abs}} = \frac{W_{\text{abs}}}{I_{\text{inc}}}, \tag{C.15}$$

where $I_{\text{inc}}$ is the intensity, the energy flux in direction of propagation per unit area, of the incident field. Correspondingly, these relative quantities have dimensions of area. We interpret them as a measure of a scatterer's ability to scatter or absorb light in the form of an effective size and call

2 If we allow for gain, e.g., an actively radiating scatterer adding energy to the system, $W > 0$. For a scatterer made from passive media, however, energy conservation dictates $W \leq 0$.

them *cross-sections*. Explicitly, after inserting Eqs. (C.13) into Eq. (C.6), the cross-sections read

$$\begin{aligned} C_{\mathrm{sca}} &= \frac{1}{2Z_0 Z I_{\mathrm{inc}}} \sum_{\ell',m',\lambda'} \frac{1}{k_{\lambda'}^2} p^*_{\ell'm',\lambda'} p_{\ell'm',\lambda'} \\ &= \frac{1}{2Z_0 Z I_{\mathrm{inc}}} \sum_{\ell,m,\lambda} \sum_{\ell',m',\lambda'} \sum_{\ell'',m'',\lambda''} \frac{1}{k_{\lambda'}^2} a^*_{\ell m,\lambda} T^*_{\ell'm'\lambda',\ell m\lambda} T_{\ell'm'\lambda',\ell''m''\lambda''} a_{\ell''m'',\lambda''} \\ &= \frac{1}{2Z_0 Z I_{\mathrm{inc}}} \sum_{\lambda,\lambda',\lambda''} \frac{1}{k_{\lambda'}^2} \boldsymbol{a}^{\mathsf{H}}_{\lambda} \boldsymbol{T}^{\mathsf{H}}_{\lambda'\lambda} \boldsymbol{T}_{\lambda'\lambda''} \boldsymbol{a}_{\lambda''}, \end{aligned} \tag{C.16a}$$

$$\begin{aligned} C_{\mathrm{ext}} &= \frac{-1}{2Z_0 Z I_{\mathrm{inc}}} \sum_{\ell,m,\lambda} \frac{1}{2k_{\lambda}^2} \left( a^*_{\ell m,\lambda} p_{\ell m,\lambda} + p^*_{\ell m,\lambda} a_{\ell m,\lambda} \right) \\ &= \frac{-1}{2Z_0 Z I_{\mathrm{inc}}} \sum_{\ell,m,\lambda} \sum_{\ell',m',\lambda'} \frac{1}{k_{\lambda}^2} \mathrm{Re}\left\{ a^*_{\ell m,\lambda} T_{\ell m\lambda,\ell'm'\lambda'} a_{\ell'm',\lambda'} \right\} \\ &= \frac{-1}{2Z_0 Z I_{\mathrm{inc}}} \sum_{\lambda,\lambda'} \frac{1}{k_{\lambda}^2} \mathrm{Re}\left\{ \boldsymbol{a}^{\mathsf{H}}_{\lambda} \boldsymbol{T}_{\lambda\lambda'} \boldsymbol{a}_{\lambda'} \right\}, \end{aligned} \tag{C.16b}$$

and $C_{\mathrm{abs}} = C_{\mathrm{ext}} - C_{\mathrm{sca}}$. The last lines of Eqs. (C.16) provide the formulas for the cross-sections given in Eqs. (4.28) of Section 4.1.

*Plane wave illumination and directional cross-sections*

We are frequently interested in the cross-sections of a scatterer with regard to illumination from a given direction. That is, the incident field is given by vector plane waves (VPWs) for a fixed propagation direction $\hat{\boldsymbol{k}}$,

$$\boldsymbol{E}^{\mathrm{inc}}_{\omega}(\boldsymbol{r}) = c_{\hat{\boldsymbol{k}},+} \left. \boldsymbol{A}_{\hat{\boldsymbol{k}},+}(\boldsymbol{r}) \right|_{k=k_+} + c_{\hat{\boldsymbol{k}},-} \left. \boldsymbol{A}_{\hat{\boldsymbol{k}},-}(\boldsymbol{r}) \right|_{k=k_-}, \tag{C.17a}$$

$$\boldsymbol{H}^{\mathrm{inc}}_{\omega}(\boldsymbol{r}) = \frac{-\mathrm{i}}{Z_0 Z} \left( c_{\hat{\boldsymbol{k}},+} \left. \boldsymbol{A}_{\hat{\boldsymbol{k}},+}(\boldsymbol{r}) \right|_{k=k_+} - c_{\hat{\boldsymbol{k}},-} \left. \boldsymbol{A}_{\hat{\boldsymbol{k}},-}(\boldsymbol{r}) \right|_{k=k_-} \right), \tag{C.17b}$$

a superposition of a positive and a negative helicity VPW. In an achiral embedding, such superposition corresponds to a general elliptically polarized

plane wave. The intensity of the wave given in Eqs. (C.17)—the energy flux in the direction of propagation—is

$$\begin{aligned} I_{\text{inc}} &= \langle \boldsymbol{S} \rangle \cdot \hat{\boldsymbol{k}} = \frac{1}{2} \operatorname{Re}\left\{ \boldsymbol{E}_\omega^{\text{inc}} \times \boldsymbol{H}_\omega^{\text{inc}\,*} \right\} \cdot \hat{\boldsymbol{k}} \\ &= \frac{1}{2Z_0 Z} \operatorname{Re}\left\{ \sum_{\lambda,\lambda'} \lambda' c_{\hat{\boldsymbol{k}},\lambda} c^*_{\hat{\boldsymbol{k}},\lambda'} \underbrace{\mathrm{i}\hat{\boldsymbol{k}} \cdot \left( \hat{\boldsymbol{e}}_\lambda(\boldsymbol{k}_\lambda) \times \hat{\boldsymbol{e}}^*_{\lambda'}(\boldsymbol{k}_{\lambda'}) \right)}_{\lambda \delta_{\lambda\lambda'}} \mathrm{e}^{\mathrm{i}\hat{\boldsymbol{k}} \cdot \boldsymbol{r}(k_\lambda - k_{\lambda'})} \right\} \\ &= \frac{1}{2Z_0 Z} \sum_\lambda \left| c_{\hat{\boldsymbol{k}},\lambda} \right|^2 . \end{aligned} \tag{C.18}$$

In the second line, we use the orthogonality of circular polarization vectors, Eq. (3.19), which holds in a lossless chiral medium, and Eq. (3.20). We find that the intensity is proportional to the sum of the squared magnitudes of the coefficients $c_{\hat{\boldsymbol{k}},\lambda}$; in an achiral medium, it corresponds to the squared magnitude of the amplitude of the elliptically polarized wave.

To express the plane wave illumination in terms of VSWs, matching Eqs. (C.2), we use the VSW-expansion of a VPW, given in Eq. (A.66), to obtain the expansion coefficients

$$a_{\ell m,\lambda}\left(\hat{\boldsymbol{k}}\right) = c_{\hat{\boldsymbol{k}},\lambda} 4\pi \mathrm{i}^\ell \left( X^\varphi_{\ell m}(\theta_{\boldsymbol{k}}, \varphi_{\boldsymbol{k}}) + \mathrm{i}\lambda X^\theta_{\ell m}(\theta_{\boldsymbol{k}}, \varphi_{\boldsymbol{k}}) \right)^* . \tag{C.19}$$

Finally, the directional cross-sections for a specified illumination direction $\hat{\boldsymbol{k}}$ (e.g., $C_{\text{sca}}(\hat{\boldsymbol{k}})$) are obtained from evaluating Eqs. (C.16) after inserting the incident intensity, Eq. (C.18), and the expansion coefficients, Eq. (C.19).

*Directionally averaged cross-sections*

Averaging the directional cross-sections over all illumination directions $\hat{\boldsymbol{k}}$ yields the *directionally averaged* cross-sections. Since fixing the scatterer and changing the illumination direction is entirely equivalent to rotating the scatterer with respect to a fixed illumination direction, the same quantities are also referred to as *rotationally* or *orientationally* averaged cross-sections. We denote the directional average by $\langle \cdot \rangle_{\hat{\boldsymbol{k}}}$.

We further consider the incident field to be of well-defined helicity $\lambda$, that is, for all directions $\hat{\boldsymbol{k}}$ only one of the VPW amplitudes, namely $c_{\hat{\boldsymbol{k}},\lambda}$, is

nonzero. We find that doing so yields directionally averaged cross-sections that are independent of any specification of the illumination and are directly expressed in terms of the scatterer's T-matrix. To this end, we consider the directional average of products of the expansion coefficients in Eq. (C.19), which are the only direction-dependent quantities in the directional cross-sections according to Eqs. (C.16):

$$\begin{aligned}
\left\langle a^*_{\ell' m',\lambda}\left(\hat{\boldsymbol{k}}\right) a_{\ell m,\lambda}\left(\hat{\boldsymbol{k}}\right)\right\rangle_{\hat{\boldsymbol{k}}} &= \frac{1}{4\pi}\iint \mathrm{d}\Omega_{\boldsymbol{k}}\, a^*_{\ell' m',\lambda}\left(\hat{\boldsymbol{k}}\right) a_{\ell m,\lambda}\left(\hat{\boldsymbol{k}}\right) \\
&= \left|c_{\hat{\boldsymbol{k}},\lambda}\right|^2 \frac{(4\pi)^2}{4\pi} \mathrm{i}^{\ell-\ell'} \iint \mathrm{d}\Omega_{\boldsymbol{k}} \left(X^{\varphi}_{\ell' m'} + \mathrm{i}\lambda X^{\theta}_{\ell' m'}\right)\left(X^{\varphi}_{\ell m} + \mathrm{i}\lambda X^{\theta}_{\ell m}\right)^* \\
&= \left|c_{\hat{\boldsymbol{k}},\lambda}\right|^2 4\pi \mathrm{i}^{\ell-\ell'} \iint \mathrm{d}\Omega_{\boldsymbol{k}} \left(\boldsymbol{X}_{\ell' m'} \cdot \boldsymbol{X}^*_{\ell m} + \mathrm{i}\lambda \boldsymbol{V}_{\ell' m'} \cdot \boldsymbol{X}^*_{\ell m}\right) \\
&= \left|c_{\hat{\boldsymbol{k}},\lambda}\right|^2 4\pi \delta_{\ell\ell'} \delta_{mm'}\,.
\end{aligned} \tag{C.20}$$

In the second and third line above, all VSH-related terms depend on the arguments $(\theta_{\boldsymbol{k}}, \varphi_{\boldsymbol{k}})$, which we have dropped for brevity. The fourth line follows from the orthogonality relations of the VSHs, Eqs. (A.27). Using this result and inserting the incident intensity, which now yields $2Z_0 Z I_{\mathrm{inc}} = |c_{\hat{\boldsymbol{k}},\lambda}|^2$, into Eqs. (C.16), we can derive the directionally averaged scattering cross-section for a given incident helicity $\lambda$,

$$\begin{aligned}
\left\langle C_{\mathrm{sca},\lambda}\right\rangle_{\hat{\boldsymbol{k}}} &= \sum_{\ell,m} \sum_{\ell',m',\lambda'} \sum_{\ell'',m''} \frac{1}{k^2_{\lambda'}} \frac{\left\langle a^*_{\ell m,\lambda}\left(\hat{\boldsymbol{k}}\right) a_{\ell'' m'',\lambda}\left(\hat{\boldsymbol{k}}\right)\right\rangle_{\hat{\boldsymbol{k}}}}{\left|c_{\hat{\boldsymbol{k}},\lambda}\right|^2} T^*_{\ell' m'\lambda',\ell m\lambda} T_{\ell' m'\lambda',\ell'' m''\lambda} \\
&= \sum_{\ell,m} \sum_{\ell',m',\lambda'} \frac{4\pi}{k^2_{\lambda'}} T^*_{\ell' m'\lambda',\ell m\lambda} T_{\ell' m'\lambda',\ell m\lambda} \\
&= \sum_{\lambda'} \frac{4\pi}{k^2_{\lambda'}} \operatorname{tr}\left(\boldsymbol{T}^{\mathrm{H}}_{\lambda'\lambda} \boldsymbol{T}_{\lambda'\lambda}\right) \\
&= \sum_{\lambda'} \frac{4\pi}{k^2_{\lambda'}} \left\|\boldsymbol{T}_{\lambda'\lambda}\right\|^2_{\mathrm{HS}},
\end{aligned} \tag{C.21a}$$

as well as the corresponding directionally averaged extinction cross-section,

$$\begin{aligned}\left\langle C_{\mathrm{ext},\lambda}\right\rangle_{\hat{\boldsymbol{k}}} &= \sum_{\ell,m}\sum_{\ell',m'}\frac{-1}{k_\lambda^2}\,\mathrm{Re}\left\{\frac{\left\langle a^*_{\ell m,\lambda}\left(\hat{\boldsymbol{k}}\right)a_{\ell' m',\lambda}\left(\hat{\boldsymbol{k}}\right)\right\rangle_{\hat{\boldsymbol{k}}}}{\left|c_{\hat{\boldsymbol{k}},\lambda}\right|^2}T_{\ell m\lambda,\ell' m'\lambda}\right\} \\ &= \sum_{\ell,m}\frac{-4\pi}{k_\lambda^2}\,\mathrm{Re}\left\{T_{\ell m\lambda,\ell m\lambda}\right\} \\ &= \frac{-4\pi}{k_\lambda^2}\,\mathrm{Re}\{\mathrm{tr}(\boldsymbol{T}_{\lambda\lambda})\}.\end{aligned} \tag{C.21b}$$

Again, we provide explicit formulas only for the extinction and scattering cross-sections; the absorption cross-section is obtained as their difference. We find that the directionally averaged scattering cross-section is given by the sum of a co-polarized ($\lambda' = \lambda$) and a cross-polarized term ($\lambda' = -\lambda$), each of which is proportional to the square of the Hilbert–Schmidt norm of the corresponding submatrix of $\boldsymbol{T}$. In case of a truncated representation of the T-matrix, it may be more appropriate to refer to the squared Frobenius or Schur norm. It is given by the sum over squared moduli of all matrix entries. Conversely, the directionally averaged extinction cross-section is entirely determined by the corresponding co-polarized submatrix of the T-matrix.

Another set of useful quantities are the polarization- (i.e., helicity-) and directionally averaged cross-sections, obtained after taking the average of Eqs. (C.21) with respect to the incident helicity $\lambda$,

$$\left\langle C_{\mathrm{sca}}\right\rangle_{\hat{\boldsymbol{k}}} = \frac{1}{2}\sum_{\lambda}\left\langle C_{\mathrm{sca},\lambda}\right\rangle_{\hat{\boldsymbol{k}}} = \sum_{\lambda,\lambda'}\frac{2\pi}{k_{\lambda'}^2}\|\boldsymbol{T}_{\lambda'\lambda}\|_{\mathrm{HS}}^2, \tag{C.22a}$$

$$\left\langle C_{\mathrm{ext}}\right\rangle_{\hat{\boldsymbol{k}}} = \frac{1}{2}\sum_{\lambda}\left\langle C_{\mathrm{ext},\lambda}\right\rangle_{\hat{\boldsymbol{k}}} = \sum_{\lambda}\frac{-2\pi}{k_\lambda^2}\,\mathrm{Re}\{\mathrm{tr}(\boldsymbol{T}_{\lambda\lambda})\}. \tag{C.22b}$$

In an achiral embedding, Eqs. (C.22) recover Eqs. (42) and (43) of Ref. [117]. Note that, therein, the T-matrix is written as the mapping between the expansion coefficients of incident and scattered field using VSWS of well-defined parity, $\boldsymbol{N}_{\ell m}^{(n)}$ and $\boldsymbol{M}_{\ell m}^{(n)}$, instead of the VSWS of well-defined helicity used in Eqs. (C.2) and (C.3). In an achiral embedding, $k_+ = k_- = k$, and the relation between the expansion coefficients for different sets of VSWS

(i.e., parity or helicity eigenfunctions) is determined by the transformation Eq. (4.11). Accordingly, the different T-matrices are related by

$$\begin{pmatrix} \boldsymbol{T}_{\mathrm{NN}} & \boldsymbol{T}_{\mathrm{NM}} \\ \boldsymbol{T}_{\mathrm{MN}} & \boldsymbol{T}_{\mathrm{MM}} \end{pmatrix} = \underbrace{\frac{1}{\sqrt{2}} \begin{pmatrix} \mathbf{1} & \mathbf{1} \\ \mathbf{1} & -\mathbf{1} \end{pmatrix}}_{=:\boldsymbol{U}} \begin{pmatrix} \boldsymbol{T}_{++} & \boldsymbol{T}_{+-} \\ \boldsymbol{T}_{-+} & \boldsymbol{T}_{--} \end{pmatrix} \frac{1}{\sqrt{2}} \begin{pmatrix} \mathbf{1} & \mathbf{1} \\ \mathbf{1} & -\mathbf{1} \end{pmatrix}. \tag{C.23}$$

The symmetric, involutory transformation $\boldsymbol{U} = \boldsymbol{U}^{\mathsf{T}} = \boldsymbol{U}^{-1}$ is without effect in Eqs. (C.22), hence, the expressions for the cross-sections using the helicity- or parity-related formulations of the T-matrix in an achiral embedding are equivalent. One advantage of the helicity-based description is the general applicability allowing for chiral embedding media.

*Independence of the cross-sections from the integration surface*

Above, we noted the arbitrariness of the radius of the spherical surface used in computing the energy flux leaving a volume enclosing the scatterer. We further find that the shape of the enclosed volume is arbitrary as well. By the divergence theorem, the outward flux of the time-averaged Poynting vector across a closed surface is equal to the integral of its divergence over the enclosed volume. The divergence of the time-averaged Poynting vector in a chiral medium reads

$$\begin{aligned} \boldsymbol{\nabla} \cdot \langle \boldsymbol{S} \rangle &= \frac{1}{2} \boldsymbol{\nabla} \cdot \mathrm{Re}\{\boldsymbol{E}_\omega \times \boldsymbol{H}_\omega^*\} \\ &= \frac{1}{2} \mathrm{Re}\{\boldsymbol{H}_\omega^* \cdot (\boldsymbol{\nabla} \times \boldsymbol{E}_\omega) - \boldsymbol{E}_\omega \cdot (\boldsymbol{\nabla} \times \boldsymbol{H}_\omega^*)\} \\ &= \frac{1}{2} \mathrm{Re}\left\{\boldsymbol{H}_\omega^* \cdot k_0 \left(\kappa \boldsymbol{E}_\omega + \mathrm{i} Z_0 \mu \boldsymbol{H}_\omega\right) - \boldsymbol{E}_\omega \cdot k_0 \left(\kappa \boldsymbol{H}_\omega - \frac{\mathrm{i}}{Z_0} \varepsilon \boldsymbol{E}_\omega\right)^*\right\} \\ &= \frac{-k_0}{2} \left(\mathrm{Im}\{\mu\} Z_0 |\boldsymbol{H}_\omega|^2 + \mathrm{Im}\{\varepsilon\} Z_0^{-1} |\boldsymbol{E}_\omega|^2 + 2\,\mathrm{Im}\{\kappa\}\,\mathrm{Im}\{\boldsymbol{E}_\omega \cdot \boldsymbol{H}_\omega^*\}\right), \end{aligned} \tag{C.24}$$

where the third line follows from Eq. (3.2). For brevity, we omit the frequency dependence of the material parameters and the spatial dependence of the monochromatic amplitudes. We find the divergence of the time-averaged Poynting vector to be determined by the absorption properties of the medium.

In a lossless isotropic medium, the material parameters are real (cf. Eq. (2.40)) and, hence, $\boldsymbol{\nabla} \cdot \langle \boldsymbol{S} \rangle = 0$ identically.[3] Correspondingly, the only possible nonvanishing contribution to the outward energy flux $W$ in Eq. (C.5) stems from absorption by the scatterer, substantiating the argument for identifying $-W$ as the absorbed power. Additionally, as remarked above, the shape of the integration surface can be chosen at will, provided that it encloses the scatterer.

3 Note that the absorption associated with the chirality parameter, given by $\operatorname{Im}\kappa$, is proportional to a term closely related to the optical chirality density discussed in Section 3.2.

Assuming another perspective, we may ignore the presence of the scatterer and acknowledge that the expansion coefficients $a_{\ell m,\lambda}$ via Eqs. (C.2) (resp. $p_{\ell m,\lambda}$ via Eqs. (C.3)) uniquely determine a solution to the Helmholtz equation with $k = k_\lambda$ in all of space (resp. in $\mathbb{R}^3 \setminus \{0\}$, subject to the outward radiation condition). For these fields, $\boldsymbol{\nabla} \cdot \langle \boldsymbol{S} \rangle = 0$ holds everywhere, with the exception of the origin in the case of the scattered fields, where the spherical Hankel functions are singular. Following this consideration, the incident energy flux—the first term on the right-hand side of Eq. (C.5)—is immediately found to be zero, aligning with our discussion in a previous subsection. Any nonvanishing contribution is accounted for in the singular point of the radiating VSWS and any integration surface may be chosen as long as it encloses the origin.

*Cross-sections for chiral spheres in an achiral embedding*

To obtain the cross-sections for a chiral sphere in an achiral embedding, we insert the T-matrix of a sphere, expressed via Mie coefficients in Eq. (4.23), into the formulas for the directionally averaged cross-sections, Eqs. (C.21). Note that, due to the spherical symmetry of the scatterer, the directional average is redundant. Hence, the directionally averaged cross-sections are equal to directional cross-sections for any illumination direction $\hat{\boldsymbol{k}}$. Accordingly,

$$\begin{aligned}\left\langle C_{\mathrm{sca},\lambda} \right\rangle_{\hat{\boldsymbol{k}}} = C_{\mathrm{sca},\lambda} &= \sum_{\ell,m} \sum_{\ell',m',\lambda'} \frac{4\pi}{k_{\lambda'}^2} \left| -\frac{\mathfrak{a}_\ell + \lambda\lambda' \mathfrak{b}_\ell}{2} + \delta_{\lambda\lambda'} \lambda \mathrm{i} \mathfrak{c}_\ell \right|^2 \delta_{\ell\ell'} \delta_{mm'} \\ &= \frac{2\pi}{k^2} \sum_\ell (2\ell+1) \left( |\mathfrak{a}_\ell|^2 + |\mathfrak{b}_\ell|^2 + 2|\mathfrak{c}_\ell|^2 - 2\lambda \operatorname{Im}\{(\mathfrak{a}_\ell + \mathfrak{b}_\ell)\, \mathfrak{c}_\ell^*\} \right), \end{aligned} \tag{C.25a}$$

and

$$\begin{aligned}\left\langle C_{\mathrm{ext},\lambda}\right\rangle_{\hat{\boldsymbol{k}}} = C_{\mathrm{ext},\lambda} &= \sum_{\ell m} \frac{-4\pi}{k_\lambda^2} \operatorname{Re}\left\{-\frac{\mathfrak{a}_\ell + \mathfrak{b}_\ell}{2} + \lambda \mathrm{i}\mathfrak{c}_\ell\right\} \\ &= \frac{2\pi}{k^2} \sum_\ell (2\ell+1) \operatorname{Re}\{\mathfrak{a}_\ell + \mathfrak{b}_\ell - 2\lambda \mathrm{i}\mathfrak{c}_\ell\},\end{aligned} \tag{C.25b}$$

matching Eqs. (8.17) of Ref. [93]. $k = k_+ = k_-$ is the wavenumber in the achiral embedding. Averaging over the incident helicity $\lambda$ yields the direction- and polarization-averaged cross-sections

$$\left\langle C_{\mathrm{sca}}\right\rangle_{\hat{\boldsymbol{k}}} = C_{\mathrm{sca}} = \frac{2\pi}{k^2} \sum_\ell (2\ell+1) \left(|\mathfrak{a}_\ell|^2 + |\mathfrak{b}_\ell|^2 + 2|\mathfrak{c}_\ell|^2\right), \tag{C.26a}$$

$$\left\langle C_{\mathrm{ext}}\right\rangle_{\hat{\boldsymbol{k}}} = C_{\mathrm{ext}} = \frac{2\pi}{k^2} \sum_\ell (2\ell+1) \operatorname{Re}\{\mathfrak{a}_\ell + \mathfrak{b}_\ell\}. \tag{C.26b}$$

The appearance of the cross-sections above is further simplified in the case of an achiral sphere due to $\mathfrak{c}_\ell = 0$, matching Eqs. (4.61) and (4.62) of Ref. [93].

*Approximation for small radii* · For small achiral spheres ($kr_1 \ll 1$, with the radius of the sphere $r_1$) with a relative permeability closely matching that of the embedding, $\mu_1 \approx \mu$, the scattering cross-section is in good approximation determined by $\mathfrak{a}_1$, which we further approximate according to Eqs. (4.15) as

$$\mathfrak{a}_1 \approx -\mathrm{i}\frac{2}{3}\frac{\varepsilon_1 - \varepsilon}{\varepsilon_1 + 2\varepsilon}(kr_1)^3. \tag{C.27}$$

Inserting into Eq. (C.26a), we obtain

$$C_{\mathrm{sca}} \approx \frac{8\pi}{3}\left|\frac{\varepsilon_1 - \varepsilon}{\varepsilon_1 + 2\varepsilon}\right|^2 r_1^6 k^4, \tag{C.28}$$

hence, recovering the Rayleigh scattering cross-section (cf. [258, Eq. (15.19)], [93, Eq. (5.8)]) as the limiting behavior for small particles.

For directional illumination, we choose without loss of generality $\hat{\boldsymbol{k}} = \hat{\boldsymbol{z}}$ and the helicity of the incident wave to be positive, obtaining the expansion

coefficients $a_{1m,\lambda}(\hat{\boldsymbol{z}}) = 2\sqrt{3\pi}\delta_{m,1}\delta_{\lambda,+}$ from Eq. (C.19). The truncated T-matrix ($\ell_{\max} = 1$) is approximately given by (see Eq. (4.23))

$$T_{1m'\lambda',1m\lambda} = -\frac{\mathfrak{a}_1}{2}\delta_{mm'}, \tag{C.29}$$

and, hence, $p_{\ell m,\lambda} = -\delta_{\ell,1}\delta_{m,1}\mathfrak{a}_1 a_{11,+}/2$. With $C_{\mathrm{sca}}$ evaluated as a solid angle integral, essentially the second line of Eq. (C.5), we consider the differential cross-section

$$\begin{aligned}\frac{\mathrm{d}C_{\mathrm{sca}}}{\mathrm{d}\Omega}(\theta,\varphi) &= \frac{R^2}{I_{\mathrm{inc}}}\hat{\boldsymbol{r}}\cdot\langle \boldsymbol{S}^{\mathrm{sca}}\rangle(R,\theta,\varphi) \\ &= \frac{R^2}{2I_{\mathrm{inc}}}\sum_{\lambda,\lambda'}\mathrm{Re}\left\{p_{11,\lambda}p^*_{11,\lambda'}\boldsymbol{A}^{(3)}_{11,\lambda}\times\left(\frac{-\mathrm{i}\lambda'}{Z_0 Z}\boldsymbol{A}^{(3)}_{11,\lambda'}\right)^*\right\}\cdot\hat{\boldsymbol{r}}\Bigg|_{\boldsymbol{r}=(R,\theta,\varphi)}.\end{aligned} \tag{C.30}$$

Using the far-field asymptotics of the vsws, Eq. (A.38), and the fact that $R$ may be chosen arbitrarily, the expression above comes out to

$$\frac{\mathrm{d}C_{\mathrm{sca}}}{\mathrm{d}\Omega}(\theta,\varphi) = \frac{1}{2}\left|\frac{\varepsilon_1-\varepsilon}{\varepsilon_1+2\varepsilon}\right|^2 r_1^6 k^4\left(1+\cos^2\theta\right), \tag{C.31}$$

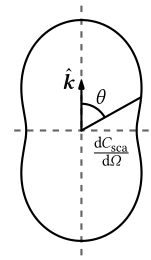

Angular distribution of Eq. (C.31).

expressing the directionality of the Rayleigh scattering cross-section (cf. [258, Eq. (15.17)], [93, Eq. (5.6)]). $\theta$ corresponds to the angle between the direction of the energy flux and the illumination direction $\hat{\boldsymbol{k}}$, with $\theta = 0$ signifying forwards and $\theta = \pi$ backwards scattering.

*Directional cross-sections for clusters of scatterers*

We consider electromagnetic scattering from a cluster of $N$ scatterers located at positions $\boldsymbol{r}_i$ with T-matrices $\boldsymbol{T}_i$, $i \in \{1,\dots,N\}$. Reconsidering Eq. (C.1), the scattered fields are now further split into contributions $\boldsymbol{E}^{\mathrm{sca},i}_\omega$, $\boldsymbol{H}^{\mathrm{sca},i}_\omega$. Each pair of fields for index $i$ is expressed analogously to Eqs. (C.3), with expansion coefficients $p^i_{\ell m,\lambda}$ and the functional dependence of the vsws evaluated at $(\boldsymbol{r}-\boldsymbol{r}_i)$. This corresponds to relocating the origin of the vsws to the position of the scatterer $\boldsymbol{r}_i$. We are further free to choose the origin with respect to which we expand the incident fields. Considering each scatterer, we construct

$N$ equivalent descriptions of the incident field, each following Eqs. (C.2) with expansion coefficients $a^i_{\ell m,\lambda}$ and the VSWS evaluated at $\boldsymbol{r}-\boldsymbol{r}_i$. The coefficients $a^i_{\ell m,\lambda}$ are related to the original $a_{\ell m,\lambda}$ by Eq. (4.39). If we ignored the multi-scattering between different scatterers, such scatterer-centered descriptions of the fields would maintain the simple relations between the coefficients $\boldsymbol{p}_i = \boldsymbol{T}_i \boldsymbol{a}_i$. The correct description including the multi-scattering gives rise to Eq. (4.38), where $\boldsymbol{p}_{\text{loc}}$ (resp. $\boldsymbol{a}_{\text{loc}}$) collects all scattered (resp. incident) field coefficients $p^i_{\ell m,\lambda}$ (resp. $a^i_{\ell m,\lambda}$) in a single column vector. Here, we further use $\boldsymbol{p}_{\text{loc},\lambda}$ and $\boldsymbol{a}_{\text{loc},\lambda}$ to refer to the vectors containing only the coefficients for a given helicity $\lambda$.

Following Eq. (C.5) and choosing an integration surface enclosing all scatterers, the scattered power now reads

$$W_{\text{sca}} = \sum_{i,j} \frac{1}{2} \iint R^2 \mathrm{d}\Omega\, \hat{\boldsymbol{r}} \cdot \mathrm{Re}\left\{ \boldsymbol{E}^{\text{sca},i}_{\omega} \times \boldsymbol{H}^{\text{sca},j*}_{\omega} \right\}, \tag{C.32}$$

with the sums for both $i$ and $j$ running over all scatterers. After inserting the expansions in VSWS centered around $\boldsymbol{r}_i$ and $\boldsymbol{r}_j$, we find terms of similar appearance as Eq. (C.8) but with the VSWS depending on $(\boldsymbol{r}-\boldsymbol{r}_i)$ and $(\boldsymbol{r}-\boldsymbol{r}_j)$, respectively. Using Eq. (A.43) to translate either one to the origin of the other and acknowledging that the shape of the integration surface and, hence, the common origin of the VSWS leaves the expressions unchanged, we find

$$W_{\text{sca}} = \sum_{i,j} \mathrm{Re}\left\{ \boldsymbol{p}_j^{\mathrm{H}} \boldsymbol{\Sigma}'^{33} \boldsymbol{C}^{(1)}\left(\boldsymbol{r}_j - \boldsymbol{r}_i\right) \boldsymbol{p}_i \right\}. \tag{C.33}$$

With regard to the extinction cross-section, we find

$$W_{\text{ext}} = -\sum_{i} \frac{1}{2} \iint R^2 \mathrm{d}\Omega\, \hat{\boldsymbol{r}} \cdot \mathrm{Re}\left\{ \boldsymbol{E}^{\text{inc}}_{\omega} \times \boldsymbol{H}^{\text{sca},i*}_{\omega} + \boldsymbol{E}^{\text{sca},i}_{\omega} \times \boldsymbol{H}^{\text{inc}*}_{\omega} \right\}. \tag{C.34}$$

In each term, it is easiest to express the incident field via its expansion centered around $\boldsymbol{r}_i$, immediately yielding expressions equivalent to Eq. (C.8). As both VSWS involved in these expressions are evaluated with respect to the same origin $\boldsymbol{r}_i$, the same results follow. Hence, the extinction power becomes

$$W_{\text{ext}} = -\sum_{i} \mathrm{Re}\left\{ \boldsymbol{a}_i^{\mathrm{H}} \boldsymbol{\Sigma}'^{13} \boldsymbol{p}_i + \boldsymbol{p}_i^{\mathrm{H}} \boldsymbol{\Sigma}'^{31} \boldsymbol{a}_i \right\}. \tag{C.35}$$

Following from the results derived before, we obtain the cross-sections

$$\begin{aligned} C_{\mathrm{sca}} &= \frac{1}{2Z_0 Z I_{\mathrm{inc}}} \sum_{\lambda} \frac{1}{k_\lambda^2} \boldsymbol{p}_{\mathrm{loc},\lambda}^{\mathsf{H}} \boldsymbol{C}_{\lambda\lambda}^{(1)} \boldsymbol{p}_{\mathrm{loc},\lambda}, \\ &= \frac{1}{2Z_0 Z I_{\mathrm{inc}}} \sum_{\lambda,\lambda',\lambda''} \frac{1}{k_\lambda^2} \boldsymbol{a}_{\mathrm{loc},\lambda'}^{\mathsf{H}} \boldsymbol{T}_{\mathrm{loc},\lambda\lambda'}^{\mathsf{H}} \boldsymbol{C}_{\lambda\lambda}^{(1)} \boldsymbol{T}_{\mathrm{loc},\lambda\lambda''} \boldsymbol{a}_{\mathrm{loc},\lambda''}, \end{aligned} \tag{C.36a}$$

$$\begin{aligned} C_{\mathrm{ext}} &= \frac{-1}{2Z_0 Z I_{\mathrm{inc}}} \sum_{\lambda} \frac{1}{k_\lambda^2} \operatorname{Re}\left\{ \boldsymbol{a}_{\mathrm{loc},\lambda}^{\mathsf{H}} \boldsymbol{p}_{\mathrm{loc},\lambda} \right\} \\ &= \frac{-1}{2Z_0 Z I_{\mathrm{inc}}} \sum_{\lambda,\lambda'} \frac{1}{k_\lambda^2} \operatorname{Re}\left\{ \boldsymbol{a}_{\mathrm{loc},\lambda}^{\mathsf{H}} \boldsymbol{T}_{\mathrm{loc},\lambda\lambda'} \boldsymbol{a}_{\mathrm{loc},\lambda'} \right\}, \end{aligned} \tag{C.36b}$$

where $\boldsymbol{C}_{\lambda\lambda}^{(1)}$ denotes the helicity-related submatrices of

$$\boldsymbol{C}^{(1)} \coloneqq \begin{pmatrix} \mathbf{1} & \boldsymbol{C}_{1,2}^{(1)} & \cdots & \boldsymbol{C}_{1,N}^{(1)} \\ \boldsymbol{C}_{2,1}^{(1)} & \mathbf{1} & \cdots & \boldsymbol{C}_{2,N}^{(1)} \\ \vdots & \vdots & \ddots & \vdots \\ \boldsymbol{C}_{N,1}^{(1)} & \boldsymbol{C}_{N,2}^{(1)} & \cdots & \mathbf{1} \end{pmatrix}, \tag{C.37}$$

using the shorthand notation $\boldsymbol{C}_{j,i}^{(1)} \coloneqq \boldsymbol{C}^{(1)}\left(\boldsymbol{r}_j - \boldsymbol{r}_i\right)$. By Eq. (A.49), $\boldsymbol{C}^{(1)}$ as well as its submatrices $\boldsymbol{C}_{\lambda\lambda}^{(1)}$ are Hermitian.

# *Publications*

The author of this work contributed to the research published in the articles and conference contributions listed below. With the exception of Ref. [P10], all of the listed contributions were developed as part of the author's doctoral research.

## *Published Peer-Reviewed Articles*


[P1] M. Gabbert, M. Nyman, L. Rebholz, C. Rockstuhl, and I. Fernandez-Corbaton, "Efficient computation of thermal radiation from biperiodic layered metasurfaces using the *T*-matrix method," Phys. Rev. B **113**, 195306 (2026) (cited on pp. 160, 189).

[P2] L. Rebholz, C. Rockstuhl, and I. Fernandez-Corbaton, "Chiral cavities made from lattices of highly electromagnetically chiral scatterers," Phys. Rev. Lett. **136**, 103802 (2026) (cited on pp. 6, 85, 147, 150–151, 164–165, 168, 170, 173, 175, 180).

[P3] M. Wasiluk, C. Goldmann, M. Bagiński, M. Pawlak, P.W. Majewski, J. Abramowicz, P. Roszkowski, L. Rebholz, C. Rockstuhl, C. Hamon, and W. Lewandowski, "From low symmetry to high dissymmetry: Chiral plasmonic films of binary and nanobipyramid assemblies," Adv. Funct. Mater. **35**, 2500933 (2025) (cited on pp. 6, 85, 126–127, 132–133, 135, 142, 146, 186, 188).

[P4] J.D. Mazo-Vásquez, M. Nyman, M. Krstić, L. Rebholz, C. Rockstuhl, and I. Fernandez-Corbaton, "Studying thermal radiation with T matrices," Phys. Rev. B **112**, 054307 (2025) (cited on pp. 160, 189).

[P5] M. Paszkiewicz-Idzik,* L. Rebholz,* C. Rockstuhl, and I. Fernandez-Corbaton, "Scalar product for the radiation of resonant modes," Phys. Rev. A **112**, 013518 (2025).

*Authors contributed equally.

[P6] M. Pawlak, A. Pierzchała, E. Benchimol, J. Tessarolo, L. Rebholz, M. Krstić, B. Zerulla, I. Fernandez-Corbaton, T. Jávorfi, G. Siligardi, G.H. Clever, C. Rockstuhl, and W. Lewandowski, "Highly dissymmetric circularly polarized luminescence via multimode chirality enhance-

ment in hierarchically ordered liquid crystal films," Adv. Opt. Mater. **13**, 2402483 (2025) (cited on pp. 94, 96, 106).

[P7] M.R. Whittam, L. Rebholz, B. Zerulla, and C. Rockstuhl, "Analyzing the acceleration time and reflectance of light sails made from homogeneous and core-shell spheres," Opt. Mater. Express **15**, 345–361 (2025).

[P8] M.R. Whittam, B. Zerulla, M. Krstić, M. Vavilin, C. Holzer, M. Nyman, L. Rebholz, I. Fernandez-Corbaton, and C. Rockstuhl, "Circular dichroism of relativistically–moving chiral molecules," Sci. Rep. **14**, 16812 (2024).

[P9] L. Rebholz, M. Krstić, B. Zerulla, M. Pawlak, W. Lewandowski, I. Fernandez-Corbaton, and C. Rockstuhl, "Separating the material and geometry contribution to the circular dichroism of chiral objects made from chiral media," ACS Photonics **11**, 1771–1779 (2024) (cited on pp. 6, 85, 93–98, 101, 105, 107–108, 110, 123–124, 184).

Article [P10] is based on research conducted as part of the author's Master's thesis.

[P10] S. Woska, L. Rebholz, P. Rietz, and H. Kalt, "Intrinsic mode coupling in mirror-symmetric whispering gallery resonators," Opt. Express **30**, 32847 (2022).

### *Articles Submitted for Review*

[S1] J.D. Fischbach, L. Rebholz, N. Ustimenko, M. Nyman, C. Rockstuhl, and I. Fernandez-Corbaton, "Broken-symmetry phenomena enhanced by quasi-bound states in the continuum," (2026) arXiv:2606.18012 [physics.optics].

[S2] J.D. Fischbach, F. Betz, L. Rebholz, P. Garg, K. Frizyuk, F. Binkowski, S. Burger, M. Hammerschmidt, and C. Rockstuhl, "Pole-expansion of the T-matrix based on a matrix-valued AAA-algorithm," (2026) arXiv:2602.18414 [physics.optics] (cited on pp. 109, 123, 140, 154, 176, 188).

### *Conference Contributions*

[†]Presenting author.

[C1] J.D. Fischbach,[†] L. Rebholz, N. Ustimenko, M. Nyman, C. Rockstuhl, and I. Fernandez-Corbaton, "Resonant symmetry breaking: Perfect

helicity-preserving reflection at near-normal incidence," *PhotonIcs and Electromagnetics Research Symposium, PIERS2026, Suzhou, China, July 27–31 2026* (oral presentation).

[C2] L. Rebholz,† C. Rockstuhl, and I. Fernandez-Corbaton, "Chiral cavities made from lattices of highly electromagnetically-chiral scatterers," *16th International Conference on Metamaterials, Photonic Crystals and Plasmonics, META 2026, Dublin, Ireland, July 14–17 2026* (invited oral presentation).

[C3] I. Fernandez-Corbaton, K. Frizyuk, M. Krstić, M. Nyman, E. Stamatopoulou, T. Sturges, A. Brandt, J.D. Fischbach, M. Gabbert, P. Garg, E. Herzog, M. Poleva, L. Rebholz, M.L. Schubert, N. Ustimenko, N. Asadova, and C. Rockstuhl,† "Model- and data-driven inverse design of nanophotonic scatterers," *Future 3D Additive Manufacturing – The 3DMM2O Conference 2026, Schöntal, Germany, March 23–26 2026* (oral presentation).

[C4] M. Gabbert, J.D. Mazo-Vásquez, M. Nyman, L. Rebholz, M. Krstić, C. Rockstuhl, and I. Fernandez-Corbaton,† "From molecules to metasurfaces: Fast multiscale modeling of thermal emission," *Future 3D Additive Manufacturing – The 3DMM2O Conference 2026, Schöntal, Germany, March 23–26 2026* (poster presentation).

[C5] L. Rebholz,† C. Rockstuhl, and I. Fernandez-Corbaton, "Chiral cavities made from lattices of highly electromagnetically-chiral scatterers," *"Future Challenges for Nanophotonic Scattering" Workshop, Bad Herrenalb, Germany, October 27–31 2025* (oral presentation).

[C6] C. Rockstuhl,† I. Fernandez-Corbaton, C. Holzer, M. Krstić, M. Nyman, T. Sturges, N. Asadova, J.D. Fischbach, P. Garg, M. Poleva, L. Rebholz, M.L. Schubert, and N. Ustimenko, "Theoretical and computational advances in nanophotonic scattering," *2025 Conference on Lasers and Electro-Optics/Europe, CLEO®/Europe-EQEC, Munich, Germany, June 23–27 2025* (invited oral presentation).

[C7] L. Rebholz,† C. Rockstuhl, and I. Fernandez-Corbaton, "Chiral optical cavities using metasurfaces of highly electromagnetically chiral scatterers," *PhotonIcs and Electromagnetics Research Symposium, PIERS2025, Abu Dhabi, UAE, May 4–8 2025* (oral presentation).

[C8] L. Rebholz,† C. Rockstuhl, and I. Fernandez-Corbaton, "Chiral optical cavities using metasurfaces of highly electromagnetically chiral scatterers," *Conference on Mathematics of Wave Phenomena, Karlsruhe, Germany, February 24–28 2025* (oral presentation).

[C9] L. Rebholz, B. Zerulla, M.R. Whittam, M. Vavilin, N. Gieseler, D. Beutel, C. Holzer, M. Nyman, M. Krstić, I. Fernandez-Corbaton, and C. Rockstuhl,† "Chirality in photonic nanostructures across different length scales," *The 18th International Congress on Artificial Materials for Novel Wave Phenomena, Metamaterials'2024, Chania, Greece, September 9–12 2024* (invited oral presentation).

[C10] L. Rebholz,† M. Krstić, B. Zerulla, M. Pawlak, W. Lewandowski, I. Fernandez-Corbaton, and C. Rockstuhl, "Separating the material and geometry contribution to the circular dichroism of chiral objects made from chiral media," *Karlsruhe Days of Optics & Photonics (KDOP), Karlsruhe, Germany, November 16–17 2023* (poster presentation).

[C11] D. Beutel, N. Perdana, B. Zerulla, N. Asadova, P. Garg, A. Lamprianidis, R. Venkitakrishnan, L. Rebholz, M. Nyman, C. Holzer, M. Krstić, I. Fernandez-Corbaton, and C. Rockstuhl,† "Current developments in describing photonic materials using a T-matrix approach: From a general data format and public repository to the solution of inverse problems," *The 17th International Congress on Artificial Materials for Novel Wave Phenomena, Metamaterials'2023, Chania, Greece, September 11–14 2023* (invited oral presentation).

[C12] L. Rebholz,† M. Krstić, B. Zerulla, M. Pawlak, W. Lewandowski, I. Fernandez-Corbaton, and C. Rockstuhl, "Separating the material and geometry contribution to the circular dichroism of chiral objects made from chiral media," *The 17th International Congress on Artificial Materials for Novel Wave Phenomena, Metamaterials'2023, Chania, Greece, September 11–14 2023* (oral presentation).

# *Bibliography*


[1] B. Kahr and O. Arteaga, "Arago's best paper," ChemPhysChem **13**, 79–88 (2012) (cited on p. 1).

[2] G. Vantomme and J. Crassous, "Pasteur and chirality: A story of how serendipity favors the prepared minds," Chirality **33**, 597–601 (2021) (cited on pp. 1, 87).

[3] A.D. Liehr, "Interaction of electromagnetic radiation with matter. I. Theory of optical rotatory power: Topic A. Trigonal dihedral compounds," J. Phys. Chem. **68**, 665–722 (1964) (cited on p. 1).

[4] J. Gal and P. Cintas, "Early history of the recognition of molecular biochirality," in *Biochirality: Origins, Evolution and Molecular Recognition*, Ed. by P. Cintas (Springer, Berlin, 2013), pp. 1–40 (cited on p. 1).

[5] J.I. Kwiecińska and M. Cieplak, "Chirality and protein folding," J. Phys. Condens. Matter **17**, S1565–S1580 (2005) (cited on pp. 1, 88).

[6] P.W. Kuchel, G. Pagès, and C. Naumann, "'Chiral compartmentation' in metabolism: Enzyme stereo-specificity yielding evolutionary options," FEBS Lett. **587**, 2790–2797 (2013) (cited on pp. 1, 88).

[7] M.T. Reetz and M. Garcia-Borràs, "The unexplored importance of fleeting chiral intermediates in enzyme-catalyzed reactions," J. Am. Chem. Soc. **143**, 14939–14950 (2021) (cited on pp. 1, 88).

[8] K. Das, H. Balaram, and K. Sanyal, "Amino acid chirality: Stereospecific conversion and physiological implications," ACS Omega **9**, 5084–5099 (2024) (cited on pp. 1, 88).

[9] W. Rehman, L.M. Arfons, and H.M. Lazarus, "The rise, fall and subsequent triumph of thalidomide: Lessons learned in drug development," Ther. Adv. Hematol. **2**, 291–308 (2011) (cited on pp. 1, 88).

[10] C. Bertucci, M. Pistolozzi, and A. De Simone, "Circular dichroism in drug discovery and development: An abridged review," Anal. Bioanal. Chem. **398**, 155–166 (2010) (cited on p. 1).

[11] P.L. Polavarapu, "Determination of the absolute configurations of chiral drugs using chiroptical spectroscopy," Molecules **21**, 1056 (2016) (cited on p. 1).

[12] J.H. Williams, "Optical activity," in *The Molecule as Meme* (Morgan & Claypool, San Rafael, CA, 2018) (cited on p. 1).

[13] H. Yao, E. Wynendaele, X. Xu, A. Kosgei, and B. De Spiegeleer, "Circular dichroism in functional quality evaluation of medicines," J. Pharm. Biomed. Anal. **147**, 50–64 (2018) (cited on p. 1).

[14] A. Lininger, G. Palermo, A. Guglielmelli, G. Nicoletta, M. Goel, M. Hinczewski, and G. Strangi, "Chirality in light–matter interaction," Adv. Mater. **35**, 2107325 (2023) (cited on p. 1).

[15] Nobel Prize Outreach, *The Nobel Prize in Chemistry 2001*, Press Release, 2001, https://www.nobelprize.org/prizes/chemistry/2001/press-release/ (accessed June 18, 2026) (cited on p. 2).

[16] Nobel Prize Outreach, *The Nobel Prize in Chemistry 2021*, Press Release, 2021, https://www.nobelprize.org/prizes/chemistry/2021/press-release/ (accessed June 18, 2026) (cited on p. 2).

[17] J.M. Brown and S.G. Davies, "Chemical asymmetric synthesis," Nature **342**, 631–636 (1989) (cited on p. 2).

[18] V. Farina, J.T. Reeves, C.H. Senanayake, and J.J. Song, "Asymmetric synthesis of active pharmaceutical ingredients," Chem. Rev. **106**, 2734–2793 (2006) (cited on p. 2).

[19] T. Akiyama and I. Ojima, (Eds.), *Catalytic Asymmetric Synthesis*, 4th ed. (Wiley, Hoboken, NJ, 2022) (cited on p. 2).

[20] B.L. Feringa and R.A. van Delden, "Absolute asymmetric synthesis: The origin, control, and amplification of chirality," Angew. Chem., Int. Ed. **38**, 3418–3438 (1999) (cited on p. 2).

[21] C. He and Y. Li, "Absolute asymmetric synthesis driven by circularly polarized light," Chin. Chem. Lett. **34**, 108077 (2023) (cited on p. 2).

[22] S.F. Mason, "Optical rotatory power," Q. Rev. Chem. Soc. **17**, 20–66 (1963) (cited on pp. 2, 163).

[23] W.R. Salzman and P.L. Polavarapu, "Calculated rotational strengths and dissymmetry factors for rotational transitions of the chiral deuterated oxiranes, methyl- and dimethyl-oxirane, and methylthirane," Chem. Phys. Lett. **179**, 1–8 (1991) (cited on pp. 2, 163).

[24] R.D. Richardson, M.G.J. Baud, C.E. Weston, H.S. Rzepa, M.K. Kuimova, and M.J. Fuchter, "Dual wavelength asymmetric photochemical synthesis with circularly polarized light," Chem. Sci. **6**, 3853–3862 (2015) (cited on p. 2).

[25] J.L. Greenfield, J. Wade, J.R. Brandt, X. Shi, T.J. Penfold, and M.J. Fuchter, "Pathways to increase the dissymmetry in the interaction of chiral light and chiral molecules," Chem. Sci. **12**, 8589–8602 (2021) (cited on p. 2).

[26] A. Garg, D. Rendina, H. Bendale, T. Akiyama, and I. Ojima, "Recent advances in catalytic asymmetric synthesis," Front. Chem. **12**, 1398397 (2024) (cited on p. 2).

[27] D. Chandra, T. Sharma, Sarthi, Sachin, and U. Sharma, "Chiral metal complexes: Design strategies for precision in asymmetric C–H activation," J. Catal. **439**, 115756 (2024) (cited on p. 2).

[28] L. Zhang and E. Meggers, "Chiral-at-metal catalysts: History, terminology, design, synthesis, and applications," Chem. Soc. Rev. **54**, 1986–2005 (2025) (cited on p. 2).

[29] X. Qiu, Y. Zhang, Y. Zhu, C. Long, L. Su, S. Liu, and Z. Tang, "Applications of nanomaterials in asymmetric photocatalysis: Recent progress, challenges, and opportunities," Adv. Mater. **33**, 2001731 (2021) (cited on p. 2).

[30] J. Wang, X. Lv, and Z. Jiang, "Visible-light-mediated photocatalytic deracemization," Chem. Eur. J. **29**, e202204029 (2023) (cited on p. 2).

[31] T. Saget, M. Mellah, P. Dauban, and E. Schulz, "Asymmetric catalysis: Recent advances toward a more sustainable synthesis," ACS Cent. Sci. **12**, 280–299 (2026) (cited on p. 2).

[32] T. Kawasaki, M. Sato, S. Ishiguro, T. Saito, Y. Morishita, I. Sato, H. Nishino, Y. Inoue, and K. Soai, "Enantioselective synthesis of near enantiopure compound by asymmetric autocatalysis triggered by asymmetric photolysis with circularly polarized light," J. Am. Chem. Soc. **127**, 3274–3275 (2005) (cited on p. 2).

[33] J.M. Ribó, C. Blanco, J. Crusats, Z. El-Hachemi, D. Hochberg, and A. Moyano, "Absolute asymmetric synthesis in enantioselective autocatalytic reaction networks: Theoretical games, speculations on chemical evolution and perhaps a synthetic option," Chem. Eur. J. **20**, 17250–17271 (2014) (cited on p. 2).

[34] M. Schäferling, N. Engheta, H. Giessen, and T. Weiss, "Reducing the complexity: Enantioselective chiral near-fields by diagonal slit and mirror configuration," ACS Photonics **3**, 1076–1084 (2016) (cited on p. 3).

[35] C. He, G. Yang, Y. Kuai, S. Shan, L. Yang, J. Hu, D. Zhang, Q. Zhang, and G. Zou, "Dissymmetry enhancement in enantioselective synthesis of helical polydiacetylene by application of superchiral light," Nat. Commun. **9**, 5117 (2018) (cited on p. 3).

[36] J. Gautier, M. Li, T.W. Ebbesen, and C. Genet, "Planar chirality and optical spin–orbit coupling for chiral Fabry–Perot cavities," ACS Photonics **9**, 778–783 (2022) (cited on pp. 3, 164).

[37] R.R. Riso, L. Grazioli, E. Ronca, T. Giovannini, and H. Koch, "Strong coupling in chiral cavities: Nonperturbative framework for enantiomer discrimination," Phys. Rev. X **13**, 031002 (2023) (cited on pp. 3, 163).

[38] R. Kumar, B. Trodden, A. Klimash, M. Bousquet, S.K. Chaubey, N.J. Fairbairn, B.A. Russell, K. Wynne, A.S. Karimullah, N. Gadegaard, P.J. Skabara, G.J. Hedley, S. Hashiyada, A. Movsesyan, A.O. Govorov, and M. Kadodwala, "Electromagnetic enantiomer: Chiral nanophotonic cavities for inducing chemical asymmetry," ACS Nano **18**, 22220–22232 (2024) (cited on p. 3).

[39] R.R. Riso, E. Ronca, and H. Koch, "Strong coupling to circularly polarized photons: Toward cavity-induced enantioselectivity," J. Phys. Chem. Lett. **15**, 8838–8844 (2024) (cited on pp. 3, 163).

[40] Y. Liu and X. Jiang, "Why microfluidics? Merits and trends in chemical synthesis," Lab Chip **17**, 3960–3978 (2017) (cited on p. 3).

[41] D. Zhang, S. Jia, Z. Jin, J. Bu, G. Guo, J. Deng, and X. Wang, "Microfluidic technology: A new strategy for controllable synthesis of metal nanomaterials," ChemElectroChem **12**, e202400666 (2025) (cited on p. 3).

[42] J.D. Jackson, *Classical Electrodynamics*, 3rd ed. (Wiley, Hoboken, NJ, 1998) (cited on pp. 10, 15, 25, 35, 51, 57, 193–195).

[43] G. Kristensson, *Scattering of Electromagnetic Waves by Obstacles* (SciTech, Edison, NJ, 2016) (cited on pp. 13, 21–22, 24–25).

[44] A. Karlsson and G. Kristensson, "Constitutive relations, dissipation, and reciprocity for the Maxwell equations in the time domain," J. Electromagn. Waves Appl. **6**, 537–551 (1992) (cited on pp. 13, 21).

[45] G. Russakoff, "A derivation of the macroscopic Maxwell equations," Am. J. Phys. **38**, 1188–1195 (1970) (cited on p. 16).

[46] R.E. Raab and O.L. de Lange, *Multipole Theory in Electromagnetism: Classical, Quantum, and Symmetry Aspects, with Applications* (Clarendon, Oxford, 2005) (cited on pp. 16–18).

[47] O.L. de Lange and R.E. Raab, "Surprises in the multipole description of macroscopic electrodynamics," Am. J. Phys. **74**, 301–312 (2006) (cited on pp. 17–19).

[48] O.L. de Lange and R.E. Raab, "Completion of multipole theory for the electromagnetic response fields D and H," Proc. R. Soc. A **459**, 1325–1341 (2003) (cited on pp. 18–19).

[49] J.H. Van Vleck, *The Theory of Electric and Magnetic Susceptibilities* (Clarendon, Oxford, 1932) (cited on p. 18).

[50] E.B. Graham and R.E. Raab, "Light propagation in cubic and other anisotropic crystals," Proc. R. Soc. Lond. A **430**, 593–614 (1990) (cited on p. 18).

[51] C. Menzel, *Characterisation of Optical Metamaterials: Effective Parameters and Beyond*, Dissertation (Friedrich-Schiller-Universität Jena, Jena, 2011) (cited on pp. 19, 21).

[52] A. Lakhtakia, *Beltrami Fields in Chiral Media* (World Scientific, Singapore, 1994) (cited on pp. 21, 30–31, 40, 52, 86–87, 155).

[53] P. Drude, *Lehrbuch der Optik*, 2nd ed. (Hirzel, Leipzig, 1906) (cited on p. 21).

[54] A. Lakhtakia, V.K. Varadan, and V.V. Varadan, *Time-Harmonic Electromagnetic Fields in Chiral Media*, Lecture Notes in Physics 335 (Springer, Berlin, 1989) (cited on p. 22).

[55] A.H. Sihvola and I.V. Lindell, "BI-isotropic constitutive relations," Microw. Opt. Technol. Lett. **4**, 295–297 (1991) (cited on p. 22).

[56] B.D.H. Tellegen, "The gyrator, a new electric network element," Philips Res. Rep. **3**, 81–101 (1948) (cited on pp. 22–23).

[57] D.K. Cheng and J.-A. Kong, "Covariant descriptions of bianisotropic media," Proc. IEEE **56**, 248–251 (1968) (cited on p. 23).

[58] J.A. Kong, *Electromagnetic Wave Theory* (EMW, Cambridge, MA, 2008) (cited on p. 23).

[59] M.S. Mirmoosa, M.H. Mostafa, A. Norrman, and S.A. Tretyakov, "Time interfaces in bianisotropic media," Phys. Rev. Res. **6**, 013334 (2024) (cited on p. 24).

[60] O.L. de Lange and R.E. Raab, "Electromagnetic boundary conditions in multipole theory," J. Math. Phys. **54**, 093513 (2013) (cited on p. 25).

[61] C.F. Bohren, "Light scattering by an optically active sphere," Chem. Phys. Lett. **29**, 458–462 (1974) (cited on pp. 30, 52).

[62] H.K. Moffatt, *Magnetic Field Generation in Electrically Conducting Fluids* (Cambridge University Press, Cambridge, UK, 1978) (cited on p. 31).

[63] L. Silberstein, "Elektromagnetische Grundgleichungen in bivektorieller Behandlung," Ann. Phys. (Berl.) **327**, 579–586 (1907) (cited on p. 31).

[64] L. Silberstein, "Nachtrag zur Abhandlung über „Elektromagnetische Grundgleichungen in bivektorieller Behandlung"," Ann. Phys. (Berl.) **329**, 783–784 (1907) (cited on p. 31).

[65] H. Weber, *Die partiellen Differential-Gleichungen der mathematischen Physik: Nach Riemann's Vorlesungen*, 4th ed., Vol. 2 (Vieweg, Braunschweig, 1901) (cited on p. 31).

[66] P.M. Morse and H. Feshbach, *Methods of Theoretical Physics*, Vol. I (McGraw-Hill, New York, 1953) (cited on p. 32).

[67] P.M. Morse and H. Feshbach, *Methods of Theoretical Physics*, Vol. II (McGraw-Hill, New York, 1953) (cited on pp. 33, 191).

[68] M. Born and E. Wolf, *Principles of Optics: Electromagnetic Theory of Propagation, Interference and Diffraction of Light*, 4th ed. (Pergamon, Oxford, 1970) (cited on pp. 37, 210).

[69] F. Crimin, N. Mackinnon, J.B. Götte, and S.M. Barnett, "Optical helicity and chirality: Conservation and sources," Appl. Sci. **9**, 828 (2019) (cited on pp. 38, 42–43).

[70] J.C. Maxwell, *A Treatise on Electricity and Magnetism*, Vol. I (Clarendon, Oxford, 1873) (cited on p. 38).

[71] H.K. Moffatt, "Helicity and singular structures in fluid dynamics," Proc. Natl. Acad. Sci. U.S.A. **111**, 3663–3670 (2014) (cited on p. 38).

[72] W.M. Elsasser, "Hydromagnetic dynamo theory," Rev. Mod. Phys. **28**, 135–163 (1956) (cited on p. 38).

[73] L. Woltjer, "A theorem on force-free magnetic fields," Proc. Natl. Acad. Sci. U.S.A. **44**, 489–491 (1958) (cited on p. 38).

[74] J.L. Trueba and A.F. Rañada, "The electromagnetic helicity," Eur. J. Phys. **17**, 141 (1996) (cited on p. 38).

[75] I. Fernandez i Corbaton, *Helicity and Duality Symmetry in Light Matter Interactions: Theory and Applications*, PhD Thesis (Macquarie University, Sydney, 2014) (cited on p. 38).

[76] D. Zwanziger, "Quantum field theory of particles with both electric and magnetic charges," Phys. Rev. **176**, 1489–1495 (1968) (cited on pp. 38–39).

[77] J. Dressel, K.Y. Bliokh, and F. Nori, "Spacetime algebra as a powerful tool for electromagnetism," Phys. Rep. **589**, 1–71 (2015) (cited on p. 39).

[78] M.G. Calkin, "An invariance property of the free electromagnetic field," Am. J. Phys. **33**, 958–960 (1965) (cited on p. 39).

[79] D.J. Griffiths, *Introduction to Electrodynamics*, 4th ed. (Pearson, Boston, 2013) (cited on p. 39).

[80] A.M. Stewart, "Does the Helmholtz theorem of vector decomposition apply to the wave fields of electromagnetic radiation?" Phys. Scr. **89**, 065502 (2014) (cited on p. 40).

[81] W.-K. Tung, *Group Theory in Physics* (World Scientific, Singapore, 1985) (cited on p. 40).

[82] L. Gross, "Norm invariance of mass-zero equations under the conformal group," J. Math. Phys. **5**, 687–695 (1964) (cited on p. 41).

[83] I. Fernandez-Corbaton, "A conformally invariant derivation of average electromagnetic helicity," Symmetry **11**, 1427 (2019) (cited on pp. 42, 209).

[84] I. Bialynicki-Birula, "Photon wave function," in *Progress in Optics*, Vol. 36, Ed. by E. Wolf (Elsevier, Amsterdam, 1996), pp. 245–294 (cited on p. 42).

[85] D.M. Lipkin, "Existence of a new conservation law in electromagnetic theory," J.Math. Phys. **5**, 696–700 (1964) (cited on p. 42).

[86] Y. Tang and A.E. Cohen, "Optical chirality and its interaction with matter," Phys. Rev. Lett. **104**, 163901 (2010) (cited on p. 42).

[87] K.Y. Bliokh and F. Nori, "Characterizing optical chirality," Phys. Rev. A **83**, 021803 (2011) (cited on p. 43).

[88] S.M. Barnett, R.P. Cameron, and A.M. Yao, "Duplex symmetry and its relation to the conservation of optical helicity," Phys. Rev. A **86**, 013845 (2012) (cited on p. 43).

[89] J.A. Stratton, *Electromagnetic Theory* (Wiley, Hoboken, NJ, 2007) (cited on pp. 46, 69, 193).

[90] Q.-C. Shang, Z.-S. Wu, T. Qu, Z.-J. Li, and L. Bai, "Scattering from a multilayered chiral sphere using an iterative method," J. Quant. Spectrosc. Radiat. Transfer **173**, 72–82 (2016) (cited on p. 46).

[91] D.T. Beutel, *A Holistic Framework for Electromagnetic Scattering Simulations Based on the T-Matrix Method*, Dissertation (Karlsruher Institut für Technologie (KIT), Karlsruhe, 2024) (cited on pp. 47–48, 56–57, 60, 202).

[92] F.W.J. Olver, A.B. Olde Daalhuis, D.W. Lozier, B.I. Schneider, R.F. Boisvert, C.W. Clark, B.R. Miller, B.V. Saunders, H.S. Cohl, and M.A. McClain, (Eds.), *NIST Digital Library of Mathematical Functions*, `https://dlmf.nist.gov/`, Release 1.2.5 (Dec. 15, 2025) (cited on pp. 48, 192–194, 201, 218).

[93] C.F. Bohren and D.R. Huffman, *Absorption and Scattering of Light by Small Particles* (Wiley, New York, 1983) (cited on pp. 49–53, 57, 191, 193, 197, 219, 226–227).

[94] H.F. Arnoldus, "Mie coefficients," Photonics **12**, 731 (2025) (cited on p. 51).

[95] P.C. Waterman, "Matrix formulation of electromagnetic scattering," Proc. IEEE **53**, 805–812 (1965) (cited on p. 53).

[96] P.C. Waterman, "Symmetry, unitarity, and geometry in electromagnetic scattering," Phys. Rev. D **3**, 825–839 (1971) (cited on p. 53).

[97] B. Peterson and S. Ström, "$T$ matrix for electromagnetic scattering from an arbitrary number of scatterers and representations of E(3)," Phys. Rev. D **8**, 3661–3678 (1973) (cited on pp. 53, 60–61).

[98] D.W. Mackowski, "Analysis of radiative scattering for multiple sphere configurations," Proc. R. Soc. Lond. A **433**, 599–614 (1991) (cited on p. 53).

[99] D. Beutel, A. Groner, C. Rockstuhl, and I. Fernandez-Corbaton, "Efficient simulation of biperiodic, layered structures based on the T-matrix method," J. Opt. Soc. Am. B **38**, 1782–1791 (2021) (cited on pp. 53, 64, 70, 80).

[100] D. Beutel, *treams*, version 0.4.5 (TFP Photonics, Karlsruhe, 2024) (cited on pp. 53, 62, 70, 75, 97, 132, 151).

[101] D. Beutel, I. Fernandez-Corbaton, and C. Rockstuhl, "*treams* – a T-matrix-based scattering code for nanophotonics," Comput. Phys. Commun. **297**, 109076 (2024) (cited on pp. 53, 60, 63, 65, 132, 193–195, 197, 200–201, 204, 206–207).

[102] D. Beutel, I. Fernandez-Corbaton, and C. Rockstuhl, "Unified lattice sums accommodating multiple sublattices for solutions of the Helmholtz equation in two and three dimensions," Phys. Rev. A **107**, 013508 (2023) (cited on pp. 53, 63, 65).

[103] B. Auguié, W.R.C. Somerville, S. Roache, and E.C. Le Ru, "Numerical investigation of the Rayleigh hypothesis for electromagnetic scattering by a particle," J. Opt. **18**, 075007 (2016) (cited on pp. 55, 61).

[104] V.G. Farafonov, "Applicability of the T-matrix method and its modifications," Opt. Spectrosc. **92**, 748–760 (2002) (cited on pp. 55, 61).

[105] M.V.K. Chari and S.J. Salon, *Numerical Methods in Electromagnetism* (Academic Press, San Diego, 2000) (cited on p. 56).

[106] N. Asadova, K. Achouri, K. Arjas, B. Auguié, R. Aydin, A. Baron, D. Beutel, B. Bodermann, K. Boussaoud, S. Burger, M. Choi, K.M. Czajkowski, A.B. Evlyukhin, A. Fazel-Najafabadi, I. Fernandez-Corbaton, P. Garg, D. Globosits, U. Hohenester, H. Kim, S. Kim, et al., "T-matrix representation of optical scattering response: Suggestion for a data format," J. Quant. Spectrosc. Radiat. Transfer **333**, 109310 (2025) (cited on pp. 56–57, 119, 125).

[107] S.C. Brenner and L.R. Scott, *The Mathematical Theory of Finite Element Methods*, Ed. by J.E. Marsden, L. Sirovich, and S.S. Antman, 3rd ed., Texts in Applied Mathematics 15 (Springer, New York, 2008) (cited on p. 56).

[108] P. Monk, "Analysis of a finite element method for Maxwell's equations," SIAM J. Numer. Anal. **29**, 714–729 (1992) (cited on p. 56).

[109] P. Monk, *Finite Element Methods for Maxwell's Equations* (Clarendon, Oxford, 2003) (cited on p. 56).

[110] R. Hiptmair, "Finite elements in computational electromagnetism," Acta Numer. **11**, 237–339 (2002) (cited on p. 56).

[111] S. Zaglmayr, *High Order Finite Element Methods for Electromagnetic Field Computation*, Dissertation (Johannes Kepler Universität Linz, Linz, 2006) (cited on p. 56).

[112] J. Pomplun, S. Burger, L. Zschiedrich, and F. Schmidt, "Adaptive finite element method for simulation of optical nano structures," Phys. Status Solidi B **244**, 3419–3434 (2007) (cited on p. 56).

[113] M. Fruhnert, I. Fernandez-Corbaton, V. Yannopapas, and C. Rockstuhl, "Computing the T-matrix of a scattering object with multiple plane wave illuminations," Beilstein J. Nanotechnol. **8**, 614–626 (2017) (cited on p. 56).

[114] JCMwave, *JCMsuite*, version 6.0.10 (JCMwave GmbH, Berlin, 2024) (cited on pp. 57, 151).

[115] S. Burger, L. Zschiedrich, J. Pomplun, and F. Schmidt, "JCMsuite: An adaptive FEM solver for precise simulations in nano-optics," in *Integrated Photonics and Nanophotonics Research and Applications 2008* (OSA, 2008), ITuE4 (cited on pp. 57, 96).

[116] X. Garcia-Santiago, M. Hammerschmidt, S. Burger, C. Rockstuhl, I. Fernandez-Corbaton, and L. Zschiedrich, "Decomposition of scattered electromagnetic fields into vector spherical wave functions on surfaces with general shapes," Phys. Rev. B **99**, 045406 (2019) (cited on p. 57).

[117] M.I. Mishchenko, L.D. Travis, and D.W. Mackowski, "T-matrix computations of light scattering by nonspherical particles: A review," J. Quant. Spectrosc. Radiat. Transfer **55**, 535–575 (1996) (cited on pp. 60, 65, 119, 125, 130, 197, 207, 223).

[118] D. Schebarchov, E.C. Le Ru, J. Grand, and B. Auguié, "Mind the gap: Testing the Rayleigh hypothesis in T-matrix calculations with adjacent spheroids," Opt. Express **27**, 35750–35760 (2019) (cited on p. 61).

[119] C. Kittel, *Introduction to Solid State Physics*, 8th ed. (Wiley, Hoboken, NJ, 2005) (cited on pp. 63, 129).

[120] P.P. Ewald, "Die Berechnung optischer und elektrostatischer Gitterpotentiale," Ann. Phys. (Berl.) **369**, 253–287 (1921) (cited on p. 65).

[121] K. Kambe, "Theory of low-energy electron diffraction: I. Application of the cellular method to monatomic layers," Z. Naturforsch. A **22**, 322–330 (1967) (cited on p. 65).

[122] E.C. Le Ru, W.R.C. Somerville, and B. Auguié, "Radiative correction in approximate treatments of electromagnetic scattering by point and body scatterers," Phys. Rev. A **87**, 012504 (2013) (cited on pp. 65–66).

[123] P.V. Landshoff, "Cayley transform of the S matrix," J. Math. Phys. **9**, 2279–2282 (1968) (cited on p. 65).

[124] M. Nyman, A. Shevchenko, and M. Kaivola, "Fluorescence enhancement and nonreciprocal transmission of light waves by nanomaterial interfaces," Phys. Rev. A **96**, 053828 (2017) (cited on p. 75).

[125] G.P. Ortiz and W.L. Mochán, "Nonadditivity of Poynting vector within opaque media," J. Opt. Soc. Am. A **22**, 2827–2837 (2005) (cited on p. 75).

[126] R. Redheffer, "Inequalities for a matrix Riccati equation," J. Math. Mech. **8**, 349–367 (1959) (cited on p. 81).

[127] Y. Yang, R.C. da Costa, D.-M. Smilgies, A.J. Campbell, and M.J. Fuchter, "Induction of circularly polarized electroluminescence from an achiral light-emitting polymer via a chiral small-molecule dopant," Adv. Mater. **25**, 2624–2628 (2013) (cited on p. 86).

[128] A. Slosar, K. Land, S. Bamford, C. Lintott, D. Andreescu, P. Murray, R. Nichol, M.J. Raddick, K. Schawinski, A. Szalay, D. Thomas, and J. Vandenberg, "Galaxy Zoo: Chiral correlation function of galaxy spins," Mon. Not. R. Astron. Soc. **392**, 1225–1232 (2009) (cited on p. 86).

[129] L.D. Barron, "An introduction to chirality at the nanoscale," in *Chirality at the Nanoscale: Nanoparticles, Surfaces, Materials and More*, Ed. by D.B. Amabilino (Wiley-VCH, Weinheim, 2009), pp. 1–28 (cited on p. 88).

[130] M.R. Islam, J.G. Mahdi, and I.D. Bowen, "Pharmacological importance of stereochemical resolution of enantiomeric drugs," Drug Saf. **17**, 149–165 (1997) (cited on p. 88).

[131] W.H. Brooks, W.C. Guida, and K.G. Daniel, "The significance of chirality in drug design and development," Curr. Top. Med. Chem. **11**, 760–770 (2011) (cited on p. 88).

[132] T.G. Mayerhöfer, S. Pahlow, and J. Popp, "The Bouguer-Beer-Lambert law: Shining light on the obscure," ChemPhysChem **21**, 2029–2046 (2020) (cited on p. 90).

[133] H.C. van de Hulst, *Light Scattering by Small Particles*, corrected republication (Dover, New York, 1981) (cited on p. 90).

[134] R.W. Woody, "Circular dichroism," in *Biochemical Spectroscopy*, Methods in Enzymology 246 (Academic Press, New York, 1995), pp. 34–71 (cited on p. 91).

[135] X. Wang and Z. Tang, "Circular dichroism studies on plasmonic nanostructures," Small **13**, 1601115 (2017) (cited on p. 91).

[136] M.L. Solomon, A.A.E. Saleh, L.V. Poulikakos, J.M. Abendroth, L.F. Tadesse, and J.A. Dionne, "Nanophotonic platforms for chiral sensing and separation," Acc. Chem. Res. **53**, 588–598 (2020) (cited on p. 91).

[137] L.A. Warning, A.R. Miandashti, L.A. McCarthy, Q. Zhang, C.F. Landes, and S. Link, "Nanophotonic approaches for chirality sensing," ACS Nano **15**, 15538–15566 (2021) (cited on p. 91).

[138] J.E. Vázquez-Lozano and A. Martínez, "Toward chiral sensing and spectroscopy enabled by all-dielectric integrated photonic waveguides," Laser Photonics Rev. **14**, 1900422 (2020) (cited on p. 91).

[139] J. García-Guirado, M. Svedendahl, J. Puigdollers, and R. Quidant, "Enhanced chiral sensing with dielectric nanoresonators," Nano Lett. **20**, 585–591 (2020) (cited on p. 91).

[140] J. Olmos-Trigo, H. Sugimoto, and M. Fujii, "Far-field detection of near-field circular dichroism enhancements induced by a nanoantenna," Laser Photonics Rev. **18**, 2300948 (2024) (cited on p. 91).

[141] S. Zhou, J. Bian, P. Chen, M. Xie, J. Chao, W. Hu, Y. Lu, and W. Zhang, "Polarization-dispersive imaging spectrometer for scattering circular dichroism spectroscopy of single chiral nanostructures," Light Sci. Appl. **11**, 64 (2022) (cited on p. 91).

[142] H. Hu, Q. Gan, and Q. Zhan, "Generation of a nondiffracting superchiral optical needle for circular dichroism imaging of sparse subdiffraction objects," Phys. Rev. Lett. **122**, 223901 (2019) (cited on p. 91).

[143] M. Quack, "Structure and dynamics of chiral molecules," Angew. Chem., Int. Ed. **28**, 571–586 (1989) (cited on p. 93).

[144] S.-W. Choi, T. Izumi, Y. Hoshino, Y. Takanishi, K. Ishikawa, J. Watanabe, and H. Takezoe, "Circular-polarization-induced enantiomeric excess in liquid crystals of an achiral, bent-shaped mesogen," Angew. Chem., Int. Ed. **45**, 1382–1385 (2006) (cited on p. 94).

[145] A. Jedrych, M. Pawlak, E. Gorecka, W. Lewandowski, and M.M. Wojcik, "Light-responsive supramolecular nanotubes-based chiral plasmonic assemblies," ACS Nano **17**, 5548–5560 (2023) (cited on p. 94).

[146] G. Albano, G. Pescitelli, and L. Di Bari, "Chiroptical properties in thin films of π-conjugated systems," Chem. Rev. **120**, 10145–10243 (2020) (cited on p. 94).

[147] J. Wade, J.N. Hilfiker, J.R. Brandt, L. Liirò-Peluso, L. Wan, X. Shi, F. Salerno, S.T.J. Ryan, S. Schöche, O. Arteaga, T. Jávorfi, G. Siligardi, C. Wang, D.B. Amabilino, P.H. Beton, A.J. Campbell, and M.J. Fuchter, "Natural optical activity as the origin of the large chiroptical properties in π-conjugated polymer thin films," Nat. Commun. **11**, 6137 (2020) (cited on p. 94).

[148] M.E. Casida, "Time-dependent density-functional theory for molecules and molecular solids," J. Mol. Struct. THEOCHEM **914**, 3–18 (2009) (cited on p. 94).

[149] B. Zerulla, M. Krstić, D. Beutel, C. Holzer, C. Wöll, C. Rockstuhl, and I. Fernandez-Corbaton, "A multi-scale approach for modeling the optical response of molecular materials inside cavities," Adv. Mater. **34**, 2200350 (2022) (cited on p. 95).

[150] T. Schwartz, J.A. Hutchison, J. Léonard, C. Genet, S. Haacke, and T.W. Ebbesen, "Polariton dynamics under strong light–molecule coupling," ChemPhysChem **14**, 125–131 (2013) (cited on p. 95).

[151] JCMwave, *JCMsuite*, version 5.4.0 (JCMwave GmbH, Berlin, 2022) (cited on p. 96).

[152] R. Hunger, *An Introduction to Complex Differentials and Complex Differentiability*, Technical Report TUM-LNS-TR-07-06 (Technische Universität München, München, 2007) (cited on p. 111).

[153] A. Hjørungnes, *Complex-Valued Matrix Derivatives: With Applications in Signal Processing and Communications* (Cambridge University Press, Cambridge, UK, 2011) (cited on p. 111).

[154] C. Rollo, *cmcrameri*, version 1.9 (2024) (cited on pp. 116, 118, 133, 135–136, 138, 158, 179, 205).

[155] F. Crameri, *Scientific colour maps*, version 8.0.1 (Zenodo, 2023) (cited on pp. 116, 118, 133, 135–136, 138, 158, 179, 205).

[156] A.H. Sihvola, "Effective-medium theories for bi-isotropic mixtures," in *Advances in Complex Electromagnetic Materials*, Ed. by A. Priou, A. Sihvola, S. Tretyakov, and A. Vinogradov (Springer, Dordrecht, 1997), pp. 131–144 (cited on p. 125).

[157] B. Michel, A. Lakhtakia, W.S. Weiglhofer, and T.G. Mackay, "Incremental and differential Maxwell Garnett formalisms for bi-anisotropic composites," Compos. Sci. Technol. **61**, 13–18 (2001) (cited on p. 125).

[158] S. Tretyakov, *Analytical Modeling in Applied Electromagnetics* (Artech House, Boston, 2003) (cited on p. 125).

[159] I. Sersic, C. Tuambilangana, T. Kampfrath, and A.F. Koenderink, "Magnetoelectric point scattering theory for metamaterial scatterers," Phys. Rev. B **83**, 245102 (2011) (cited on p. 125).

[160] P. Stehle, *Electromagnetic Chirality of an Isotropic, Chiral and Spherical Scatterer*, Master's Thesis (Karlsruher Institut für Technologie (KIT), Karlsruhe, 2018) (cited on p. 125).

[161] P. Scott, X. Garcia-Santiago, D. Beutel, C. Rockstuhl, M. Wegener, and I. Fernandez-Corbaton, "On enhanced sensing of chiral molecules in optical cavities," Appl. Phys. Rev. **7**, 041413 (2020) (cited on pp. 125, 164, 181).

[162] A. Griewank and A. Walther, *Evaluating Derivatives: Principles and Techniques of Algorithmic Differentiation*, 2nd ed. (SIAM, Philadelphia, 2008) (cited on p. 125).

[163] S. Burger, L. Zschiedrich, J. Pomplun, F. Schmidt, and B. Bodermann, "Fast simulation method for parameter reconstruction in optical metrology," in *Metrology, Inspection, and Process Control for Microlithography XXVII*, Ed. by A. Starikov and J.P. Cain, 8681 (2013), p. 868119 (cited on p. 125).

[164] T.W. Hughes, I.A.D. Williamson, M. Minkov, and S. Fan, "Forward-mode differentiation of Maxwell's equations," ACS Photonics **6**, 3010–3016 (2019) (cited on p. 125).

[165] A.M. Hammond, *High-Efficiency Topology Optimization for Very Large-Scale Integrated-Photonics Inverse Design*, Dissertation (Georgia Institute of Technology, Atlanta, 2022) (cited on p. 125).

[166] N. Asadova, J.D. Fischbach, R. Vallée, O. Kuster, Y. Augenstein, D. Vovchuk, A. Kharchevskii, P. Ginzburg, and C. Rockstuhl, "Gradient-based optimization of scatterer arrangements based on the T-matrix method," APL Photonics **11**, 056116 (2026) (cited on p. 125).

[167] M. Hentschel, M. Schäferling, X. Duan, H. Giessen, and N. Liu, "Chiral plasmonics," Sci. Adv. **3**, e1602735 (2017) (cited on pp. 126, 142).

[168] J.T. Collins, C. Kuppe, D.C. Hooper, C. Sibilia, M. Centini, and V.K. Valev, "Chirality and chiroptical effects in metal nanostructures: Fundamentals and current trends," Adv. Opt. Mater. **5**, 1700182 (2017) (cited on p. 126).

[169] V.K. Valev, J.J. Baumberg, C. Sibilia, and T. Verbiest, "Chirality and chiroptical effects in plasmonic nanostructures: Fundamentals, recent progress, and outlook," Adv. Mater. **25**, 2517–2534 (2013) (cited on p. 126).

[170] P.E. Stamatopoulou, S. Droulias, G.P. Acuna, N.A. Mortensen, and C. Tserkezis, "Reconfigurable chirality with achiral excitonic materials in the strong-coupling regime," Nanoscale **14**, 17581–17588 (2022) (cited on p. 126).

[171] T. Okamoto, "Near-field spectral analysis of metallic beads," in *Near-Field Optics and Surface Plasmon Polaritons*, Ed. by S. Kawata, Topics in Applied Physics 81 (Springer, Berlin, 2001), pp. 97–123 (cited on pp. 128–129).

[172] P. Drude, "Zur Elektronentheorie der Metalle," Ann. Phys. (Berl.) **306**, 566–613 (1900) (cited on p. 128).

[173] N.W. Ashcroft and N.D. Mermin, *Solid State Physics* (Harcourt, Fort Worth, TX, 1976) (cited on p. 128).

[174] P.B. Johnson and R.W. Christy, "Optical constants of the noble metals," Phys. Rev. B **6**, 4370–4379 (1972) (cited on p. 129).

[175] N.A. Mortensen, "Mesoscopic electrodynamics at metal surfaces," Nanophotonics **10**, 2563–2616 (2021) (cited on p. 129).

[176] M. Magnozzi, M. Ferrera, L. Mattera, M. Canepa, and F. Bisio, "Plasmonics of Au nanoparticles in a hot thermodynamic bath," Nanoscale **11**, 1140–1146 (2019) (cited on pp. 129–130).

[177] M.N. Polyanskiy, "Refractiveindex.info database of optical constants," Sci. Data **11**, 94 (2024) (cited on pp. 130, 150).

[178] V. Klimov, *Nanoplasmonics* (CRC, Boca Raton, FL, 2013) (cited on p. 133).

[179] P.S. Kalsi, *Spectroscopy of Organic Compounds*, 6th ed., reprinted (New Age International, New Delhi, 2005) (cited on p. 137).

[180] M. Sujith, E. Aiswarya, M. Mohankumar, M. Anzola, A. Painelli, C. Sissa, L. Grisanti, and K.G. Thomas, "Unraveling the handedness of chiral assemblies: The hidden role of interchromophoric interactions in bisignate CD," J. Phys. Chem. Lett. **16**, 7481–7489 (2025) (cited on p. 137).

[181] V. Volkov and R. Pfister, "Cotton effect in copper-proline complexes in the visible region," J. Chem. Educ. **82**, 1663 (2005) (cited on p. 137).

[182] N.S.S. Nizar, M. Sujith, K. Swathi, C. Sissa, A. Painelli, and K.G. Thomas, "Emergent chiroptical properties in supramolecular and plasmonic assemblies," Chem. Soc. Rev. **50**, 11208–11226 (2021) (cited on p. 137).

[183] J.A. Schellman and P. Oriel, "Origin of the Cotton effect of helical polypeptides," J. Chem. Phys. **37**, 2114–2124 (1962) (cited on p. 137).

[184] A. Rodger and D. Marshall, "Beginners guide to circular dichroism," Biochemist **43**, 58–64 (2021) (cited on p. 137).

[185] Z. Fan and A.O. Govorov, "Plasmonic circular dichroism of chiral metal nanoparticle assemblies," Nano Lett. **10**, 2580–2587 (2010) (cited on p. 137).

[186] B. Auguié, J.L. Alonso-Gómez, A. Guerrero-Martínez, and L.M. Liz-Marzán, "Fingers crossed: Optical activity of a chiral dimer of plasmonic nanorods," J. Phys. Chem. Lett. **2**, 846–851 (2011) (cited on p. 137).

[187] C. Tserkezis, A.T.M. Yeşilyurt, J.-S. Huang, and N.A. Mortensen, "Circular dichroism in nanoparticle helices as a template for assessing quantum-informed models in plasmonics," ACS Photonics **5**, 5017–5024 (2018) (cited on p. 137).

[188] J. Bisgard, *Analysis and Linear Algebra: The Singular Value Decomposition and Applications*, Student Mathematical Library 94 (Amer. Math. Soc., Providence, 2021) (cited on p. 140).

[189] R.N.S. Suryadharma, M. Fruhnert, C. Rockstuhl, and I. Fernandez-Corbaton, "Singular-value decomposition for electromagnetic-scattering analysis," Phys. Rev. A **95**, 053834 (2017) (cited on p. 140).

[190] B. Frank, X. Yin, M. Schäferling, J. Zhao, S.M. Hein, P.V. Braun, and H. Giessen, "Large-area 3D chiral plasmonic structures," ACS Nano **7**, 6321–6329 (2013) (cited on p. 142).

[191] L. Hu, Y. Huang, L. Pan, and Y. Fang, "Analyzing intrinsic plasmonic chirality by tracking the interplay of electric and magnetic dipole modes," Sci. Rep. **7**, 11151 (2017) (cited on p. 142).

[192] T.A.R. Purcell and T. Seideman, "Modeling the chiral imprinting response of oriented dipole moments on metal nanostructures," ACS Photonics **5**, 4801–4809 (2018) (cited on p. 142).

[193] T. Wu, Z. Luo, H. Wang, Z. Zhang, G. Wang, and F. Bai, "Chiral plasmonic structures: From intrinsically optical properties to nanophotonic applications," ACS Mater. Lett. **7**, 2617–2632 (2025) (cited on p. 142).

[194] B. Zerulla, R. Venkitakrishnan, D. Beutel, M. Krstić, C. Holzer, C. Rockstuhl, and I. Fernandez-Corbaton, "A T-matrix based approach to homogenize artificial materials," Adv. Opt. Mater. **11**, 2201564 (2023) (cited on p. 144).

[195] D. Grzelak, M. Tupikowska, D. Vila-Liarte, D. Beutel, M. Bagiński, S. Parzyszek, M. Góra, C. Rockstuhl, L.M. Liz-Marzán, and W. Lewandowski, "Liquid crystal templated chiral plasmonic films with dynamic tunability and moldability," Adv. Funct. Mater. **32**, 2111280 (2022) (cited on p. 146).

[196] P.D. Fowler, "Quantification of chirality: Attempting the impossible," Symmetry Cult. Sci. **16**, 321–334 (2005) (cited on p. 148).

[197] A.B. Buda, T. Auf der Heyde, and K. Mislow, "On quantifying chirality," Angew. Chem., Int. Ed. **31**, 989–1007 (1992) (cited on p. 148).

[198] I. Fernandez-Corbaton, M. Fruhnert, and C. Rockstuhl, "Objects of maximum electromagnetic chirality," Phys. Rev. X **6**, 031013 (2016) (cited on pp. 148–149).

[199] M. Vavilin and I. Fernandez-Corbaton, "Multidimensional measures of electromagnetic chirality and their conformal invariance," New J. Phys. **24**, 033022 (2022) (cited on p. 149).

[200] M. Vavilin, *Polychromatic T-Matrix: Group-Theoretical Derivation and Applications*, Dissertation (Karlsruher Institut für Technologie (KIT), Karlsruhe, 2024) (cited on p. 149).

[201] X. Garcia-Santiago, M. Hammerschmidt, J. Sachs, S. Burger, H. Kwon, M. Knöller, T. Arens, P. Fischer, I. Fernandez-Corbaton, and C. Rockstuhl, "Toward maximally electromagnetically chiral scatterers at optical frequencies," ACS Photonics **9**, 1954–1964 (2022) (cited on pp. 149–150, 155, 160, 181).

[202] P. Woźniak, I.D. Leon, K. Höflich, C. Haverkamp, S. Christiansen, G. Leuchs, and P. Banzer, "Chiroptical response of a single plasmonic nanohelix," Opt. Express **26**, 19275–19293 (2018) (cited on pp. 149, 160, 181).

[203] K. Höflich, T. Feichtner, E. Hansjürgen, C. Haverkamp, H. Kollmann, C. Lienau, and M. Silies, "Resonant behavior of a single plasmonic helix," Optica **6**, 1098–1105 (2019) (cited on pp. 149, 160, 181).

[204] P. Woźniak, I.D. Leon, K. Höflich, G. Leuchs, and P. Banzer, "Interaction of light carrying orbital angular momentum with a chiral dipolar scatterer," Optica **6**, 961–965 (2019) (cited on pp. 149, 160, 181).

[205] R. Lingstädt, F. Davoodi, K. Elibol, M. Taleb, H. Kwon, P. Fischer, N. Talebi, and P.A. Van Aken, "Electron beam induced circularly polarized light emission of chiral gold nanohelices," ACS Nano **17**, 25496–25506 (2023) (cited on pp. 149, 160, 181).

[206] A. Tsarapkin, L. Zurak, K. Maćkosz, L. Löffler, V. Deinhart, I. Utke, T. Feichtner, and K. Höflich, "Double helical plasmonic antennas," Adv. Funct. Mater. **36**, 2507471 (2026) (cited on pp. 149, 160, 181).

[207] X. García Santiago, *Numerical Methods for Shape Optimization of Photonic Nanostructures*, Dissertation (Karlsruher Institut für Technologie (KIT), Karlsruhe, 2021) (cited on p. 150).

[208] H.-J. Hagemann, W. Gudat, and C. Kunz, *Optical Constants from the Far Infrared to the X-Ray Region: Mg, Al, Cu, Ag, Au, Bi, C, and $Al_2O_3$*, DESY SR-74/7 (Deutsches Elektronen-Synchroton, Hamburg, 1974) (cited on p. 150).

[209] H.-J. Hagemann, W. Gudat, and C. Kunz, "Optical constants from the far infrared to the x-ray region: Mg, Al, Cu, Ag, Au, Bi, C, and $Al_2O_3$," J. Opt. Soc. Am. **65**, 742 (1975) (cited on p. 150).

[210] P.-I. Schneider, X. Garcia Santiago, V. Soltwisch, M. Hammerschmidt, S. Burger, and C. Rockstuhl, "Benchmarking five global optimization approaches for nano-optical shape optimization and parameter reconstruction," ACS Photonics **6**, 2726–2733 (2019) (cited on p. 151).

[211] A. Canaguier-Durand, J.A. Hutchison, C. Genet, and T.W. Ebbesen, "Mechanical separation of chiral dipoles by chiral light," New J. Phys. **15**, 123037 (2013) (cited on p. 163).

[212] M.L. Solomon, J. Hu, M. Lawrence, A. García-Etxarri, and J.A. Dionne, "Enantiospecific optical enhancement of chiral sensing and separation with dielectric metasurfaces," ACS Photonics **6**, 43–49 (2019) (cited on p. 163).

[213] J. Martínez-Romeu, I. Diez, S. Golat, F.J. Rodríguez-Fortuño, and A. Martínez, "Longitudinal chiral forces in photonic integrated waveguides to separate particles with realistically small chirality," Nanophotonics **13**, 4275–4289 (2024) (cited on p. 163).

[214] J. Martínez-Romeu, D. Arenas-Ortega, I. Diez, and A. Martínez, "Chiral optical forces in a slot waveguide for the separation of molecules in gas," Opt. Lett. **51**, 45–48 (2026) (cited on p. 163).

[215] G. Tkachenko and E. Brasselet, "Optofluidic sorting of material chirality by chiral light," Nat. Commun. **5**, 3577 (2014) (cited on p. 163).

[216] G. Tkachenko, A. Suda, H.-Y. Ahn, Y. Iida, I. Kurihara, K. Saito, I.H. Ha, Y. Xuan, K.T. Nam, H. Okamoto, and M. Sadgrove, "Chirality-selective optical transport of nanoparticles in the evanescent field of a nanofibre," Nat. Commun. **17**, 3463 (2026) (cited on p. 163).

[217] N.S. Baßler, A. Aiello, K.P. Schmidt, C. Genes, and M. Reitz, "Metasurface-based hybrid optical cavities for chiral sensing," Phys. Rev. Lett. **132**, 043602 (2024) (cited on p. 163).

[218] J.A. Hutchison, T. Schwartz, C. Genet, E. Devaux, and T.W. Ebbesen, "Modifying chemical landscapes by coupling to vacuum fields," Angew. Chem., Int. Ed. **51**, 1592–1596 (2012) (cited on p. 163).

[219] A. Thomas, J. George, A. Shalabney, M. Dryzhakov, S.J. Varma, J. Moran, T. Chervy, X. Zhong, E. Devaux, C. Genet, J.A. Hutchison, and T.W. Ebbesen, "Ground-state chemical reactivity under vibrational coupling to the vacuum electromagnetic field," Angew. Chem., Int. Ed. **55**, 11462–11466 (2016) (cited on p. 163).

[220] A. Sau, K. Nagarajan, B. Patrahau, L. Lethuillier-Karl, R.M.A. Vergauwe, A. Thomas, J. Moran, C. Genet, and T.W. Ebbesen, "Modifying Woodward–Hoffmann stereoselectivity under vibrational strong coupling," Angew. Chem., Int. Ed. **60**, 5712–5717 (2021) (cited on p. 163).

[221] J. Fregoni, F.J. Garcia-Vidal, and J. Feist, "Theoretical challenges in polaritonic chemistry," ACS Photonics **9**, 1096–1107 (2022) (cited on p. 163).

[222] P.A. Thomas, W.J. Tan, V.G. Kravets, A.N. Grigorenko, and W.L. Barnes, "Non-polaritonic effects in cavity-modified photochemistry," Adv. Mater. **36**, 2309393 (2024) (cited on p. 163).

[223] A. Maksimov, E. Filatov, I.I. Tartakovskii, V. Kulakovskii, S. Tikhodeev, C. Schneider, and S. Höfling, "Circularly polarized laser emission from an electrically pumped chiral microcavity," Phys. Rev. Appl. **17**, L021001 (2022) (cited on p. 163).

[224] I. Katsantonis, A.C. Tasolamprou, E.N. Economou, T. Koschny, and M. Kafesaki, "Ultrathin, dynamically controllable circularly polarized emission laser enabled by resonant chiral metasurfaces," ACS Photonics **12**, 71–78 (2025) (cited on p. 163).

[225] S. Kim, S.-C. An, Y. Kim, Y.S. Shin, A.A. Antonov, I.C. Seo, B.H. Woo, Y. Lim, M.V. Gorkunov, Y.S. Kivshar, J.Y. Kim, and Y.C. Jun, "Chiral electroluminescence from thin-film perovskite metacavities," Sci. Adv. **9**, eadh0414 (2023) (cited on p. 163).

[226] A. Taradin and D.G. Baranov, "Chiral light in single-handed Fabry-Perot resonators," J. Phys. Conf. Ser. **2015**, 012012 (2021) (cited on p. 164).

[227] H. Hübener, U. De Giovannini, C. Schäfer, J. Andberger, M. Ruggenthaler, J. Faist, and A. Rubio, "Engineering quantum materials with chiral optical cavities," Nat. Mater. **20**, 438–442 (2021) (cited on p. 164).

[228] K. Voronin, A.S. Taradin, M.V. Gorkunov, and D.G. Baranov, "Single-handedness chiral optical cavities," ACS Photonics **9**, 2652–2659 (2022) (cited on p. 164).

[229] S.A. Dyakov, N.S. Salakhova, A.V. Ignatov, I.M. Fradkin, V.P. Panov, J.-K. Song, and N.A. Gippius, "Chiral light in twisted Fabry–Pérot cavities," Adv. Opt. Mater. **12**, 2302502 (2024) (cited on p. 164).

[230] T. Jia, Y. Jeon, L. Feng, H. Kim, B. Li, G. Rui, and J. Rho, "Superchirality induced ultrasensitive chiral detection in high-Q optical cavities," Opto-Electron. Adv. **8**, 250079–14 (2025) (cited on p. 164).

[231] S. Dyakov, I. Smagin, N. Salakhova, O. Blokhin, D.G. Baranov, I. Fradkin, and N. Gippius, "Strong coupling of chiral light with chiral matter: A macroscopic study," Optica **12**, 1406–1416 (2025) (cited on p. 164).

[232] E. Plum and N.I. Zheludev, "Chiral mirrors," Appl. Phys. Lett. **106**, 221901 (2015) (cited on p. 164).

[233] B. Semnani, J. Flannery, R. Al Maruf, and M. Bajcsy, "Spin-preserving chiral photonic crystal mirror," Light Sci. Appl. **9**, 23 (2020) (cited on p. 164).

[234] J. Yan, I. Katsantonis, S. Papamakarios, P. Konstantakis, M. Loulakis, T. Koschny, M. Farsari, S. Tzortzakis, and M. Kafesaki, "3D-printed mirror-less helicity preserving metasurface "mirror" for THz applications," Nanophotonics **14**, 4029–4038 (2025) (cited on p. 164).

[235] N. Salakhova, A. Demenev, O. Klimenko, V. Kulakovskii, V. Antonov, N. Gippius, and S. Dyakov, "Broadband wide-view all-dielectric handedness-preserving mirror," (2026) arXiv:2601.08695 [physics.optics] (cited on p. 164).

[236] A. Pozharkova, O. Blokhin, S.A. Dyakov, and D.G. Baranov, "Low-symmetry lattices of non-chiral meta-atoms for resonant handedness-preserving reflection," (2026) arXiv:2606.12067 [physics.optics] (cited on p. 164).

[237] J. Feis, D. Beutel, J. Köpfler, X. Garcia-Santiago, C. Rockstuhl, M. Wegener, and I. Fernandez-Corbaton, "Helicity-preserving optical cavity modes for enhanced sensing of chiral molecules," Phys. Rev. Lett. **124**, 033201 (2020) (cited on pp. 164, 166, 179).

[238] D. Beutel, P. Scott, M. Wegener, C. Rockstuhl, and I. Fernandez-Corbaton, "Enhancing the optical rotation of chiral molecules using helicity preserving all-dielectric metasurfaces," Appl. Phys. Lett. **118**, 221108 (2021) (cited on p. 164).

[239] P. Scott, M. Nyman, B. Zerulla, A.F. Pérez Mellor, T. Bürgi, C. Rockstuhl, I. Fernandez-Corbaton, and M. Wegener, "A metasurface-based microcavity for enhanced vibrational circular dichroism spectroscopy," in *Photonic and Phononic Properties of Engineered Nanostructures XV*, Ed. by A. Adibi, S.-Y. Lin, and A. Scherer, Proceedings of SPIE 13377 (2025) (cited on pp. 164, 181).

[240] R. Schurr, *Inverse Scattering Problems and Shape Optimization with Respect to Electromagnetic Chirality for Long Tubular Objects*, Dissertation (Karlsruher Institut für Technologie (KIT), Karlsruhe, 2026) (cited on p. 181).

[241] M. Decker, M. Ruther, C.E. Kriegler, J. Zhou, C.M. Soukoulis, S. Linden, and M. Wegener, "Strong optical activity from twisted-cross photonic metamaterials," Opt. Lett. **34**, 2501–2503 (2009) (cited on p. 188).

[242] R. Zhao, T. Koschny, and C.M. Soukoulis, "Chiral metamaterials: Retrieval of the effective parameters with and without substrate," Opt. Express **18**, 14553–14567 (2010) (cited on p. 188).

[243] K. Baranov, D. Vagin, and M.A. Gorlach, "Effective chiral response of anisotropic multilayered metamaterials," Phys. Rev. B **110**, 235150 (2024) (cited on p. 188).

[244] T. Zhao, X. Dang, K. Manos, S. Zang, J. Mandal, M. Chen, and G.H. Paulino, "Modular chiral origami metamaterials," Nature **640**, 931–940 (2025) (cited on p. 188).

[245] B.A.R. Zerulla, *Photonic Devices Made from Molecular Materials: A Multi-Scale Modeling Approach*, Dissertation (Karlsruher Institut für Technologie (KIT), Karlsruhe, 2024) (cited on p. 189).

[246] M.I. Mishchenko, L.D. Travis, and A.A. Lacis, *Scattering, Absorption, and Emission of Light by Small Particles*, 3rd revised electronic ed. (Cambridge University Press, Cambridge, UK, 2002) (cited on pp. 193–195, 197).

[247] G.B. Arfken, H.J. Weber, and F.E. Harris, *Mathematical Methods for Physicists: A Comprehensive Guide*, 7th ed. (Elsevier, Amsterdam, 2013) (cited on pp. 193–195).

[248] E.U. Condon and G.H. Shortley, *The Theory of Atomic Spectra*, reprinted with corrections (Cambridge University Press, Cambridge, UK, 1959) (cited on p. 194).

[249] J.G. Van Bladel, *Electromagnetic Fields*, 2nd ed. (Wiley, Hoboken, NJ, 2007) (cited on p. 199).

[250] S. Stein, "Addition theorems for spherical wave functions," Q. Appl. Math. **19**, 15–24 (1961) (cited on p. 200).

[251] O.R. Cruzan, "Translational addition theorems for spherical vector wave functions," Q. Appl. Math. **20**, 33–40 (1962) (cited on p. 200).

[252] Y.-l. Xu, "Efficient evaluation of vector translation coefficients in multiparticle light-scattering theories," J. Comput. Phys. **139**, 137–165 (1998) (cited on p. 201).

[253] D.A. Varshalovich, A.N. Moskalev, and V.K. Khersonskii, *Quantum Theory of Angular Momentum* (World Scientific, Singapore, 1988) (cited on p. 201).

[254] H. Dachsel, "Fast and accurate determination of the Wigner rotation matrices in the fast multipole method," J. Chem. Phys. **124**, 144115 (2006) (cited on p. 201).

[255] A. Erdélyi, "Zur Theorie der Kugelwellen," Physica **4**, 107–120 (1937) (cited on p. 202).

[256] R.C. Wittmann, "Spherical wave operators and the translation formulas," IEEE Trans. Antennas Propag. **36**, 1078–1087 (1988) (cited on pp. 202, 204).

[257] I. Bialynicki-Birula, E.T. Newman, J. Porter, J. Winicour, B. Lukacs, Z. Perjes, and A. Sebestyen, "A note on helicity," J. Math. Phys. **22**, 2530–2532 (1981) (cited on p. 213).

[258] J.H. Seinfeld and S.N. Pandis, *Atmospheric Chemistry and Physics: From Air Pollution to Climate Change*, 2nd ed. (Wiley, Hoboken, NJ, 2006) (cited on pp. 226–227).